Resource-aware motion control

Resource-Aware Motion Control

Feedforward, Learning and Feedback

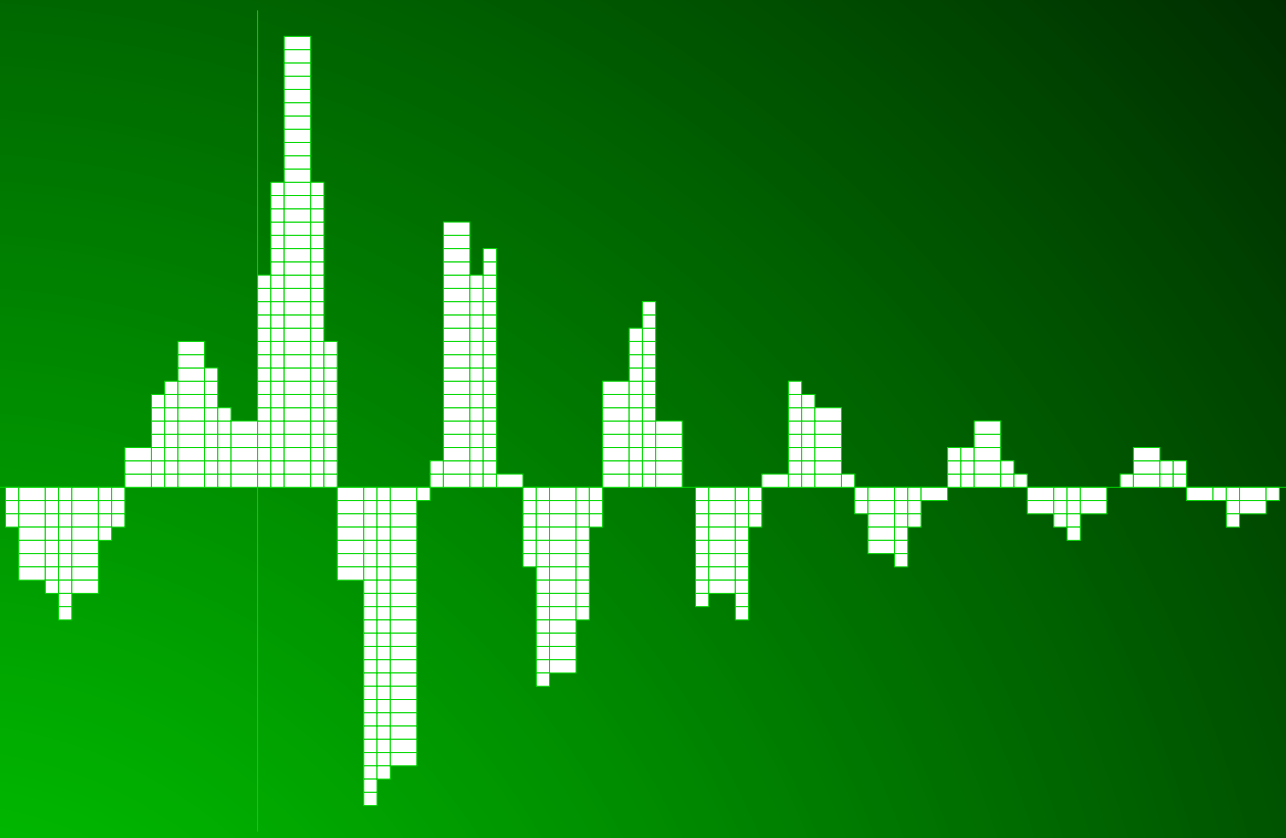

Jurgen van Zundert

Resource-Aware Motion Control

Feedforward, Learning, and Feedback

Jurgen van Zundert

The author has successfully completed the educational program of the Graduate School of the Dutch Institute of Systems and Control (DISC).

This work is part of the research programme Robust Cyber Physical Systems (RCPS) with project number 12694, which is (partly) financed by the Netherlands Organisation for Scientific Research (NWO).

A catalogue record is available from the Eindhoven University of Technology Library.
ISBN: 978-90-386-4630-5
Reproduction: Dereumaux, Eindhoven, The Netherlands.

Resource-Aware Motion Control
Feedforward, Learning, and Feedback

PROEFSCHRIFT

ter verkrijging van de graad van doctor aan de
Technische Universiteit Eindhoven, op gezag van de
rector magnificus prof.dr.ir. F.P.T. Baaijens, voor een
commissie aangewezen door het College voor
Promoties, in het openbaar te verdedigen
op woensdag 28 november 2018 om 16.00 uur

door

Jurgen Cornelis Dimphna van Zundert

geboren te Zundert

Dit proefschrift is goedgekeurd door de promotoren en de samenstelling van de promotiecommissie is als volgt:

voorzitter:	prof.dr. L.P.H. de Goey
1e promotor:	dr.ir. T.A.E. Oomen
2e promotor:	prof.dr.ir. W.P.M.H. Heemels
leden:	prof.dr.ir. H. Butler
	dr. B. Chu (University of Southampton)
	dr. H. Fujimoto (University of Tokyo)
	prof.dr.ir. J.P.M. Voeten
adviseur:	dr.ir. W.H.T.M. Aangenent (ASML)

Het onderzoek dat in dit proefschrift wordt beschreven is uitgevoerd in overeenstemming met de TU/e Gedragscode Wetenschapsbeoefening.

Summary

Resource-Aware Motion Control
Feedforward, Learning, and Feedback

There is an ever-increasing desire for technological advancements in many areas, including health care, additive manufacturing, space exploration, nanotechnology, and transportation. Motion systems have an essential role in all these areas, for example, by moving components or adding/removing material. The desire for technological advancements leads to a demand for increased throughput and accuracy at low cost in motion systems. This calls for new designs of motion systems.

The design of motion systems involves many different domains, including embedded software and control engineering. Traditionally, the different domains are considered separately, leading to a suboptimal trade-off between performance and cost. This thesis provides a novel resource-aware control design framework for motion systems that facilitates in bridging the gap between the different domains and enables to transcend the traditional performance/cost trade-off in motion systems.

A crucial factor that affects both the performance and the cost of motion systems is the controller implementation. Driven by the exponential growth in computing power, known as Moore's law, digital control has become the prevailing type of controller implementation. An important aspect in digital control, which directly influences the implementation cost and performance, is the sampling scheme, i.e., the selection of data that is available to the digital controller. Traditionally, control engineers demand equidistant, time-triggered sampling schemes from the embedded software engineers to enable the use of well-established frequency-domain control design techniques. In this thesis, the equidistant sampling paradigm is abandoned and non-equidistant sampling schemes are explored. This results in a unified framework for resource-aware motion control. On the one hand, it is driven by industrial application as it provides a direct extension of state-of-the-art industrial control designs. On the

other hand, it incorporates solid control theory and in particular linear periodically time-varying (LPTV) system theory.

The thesis covers feedback, feedforward, and learning control. In particular, a new feedback control design approach for LPTV systems is presented. The approach enables to go beyond feedback control for equidistant sampling through a sequence of industry-standard loop-shaping design steps that are supported by solid LPTV system theory. Furthermore, a comprehensive overview of system inversion approaches for nonminimum-phase, linear time-invariant (LTI) systems is presented, including several new approaches, which leads to new insights for both feedforward and learning control. Based on this, feedforward control approaches for LPTV systems are presented that outperform traditional LTI approaches. The approaches address, among other aspects, nonminimum-phase dynamics, intersample behavior, and overactuation. Similarly, learning control approaches for LPTV systems are presented, which achieve superior performance for repeating tasks, but also for non-exactly repeating tasks through basis functions for LPTV systems. Finally, a method for joint design of feedback, feedforward, and learning control is presented.

Experimental case studies on a variety of relevant industrial motion systems, including industrial printing systems and wafer stage setups, confirm the advantages of the proposed control approaches. The overall result is a resource-aware motion control design framework with new theoretical contributions and new perspectives for industrial motion control.

Contents

Chapter 1

Introduction

1.1 The long history of control: From mechanical to embedded implementations

Technology has a large impact on daily life and control plays a major role in the technological development. Key examples of influential technological innovations are, see for example Fallows (2013), the printing press (1430), steam engines (1712), telephones (1876), internal combustion engines (late 19th century), automobiles (late 19th century), airplanes (1903), radios (1906), televisions (early 20th century), personal computers (1970s), and smartphones (2000). All these devices need to be manufactured. Starting from the industrial revolution around 1760 and driven by a demand for increased productivity and accuracy at low cost, many of the manufacturing processes are performed by machines. Nowadays, most of these processes are even automated, for example, car assembly lines, packaging, welding, printing, and production lines. Virtually all manufacturing processes involve control systems to regulate temperature, to control chemical compositions, to ensure goods arrive on time, to weld, to accurately place components, and so on. Besides manufacturing, control also finds application in other areas such as power, communications, transportation, and many more (Murray et al., 2003). Control thus plays a major role in technological development and is everywhere around us in daily life.

The first control systems can be traced back to over two thousand years ago. One of the first feedback control mechanism is found in the ancient water clock of Ktesibios in Alexandria, Egypt, around the third century B.C. (Kang, 2016) shown in Figure 1.1(a). For more than 1800 years, the water clock was the most accurate clock, until the Dutch physicist Christiaan Huygens invented the pendulum clock in 1656. The industrial revolution (1760 to 1830) marks the

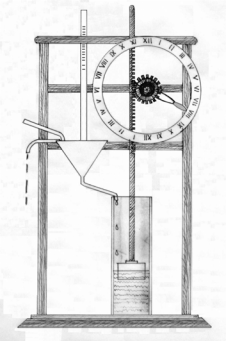

(a) Ktesibios water clock. The water clock keeps time by measuring the amount of water of a constant water flow from one chamber to another. A floater is used to regulate a valve and keep the water level in the top chamber constant

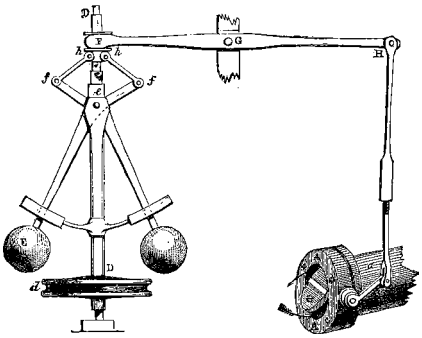

(b) Centrifugal governor for a Watt steam engine to maintain constant engine speed. An increase in engine speed moves the balls outside, which, via linkages, closes the valve and thereby reduce the engine speed. Image: Routledge (1881, Figure 4).

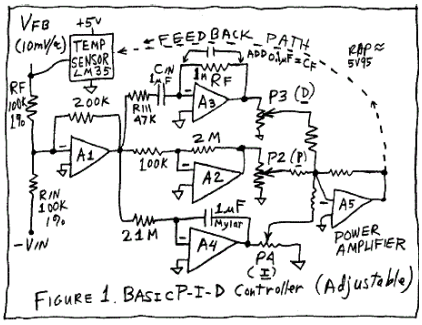

(c) Schematic drawing of an electrical implementation of a PID controller using resistors, capacitors, and amplifiers. Image from Electronic Design, August 4, 1977.

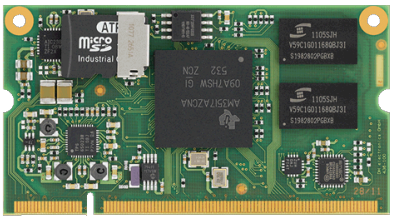

(d) Embedded control system. Image: DHCOM AM35xx from DH Electronics.

Figure 1.1. Overview of control implementations over time. The first control designs, including (a) and (b), are based on mechanical implementations. Later, electrical implementations as shown in (c) became popular. Nowadays, the control is digital and embedded in software (d).

transition to new manufacturing processes and led to an increase in control applications and designs. A prime and well-known example is the centrifugal governor in the Watt steam engine in 1788 shown in Figure 1.1(b). Until a few decades ago, all control designs were based on mechanical implementations. From then on, electrical implementations using circuits, see Figure 1.1(c), became popular. Nowadays, controllers are implemented digitally and embedded in software as shown in Figure 1.1(d). An embedded control system is in essence a technology containing a microprocessor for control. Embedded controllers find, among others, application in systems consisting of combinations of cyber (computation, communication, control) and physical (sensors, mechanics) elements, known as cyber-physical systems (Khaitan and McCalley, 2015), a term emerged around 2006 (Lee, 2015). In summary, control has a long history in which the controller implementations shifted from mechanical to embedded implementations.

1.2 The impact of high-tech systems on society

At present, control technology finds application in many high-tech systems. In this thesis, the focus is on control of high-tech motion systems such as printing systems (Pond, 2000), X-ray systems (Suetens, 2009, Chapter 3), electron microscopes (Egerton, 2016), scanning probe microscopes (Voigtländer, 2015), and semiconductor lithography systems (Mack, 2007). All these systems have a large impact on society, as highlighted by the following examples of X-ray systems and semiconductor lithography systems.

Since the discovery of X-ray by Wilhelm Röntgen in 1895, X-ray systems have become a fundamental tool for medical imaging. Over the years, X-ray systems have been used to trace the process of digestion, to diagnose tuberculosis, to detect broken bones, and to provide cross-sectional images of human bodies using computed tomography (CT) scans. The variety of medical applications makes X-ray systems vital instruments in health care and an indispensable tool in understanding the human body.

Consumer electronics, such as smartphones, televisions, and laptops, are everywhere around us in daily life. Semiconductor lithography machines play a key role in the technological development of these devices. To meet the ever-increasing societal demand for more functionality in consumer electronics, integrated circuits, which are at the heart of these devices, with smaller feature sizes are required. A key step in the production of integrated circuits is the lithography step performed by semiconductor lithography machines. In this step, a blueprint of the integrated circuit is scaled and projected on a thin slice of silicon to create the feature on the integrated circuit. This process requires extreme accuracies up to nanometer level and the quality of the structures directly determines the functionality of the integrated circuit and hence the electronic device. Semiconductor lithography machines are thus key enablers in the technological

advancement of consumer electronics.

The examples show that the impact of high-tech motion systems on society is large. A key enabler to meet the ever-increasing performance and cost requirements for these systems are high-tech motion systems.

1.3 Control design and implementation for high-tech motion systems

High-tech motion systems are mechatronic systems (Munnig Schmidt et al., 2011; Verbaan, 2015) and the design involves various disciplines such as mechanics, electronics, embedded software, control engineering, computer engineering, and systems engineering. This thesis focuses on the embedded control aspect of the mechatronics design.

Embedded software is a relatively new discipline, especially compared to control, see also Section 1.1. One of the first modern embedded systems is the Apollo Guidance Computer in 1965 used for the computation and electronic interfaces for guidance, navigation, and control of the Apollo spacecraft (Hall, 1996). The main advantage of embedded controller implementations is that they provide implementation flexibility at low cost. The driving force for the widespread application of embedded control is the exponential growth in computing power shown in Figure 1.2(a) and known as Moore's law. It is named after Fairchild Semiconductor and Intel co-founder Gordon Moore who observed in 1965 that the number of components per integrated circuit doubled every year (Moore, 1965). In 1975, Moore revised it to doubling every two years (Moore, 1975), which is the current definition of Moore's law. Since the production cost of integrated circuits is mainly determined by feature sizes, the average production cost of transistors decreases exponentially as shown by Figure 1.2(b). These developments make embedded control accessible on a large scale and make them the main form of implementing control technology in high-tech motion systems.

Control design for motion systems evolved independently from embedded control. Starting from control approaches such as PID control (Åström and Hägglund, 1995), robust control (Zhou et al., 1996) and sampled-data control (Chen and Francis, 1995), the field of control lead to control approaches for motion systems such as $\mathcal{H}_2/\mathcal{H}_\infty$ control (Van de Wal et al., 2002), (mass) feedforward control, multirate control (Fujimoto et al., 2001), and learning control (Bristow et al., 2006; De Roover and Bosgra, 2000; Steinbuch, 2002). The solid control theory and variety of applications makes motion control indispensable in high-tech motion systems.

Embedded control for high-tech motion systems involves both the design and implementation of (motion) controllers. However, both domains evolved independently and are often considered as two separate domains during control design for high-tech systems.

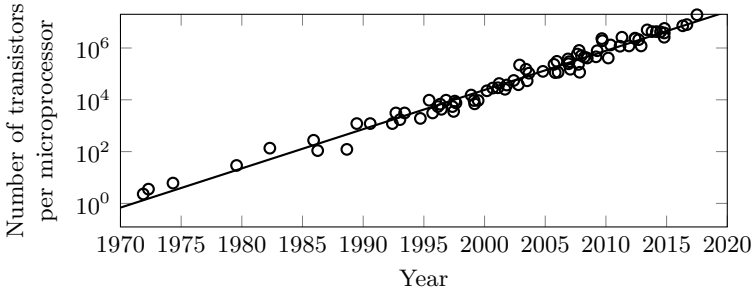

(a) Over a period of 42 years, the number of transistors per microprocessor has doubled every two years, i.e., increased with 42% every year. Source: Karl Rupp, "42 Years of Microprocessor Trend Data".

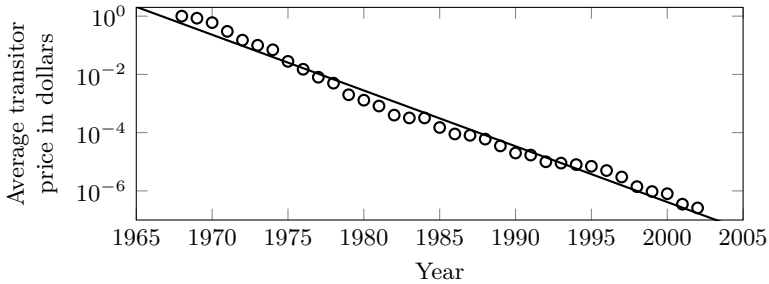

(b) The average transitor price decreases by 35% every year corresponding to a halving time of 19 months. Source: Kurzweil (2005, p. 59).

Figure 1.2. Moore's law: exponential growth in computation power and exponential decay in price.

1.4 Bridging the gap between control design and implementation

Traditional motion control approaches consider control design and implementation as two separate domains, resulting in a big gap between the two domains. The control engineer designs a controller for high performance and hands it over to the software engineer who implements the controller based on the available resources. How well the implemented controller matches the designed controller directly influences the true performance and is mainly determined by the cost of implementation. Indeed, higher implementation cost, i.e., more and/or better resources, allows for better performance. This directly leads to a performance/cost trade-off as illustrated in Figure 1.3. For the conventional two-step approach, the trade-off might be suboptimal due to the separate designs.

Resource-aware motion control approaches can bridge the gap between con-

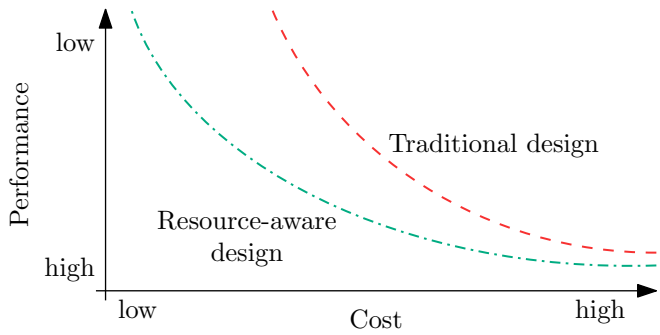

Figure 1.3. Traditional controller design and implementation leads to a performance/cost trade-off, where higher cost yields higher performance. Resource-aware control design enhances this trade-off.

troller design and implementation. By bridging the gap, the performance/cost trade-off can be significantly improved as illustated in Figure 1.3. The first steps towards bridging the gap are related to discrete-time sampled-data control in the 1960s (Zadeh, 1962) as illustrated in Figure 1.4(a). In the 1990s, the importance of discretization aspects and intersample behavior were recognized (Yamamoto, 1994; Chen and Francis, 1995). Further developments along this line mainly focus on $\mathcal{H}_\infty$-optimal and $\mathcal{H}_2$-optimal control, starting with Bamieh et al. (1991); Toivonen (1992); Bamieh and Pearson Jr. (1992); Yamamoto (1994); Chen and Francis (1995). However, the application of these model-based techniques to industrial motion systems is limited since (i) obtaining a parametric model is difficult; and (ii) expert knowledge is required for design.

In this thesis, a resource-aware control design approach is developed to bridge the gap between controller design and implementation for motion systems, aimed at application in industry. For this purpose, this thesis focuses on time-triggered control, i.e., the sampling/transmission instants are scheduled a priori based on time. Alternatives to time-triggered control are event-triggered control and self-triggered control, of which an introductory overview can be found in Heemels et al. (2012). In event-triggered control (Heemels et al., 2008; Tabuada, 2007), the triggering is based on continuous measurements. In self-triggered control (Anta and Tabuada, 2010; Wang and Lemmon, 2009), the triggering is precomputed based on predictions using received data and knowledge on the system dynamics. In view of the application in industry, time-triggered control is preferred since the sampling instances are known a priori and the sampling scheme is easy to implement. The required predictability of such a sampling scheme is provided by state-of-the-art platforms such as CompSOC (Goossens et al., 2017).

In view of the performance/cost trade-off in Figure 1.3, this thesis considers time-triggered control in which the sampling instances are distributed non-equidistantly in time. Note that, opposed to event-triggered and self-triggered

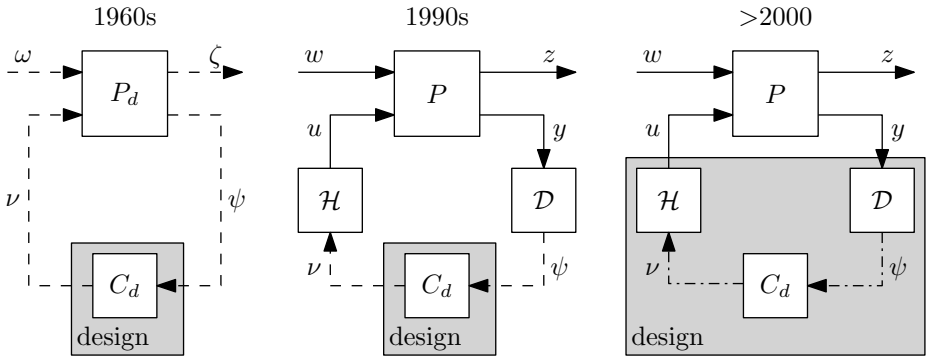

(a) In the 1960s, only the discrete-time system was considered.

(b) In the 1990s, the continuous-time system with discretization aspects and intersample behavior were considered.

(c) Starting in the 2000s, implementation and communication cost have become part of the performance variable z and the sampling scheme is part of the design.

Figure 1.4. Sampled-data control design in standard plant formulation throughout time. Over the years, more aspects are taken into account. In this thesis, the formulation in (c) is considered, where the communication and implementation cost are taken into account through periodic, non-equidistant time-triggered control.

control approaches, such non-equidistant sampling schemes are still periodic in nature due to periodic scheduling. The non-equidistant sampling scheme provides more design flexibility to balance the performance/cost trade-off than in conventional time-triggered control in which the sampling instances are distributed equidistantly in time. Indeed, equidistant sampling is a special case of non-equidistant sampling. The time-triggered control with periodic, non-equidistant sampling leads to a control design framework that addresses both performance and cost and thereby improves the overall performance/cost trade-off as illustrated in Figure 1.3.

1.5 Introduction to motion control design: Feedback, feedforward, and learning

In this section, the basics of motion control design are presented. The concepts are extensively used throughout the thesis. The three main types of control, i.e., feedback, feedforward, and learning control, are introduced.

A simple example of a motion system is shown in Figure 1.5. The system can be moved by actuator force u generated by, for example, a motor. The position y

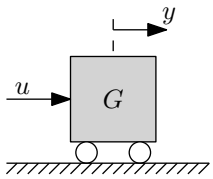

Figure 1.5. Example of a motion system. The system G can move in horizontal direction by applying an actuator force u. The position of the system y is measured through an encoder. The control objective is to let position y track a reference trajectory through design of actuator force u.

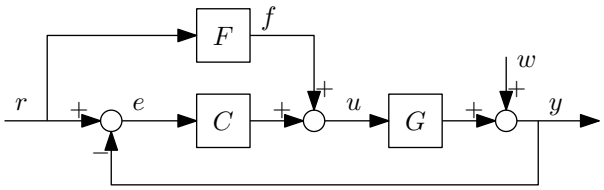

Figure 1.6. Traditional two degrees-of-freedom control of system G, consisting of feedback controller C and feedforward controller F.

of the system is measured through, for example, an encoder. The aim in motion control design is to determine u such that there is perfect tracking $y = r$, where r denotes the desired position of the system and may vary over time. The control input u is determined by control algorithms. A common approach (Franklin et al., 2015; Steinbuch et al., 2010) is to compose the control input as

$$u = Ce + Fr, \tag{1.1}$$

where C is a feedback controller, $e = r - y$ is the tracking error, F is a feedforward controller, and r is the reference trajectory. Note that these relations are in the Laplace domain. The control architecture is captured in the block diagram shown in Figure 1.6. Note that position measurement y is contaminated by disturbances w, including sensor noise. The tracking error $e = r - y$ is given by

$$e = \underbrace{S}_{\text{FB}}((I - G\underbrace{F}_{\text{FF}})r - w), \tag{1.2}$$

with (output) sensitivity function $S = (I + GC)^{-1}$. From (1.2) it directly follows that i) $S = 0$ eliminates all errors, and ii) $F = G^{-1}$ eliminates the reference induced error $e_r = S(I - GF)r$. Next, both these control designs are elaborated on.

The first design $S = 0$ relates to the feedback controller C. The feedback control action is based on measurements y of the position. The measurement is compared with the desired trajectory r and the controller action is based on

the difference $e = r - y$. However, achieving $S = 0$ is unfeasible due to Bode's sensitivity integral (Seron et al., 1997), also known as the waterbed effect. This is caused by the inherent causality of feedback control as it relies on measurements of output y. Since feedback control is based on measurements, it can provide robustness against model uncertainties (Zhou et al., 1996). Furthermore, it is the only means to attenuate the error $e_w = Sw$ induced by the unknown disturbances w.

The second design $F = G^{-1}$ relates to the feedforward controller F. The feedforward control action is based on knowledge of the system. Indeed, if G is exactly known, the inverse model feedforward controller $F = G^{-1}$ yields $e_r = S(I - GF)r = 0$. Note that noncausality of G^{-1} is not an issue since no measured signals are involved and r is generally known in advance. Obviously, the performance of the inverse model feedforward controller strongly depends on the model accuracy. Due to the inherent mismatch between the physical system and the model, i.e., $F \neq G^{-1}$, the achievable performance is moderate.

An extension to feedforward control approaches are learning control approaches (Bristow et al., 2006; Moore, 1993). Learning control approaches iteratively update the feedforward action based on models and data of previous tasks and/or predictions of future tasks (Chu et al., 2016). An example of learning control is iterative learning control (ILC). The concept of ILC is illustrated in Figure 1.7, where for simplicity of notation it is assumed that $w = 0$. In standard ILC, finite-time tasks are considered and the feedforward signal rather than the feedforward controller F is updated. In the first task, task $j = 0$, a feedforward signal f_0 is applied yielding $e_0 = Sr - SGf_0$. In the second task, task $j = 1$, the feedforward signal is updated by learning from the error of the previous task through $f_1 = f_0 + Le_0$, with learning filter L. Repeating this process yields the learning update

$$f_{j+1} = f_j + Le_j \tag{1.3}$$

and error dynamics

$$\begin{aligned} e_{j+1} &= Sr - SGf_{j+1} && \text{(1.4a)} \\ &= e_j - SG(f_{j+1} - f_j) && \text{(1.4b)} \\ &= (I - SGL)e_j. && \text{(1.4c)} \end{aligned}$$

It directly follows that $e_{j+1} = 0$ for $L = (SG)^{-1}$, which faces the same challenges as feedforward control. The main advantage of ILC is that, even if there are model mismatches $L \neq (SG)^{-1}$, it can still obtain high performance. The key aspect is convergence of the error (1.4), i.e., $\|e_{j+1}\| < \|e_j\|$. Essentially, ILC exploits the fact that many systems perform repeating tasks, i.e., $r_j = r$, for all j, which is exploited in (1.4). As a result, ILC is able to compensate for all repeating disturbances, even if the related dynamics are not modeled.

The presented feedforward approaches either result in moderate performance for a large class of reference trajectories (inverse model feedforward) or high

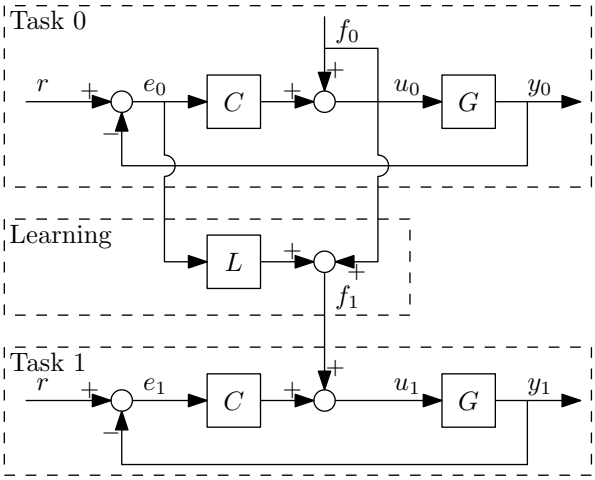

Figure 1.7. Two tasks of iterative learning control (ILC) using update (1.3).

performance for a specific reference trajectory (ILC). This directly leads to the trade-off between performance and task flexibility visualized in Figure 1.8. To achieve high performance with high task flexibility, basis functions have been proposed. Instead of learning the full signal f_j, in learning control with basis functions the feedforward filter parameters θ_j are learned by constructing the feedforward signal as

$$f_j = F(\theta_j) r_j, \tag{1.5}$$

i.e., the learning is decoupled from the reference trajectory. Different parameterizations of $F(\theta_j)$ have been proposed, including a linear combination of polynomial basis functions (Phan and Frueh, 1996; Van der Meulen et al., 2008; Van de Wijdeven and Bosgra, 2010), a rational combination of basis functions (Bolder and Oomen, 2015; Blanken et al., 2017a; Chapter 9), and a linear combination of rational basis functions (Blanken et al., 2017b). Each of these parameterizations has its own advantages and disadvantages. In general, learning control with basis functions combines high performance with high task flexibility.

In summary, motion control design includes a combination of feedforward, learning, and feedback, where each has its own advantages and disadvantages.

1.6 Digital controller implementation

Driven by the performance/cost trade-off in Figure 1.3, (motion) controllers are typically implemented digitally to reduce cost, see also Section 1.1. In this section, the digital implementation and related aspects are considered.

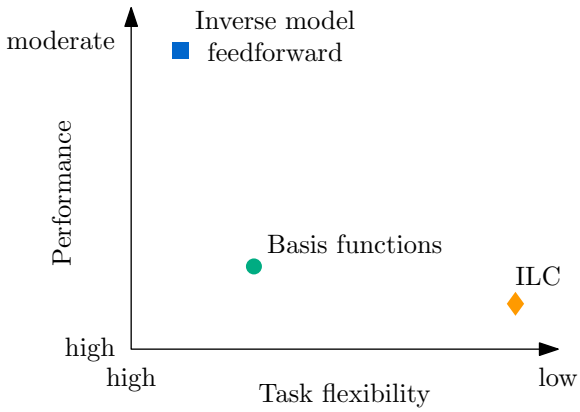

Figure 1.8. Basis functions balance the moderate performance and high task flexibility of inverse model feedforward with high performance and low task flexibility of ILC.

The digital implementation of a controller (Chen and Francis, 1995, Chapter 1) is illustrated in Figure 1.9(a) with mathematical idealization in Figure 1.9(b), where

- Roman letters: continuous-time signals, indicated by solid lines;
- Greek letters: discrete-time signals, indicated by nonsolid lines;
- A/D: analog-to-digital converter, including quantizer;
- D/A: digital-to-analog converter;
- µ: microprocessor;
- C_d: discrete-time controller;
- $\mathcal{D}$: ideal (down)sampler, possibly non-equidistant; and
- $\mathcal{H}$: hold operator, typically zero-order-hold.

A typical digital controller implementation of Figure 1.6 is shown in Figure 1.10. The configuration is in line with the developments in sampled-data control in Figure 1.4.

In this thesis, time-triggered, non-equidistant sampling schemes are considered, see also Section 1.4. Examples of time-triggered sampling with downsampler $\mathcal{D}$ and zero-order hold $\mathcal{H}$ are shown in Figure 1.11. Note that both the sampling and hold can be non-equidistant in time, i.e., with time-varying sampling intervals. The time-varying behavior of periodic, non-equidistant sampling poses challenges for control design. In particular, periodic, non-equidistant sampling of continuous-time, linear time-invariant (LTI) systems leads to linear periodically time-varying (LPTV) behavior, as shown in, for example, Chapter 2. In summary, the digital controller implementation is an important aspect for controller design.

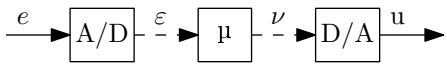

(a) Controller components: A/D converter, microprocessor µ, and D/A converter.

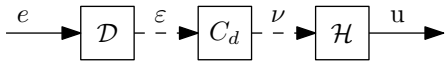

(b) Mathematical equivalent of (a) with (down)sampler $\mathcal{D}$, discrete-time controller C_d, and hold $\mathcal{H}$.

Figure 1.9. Digital controller implementation.

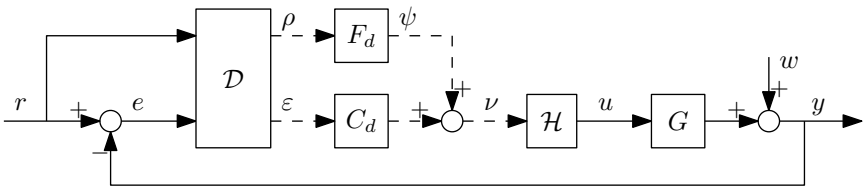

Figure 1.10. In resource-aware control design, the digital implementation is explicitly taken into account during controller design. The shown control configuration conforms to that in Figure 1.4(c).

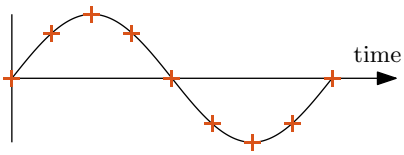

(a) Equidistant sampling (+) of a continuous-time signal (——).

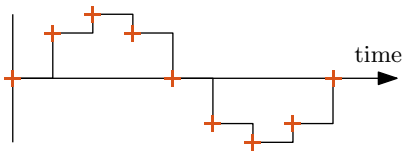

(b) Zero-order-hold (——) on an equidistantly-sampled signal (+).

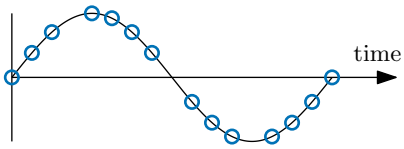

(c) Non-equidistant sampling (○) of a continuous-time signal (——).

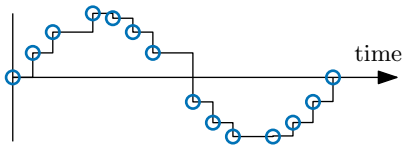

(d) Zero-order-hold (——) on a non-equidistantly-sampled signal (○).

Figure 1.11. Examples of time-triggered upsampling and downsampling, both equidistant and non-equidistant in time.

1.7 Problem statement

Traditionally, control design and embedded software are treated as two separate domains, resulting in a suboptimal performance/cost trade-off as shown in Figure 1.3. Over the last decade, developments in embedded software have enabled much more design freedom in controller implementation and opened up possibilities to improve the performance/cost trade-off by employing sampling schemes other than conventional time-triggered, equidistant ones. In particular, time-triggered schemes with periodic, non-equidistant sampling are promising since they are predictable, easy to implement, and provide more design freedom. Such sampling schemes typically result in LPTV behavior. In order to exploit the potential of these sampling schemes, a considerable amount of research into controller design for LPTV systems has been conducted. However, many of these approaches do not find application in industrial motion systems since they require parametric LPTV models and expert knowledge. This leads to the following research goal of this thesis.

Research goal: *Develop a framework for resource-aware motion control design by exploiting periodic, non-equidistant sampling that is suitable for industrial application.*

In view of the research goal, this thesis contributes to bridging the gap between control design and embedded software in the context of motion systems. The envisioned end goal is a resource-aware motion control design framework based on periodic, non-equidistant sampling, which is suitable for application in industry.

1.8 Research challenges and contributions

In this section, the research contributions of this thesis towards the research goal are presented. The resource-aware motion control design framework can be divided into four categories: feedback control, system inversion, feedforward control, and learning control.

1.8.1 Feedback control

Feedback control forms an essential part in motion control design. The main purpose is suppression of unknown disturbances and providing robustness against model uncertainties, see also Section 1.5. Due to the time-varying behavior introduced by periodic, non-equidistant sampling, typical frequency-domain control design techniques, based on Bode diagrams and Nyquist plots, are not directly applicable. Most control designs for LPTV systems require a parametric model

of the system. However, despite the availability of a solid control theory, model-based designs are demanding since obtaining a parametric LPTV model is difficult and typical LTI interpretations are not valid. With the aim of industrial application, control design approaches closely related to well-known existing approaches are desired. Many of these approaches are based on non-parametric models and heuristic design rules.

This inspires the following contribution.

Contribution I: *Resource-aware feedback control approach in the form of a loop-shaping control design framework for LPTV systems based on frequency response function measurements and LTI design insights.*

1.8.2 System inversion

System inversion is essential in feedforward and learning control, see also Section 1.5. The quality of inversion directly determines the achievable performance.

One of the main challenges associated with inversion is nonminimum-phase behavior since the inverse system is unstable in that case and traditional approaches yield an unbounded output. Many algorithms and approaches are available for system inversion of linear time-invariant (LTI), nonminimum-phase systems. However, the choice for a technique is sometimes made arbitrarily without a full understanding of the implications, the alternatives, and their underlying mechanisms. In particular, guidelines on proper use of inversion techniques for both inverse model feedforward and learning control are lacking. Furthermore, the applicability to time-varying and multivariable systems is often not addressed.

This gives rise to the following contribution.

Contribution II: *Overview and comparison of inversion techniques from the perspective of the control goal and applicability to multivariable and time-varying systems.*

1.8.3 Feedforward control

Inverse model feedforward yields good performance for a large class of reference trajectories, see also Section 1.5. Also for periodic, non-equidistant sampling, nonminimum-phase behavior is observed, posing similar challenges as for equidistantly sampled systems. Contribution II provides inversion techniques to obtain bounded feedforward signals, even for nonminimum-phase systems, but is mainly focused on LTI systems. As a consequence, application of inverse model feedforward for systems with periodic, non-equidistant sampling is hampered by a lack of inversion techniques for general LPTV systems.

Ideally, high performance in terms of the continuous-time error signal is achieved. However, due to the digital implementation, inverse model control techniques typically only address the discrete-time behavior and yield good on-sample behavior. The continuous-time behavior between the samples, i.e., the intersample behavior, is not addressed and may be poor. In traditional control design approaches, a high sampling rate is used such that good on-sample behavior typically also yields good intersample behavior. However, such an approach is undesired in view of the performance/cost trade-off in Figure 1.3 and the research goal. Therefore, discrete-time controller designs that also address the intersample behavior are desired.

Perfect tracking for nonminimum-phase systems can be obtained through noncausal control, i.e., by pre-actuating the system. However, in some applications preview is absent or pre-actuation is undesired, for example in applications in which the reference trajectory is updated online. In many systems, additional actuators can be used to overcome this limitation.

This inspires the following contribution.

Contribution III: *Resource-aware feedforward control approaches.*

III.A Exact inversion for LPTV systems, including nonminimum-phase systems, using bounded inputs.

III.B Discrete-time system inversion that addresses both on-sample and intersample behavior.

III.C Exact and causal inversion of overactuated nonminimum-phase systems.

1.8.4 Learning control

Learning control yields high performance for repeating tasks, see also Section 1.5. However, the application of learning control to systems with non-equidistant sampling strategies, such as multirate systems, is limited as most approaches rely on frequency-domain techniques.

For non-exactly repeating tasks, the performance of standard ILC approaches deteriorates, see also Section 1.5. To enhance the task flexibility, basis functions can be used, see also Figure 1.8. However, at present basis functions are mainly restricted to time-invariant systems, limiting their application.

The parameterizations of basis functions can be divided into two categories: parameterizations that are linear in the parameters and parameterizations that are nonlinear in the parameters. The first category is suboptimal in terms of performance since only the zeros of the filter are updated, i.e., only the poles of the system can be learned. However, from a computational point of view these methods are attractive since the associated optimization problem is convex, giving rise to fast computations. The second category enables optimization of

both poles and zeros and thereby higher performance. However, it involves solving nonconvex optimization problems, which is undesired from a cost point of view. Hence, an approach that can learn both the poles and zeros of a system through convex optimization is desired.

Traditional ILC approaches learning the full signal f_j yield optimal performance for repeating tasks. Although optimal from a control point of view, the implementation of these approaches is often cumbersome. Especially for large tasks, the computational load increases rapidly, which is undesired in view of Figure 1.3 and limits applicability to large (industrial) tasks.

Traditionally, feedforward/learning control and feedback control are designed separately. Feedback control is used to minimize the error between the reference trajectory and the measured variable. Feedforward/learning control is used to minimize the error between the reference trajectory and the performance variable. However, in many applications the performance variable and the measured variable differ since the performance variable cannot be measured in real-time, for example, due to obstruction or extensive processing times. Hence, in such an inferential setting, there is a mismatch between the control design objectives of feedforward/learning control and feedback control, leading to suboptimal performance. For an optimal design, the connections between feedforward, learning, and feedback control are essential.

This gives rise to the following contribution.

Contribution IV: *Resource-aware learning control approaches.*

IV.A Iterative learning control for multirate systems for an enhanced performance/cost trade-off.

IV.B Basis functions for LPTV systems for high performance and task flexibility for systems with periodic, non-equidistant sampling.

IV.C Rational basis functions with convex optimization for high performance and task flexibility at low computational cost.

IV.D Resource-efficient ILC approach to enable ILC for large tasks.

IV.E Connections between feedforward, learning, and feedback for inferential control.

1.9 Overview of the thesis

An overview of the thesis is presented in Figure 1.12. Each of the (sub)contributions is addressed in a separate chapter. The main application of a chapter is indicated by a photograph for experiments and an illustration for simulations. All chapters are sell-contained and can be read independently of each other.

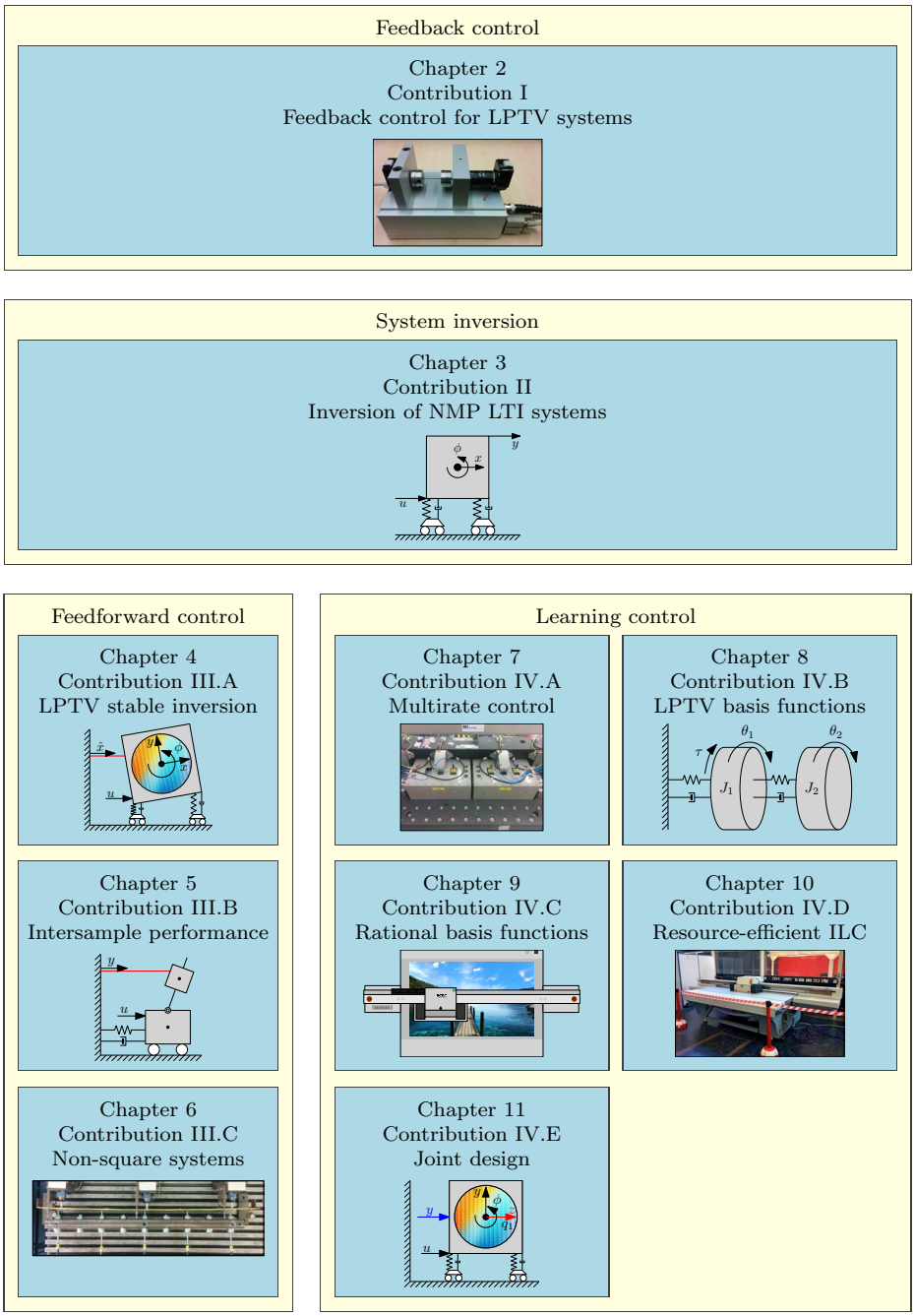

Figure 1.12. Overview of the thesis.

Chapter 2

Feedback control for LPTV systems: A loop-shaping approach

The performance/cost trade-off in Figure 1.3 can be enhanced by exploiting sampling strategies that go beyond traditional equidistant sampling. The aim of this chapter is to develop a systematic feedback control design approach for systems that go beyond equidistant sampling. A loop-shaping design framework for such non-equidistantly sampled systems is developed that addresses both stability and performance. The framework only requires frequency response function measurements of the LTI system, while it appropriately addresses the LPTV behavior introduced by the non-equidistant sampling. Experimental validation on a motion system demonstrates the superiority of the design framework for non-equidistantly sampled systems compared to traditional designs that rely on equidistant sampling. The design framework constitutes Contribution I.

2.1 Introduction

Digital implementations of motion controllers provide a large design flexibility at a low cost (Chen and Francis, 1995). Most of the digital implementations are based on fixed, equidistant sampling schemes. Such schemes are favorable from a control design perspective since time invariance of continuous-time systems

The contents of this chapter also appear in:
Jurgen van Zundert and Tom Oomen. Beyond Equidistant Sampling for Performance and Cost: A Loop-Shaping Approach Applied to a Motion System. *Accepted for International Journal of Robust and Nonlinear Control*, 2018.

is preserved. In particular, for linear time-invariant (LTI) systems, equidistant sampling allows the use of frequency-domain control design approaches, including the use of Bode plots and Nyquist diagrams (Skogestad and Postlethwaite, 2005).

From the perspective of cost-effective and high performance control design, flexible sampling is preferred over fixed sampling. Nowadays, digital controllers are often embedded in software and task scheduling policies allocate resources to the different software applications. The scheduling is often periodic and generally leads to periodic, non-equidistant sampling of the individual applications. Due to the periodicity, equidistant sampling can always be obtained by simply discarding part of the sampling instances. However, such an approach goes at the expense of the achievable performance since not all data and decision variables are exploited. Flexible sampling, including non-equidistant sampling, is preferred since it allows to exploit all available data and decision variables with identical hardware cost and thereby improve the performance/cost trade-off compared to fixed sampling. Examples of flexible sampling include non-equidistant sampling (Chapter 8; Valencia et al., 2016), multirate control (Fujimoto et al., 2001; Fujimoto and Hori, 2002; Salt and Albertos, 2005; Chapter 7), and sparse control (Oomen and Rojas, 2017).

Flexible sampling potentially improves the performance/cost trade-off, but is challenging from a control design perspective. In particular, flexible sampling of continuous-time LTI systems leads to linear periodically time-varying (LPTV) behavior, see also Chapter 8. Hence, typical frequency-domain control design techniques are not directly applicable. Most control designs for LPTV systems require a parametric model of the system, including pole placement (Hernández and Urbano, 1989; Kono, 1980), linear quadratic regulator (LQR) control, linear quadratic Gaussian (LQG) control, $\mathcal{H}_2/\mathcal{H}_\infty$ approaches (Nie et al., 2013; Shahsavari et al., 2013; Ravi et al., 1991), internal model principle (Grasselli and Longhi, 1991), and LTI approximations (Chen and Qiu, 1997). Also, designs based on time-invariant reformulations are often based on parametric models, including Floquet-Lyapunov transformations (Bittanti and Colaneri, 2009, Section 1.2) and lifting approaches (Bittanti and Colaneri, 2009, Section 1.6), which enable the use of full state feedback (Sinha and Joseph, 1994), pole placement (Colaneri, 1991), model matching (Colaneri and Kučera, 1997), LQR (Kalender and Flashner, 2008), LQG (Conway and Horowitz, 2008), and $\mathcal{H}_2/\mathcal{H}_\infty$ control (Bamieh et al., 1991; Voulgaris et al., 1994). However, as is argued in Oomen et al. (2007), despite the availability of solid control theory, such model-based designs are demanding since (i) obtaining a parametric LPTV model is difficult; and (ii) typical LTI interpretations are not valid, leading to complications for the actual design (Cantoni and Glover, 1997; Lindgärde and Lennartson, 1997).

Although non-equidistant sampling has a large potential and the underlying theory has been substantially developed, at present there is a lack of suitable control design techniques to address stability, performance, and robustness. The

aim of this chapter is to develop a non-parametric loop-shaping control design framework for non-equidistantly sampled systems based on frequency response function (FRF) measurements. Such a framework is well-developed for traditional equidistantly sampled, single-variable systems (Skogestad and Postlethwaite, 2005, Section 2.6; Steinbuch et al., 2010; Franklin et al., 2015, Chapter 6). The presented framework builds on the multirate approach in Oomen et al. (2005); Oomen et al. (2007), exploits w-plane loop-shaping (Oomen et al., 2007, Section 5.1), explicitly incorporates time-varying aspects, and addresses key objectives such as stability and performance.

The main contribution of this chapter is a framework for LPTV loop-shaping feedback control design based on FRF measurements, which enables to exploit non-equidistant sampling for improved control performance. This chapter has the following contributions.

2.I Development of a suitable stability test: an FRF measurement based Nyquist test for LPTV systems.

2.II Quantification of performance: LPTV generalizations of FRFs for non-equidistantly sampled systems.

2.III Design through loop-shaping: systematic framework based on FRF measurements and LTI insights.

2.IV Application of the design framework to a motion system demonstrating the potential of non-equidistant sampling.

2.V Validation of the designed controllers through experiments.

The outline of this chapter is as follows. In Section 2.2, the potential of non-equidistant sampling is demonstrated via an illustrative example and the control objective is formulated. The Nyquist stability test for non-equidistantly sampled systems (Contribution 2.I) is presented in Section 2.3. The performance quantification based on FRFs (Contribution 2.II) is presented in Section 2.4. The loop-shaping design (Contribution 2.III) is presented in Section 2.5. Application of the design framework to a motion system (Contribution 2.IV) is presented in Section 2.6. In Section 2.7, the designed controllers are validated in experiments (Contribution 2.V). Conclusions and an outlook are presented in Section 2.8.

Notation. For notation convenience, single-input, single-output (SISO) systems are considered. The results can directly be generalized to multivariable systems. Let $\lfloor x \rfloor = \max\{m \in \mathbb{Z} \mid m \leq x\}$. Lifted variables are underlined, with $\underline{I}_n$ the $n \times n$ identity matrix and $\underline{0}$ the zero matrix of suitable dimensions.

2.2 Non-equidistant sampling in motion control

In this section, the potential of non-equidistant sampling in motion control applications is explored and the control objective is defined.

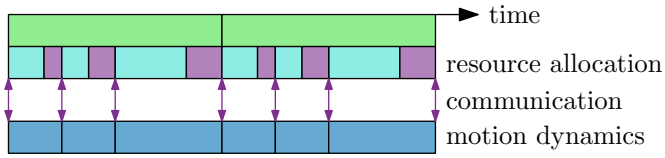

Figure 2.1. Example of resource allocation to a motion control application (■) and other applications (■). The communication (actuation and sensing) to the motion application at the end of each interval results in periodic (■) non-equidistant sampling of the motion system (■).

2.2.1 Non-equidistant sampling for cost-effective embedded implementations

Multiple software applications are often embedded on a single platform to reduce the overall implementation cost. An example of such a platform is CompSOC (Goossens et al., 2017). A scheduling policy is used to allocate the platform resources to the different applications. The scheduling is often periodic and typically results in periodic, non-equidistant sampling of the individual applications as is illustrated in Figure 2.1.

Non-equidistant sampling introduces time variance, also for underlying time-invariant continuous-time dynamics, which poses challenges from a control design perspective. In particular, periodic, non-equidistant sampling of a linear time-invariant (LTI) system results in linear periodically time-varying (LPTV) behavior, see Section 2.2.3.

2.2.2 Exploiting non-equidistant sampling in control design

The potential of non-equidistant sampling in control is illustrated via the example in Figure 2.2. The figure shows a continuous-time sine wave with frequency $\frac{3}{8}$ Hz. The digital controller only has access to the non-equidistantly sampled signal. Control techniques for LTI systems are unsuited for the sampling sequence provided by the hardware since the sampling is non-equidistant and thus yields time-varying behavior.

The typical way for traditional LTI control designs is to use the equidistant sampling sequence with the highest sampling frequency, i.e., $\frac{1}{2}$ Hz for the example in Figure 2.2. Clearly, such a design does not exploit all available data, which may yield suboptimal performance. In fact, for the example in Figure 2.2 aliasing occurs and a sine wave with frequency $\frac{1}{8}$ Hz instead of $\frac{3}{8}$ Hz can be observed. This poses substantial performance limitations for continuous-time performance. Indeed, typical LTI control designs may improve on-sample behavior, but often degrade intersample behavior (Oomen et al., 2007). This observation is corrob-

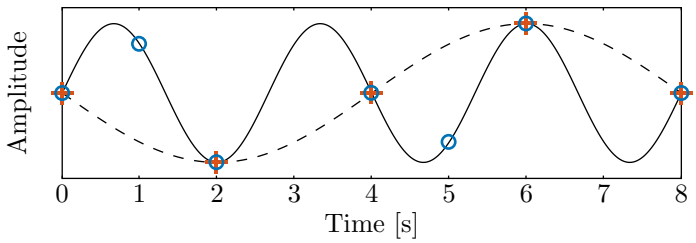

Figure 2.2. Example demonstrating the potential of non-equidistant sampling in control. The underlying continuous-time signal (——) is sampled non-equidistantly (○) with period 4s. Equidistant sampling (+) is obtained by discarding part of the samples, which obstructs reconstruction of the true continuous-time signal. Instead, the aliased signal (- - -) is observed, posing severe limitations for control. Control for the non-equidistant sampling sequence (○) has the potential to enhance the performance since the continuous-time signal can be reconstructed.

orated by experiments in Section 2.7.

In the proposed approach, the control design is explicitly based on the non-equidistant sampling sequence. Such an approach exploits all available data and design freedom and therefore has the potential to outperform traditional LTI control. The experiments in Section 2.7 confirm that control design on the non-equidistant rate is superior to LTI control on the equidistant rate in situations similar to that illustrated in Figure 2.2.

2.2.3 Non-equidistant control architecture

In this chapter, the focus is on feedback control of non-equidistantly sampled LTI motion applications according to the control diagram in Figure 2.3. The following definitions are adopted.

Definition 2.1 (Linear system)**.** *Let $y_1 = Hu_1$ and $y_2 = Hu_2$, then H is linear if $\alpha y_1 + \beta y_2 = H(\alpha u_1 + \beta u_2)$, for all $\alpha, \beta \in \mathbb{R}$.*

Definition 2.2 (LPTV system)**.** *A system H is LPTV with period $\tau \in \mathbb{N}$ if it is linear (Definition 2.1) and it commutes with the delay operator $\mathcal{D}_\tau$ defined by $\mathcal{D}_\tau u[k] = u[k-\tau]$, i.e., $\mathcal{D}_\tau H = H\mathcal{D}_\tau$.*

Definition 2.3 (LTI system)**.** *A system H is LTI if it is LPTV (Definition 2.2) with period $\tau = 1$.*

The following two assumptions are made.

Assumption 2.4. *The discrete-time system $G_{b,d}$ in Figure 2.3 is LTI (Definition 2.3).*

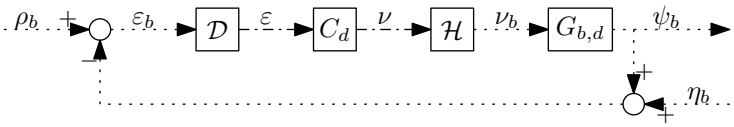

Figure 2.3. Control diagram with base rate (·····) defined by Δ_b in (2.1) and non-equidistant rate (-·-·) defined by Δ_{ne} in (2.2). Upsampler $\mathcal{H}$, including zero-order-hold interpolation, and downsampler $\mathcal{D}$ provide the conversion between Δ_b and Δ_{ne}. The control goal is to design feedback controller C_d operating on the non-equidistant sampling sequence Δ_{ne} based on FRF measurement $G_{b,d}$ obtained on the base sampling sequence Δ_b.

Assumption 2.5. *The base rate sampling sequence is given by*

$$\Delta_b := (\delta_b, \delta_b, \ldots), \tag{2.1}$$

with $\delta_b \in \mathbb{R}_{>0}$ and only available for dedicated identification experiments and performance evaluation, and not available for control. The non-equidistant sampling sequence with periodicity $\tau \in \mathbb{N}$ available for control is given by

$$\Delta_{ne} := (\delta_1, \delta_2, \ldots, \delta_\tau, \delta_1, \delta_2, \ldots, \delta_\tau, \ldots), \tag{2.2}$$

with $\delta_i = \gamma_i \delta_b$, $\gamma_i \in \mathbb{N}$, $1 \leq i \leq \tau$, and is defined by $\Gamma_{ne} := (\gamma_1, \gamma_2, \ldots, \gamma_\tau) \in \mathbb{N}^\tau$.

A key observation is that the non-equidistant sampling sequence Δ_{ne} in Figure 2.3 introduces periodic time-varying behavior. In particular, by Assumption 2.5, Δ_b has periodicity 1 and period time δ_b, and Δ_{ne} has periodicity τ and period time $\sum_{i=1}^{\tau} \delta_i = T\delta_b$, with $T := \sum_{i=1}^{\tau} \gamma_i$. Hence, for linear controllers C_d, the system in Figure 2.3 is LPTV (Definition 2.2) with period time $T\delta_b$.

Traditional LTI approaches typically use the equidistant sampling sequence with the highest possible sampling frequency as given by Definition 2.6. Note that by periodicity of Δ_{ne} in (2.2) such a sequence always exists since $\delta_{eq} \leq T\delta_b$. The sampling sequences are illustrated by Example 2.7.

Definition 2.6. *Given Assumption 2.5, let $\tilde{\Gamma}_{ne} = \{\sum_{i=1}^{j} \gamma_i \mid 1 \leq j \leq \tau\}$, then the equidistant sampling sequence is defined as*

$$\Delta_{eq} := (\delta_{eq}, \delta_{eq}, \ldots), \tag{2.3}$$

where $\delta_{eq} = \gamma_{eq}\delta_b$, with

$$\gamma_{eq} := \min\{\gamma \in \mathbb{N} \mid \forall 1 \leq n \leq \tfrac{T}{\gamma},\ n\gamma \in \tilde{\Gamma}_{ne}\}, \tag{2.4}$$

and is defined by $\Gamma_{eq} = \gamma_{eq} \in \mathbb{N}$.

Example 2.7. *The sampling sequences for the example in Figure 2.2 are illustrated in Figure 2.4. The non-equidistant sampling sequence has periodicity*

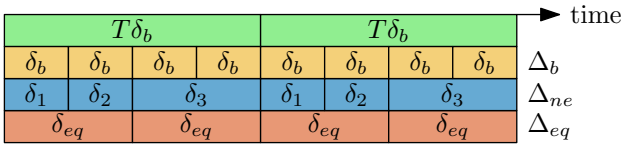

Figure 2.4. Illustration of the sampling sequences for the example in Figure 2.2, with Δ_{ne} (■) given by $\Gamma_{ne} = \begin{bmatrix}1 & 1 & 2\end{bmatrix}$ and Δ_{eq} (■) given by $\Gamma_{eq} = 2$.

$\tau = 3$ with $\delta_1 = \delta_2 = 1$ s and $\delta_3 = 2$ s. Let $\delta_b = 1$ s, then $\Gamma_{ne} = \begin{bmatrix}1 & 1 & 2\end{bmatrix}$, i.e., $\gamma_1 = \gamma_2 = 1$, $\gamma_3 = 2$, and $T = 4$. By Definition 2.6, $\tilde{\Gamma}_{ne} = \{1, 2, 4\}$. For $\gamma = 1$, $\frac{T}{\gamma} = 4$, but $n\gamma \notin \tilde{\Gamma}_{ne}$ for $n = 3$. For $\gamma = 2$, $\frac{T}{\gamma} = 2$ and $n\gamma \in \tilde{\Gamma}_{ne}$ for $n = 1, 2$, hence $\Gamma_{eq} = 2$.

In the next section, the control objective is presented.

2.2.4 Control objective

The control objective considered in this chapter is given as follows.

Main problem. *Let the control diagram in Figure 2.3 and a frequency response function measurement $G_{b,d}(e^{j\omega\delta_b})$ be given, and let Assumption 2.4 and Assumption 2.5 be satisfied. Design a feedback controller C_d that provides*

(A) robust stability, and

(B) robust performance in terms of ε_b,

with robust stability and performance according to McFarlane and Glover (1990, Section 6).

In this chapter, the feedback control design is based on loop-shaping techniques since these are directly applicable to FRF measurements, which are fast, accurate, and inexpensive to obtain for motion systems, in contrast to parametric identification methods (Oomen et al., 2007). The key challenge in this chapter is that conventional loop-shaping for LTI systems (Skogestad and Postlethwaite, 2005, Section 2.6; Steinbuch et al., 2010; Franklin et al., 2015, Chapter 6) is performed in the frequency domain, whereas the non-equidistantly sampled systems considered in this chapter are time-varying. In this chapter, the frequency-domain insights for LTI systems are generalized to non-equidistantly sampled systems.

The stability and performance aspects are addressed in Section 2.3 and Section 2.4, respectively. The loop-shaping design framework is presented in Section 2.5. Application and experimental validation of the framework is presented in Section 2.6 and Section 2.7, respectively.

Remark 2.8. *Although C_d in Figure 2.3 uses signal ε operating on the non-equidistant sampling sequence Δ_{ne}, the loop-shaping nominal performance goal of this chapter addresses the fictitious signal ε_b operating on sampling sequence Δ_b to also take intersample behavior into account (Oomen et al., 2007). This is also illustrated in Section 2.7.*

Remark 2.9. *The FRF measurement $G_{b,d}(e^{j\omega\delta_b})$ is assumed to be sufficiently dense in view of integral behavior (Geerardyn and Oomen, 2017).*

2.3 Stability: Nyquist test for LPTV systems

In this section, a stability test for the closed-loop system in Figure 2.3 is presented, which addresses subproblem (A). The proposed stability test is a Nyquist stability test for LPTV systems based on FRF measurements and constitutes Contribution 2.I.

2.3.1 LPTV stability

Consider the LPTV open-loop transfer function $L_{b,d} = G_{b,d}\mathcal{H}C_d\mathcal{D}$ in Figure 2.3 and assume that there are no pole/zero cancellations. Then, internal closed-loop stability in Figure 2.3 is equivalent to stability of $S_{b,d} = (1 + L_{b,d})^{-1}$, see also Zhou et al. (1996, Section 5.3). Let $S_{b,d} \stackrel{z}{=} (A[i], B[i], C[i], D[i])$, $i = 1, 2, \ldots, T$, then closed-loop stability can be directly analyzed based on the monodromy matrix of $S_{b,d}$ given by (Bittanti and Colaneri, 2009, Section 1.2)

$$\Psi = A[\tau]A[\tau - 1]\ldots A[1]. \tag{2.5}$$

More specific, the closed-loop system is stable (Bittanti and Colaneri, 2009, Section 1.2.3) if and only if

$$|\lambda_i(\Psi)| < 1, \quad \text{for all } i, \tag{2.6}$$

where the eigenvalues $\lambda_i(\Psi)$ are the roots of the characteristic polynomial

$$\phi(z) = \det(zI - \Psi). \tag{2.7}$$

Condition (2.6) provides a stability test for parametric models based on (2.7). However, there is no parametric model of $G_{b,d}$ available, see Section 2.2.4. Therefore, a Nyquist stability test based on FRF measurement $G_{b,d}(e^{j\omega\delta_b})$ is proposed instead.

2.3.2 Towards a Nyquist stability test for $\phi(z)$

Nyquist stability tests for LTI systems are not directly applicable to the LPTV system in Figure 2.3 due to the time-varying behavior. The main idea is to

connect the characteristic polynomial $\phi(z)$ in (2.7) to a Nyquist stability test. This is achieved through lifting of which preliminary results are presented in this section.

Let $u[k] \in \mathbb{R}$ and

$$\underline{u}[k] = \begin{bmatrix} u[kT] \\ u[kT+1] \\ \vdots \\ u[kT+T-1] \end{bmatrix} \in \mathbb{R}^T, \tag{2.8}$$

with $T \in \mathbb{N}$. The lifting operator $\mathcal{L}_T$ is defined to be the map $u \mapsto \underline{u}$, with inverse given by $u = \mathcal{L}_T^{-1}\underline{u}$. Let $y = Hu$ with H a linear system (Definition 2.1), then $\underline{y} = \mathcal{L}_T y = (\mathcal{L}_T H \mathcal{L}_T^{-1})(\mathcal{L}_T u) = \underline{H}\underline{u}$ with lifted system $\underline{H} = \mathcal{L}_T H \mathcal{L}_T^{-1}$.

Lifted controller $\underline{C}_d$ is given by Lemma 2.10 and obtained by lifting the LPTV state-space controller C_d operating on sampling sequence Δ_{ne} in (2.2) over period $T\delta_b$, which corresponds to lifting over τ samples. For a proof see Bittanti and Colaneri (2009, Section 6.2.3).

Lemma 2.10 (Lifting C_d)**.** *The $\tau \in \mathbb{N}$ periodic state-space controller $C_d \overset{z}{=} (A[k], B[k], C[k], D[k])$, $k = 0, 1, 2, \ldots$, with $A[k+\tau] = A[k]$, $B[k+\tau] = B[k]$, $C[k+\tau] = C[k]$, $D[k+\tau] = D[k]$, lifted over τ samples is given by $\underline{C}_d(z) = \mathcal{L}_\tau C_d \mathcal{L}_\tau^{-1} \in \mathbb{C}^{\tau\times\tau}$,*

$$\underline{C}_d \overset{z}{=} \left[\begin{array}{c|cccc} \Psi & \Phi_{\tau,2}B[1] & \Phi_{\tau,3}B[2] & \cdots & B[\tau] \\ \hline C[1] & D[1] & 0 & \cdots & 0 \\ C[2]\Phi_{2,1} & C[2]B[1] & D[2] & \ddots & \vdots \\ \vdots & \vdots & \ddots & \ddots & 0 \\ C[\tau]\Phi_{\tau,1} & C[\tau]\Phi_{\tau,2}B[1] & \cdots & C[\tau]B[\tau-1] & D[\tau] \end{array}\right], \tag{2.9}$$

with transition matrix

$$\Phi_{k_2,k_1} = \begin{cases} I, & k_2 = k_1, \\ A[k_2-1]A[k_2-2]\ldots A[k_1], & k_2 > k_1, \end{cases} \tag{2.10}$$

and monodromy matrix $\Psi = \Phi_{\tau+1,1}$.

Lemma 2.11 shows that LPTV systems lifted over their period are LTI and that stability is preserved under lifting, see also Bamieh et al. (1991, Section 2). Both properties are used in the Nyquist stability test presented in the next section. In the remainder of this section, preliminary results related to lifting are presented.

Lemma 2.11. *Let H be an LPTV system with period T (Definition 2.2) and let $\underline{H} = \mathcal{L}_T H \mathcal{L}_T^{-1}$, then*

(i) $\underline{H}$ *is LTI (Definition 2.3), and*

(ii) $\underline{H}$ *is stable if and only if* H *is stable.*

Proof. The LTI properties are evident from Lemma 2.10. LTI system $\underline{H} = (A_{\underline{H}}, B_{\underline{H}}, C_{\underline{H}}, D_{\underline{H}})$ is stable if and only if $|\lambda_i(A_{\underline{H}})| < 1$, for all i. By Lemma 2.10, $A_{\underline{H}} = \Psi$ in (2.5), and hence the stability condition is identical to (2.6). □

The lifted system $\underline{G}_{b,d}$ is given by Lemma 2.12 and obtained by lifting $G_{b,d}$ operating on sampling sequence Δ_b in (2.1) over period $T\delta_b$, which corresponds to lifting over T samples. For a proof, see Bittanti and Colaneri (2009, Section 6.2.1). Lemma 2.12 is expressed in terms of transfer functions to facilitate application to FRF measurements by replacing z with $e^{j\omega T\delta_b}$.

Lemma 2.12 (Lifting $G_{b,d}$)**.** *The LTI transfer function* $G_{b,d}(z)$ *lifted over* $T \in \mathbb{N}$ *samples is given by* $\underline{G}_{b,d} = \mathcal{L}_T G_{b,d} \mathcal{L}_T^{-1} \in \mathbb{C}^{T\times T}$*, with element* $\underline{G}_d(z)[i,j]$*,* $i,j = 1,2,\ldots,T$*, given by*

$$\underline{G}_d(z)[i,j] = G_{(|i-j|)}(z), \tag{2.11}$$

where

$$G_{(s)}(z^T) = \frac{z^s}{T}\sum_{k=0}^{T-1} G_{b,d}(z\phi^k)\phi^{ks}, \quad \phi = e^{\frac{2\pi j}{T}}. \tag{2.12}$$

Next, the downsampler and upsampler are lifted. Let

$$\mu_T[i] := i-1, \qquad i = 1,2,\ldots,T, \tag{2.13}$$

$$\mu_\tau[i] := \begin{cases} 0, & i = 1, \\ \displaystyle\sum_{j=1}^{i-1}\gamma_i, & i = 2,3,\ldots,\tau+1, \end{cases} \tag{2.14}$$

then lifting $\mathcal{D}$ and $\mathcal{H}$ over period time $T\delta_b$ yields the non-square systems given by Lemma 2.13 and Lemma 2.14, respectively. The results follow directly from (2.13), (2.14), and Assumption 2.5. Note that the input and output are lifted over a different number of samples due to the different sampling sequences.

Lemma 2.13 (Lifting $\mathcal{D}$)**.** *Lifting downsampler* $\mathcal{D}$ *in Figure 2.3 over period* $T\delta_b$ *yields* $\underline{\mathcal{D}} = \mathcal{L}_\tau \mathcal{D} \mathcal{L}_T^{-1} \in \mathbb{N}^{\tau\times T}$*, with element* $\underline{\mathcal{D}}[i,j]$*,* $i = 1,2,\ldots,\tau$*,* $j = 1,2,\ldots,T$*, given by*

$$\underline{\mathcal{D}}[i,j] := \begin{cases} 1, & \mu_\tau[i] = \mu_T[j], \\ 0, & \textit{otherwise}, \end{cases} \tag{2.15}$$

with μ_T, μ_τ *in* (2.13) *and* (2.14)*, respectively.*

Lemma 2.14 (Lifting $\mathcal{H}$)**.** *Lifting upsampler with zero-order-hold interpolation $\mathcal{H}$ in Figure 2.3 over period $T\delta_b$ yields $\underline{\mathcal{H}} = \mathcal{L}_T \mathcal{H} \mathcal{L}_\tau^{-1} \in \mathbb{N}^{T\times\tau}$, with element $\underline{\mathcal{H}}[i,j]$, $i = 1,2,\ldots,T$, $j = 1,2,\ldots,\tau$, given by*

$$\underline{\mathcal{H}}[i,j] := \begin{cases} 1, & \mu_\tau[j] \leq \mu_T[i] < \mu_\tau[j+1], \\ 0, & \textit{otherwise}, \end{cases} \tag{2.16}$$

with μ_T, μ_τ in (2.13) *and* (2.14)*, respectively.*

An important observation is that all lifted systems are LTI, see also Lemma 2.11, and hence any interconnection of lifted systems is LTI. The results in this section form the basis for the Nyquist stability test for LPTV systems presented in the next section.

Remark 2.15. *Note that all lifted systems correspond to lifting over period $T\delta_b$, although the periodicities, and hence the dimensions, differ depending on the sampling sequence, i.e., T for Δ_b and τ for Δ_{ne}.*

2.3.3 Nyquist stability test

The results of the previous sections are used in this section for the stability test of the closed-loop LPTV system in Figure 2.3. The presented Nyquist stability test constitutes Contribution 2.I.

The stability test makes use of the principle of the argument (Vinnicombe, 2001, Section 1.2.2) in Lemma 2.16 and the results of Lemma 2.17.

Lemma 2.16. *Let $f(z) \in \mathcal{R}$ and let C denote a closed contour in the complex plane. Assume that*

(i) $f(z)$ is analytic on C, i.e., $f(z)$ has no poles on C,

(ii) $f(z)$ has Z zeros inside C, and

(iii) $f(z)$ has P poles inside C.

Then, the image $f(z)$ as z traverses the contour C once in a clockwise direction will make $N = Z - P$ clockwise encirclements of the origin.

Lemma 2.17. *Let $\underline{L}_{b,d} = \underline{G}_{b,d}\underline{\mathcal{H}}\underline{C}_d\underline{\mathcal{D}}$ and $\underline{L}_d = \underline{\mathcal{D}}\underline{G}_{b,d}\underline{\mathcal{H}}\underline{C}_d$ with $\underline{C}_d$ in Lemma 2.10, $\underline{G}_d$ in Lemma 2.12, $\underline{\mathcal{D}}$ in Lemma 2.13, and $\underline{\mathcal{H}}$ in Lemma 2.14, then*

$$\det(\underline{I}_T + \underline{L}_{b,d}) = \det(\underline{I}_\tau + \underline{L}_d). \tag{2.17}$$

Proof. By properties of determinants (Kolman and Hill, 2008, Section 3.2) and $\operatorname{rank}\{\underline{\mathcal{D}}\} = \tau$ follows

$$\det(\underline{I}_T + \underline{L}_{b,d}) = \det(\underline{I}_T + \underline{G}_{b,d}\underline{\mathcal{H}}\,\underline{C}_d\underline{\mathcal{D}}) \tag{2.18a}$$

$$= \det\left(\underline{I}_T + \begin{bmatrix} \underline{\mathcal{D}}\,\underline{G}_{b,d}\underline{\mathcal{H}}\,\underline{C}_d & \underline{0} \\ \underline{0} & \underline{0}_{T-\tau} \end{bmatrix}\right) \tag{2.18b}$$

$$= \det\left(\begin{bmatrix} \underline{I}_\tau + \underline{\mathcal{D}}\,\underline{G}_{b,d}\underline{\mathcal{H}}\,\underline{C}_d & \underline{0} \\ \underline{0} & \underline{I}_{T-\tau} \end{bmatrix}\right) \tag{2.18c}$$

$$= \det(\underline{I}_\tau + \underline{\mathcal{D}}\,\underline{G}_{b,d}\underline{\mathcal{H}}\,\underline{C}_d) \tag{2.18d}$$

$$= \det(\underline{I}_\tau + \underline{L}_d). \tag{2.18e}$$

□

In Lemma 2.17, $\underline{I}_T + \underline{L}_{b,d}$ has dimensions $T \times T$ and $\underline{I}_\tau + \underline{L}_d$ has dimensions $\tau \times \tau$. Since $\tau \leq T$, the latter is preferred to calculate the determinant and used in the stability test. The stability test for LPTV systems is presented in Theorem 2.18.

Theorem 2.18. *Given $\underline{C}_d$ in Lemma 2.10, $\underline{G}_d$ in Lemma 2.12, $\underline{\mathcal{D}}$ in Lemma 2.13, and $\underline{\mathcal{H}}$ in Lemma 2.14, the closed-loop transfer function $\rho_b \mapsto \varepsilon_b$ in Figure 2.3 given by $S_{b,d}$ is stable if and only if the image of* $\det(\underline{I}_\tau + \underline{L}_d)$, *with*

$$\underline{L}_d(e^{j\omega T\delta_b}) = \underline{\mathcal{D}}\,\underline{G}_d(e^{j\omega T\delta_b})\,\underline{\mathcal{H}}\,\underline{C}_d(e^{j\omega T\delta_b}), \tag{2.19}$$

(i) does not pass through the origin, and

(ii) makes P anti-clockwise encirclements of the origin,

with P the number of unstable poles of $\underline{L}_d$ counting multiplicities.

Proof. By Lemma 2.11, the state matrix of $\mathcal{L}_T S_{b,d}\mathcal{L}_T^{-1}$ is given by Ψ in (2.5), hence the roots of $\phi(z)$ in (2.7) are the poles of $\mathcal{L}_T S_{b,d}\mathcal{L}_T^{-1} = \mathcal{L}_T(1+L_{b,d})^{-1}\mathcal{L}_T^{-1}$ $= (\underline{I}_T + \mathcal{L}_T L_{b,d}\mathcal{L}_T^{-1})^{-1} = (\underline{I}_T + \underline{L}_{b,d})^{-1}$, i.e., the roots of $\det(\underline{I}_T + \underline{L}_{b,d})$, which by Lemma 2.17 are the roots of $\det(\underline{I}_\tau + \underline{L}_d)$. Let $\underline{L}_d \overset{z}{=} (A, B, C, D)$, then the open-loop and closed-loop characteristic polynomials are $\phi_{ol}(z) = \det(zI - A)$ and $\phi_{cl}(z) = \det(zI - A_{cl})$, with $A_{cl} = A - B(\underline{I}_\tau + D)^{-1}C$. Using the Schur complement,

$$\det(\underline{I}_\tau + \underline{L}_d) = \det(\underline{I}_\tau + C(zI - A)^{-1}B + D) \tag{2.20a}$$

$$= \frac{1}{\det(zI - A)} \det \begin{bmatrix} zI - A & B \\ -C & \underline{I}_\tau + D \end{bmatrix} \tag{2.20b}$$

$$\begin{aligned} &= \frac{1}{\det(zI - A)} \det(\underline{I}_\tau + D) \\ &\qquad \times \det(zI - A + B(\underline{I}_\tau + D)^{-1}C) \end{aligned} \tag{2.20c}$$

$$\det(\underline{I}_\tau + \underline{L}_d) = \frac{\det(zI - A_{cl})}{\det(zI - A)} \det(\underline{I}_\tau + D) \tag{2.20d}$$

$$= \frac{\phi_{cl}(z)}{\phi_{ol}(z)} c, \tag{2.20e}$$

with constant $c = \det(\underline{I}_\tau + D)$. Hence, the closed-loop poles are the roots of $\phi_{cl}(z)$ and the closed-loop zeros are the roots of $\phi_{ol}(z)$.

The stability conditions follow from applying Lemma 2.16 to (2.20e), with C being the contour encircling the region outside the unit disk such that Z is the number of unstable closed-loop poles (roots of $\phi_{cl}(z)$ with $|z| > 1$) and P is the number of unstable closed-loop zeros (roots of $\phi_{ol}(z)$ with $|z| > 1$). The first condition ensures $\det(\underline{I}_\tau + \underline{L}_d)$ is analytic on C. The second condition ensures closed-loop stability through $Z = 0$ as follows from the choice of contour C and (2.6). □

The number of unstable poles P in Theorem 2.18 follows from the design of C_d and the number of unstable poles of $G_{b,d}$. The number is typically known and for motion systems often given by the number of rigid body modes in $G_{b,d}$.

Interestingly, in view of Theorem 2.18, Lemma 2.17 essentially shows that stability on the equidistant base rate Δ_b is equivalent to stability on the non-equidistant rate Δ_{ne}. The result is explained by the fact that feedback is only applied on the non-equidistant rate, i.e., in between these sampling instances the system is in open-loop, and therefore it suffices to check stability on Δ_{ne}. Importantly, it does not suffice to check stability on Δ_{eq}.

Remark 2.19. *For multivariable systems, care has to be taken regarding indentations (Desoer and Wang, 1980), since indentations outside the unit disc may lead to undesirable results for multivariable systems.*

Remark 2.20. *The sampling in Figure 2.3 should be non-pathological to preserve controllability and observability (Chen and Francis, 1995, Section 2.2).*

2.4 Performance: FRFs for LPTV systems

In this section, the performance of the system in Figure 2.3 is quantified, which addresses subproblem (B). The performance is quantified in terms of FRFs and constitutes Contribution 2.II. Importantly, Bode plots, used for performance characterization of LTI systems, are not directly applicable for performance characterization of LPTV systems since for LPTV systems a single input frequency generally yields multiple output frequencies. In this section, the periodicity is exploited to obtain equivalent Bode plots for performance characterization, extending the multirate approach in Oomen et al. (2007) to non-equidistantly sampled systems. Indeed, the results in Oomen et al. (2007) are recovered as a special case.

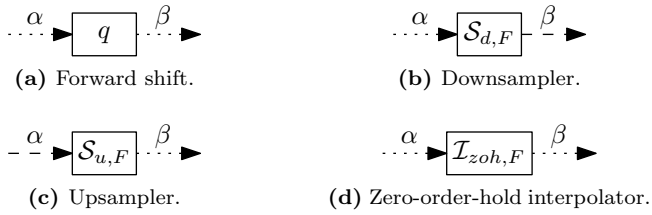

(a) Forward shift. **(b)** Downsampler. **(c)** Upsampler. **(d)** Zero-order-hold interpolator.

Figure 2.5. Multirate building blocks for conversion between equidistantly sampled signals, where dashed lines (- - -) are signals at low rate and dotted lines (·····) are signals at high rate.

First, several preliminary results are presented. In Section 2.4.1, the conversion between equidistant rates based on multirate building blocks is presented. The building blocks are used in Section 2.4.2 to describe the system in Figure 2.3 through filter banks. Based on the filter banks, frequency response functions (FRFs) are presented in Section 2.4.3. The FRFs provide a full characterization of the system but are not convenient for control design. The main result, performance functions for the system in Figure 2.3 based on FRFs, is presented in Section 2.4.4 and used for control design in Section 2.5.

2.4.1 Multirate building blocks

Conversion between equidistant rates is described by the multirate operators in Figure 2.5. These operators are defined in Definitions 2.21 to 2.24, with A, B the Fourier transforms of the signals α, β, respectively.

Definition 2.21 (Forward shift)**.** *The forward shift operator q in Figure 2.5(a) is defined as*

$$\beta[k] = \alpha[k+1], \qquad B(e^{j\omega h}) = e^{j\omega h} A(e^{j\omega h}). \tag{2.21}$$

Definition 2.22 (Downsampler)**.** *The downsampling operator $\mathcal{S}_{d,F}$ in Figure 2.5(b) with downsample factor $F \in \mathbb{N}$ is defined as*

$$\beta[k] = \alpha[Fk], \qquad B(e^{j\omega h}) = \frac{1}{F} \sum_{f=0}^{F-1} A\left(e^{j\frac{1}{F}(\omega h - 2\pi f)}\right). \tag{2.22}$$

Definition 2.23 (Upsampler)**.** *The upsampling operator $\mathcal{S}_{u,F}$ in Figure 2.5(c) with upsample factor $F \in \mathbb{N}$ is defined as*

$$\beta[k] = \begin{cases} \alpha[\frac{k}{F}], & \frac{k}{F} \in \mathbb{Z}, \\ 0, & \frac{k}{F} \notin \mathbb{Z}, \end{cases} \qquad B(e^{j\omega h}) = A(e^{j\omega F h}). \tag{2.23}$$

Definition 2.24 (Zero-order-hold interpolator)**.** *The zero-order-hold interpolator $\mathcal{I}_{zoh,F}$ in Figure 2.5(d) with interpolation factor $F \in \mathbb{N}$ is defined as*

$$\beta[k] = \alpha[F\lfloor \tfrac{k}{F} \rfloor], \qquad B(e^{j\omega h}) = A(e^{j\omega h}) \sum_{f=0}^{F-1} e^{-j\omega h f}. \tag{2.24}$$

In control, the zero-order-hold interpolator in Definition 2.24 is commonly used in combination with the upsampler in Definition 2.23. Further properties are available in, e.g., Vaidyanathan (1993, Section 4.1.1).

In the next section, the multirate building blocks in Figure 2.5 are used to construct the conversion between the base sampling sequence Δ_b and the non-equidistant sampling sequence Δ_{ne} present in Figure 2.3.

2.4.2 Composed closed-loop of LPTV systems

In this section, the complete characterization of the system in Figure 2.3 is presented. The non-equidistant downsampler $\mathcal{D}$ and zero-order-hold upsampler $\mathcal{H}$ in Figure 2.3, and the lifted controller $\underline{C}_d$ in Lemma 2.10 are constructed from the multirate building blocks of Figure 2.5 as shown in Figure 2.6. The construction is based on filter banks by splitting the signals into subband signals (Vaidyanathan, 1993, Section 4.1.2).

The decomposition of the product $\mathcal{H}C_d\mathcal{D}$ into the multirate building blocks of Figure 2.5 is presented in Figure 2.7. The result follows directly from connecting the non-equidistant downsampler $\mathcal{D}$ in Figure 2.6(a), the lifted controller $\underline{C}_d$ in Lemma 2.10, and the non-equidistant zero-order-hold upsampler $\mathcal{H}$ in Figure 2.6(b). An illustrative example of the different steps is provided in Appendix 2.A.

In the next section, the filter banks are used to construct frequency response functions of LPTV systems.

2.4.3 Frequency response functions of LPTV systems

In this section, frequency response functions (FRFs) of LPTV systems are presented. The FRF of $\mathcal{H}C_d\mathcal{D}$ is given by Theorem 2.25.

Theorem 2.25. *Let $E_b(e^{j\omega\delta_b})$ be the Fourier transform of ε_b, then the Fourier transform of $\nu_b = \mathcal{H}C_d\mathcal{D}\varepsilon_b$ in Figure 2.7 is given by*

$$\begin{aligned} N_b(e^{j\omega\delta_b}) = \sum_{i=1}^{\tau} e^{-j\omega\tilde{\gamma}_i\delta_b} \Bigg(\sum_{f=0}^{\gamma_i-1} e^{-j\omega\delta_b f} \Bigg) \Bigg(\sum_{k=1}^{\tau} \underline{C}_d[i,k](e^{j\omega T^2\delta_b}) \\ \times \frac{1}{T} \sum_{f_i=0}^{T-1} \Big(e^{j\tilde{\gamma}_k(\omega\delta_b - 2\pi\frac{f_i}{T})} E_b(e^{j(\omega\delta_b - 2\pi\frac{f_i}{T})}) \Big) \Bigg), \end{aligned} \tag{2.25}$$

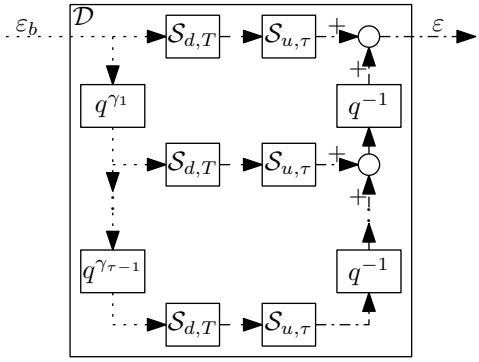

(a) Non-equidistant downsampler $\mathcal{D}$.

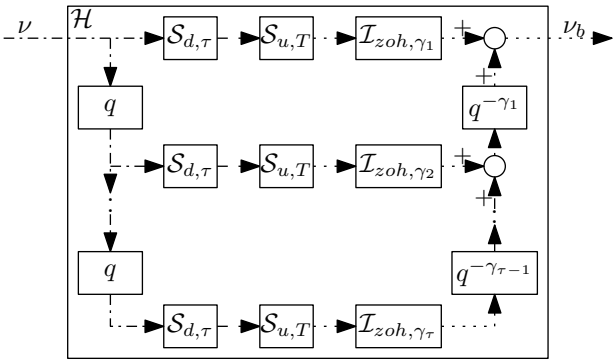

(b) Non-equidistant zero-order-hold upsampler $\mathcal{H}$.

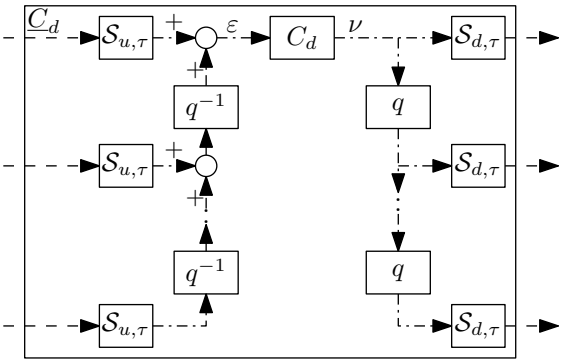

(c) Lifted controller $\underline{C}_d$.

Figure 2.6. Non-equidistant downsampler $\mathcal{D}$, zero-order-hold upsampler $\mathcal{H}$, and lifted controller $\underline{C}_d$ constructed from the multirate building blocks in Figure 2.5, with base rate (·····) defined by Δ_b in (2.1) and non-equidistant rate (-·-·) defined by Δ_{ne} in (2.2).

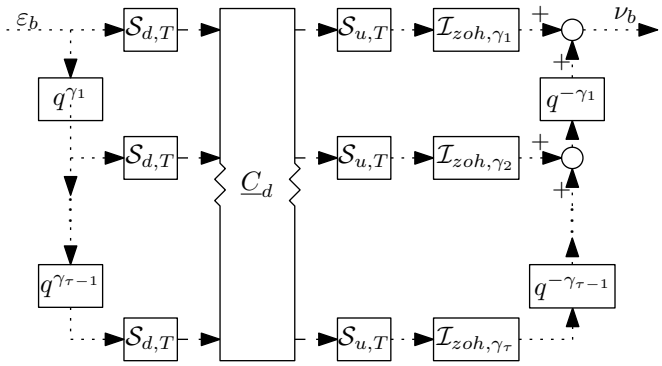

Figure 2.7. Filter bank of the transfer function $\varepsilon_b \mapsto \nu_b$ in Figure 2.3, i.e., $\mathcal{H}C_d\mathcal{D}$, with base rate (·····) defined by Δ_b in (2.1) and non-equidistant rate (-·-·-·) defined by Δ_{ne} in (2.2). The left side decomposes the equidistantly sampled signal ε_b into τ subband signals with periodicity T which are the input to the lifted controller $\underline{C}_d$. The right side constructs the equidistantly sampled signal ν_b through upsampling with zero-order-hold interpolation.

with $\tilde{\gamma}_i = \sum_{j=1}^{i-1} \gamma_j$.

Proof. The dependency is given by Figure 2.7. The result follows from substitution of the Fourier transforms of the multirate building blocks given by Definitions 2.21 to 2.24. □

Importantly, Theorem 2.25 shows that the output $N_b(e^{j\omega\delta_b})$ at frequency ω depends on the T input frequencies $(\omega\delta_b - 2\pi\frac{f_i}{T})$, $f_i = 0, 1, \ldots, T$, of E_b. Vice versa, a single frequency in E_b contributes to T frequencies in N_b. The result directly leads to the frequency response matrix $\overline{\mathcal{H}C_d\mathcal{D}}$ satisfying $N_b = \overline{\mathcal{H}C_d\mathcal{D}}E_b$. Since the system is LPTV with period T, the FRM has the structure

$$\overline{\mathcal{H}C_d\mathcal{D}} : \begin{bmatrix} \ddots & \cdots & \ddots \\ \vdots & \ddots & \vdots \\ \ddots & \cdots & \ddots \end{bmatrix} \tag{2.26}$$

consisting of $T \times T$ diagonal submatrices. Since $G_{b,d}$ is LTI, the Fourier transform of ψ_b is given by $Y_b(e^{j\omega\delta_b}) = \overline{G_{b,d}}N_b(e^{j\omega\delta_b})$, where $\overline{G_{b,d}}$ has the diagonal structure

$$\overline{G_{b,d}} : \begin{bmatrix} \ddots \end{bmatrix}. \tag{2.27}$$

Let $R_b(e^{j\omega\delta_b}), H_b(e^{j\omega\delta_b})$ be the Fourier transforms of ρ_b, η_b in Figure 2.3, then

$$E_b(e^{j\omega\delta_b}) = \overline{S_{b,d}} R_b(e^{j\omega\delta_b}) - \overline{S_{b,d}} H_b(e^{j\omega\delta_b}), \tag{2.28}$$

with $\overline{S_{b,d}} = \left(I + \overline{G_{b,d}\mathcal{H}C_d\mathcal{D}}\right)^{-1}$ which has the same structure as $\overline{\mathcal{H}C_d\mathcal{D}}$, see (2.26). In the next section, the structure of the FRM is exploited for performance evaluation.

Remark 2.26. *For equidistant control on Δ_b, it follows that $\Gamma_{ne} = 1$, $T = 1$, and hence the controller is LTI where* (2.25) *reduces to*

$$N_b(e^{j\omega\delta_b}) = \underline{C}_d(e^{j\omega\delta_b}) E_b(e^{j\omega\delta_b}), \tag{2.29}$$

and the FRM in (2.26) *has the structure*

$$\overline{\mathcal{H}C_d\mathcal{D}}\big|_{\Gamma_{ne}=1} : \begin{bmatrix} \diagdown \end{bmatrix}. \tag{2.30}$$

2.4.4 Frequency-domain performance of LPTV systems

In traditional loop-shaping control design for LTI systems, Bode plots are used to quantify the performance and based on the frequency separation principle. As shown by Theorem 2.25, the frequency separation principle does not hold for the LPTV system in Figure 2.3. Aimed at loop-shaping control design for LPTV systems, the interest is in performance functions that only depend on the input frequency, similar as in Bode plots for LTI systems. In this section, two such performance functions are presented. The functions show those aspects of the FRFs most relevant for controller design.

The two functions are generalizations of the fundamental transfer function (FTF) $\mathcal{F}$ and the performance frequency gain (PFG) $\mathcal{P}$ as used for multirate and sampled-data systems, see Oomen et al. (2007); Lindgärde and Lennartson (1997) and references therein. Generalizations for LPTV systems in terms of the FRM are given by Definition 2.27 and Definition 2.28 and follow from the multirate definitions in Oomen et al. (2007) and the structure of the FRM.

Definition 2.27 (Fundamental transfer function (FTF))**.** *Given a frequency response matrix $\bar{G}$ with elements $\bar{G}[i,j]$ corresponding to the ith output frequency and the jth input frequency, the fundamental transfer function (FTF) for the kth input frequency is defined by*

$$\mathcal{F}_k = \bar{G}[k,k] \in \mathbb{C}. \tag{2.31}$$

Definition 2.28 (Performance frequency gain (PFG))**.** *Given a frequency response matrix $\bar{G}$ with elements $\bar{G}[i,j]$ corresponding to the ith output frequency*

and the jth input frequency, the performance frequency gain (PFG) for the kth input frequency is defined by

$$\mathcal{P}_k = \sqrt{\sum_i \left\|\bar{G}[i,k]\right\|_2^2} \in \mathbb{R}. \tag{2.32}$$

Note that both the FTF and the PFG are defined in terms of the input frequency. The FTF corresponds to the diagonal of the FRM and hence only takes into account the fundamental frequency component. The PFG takes into account the full intersample behavior and relates the root-mean-square (rms) value of the input to that of the output. This is particularly relevant to quantify control performance as also shown in Section 2.6 and Section 2.7.

In the next section, the stability test presented in Section 2.3 and the performance functions presented in this section are used for LPTV loop-shaping controller design.

Remark 2.29. *For LTI systems, the FRM is diagonal and hence the output frequencies equal the input frequencies, the FTF (Definition 2.27) equals the FRF, and the PFG (Definition 2.28) equals the magnitude response of the FRF. See also Remark 2.26.*

2.5 Loop-shaping control design

In the previous two sections, the stability and performance aspects of the main problem in Section 2.2.4 are addressed. In this section, the loop-shaping control design based on FRF measurements is presented, which constitutes Contribution 2.III.

First, different approaches for loop-shaping control design for LTI systems are evaluated. Second, a loop-shaping design procedure for LTI systems is presented. Finally, loop-shaping design procedures for LPTV systems are presented.

2.5.1 Control design approaches for LTI systems

In this section, the design of a discrete-time LTI controller $C_d(z)$ using loop-shaping techniques is considered. The starting point is an identification experiment from which a continuous-time FRF measurement $G_c(j\omega)$ or a discrete-time FRF measurement $G_d(e^{j\omega\delta})$ with sampling time δ can be obtained.

There are two main requirements for loop-shaping design for LPTV systems. First, the frequency response behavior should be asymptotic with respect to the frequency since stability and performance specifications are defined in terms of cut-off frequencies and asymptotes (Van de Wal et al., 2002). Second, the discretization should be exact. Discretization methods such as zero-order-hold and Tustin introduce approximation errors close to the Nyquist frequency, as

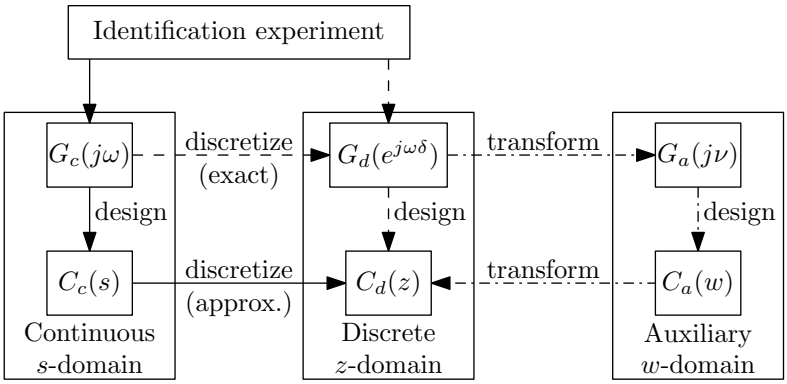

Figure 2.8. Discrete-time controller $C_d(z)$ can be designed using the continuous-time s-domain (——), the discrete-time z-domain (- - -), or the auxiliary w-domain (-·-·), see also Oomen et al. (2005). Design via the w-domain is preferred since it facilitates loop-shaping design and provides an exact transformation.

illustrated in Appendix 2.B. For most LTI control designs this does not pose problems since the designs do not include features near the Nyquist frequency. However, for LPTV controller designs, features near the Nyquist frequency are relevant, as also shown in Section 2.7.

The three main design approaches are visualized in Figure 2.8, see also Oomen et al. (2005), and evaluated in the subsequent sections.

2.5.1.1 Discrete-time design

The first approach is a discrete-time design based on the discrete-time FRF $G_d(e^{j\omega\delta})$. Since the FRF is non-rational in frequency ω, the asymptotic behavior of the frequency response with respect to the frequency is lost and therefore the approach is unsuited for loop-shaping design.

2.5.1.2 Continuous-time design

The second approach is based on the continuous-time FRF $G_c(j\omega)$ obtained from the identification experiment. FRF $G_c(j\omega)$ is rational in ω and hence suited for continuous-time loop-shaping control design. However, the approach is not suited for discrete-time control design since (i) $G_c(j\omega)$ does not capture discrete-time aspects; and (ii) the discretization of $C_c(s)$ to $C_d(z)$ is approximate rather than exact.

2.5.1.3 w-plane design

The third approach is based on transforming the FRF $G_d(e^{j\omega\delta})$ to $G_a(j\nu)$ in the auxiliary w-domain and combines the advantages of the previous two approaches. The approach, which is detailed below, enables loop-shaping design and provides exact discretization.

The transformation from the discrete-time z-domain to the auxiliary w-domain and vice versa is performed using bilinear Tustin transformations, a special case of linear fractional or Möbius transformations (Brown and Churchill, 2009), given by

$$w = \frac{2(z-1)}{\delta(z+1)}, \qquad z = \frac{1+\frac{w\delta}{2}}{1-\frac{w\delta}{2}}. \tag{2.33}$$

Let controller $C_a(w)$ have state-space realization $C_a \overset{w}{=} (A_a, B_a, C_a, D_a)$, then the discrete-time controller C_d with sampling time δ is given by $C_d \overset{z}{=} (A_d, B_d, C_d, D_d)$, with

$$A_d = (I - \tfrac{\delta}{2}A_a)^{-1}(I + \tfrac{\delta}{2}A_a), \tag{2.34a}$$

$$B_d = \delta(I - \tfrac{\delta}{2}A_a)^{-1}B_a, \tag{2.34b}$$

$$C_d = C_a(I - \tfrac{\delta}{2}A_a)^{-1}, \tag{2.34c}$$

$$D_d = D_a + \tfrac{1}{2}\delta C_a(I - \tfrac{\delta}{2}A_a)^{-1}B_a. \tag{2.34d}$$

Transformation (2.33) preserves all magnitude and phase characteristics, but introduces frequency warping, i.e., $G_d(e^{j\omega\delta}) = G_a(j\nu)$ where frequency axis $z = e^{j\omega\delta}$ is mapped to frequency axis $w = j\nu$ with fictitious frequency

$$\nu = \frac{2}{\delta}\tan\left(\frac{\omega\delta}{2}\right). \tag{2.35}$$

The frequency warping is compensated by implementing a characteristic at discrete-time frequency ω at the fictitious frequency ν given by (2.35). An example of this pre-warping is presented in Appendix 2.B.

Importantly, the auxiliary w-plane has the same characteristics as the continuous-time s-plane (Oomen et al., 2005) and thus enables loop-shaping of $C_a(w)$ based on $G_a(j\nu)$ similar to continuous-time approaches. Since the w-plane approach has asymptotic behavior of the frequency response with respect to the frequency and yields exact discretization, the approach is used in the loop-shaping design procedures presented in the next sections.

2.5.2 Loop-shaping for LTI systems

In this section, a loop-shaping design procedure is presented for the design of a discrete-time LTI controller $C_d(z)$ based on an FRF measurement $G_d(e^{j\omega\delta})$. The loop-shaping design procedure for LPTV systems is presented in Section 2.5.3.

The LTI control design is performed in the w-plane, with the bandwidth (gain crossover frequency (Skogestad and Postlethwaite, 2005, (2.44))) defined as the first 0 dB crossing of the discrete-time open-loop system $L_d(z) = G_d(z)C_d(z)$, i.e., $\omega_{bw} := \min_\omega |L_d(e^{j\omega\delta})| = 1$. The procedure provides general guidelines for the design, which may need adjustment to the specific situation. The rationale behind the procedure can be found in Steinbuch et al. (2010). The procedure is given by Procedure 2.30.

Procedure 2.30 (LTI loop-shaping via the w-plane)**.** *Let FRF measurement $G_d(e^{j\omega\delta})$ be given.*

1. *Transform $G_d(e^{j\omega\delta})$ to $G_a(j\nu)$ by warping the frequency axis using* (2.35)*.*
2. *Define a desired bandwidth ω_{bw} and determine ν_{bw} using* (2.35)*.*
3. *Stabilize the system.*
   - *3.a Create phase lead at the bandwidth by adding a lead filter $\frac{\frac{1}{\nu_{l1}}w+1}{\frac{1}{\nu_{l2}}w+1}$ (e.g., $\nu_{l1} = \frac{1}{3}\nu_{bw}$, $\nu_{l2} = 3\nu_{bw}$).*
   - *3.b Adjust gain such that $|L_a(j\nu_{bw})| = 1$, with $L_a(w) = G_a(w)C_a(w)$.*
   - *3.c Use the Nyquist plot of $1+L_a(w)$ to check closed-loop stability and the phase margin $\angle L_a(j\nu_{bw}) + 180°$ (Skogestad and Postlethwaite, 2005, (2.43)) (typically $30° - 60°$). If the closed-loop system is unstable or the phase margin is unsatisfactory, go back to step 2 and lower the bandwidth ω_{bw}, or go back to step 3.a and retune ν_{l1}, ν_{l2}.*
4. *Increase performance. Check stability after each step. If the system is unstable, retune the parameters or go back to step 2 and lower the bandwidth ω_{bw}.*
   - *4.a Remove resonances to improve stability margins or shape closed-loop transfer functions in specific frequency ranges using (skewed) notch filters $\frac{\frac{1}{\nu_{n1}}w^2+\frac{2\beta_1}{\nu_{n1}}w+1}{\frac{1}{\nu_{n2}}w^2+\frac{2\beta_2}{\nu_{n2}}w+1}$ (typically: modulus margin (Skogestad and Postlethwaite, 2005, (2.46)) $\max_\omega \left|\frac{1}{1+G_d(j\omega)C_d(j\omega)}\right| < 6$ dB).*
   - *4.b Improve steady-state behavior by adding integrators with cut-off $\frac{w+\nu_i}{w}$ (e.g., $\nu_i = \frac{1}{5}\nu_{bw}$).*
   - *4.c Cut-off high frequent controller gain by adding a first-order low-pass filter $\frac{1}{\frac{1}{\nu_c}w+1}$ (e.g., $\nu_c = 6\nu_{bw}$) or a second-order low-pass filter $\frac{1}{\frac{1}{\nu_c^2}w^2+\frac{2\beta}{\nu_c}w+1}$ (e.g., $\nu_c = 6\nu_{bw}$, $\beta = 0.5$).*
   - *4.d Check performance by evaluating the Bode plot of the relevant transfer functions. If unsatisfactory, retune the parameters.*

5. *Transform $C_a(w)$ to $C_d(z)$ using* (2.34).

Note that closed-loop stability and performance with controller $C_d(z)$ is guaranteed by virtue of the bilinear transformation in (2.33) and the design of $C_a(w)$ since the only difference is the frequency warping. The procedure for LTI systems presented in this section forms the basis of the LPTV loop-shaping design procedures presented in the next section.

2.5.3 Loop-shaping for LPTV systems

In this section, three loop-shaping control designs for the LPTV system in Figure 2.3 are presented. The first procedure, Procedure 2.31, provides an LTI controller design for the equidistant sampling sequence Δ_{eq} in (2.3).

Procedure 2.31 (LTI control design)**.** *Let Assumption 2.4 and Assumption 2.5 be satisfied and $G_{b,d}(e^{j\omega\delta_b})$ be given.*

1. *Design an LTI controller C_a in the w-plane based on $G_{b,d}(e^{j\omega\delta_b})$ using Procedure 2.30.*

2. *Determine sampling sequence Δ_{eq} in* (2.3).

3. *Transform C_a to C_d using* (2.34) *with $\delta = \delta_{eq}$.*

4. *Check closed-loop stability for Δ_b using Theorem 2.18. If the closed-loop system is unstable, go back to step 1 and redesign C_a.*

5. *Check performance by evaluating $\mathcal{F}$ and/or $\mathcal{P}$ in Definition 2.27 and Definition 2.28, respectively. If unsatisfactory, go back to step 1 and adjust C_a accordingly.*

Importantly, although the controller design in Procedure 2.31 is LTI, stability and performance should be checked through Theorem 2.18 and $\mathcal{F}, \mathcal{P}$ since Δ_{eq} differs from Δ_b and hence the closed-loop system is LPTV, see also Oomen et al. (2007).

To exploit the potential of non-equidistant sampling, two design procedures for the non-equidistant sampling sequence Δ_{ne} are presented. Procedure 2.32 provides an LPTV control design based on a single w-plane LTI control design.

Procedure 2.32 (LPTV control: single design)**.** *Let Assumption 2.4 and Assumption 2.5 be satisfied and $G_{b,d}(e^{j\omega\delta_b})$ be given.*

1. *Design an LTI controller C_a in the w-plane based on $G_{b,d}(e^{j\omega\delta_b})$ using Procedure 2.30.*

2. *Determine the state-space representation of LPTV controller $C_d[i]$ during interval i, $i = 1, 2, \ldots, \tau$, by transforming C_a using* (2.34) *with $\delta = \delta_i$.*

Table 2.1. Overview of proposed controller design procedures for LPTV systems in terms of the w-plane controller design.

Description	Reference	Control sequence w-plane
LTI control	Procedure 2.31	$(C_a, C_a, \ldots)$ on Δ_{eq}
LPTV control: single	Procedure 2.32	$(C_a, C_a, \ldots)$ on Δ_{ne}
LPTV control: multiple	Procedure 2.33	$(C_a[1], \ldots, C_a[\tau], C_a[1], \ldots)$ on Δ_{ne}

3. *Check closed-loop stability for Δ_b using Theorem 2.18. If the closed-loop system is unstable, go back to step 1 and redesign C_a.*

4. *Check performance by evaluating $\mathcal{F}$ and/or $\mathcal{P}$ in Definition 2.27 and Definition 2.28, respectively. If unsatisfactory, go back to step 1 and adjust C_a accordingly.*

Procedure 2.32 is based on the same LTI controller design for each time interval δ_i. To exploit the full potential of non-equidistant sampling, Procedure 2.33 provides separate control designs for each time interval δ_i.

Procedure 2.33 (LPTV control: multiple designs)**.** *Let Assumption 2.4 and Assumption 2.5 be satisfied and $G_{b,d}(e^{j\omega\delta_b})$ be given.*

1. *For each time interval δ_i, $i = 1, 2, \ldots, \tau$, design an LTI controller $C_a[i]$ in the w-plane based on $G_{b,d}(e^{j\omega\delta_b})$ using Procedure 2.30.*

2. *Determine the state-space representation of LPTV controller $C_d[i]$ during interval i, $i = 1, 2, \ldots, \tau$, by transforming $C_a[i]$ using (2.34) with $\delta = \delta_i$.*

3. *Check closed-loop stability for Δ_b using Theorem 2.18. If the closed-loop system is unstable, go back to step 1 and redesign $C_a[i]$.*

4. *Check performance by evaluating $\mathcal{F}$ and/or $\mathcal{P}$ in Definition 2.27 and Definition 2.28, respectively. If unsatisfactory, go back to step 1 and adjust $C_a[i]$ accordingly.*

The w-plane controller designs for the three design procedures are summarized in Table 2.1. Importantly, for all three design procedures closed-loop stability should be checked for the discrete-time controller C_d since there is no guarantee closed-loop stability is preserved under equidistant sampling (Procedure 2.31), non-equidistant sampling (Procedure 2.32), or concatenating controllers (Procedure 2.33).

In the next section, the control design procedures are used in controller design for a motion system.

Remark 2.34. *Note that the states of controllers $C_d[i]$, $i = 1, 2, \ldots, \tau$, in Procedure 2.33 should match.*

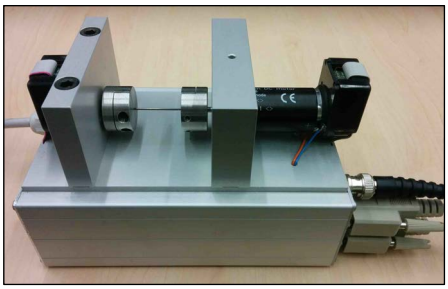

Figure 2.9. Experimental setup: a two-mass-spring-damper system. The two rotating masses are connected via a flexible shaft. The collocated motor and encoder on the right-hand side are used as input and output, respectively.

2.6 Application to a motion system

In this section, the LPTV control design procedures presented in Section 2.5 are used in controller design for a motion system. The designs show the advantages of non-equidistant sampling over equidistant sampling and constitute Contribution 2.IV. In Section 2.7, the presented controller designs are validated in experiments.

2.6.1 Experimental motion system

The experimental setup is shown in Figure 2.9. The system consists of two rotating masses that are connected via a flexible shaft. The FRF measurement $G_{b,d}$ is shown in Figure 2.10 and obtained through a dedicated identification procedure (Pintelon and Schoukens, 2012, Chapter 2) for sampling sequence Δ_b, with sampling time $\delta_b = 0.25$ ms.

Analysis of the system reveals that there are two rigid body modes in $G_{b,d}$ and no unstable poles. In the remainder, only stable controllers are considered, hence $P = 2$ in Theorem 2.18. Consequently, by application of Theorem 2.18, the closed-loop system is stable if and only if the Nyquist plot does not pass through the origin and has two anti-clockwise encirclements of the origin, see also Remark 2.19.

2.6.2 Case study

The control diagram in Figure 2.3 is considered where Δ_{ne} in (2.3) is given by $\Gamma_{ne} = \begin{bmatrix} 2 & 2 & 4 \end{bmatrix}$. By Definition 2.6, Δ_{eq} is given by $\Gamma_{eq} = 4$, i.e., $\delta_{eq} = 1$ ms, and has Nyquist frequency $f_{eq,n} = \frac{1}{2}\frac{1}{\delta_{eq}} = 500$ Hz.

The controller designs are evaluated for non-aliased and aliased disturbances

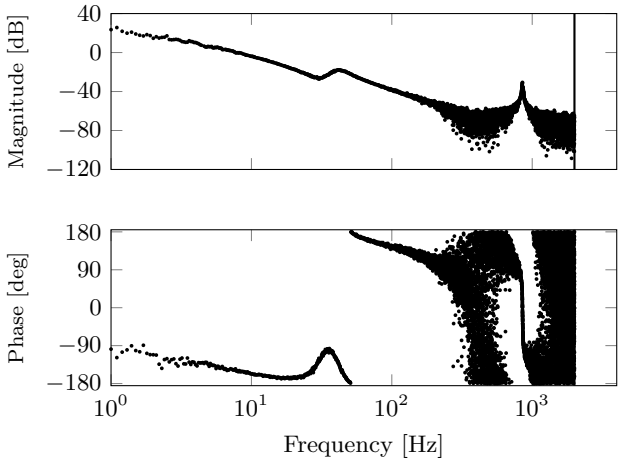

Figure 2.10. FRF measurement $G_{b,d}(e^{j\omega\delta_b})$ of the system in Figure 2.9 obtained by a dedicated identification experiment using Δ_b. The frequency resolution is 0.1 Hz.

(Riggs and Bitmead, 2013; Oomen et al., 2007) by setting

$$\eta_b[k] = 0.04\sqrt{2}\sin(2\pi f_1 k) + 0.015\sqrt{2}\sin(2\pi f_2 k), \tag{2.36}$$

with $f_1 = 10$ Hz and $f_2 = 890$ Hz such that $f_1 < f_{eq,n}$ and $f_2 > f_{eq,n}$. The reference trajectory is set to zero, i.e., $\rho_b[k] = 0$, for all k. The relevant transfer function $\eta_b \mapsto \varepsilon_b$ is given by $-S_{b,d}$, with $S_{b,d} = (1 + G_{b,d}\mathcal{H}C_d\mathcal{D})^{-1}$. For a fair comparison, the desired bandwidth in the w-plane is fixed at $\nu_{bw} = 25 \cdot 2\pi$ rad/s for all controller designs. Note that ω_{bw} in the z-domain does not provide a fair comparison since it depends on δ_i.

Next, five controller designs based on the procedures in Section 2.5 are presented. An overview is presented in Table 2.2. Experimental validation of the designs is presented in Section 2.7.

2.6.3 Design 1: Equidistant control for stability

The first controller is designed for Δ_{eq} and based on Procedure 2.31 with the following steps.

1. In Procedure 2.30, the bandwidth of C_{a1} is set to $\nu_{bw} = 25 \cdot 2\pi$ rad/s. A lead filter with $\nu_{l1} = \frac{1}{3}\nu_{bw}$ and $\nu_{l2} = 3\nu_{bw}$ is used to create phase margin near the bandwidth ν_{bw}. An integrator with cut-off at $\frac{1}{5}\nu_{bw}$ is used to overcome friction.

2. Δ_{eq} is equidistant with sampling interval $\delta_{eq} = 1$ ms, see Section 2.6.2.

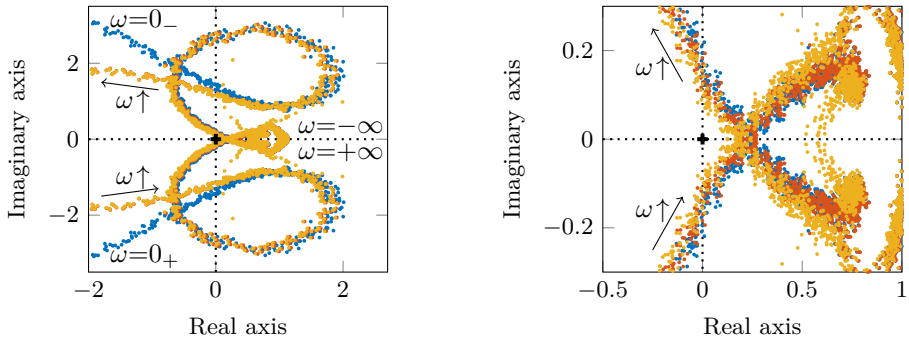

(a) Nyquist plot. **(b)** Zoom view around the origin.

Figure 2.11. Nyquist plot of $\det(\underline{I}_\tau + \underline{L}_d)$ for designs C_{d1} (●), C_{d2} (●), and C_{d3} (●). By application of the LPTV Nyquist test of Theorem 2.18, all three controllers stabilize the system.

3. C_{d1} is obtained from C_{a1} using (2.34) with $\delta = \delta_{eq}$.
4. Closed-loop stability for Δ_{ne} is verified using Theorem 2.18 based on the Nyquist plot in Figure 2.11.
5. The performance functions are not shown since the design is not aimed at performance.

Design C_{d1} stabilizes the system, but achieves moderate performance since step 4 in Procedure 2.30 is omitted. Next, the performance is improved by also designing for performance.

2.6.4 Design 2: Equidistant control for performance

Controller design C_{d2} is an extension of controller design C_{d1} in which performance is taken into account by suppressing disturbance frequency f_1 using step 4 in Procedure 2.30. The steps in Procedure 2.31 are as follows.

1. C_{2a} is obtained by adding an inverse notch filter to design C_{1a}, with $\nu_{n1} = \nu_{n2} = \nu_1$, $\beta_1 = 0.1$, $\beta_2 = 0.01$, where $\nu_1 = 10 \cdot 2\pi$ rad/s follows from f_1 through (2.35). The sensitivity function S_{a2} in Figure 2.12(b) shows the additional suppression at ν_1.
2. Δ_{eq} is equidistant with sampling interval $\delta_{eq} = 1$ ms.
3. C_{d2} is obtained from C_{a2} using (2.34) with $\delta = \delta_{eq}$.
4. Closed-loop stability for Δ_{ne} is verified using Theorem 2.18 based on the Nyquist plot in Figure 2.11 similar as for C_{d1}.

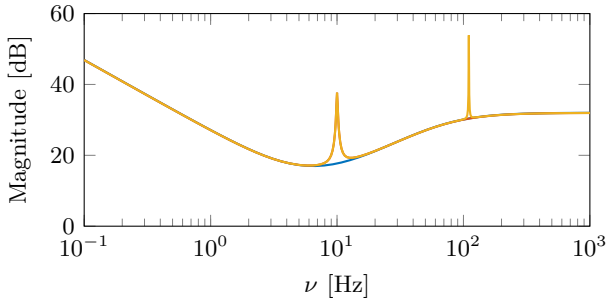

(a) Controller designs C_{a1} (——), C_{a2} (——), and C_{a3} (——).

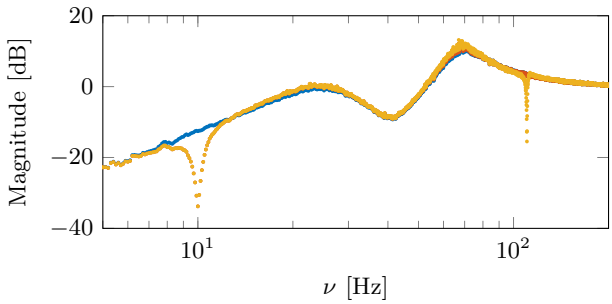

(b) Sensitivity functions in the w-plane. Compared to design S_{a1} (●), design S_{a2} (●) suppresses frequency $\nu_1 = 10 \cdot 2\pi$ rad/s. Design S_{a3} (●) also suppresses frequency $\nu_{2a} = 110 \cdot 2\pi$ rad/s.

Figure 2.12. Bode magnitude diagrams for LTI controller designs C_{a1}, C_{a2}, and C_{a3} in the w-plane.

5. The PFG of $S_{b,d2}$ is shown in Figure 2.13 and shows suppression at f_1.

The FRM, see Section 2.4.3, of the LPTV sensitivity function $S_{b,d2}$ (not shown) reveals that the frequencies most dominantly contributing to ε_b are $f_2 =$ 890 Hz and the aliased frequency $f_{2a} = \frac{1}{\delta_{eq}} - f_2 = 110$ Hz, where $\frac{1}{\delta_{eq}} = 1000$ Hz corresponds to the sampling periodicity of sequence Δ_{eq}. Aliasing of f_2 also yields contributions at other output frequencies, but these contributions are negligible compared to those at f_2, f_{2a}.

2.6.5 Design 3: Equidistant control suppressing aliased components

An important observation for design C_{d2} is that the component at f_2 cannot be suppressed since $f_2 > f_{eq,n}$. To suppress the component at f_{2a}, a notch filter is used in design C_{d3}. The steps for designing C_{d3} using Procedure 2.31 are as

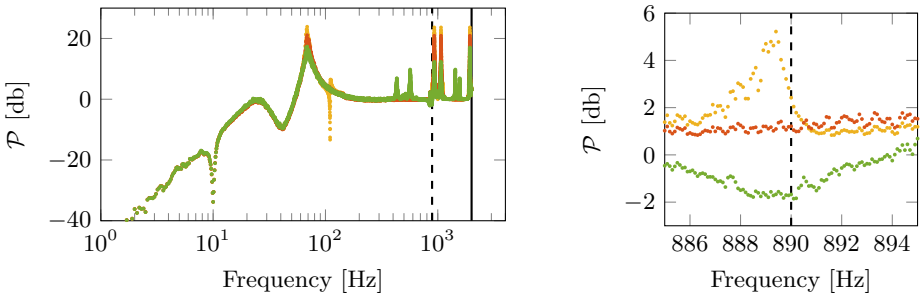

(a) View for all frequencies. **(b)** Detailed view around f_2.

Figure 2.13. Performance frequency gain $\mathcal{P}$ of $S_{b,d2}$ (●), $S_{b,d3}$ (●), and $S_{b,d5}$ (●). All designs suppress $f_1 = 10$ Hz. Design $S_{b,d5}$ yields the smallest amplification at $f_2 = 890$ Hz, and hence the best performance, due to a dedicated design.

follows.

1. C_{3a} is obtained by adding an inverse notch filter to design C_{2a}, with $\nu_{n1} = \nu_{n2} = \nu_{2a}$, $\beta_1 = -0.015$, $\beta_2 = 0.001$, where $\nu_{2a} = 110.27 \cdot 2\pi$ rad/s follows from f_{2a} through (2.35). The sensitivity function S_{a3} in Figure 2.12(b) shows the additional suppression at ν_{2a}.

2. Δ_{eq} is equidistant with sampling interval $\delta_{eq} = 1$ ms.

3. C_{d2} is obtained from C_{a2} using (2.34) with $\delta = \delta_{eq}$.

4. Closed-loop stability for Δ_{ne} is verified using Theorem 2.18 based on the Nyquist plot in Figure 2.11 similar as for C_{d1} and C_{d2}.

5. The PFG of $S_{b,d3}$ is shown in Figure 2.13.

The PFG in Figure 2.13 shows that design C_{d3} yields a performance degradation, instead of a performance improvement, for frequency f_{2a} compared to design C_{d2}. The performance degrades since f_{2a} results from aliasing and is not present in η_b, see (2.36).

The equidistant controller designs C_{d1}, C_{d2}, C_{d3} show that disturbances below the Nyquist frequency can be effectively suppressed. The aliased components of disturbances above the Nyquist frequency can be compensated, which improves the on-sample behavior, but degrades the intersample behavior, see C_{d3}. For these reasons, design C_{d2} is expected to yield the best performance among the equidistant controller designs. The observations are corroborated by the experiments in Section 2.7.

2.6.6 Design 4: Non-equidistant control, single design

The non-equidistant sampling sequence Δ_{ne} has periods smaller than $\frac{1}{2}\frac{1}{f_2} = 0.56$ ms and hence there is potential to suppress frequency f_2. Note that this potential is absent with Δ_{eq}. Design C_{a2} successfully suppresses f_1 and is used as starting point for design C_{d4}. The steps in Procedure 2.32 are as follows.

1. $C_{a4} = C_{a2}$.

2. C_{d4} is obtained by transforming C_{a4} using (2.34) with $\delta = \delta_i$, $i = 1, 2, 3$.

3. Closed-loop stability for Δ_{ne} is verified using Theorem 2.18 in Appendix 2.D.

4. The performance functions are not shown since the design is not aimed at performance.

Design C_{d4} only addresses the f_1 component. Next, frequency f_2 is also addressed.

2.6.7 Design 5: Non-equidistant control, multiple designs

To suppress the f_2 component, an additional inverse notch filter is used during the first two intervals only to avoid aliasing during the third interval. This leads to the LPTV control design C_{d5} consisting of multiple designs, which is designed using Procedure 2.33 as follows.

1. $C_{a5}[1] = C_{a5}[2] = C_{a2}$. $C_{a5}[3]$ is obtained by extending C_{a2} with an inverse notch filter, with $\nu_{n1} = \nu_{n2} = \nu_2$, $\beta_1 = -0.07$, $\beta_2 = 0.005$, where $\nu_2 = 1070 \cdot 2\pi$ rad/s follows from f_2 using (2.35). The additional suppression at ν_2 is shown in Appendix 2.C

2. $C_{d5}[i]$ is obtained by transforming $C_{a5}[i]$ using (2.34) with $\delta = \delta_i$, $i = 1, 2, 3$.

3. Closed-loop stability for Δ_{ne} is verified using Theorem 2.18 in Appendix 2.D.

4. The PFG of $S_{b,d5}$ is shown in Figure 2.13 and shows additional suppression at f_2 as desired.

Design 5 suppresses f_1 and f_2 and avoids aliasing. For these reasons, it is expected that C_{d5} yields the best performance among the non-equidistant controller designs. In the next section, the observations are corroborated by experiments.

Table 2.2. Overview of the different control designs. Designs C_{d4}, C_{d5} for the non-equidistant sequence Δ_{ne} outperform the designs C_{d1}, C_{d2}, C_{d3} for the equidistant sequence Δ_{eq} in terms of minimizing the rms value of ε_b. Suppressing f_{2a} in C_{d3} improves on-sample behavior ε, but degrades intersample behavior in terms of minimizing the rms value of ε_b. Design C_{d5} for the non-equidistantly sampled sequence achieves the best performance.

Label	Sampling sequence	Targeted frequencies f_1	f_{2a}	f_2	On-sample ε_{rms} [mrad]	Intersample $\varepsilon_{b,rms}$ [mrad]
C_{d1} ■	Δ_{eq}	×	×	×	24.03	19.84
C_{d2} ■	Δ_{eq}	✓	×	×	22.09	17.48
C_{d3} ■	Δ_{eq}	✓	✓	×	3.56	19.51
C_{d4} ■	Δ_{ne}	✓	×	×	19.39	16.53
C_{d5} ■	Δ_{ne}	✓	×	✓	13.54	12.65

2.7 Experimental validation

In this section, the five control designs of Section 2.6 are validated on the experimental setup presented in Section 2.6.1 and shown in Figure 2.9, which constitutes Contribution 2.V. An overview of the different control designs is presented in Table 2.2. As expected based on Section 2.6, in terms of intersample behavior, design C_{d2} yields the best performance among the equidistant controllers and design C_{d5} yields the best performance among the non-equidistant controllers. Most importantly, the non-equidistant controller designs are superior to the equidistant controller designs.

2.7.1 Equidistant control designs 1, 2, and 3

The error signals ε_b for the equidistant controller designs C_{d1}, C_{d2}, C_{d3} are shown in Figure 2.14(a) and confirm closed-loop stability. For design C_{d1}, the frequency components f_1, f_2 in (2.36) and aliased component f_{2a} are clearly visible. The corresponding cumulative power spectra (CPS) of ε_b in Figure 2.14(b) show that C_{d2} almost completely suppresses f_1 as desired.

The results in Figure 2.14(b) confirm the performance deterioration for design C_{d3} as suggested by the PFG in Figure 2.13. By Section 2.4.4, the PFG relates the root-mean-square (rms) values to the CPS values. Indeed, the PFG of $S_{b,d3}$ in Figure 2.13 relates the f_1, f_2 contributions in (2.36) to the contributions in the CPS of ε_b shown in Figure 2.14(b). Frequency f_1 yields one contribution in Figure 2.14(b) (f_1), whereas frequency f_2 yields two dominant contributions due to aliasing (f_2, f_{2a}). Note that the PFG at input frequency f_2 relates to the combination of all related output frequencies, rather than only output frequency f_2.

The analysis based on the PFG is confirmed by the CPS of ε_b shown in Figure 2.14(b). Appendix 2.E shows that the on-sample behavior, i.e., ε, does

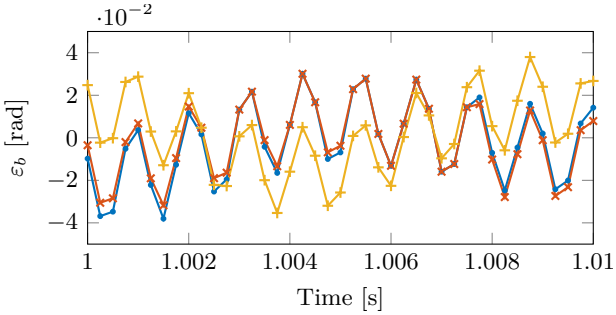

(a) Measured error signals ε_b for C_{d1} (●), C_{d2} (×), and C_{d3} (+).

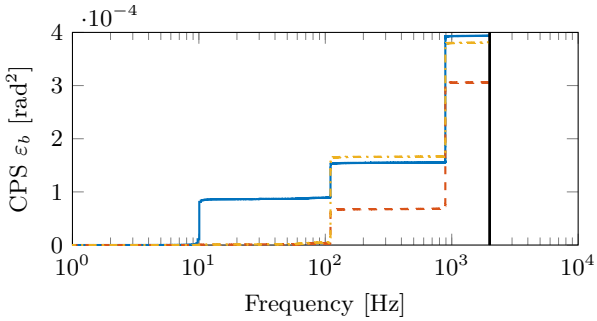

(b) Cumulative power spectrum of ε_b for C_{d1} (——), C_{d2} (- - -), and C_{d3} (-·-·-).

Figure 2.14. Error ε_b in the time and frequency domain for designs C_{d1}, C_{d2}, C_{d3}. Frequency $f_1 = 10$ Hz is successfully suppressed with design C_{d2}. The suppression of $f_{2a} = 110$ Hz with design C_{d3} is unsuccessful since f_{2a} results from aliasing and is not present in η_b. Frequency $f_2 = 890$ Hz cannot be suppressed using control on Δ_{eq} since $f_2 > f_{eq,n}$. Design C_{d2} yields the best performance among the equidistant controllers.

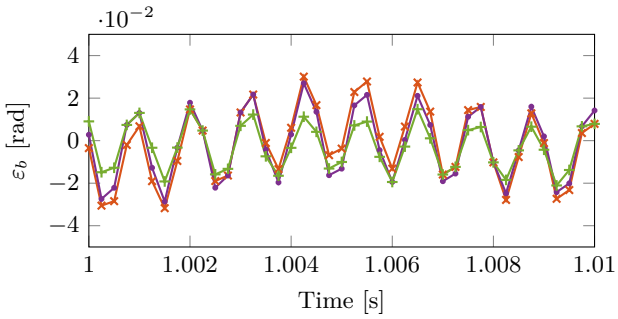

(a) Time-domain signals ε_b for C_{d2} (×), C_{d4} (•), and C_{d5} (+).

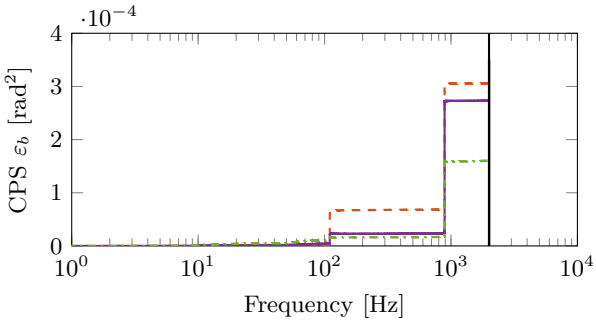

(b) Cumulative power spectrum of ε_b for C_{d2} (- - -), C_{d4} (——), and C_{d5} (-·-·-).

Figure 2.15. Error ε_b in the time and frequency domain for designs C_{d2}, C_{d4}, C_{d5}. Frequency $f_1 = 10$ Hz is also successfully suppressed for design C_{d4} which improves performance compared to C_{d2} due to the additional control variable. In addition to C_{d4}, design C_{d5} also partly suppresses $f_2 = 890$ Hz and yields the best performance among all controllers.

improve. However, the intersample behavior ε_b deteriorates, see Figure 2.14. The results corroborate the analysis in Section 2.6.5 and the reasoning in Section 2.2.2.

2.7.2 Equidistant control designs 4 and 5

Controller C_{d4} is based on the same w-plane design as controller C_{d2}, with the key difference that it is implemented for the non-equidistant sampling sequence Δ_{ne}, rather than the equidistant sampling sequence Δ_{eq}. Due to the additional control variable in each period, it is expected that design C_{d4} outperforms design C_{d2}, see also Section 2.6. The experiments indeed show that C_{d4} outperforms C_{d2}, see the CPS of ε_b in Figure 2.15(b), which corroborates the analysis in Section 2.6.6 and the reasoning in Section 2.2.3.

Design C_{d5} is based on the LPTV control design approach with multiple w-plane control designs. The CPS of ε_b for design C_{d5} is shown in Figure 2.15(b) which shows that the addition of an inverse notch filter during the first two intervals results in a smaller increase at f_2 as desired. At the same time, there is no aliasing since the notch filter is absent during the third interval. The results validate the reasoning in Section 2.6, i.e., the non-equidistant controller design C_{d5} outperforms the non-equidistant controller design C_{d4}, and the non-equidistant controller designs are superior to the equidistant controller designs.

2.7.3 Summary

The application and experimental validation of the proposed control design framework, presented in the previous and current section, show the following aspects: (i) loop-shaping design of non-equidistantly sampled controllers; (ii) application of the Nyquist stability criterion for both equidistantly and non-equidistantly sampled controller designs; (iii) application of the performance frequency gain for performance assessment; and (iv) superior performance with control design for the non-equidistant rate.

2.8 Conclusion and outlook

An intuitive design framework for loop-shaping control design for non-equidistantly sampled systems is presented. The framework facilitates non-equidistant controller design, which enables a substantial performance improvement and cost reduction for control applications compared to conventional LTI designs. The stability of the time-varying closed-loop system is evaluated using a Nyquist stability test and the performance is quantified using performance functions. Both are based on non-parametric models and frequency response functions.

The LPTV loop-shaping design procedure is based on intuitive loop-shaping techniques, similar to those for LTI systems. Application of the design framework to a motion system and the experimental validation demonstrate the potential of non-equidistant sampling and the proposed control design framework.

Ongoing research focuses on extending the presented loop-shaping design guidelines for non-equidistantly sampled systems and non-parametric identification of LPTV systems of which initial results can be found in De Rozario and Oomen (2018a). Future research focuses on design of the (non-quidistant) sampling sequence to further optimize the performance/cost trade-off with early results in Oomen and Rojas (2017) and related to that the impact of deadline misses along the lines of Geelen et al. (2016). Future research also focuses on feedforward control for flexible sampled systems of which initial results can be found in, for example, Chapter 8.

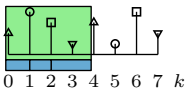

(a) Equidistant input sequence ε_b with period $T = 4$ (■), and non-equidistant sampling sequence $\Gamma_{ne} = \begin{bmatrix}1 & 1 & 2\end{bmatrix}$ (■).

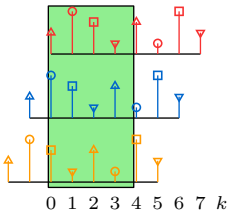

(b) $\tau = 3$ subband signals after shifts.

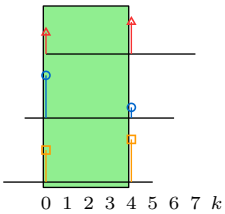

(c) Downsampling with period $T = 4$.

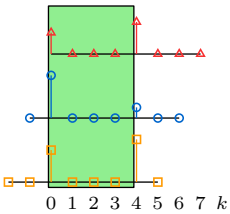

(d) Upsampling with period $T = 4$.

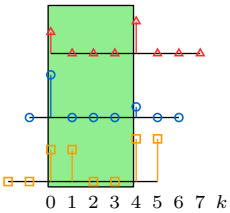

(e) Zero-order-hold interpolation with factor γ_i.

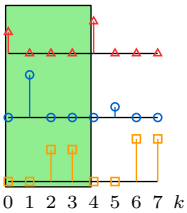

(f) Correction for shift.

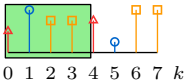

(g) Equidistant output ν_b is the sum.

Figure 2.16. Step-by-step example of the filter bank in Figure 2.7 for $\Gamma_{ne} = \begin{bmatrix}1 & 1 & 2\end{bmatrix}$ with $\underline{C}_d = \underline{I}_\tau$.

2.A Example filter bank $\mathcal{H}C_d\mathcal{D}$

The filter bank of $\mathcal{H}C_d\mathcal{D}$ in Figure 2.7 consists of multiple steps. Figure 2.16 illustrates the different steps for a simple example.

2.B Frequency distortion

Many discretizations yield approximation errors close to the Nyquist frequency as shown in Figure 2.17. To avoid these effects, controllers are designed in the w-plane. The frequency warping is eliminated by implementing a characteristic at discrete-time frequency ω at the fictitious frequency ν given by (2.35).

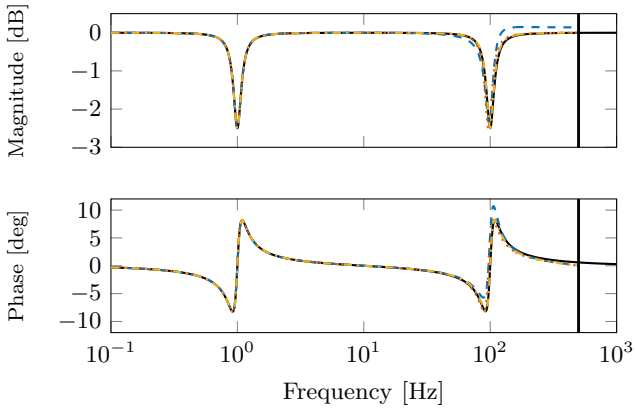

(a) The error is limited at low frequencies but significant at high frequencies.

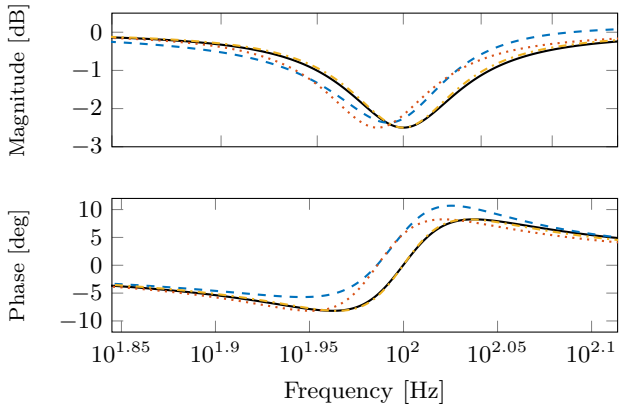

(b) Detailed view at high frequencies. There is an approximation error for the characteristics at high frequencies introduced by the discretization, except for the w-plane design.

Figure 2.17. The discretization of the continuous-time filter (——) with sampling frequency 1000 Hz yields approximation errors with the zero-order-hold (- - -) and Tustin (·····) method. Through design in the w-plane (-·-·-) the characteristics are preserved.

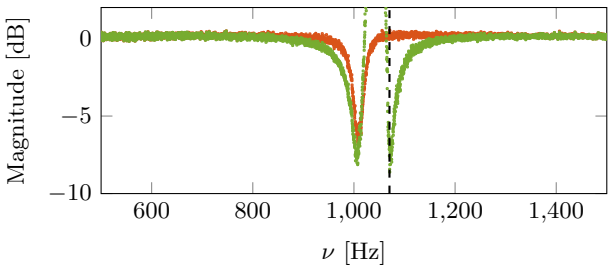

Figure 2.18. Bode magnitude diagram of sensitivity functions S_a in the w-plane near $\nu_2 = 1070 \cdot 2\pi$ rad/s. The suppression at ν_2 (- - -) is larger for $S_{a5,1} = S_{a5,2}$ (●) than for S_{a2} (●).

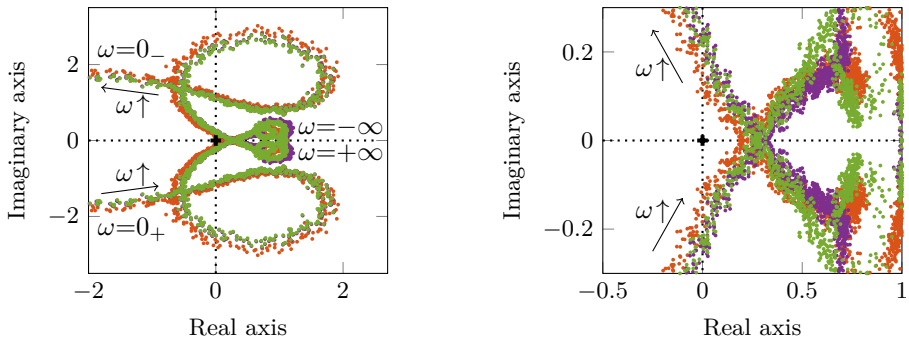

(a) Full view. **(b)** Detailed view around the origin.

Figure 2.19. Nyquist plot of $\det(\underline{I}_\tau + \underline{L}_d)$ for designs C_{d2} (●), C_{d4} (●), and C_{d5} (●). By application of the LPTV Nyquist test of Theorem 2.18, all controllers stabilize the system.

2.C Non-equidistant control to suppress ν_2

To suppress frequency ν_2 in design C_{d5}, a notch filter is used during the first two intervals, i.e., in $S_{a5}[1], S_{a5}[2]$. The suppression is shown in Figure 2.18.

2.D Nyquist stability non-equidistant sampling

Closed-loop stability for Δ_{ne} for designs C_{d4}, C_{d5} is verified using Theorem 2.18 based on the Nyquist plot in Figure 2.19. Stability follows along similar lines as for the equidistant controller designs in Figure 2.11.

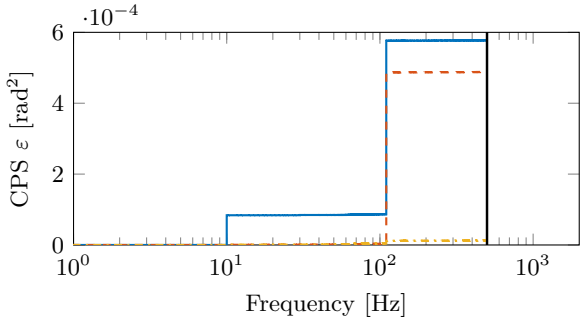

Figure 2.20. Cumulative power spectrum of ε for the equidistant designs C_{d1} (——), C_{d2} (- - -) and C_{d3} (-·-·-). Suppression of $f_{2a} = 110$ Hz with C_{d3} improves the on-sample behavior ε, but degrades the intersample behavior ε_b in Figure 2.14(b).

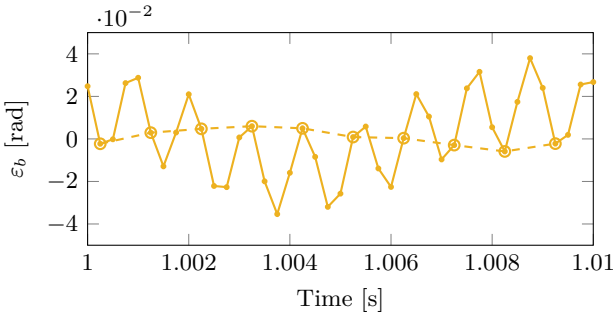

Figure 2.21. Design C_{d3} yields good on-sample behavior (○), but poor intersample behavior (●) by attenuating the aliased disturbance frequency f_{2a}, rather than the true disturbance frequency f_2.

2.E On-sample performance C_{d3}

Design C_{d3} improves the on-sample behavior compared to C_{d2} as shown by Figure 2.20. However, the intersample behavior is poor, see Figure 2.21. In fact, the intersample behavior deteriorates compared to C_{d2} as shown in Figure 2.14 and Table 2.2.

Chapter 3

System inversion for feedforward and learning control

System inversion is at the basis of many feedforward and learning control algorithms. The aim of this chapter is to analyze several of these approaches in view of their subsequent use, showing inappropriate use that is previously overlooked. This leads to different insights and new approaches for both feedforward and learning control that are exploited in subsequent chapters. The methods are compared in various aspects, including finite versus infinite preview, exact versus approximate, and quality of inversion in various norms, which directly relates to their use. In addition, extensions to multivariable and time-varying systems are presented. The results are validated on a nonminimum-phase benchmark system and constitute Contribution II.

3.1 Introduction

The quality of inversion depends on the control goal one has in mind. The aim of this chapter is to investigate, compare, and develop inversion techniques for the purpose of both feedforward and learning control. The model to be inverted can be the closed-loop process sensitivity in iterative learning control (ILC) (Boeren et al., 2016; Steinbuch and Van de Molengraft, 2000), the closed-loop complementary sensitivity in repetitive control (Hara et al., 1988; Longman, 2010; Blanken et al., 2017c), or the open-loop system in inverse model feedforward (Boeren et al., 2015). For nonminimum-phase or strictly proper systems, such

The contents of this chapter are published in:
Jurgen van Zundert and Tom Oomen. On inversion-based approaches for feedforward and ILC. *IFAC Mechatronics*, 50:282–291, 2018.

inversion is not always straightforward. In addition, multivariable systems and time-varying systems impose additional complications.

System inversion has received significant attention, also from a theoretical perspective (Silverman, 1969). Successful approximate solutions include (Tomizuka, 1975), ZPETC (Tomizuka, 1987), ZMETC, NPZ-Ignore (Gross et al., 1994), and EBZPETC (Torfs et al., 1992), see also Butterworth et al. (2012) for an overview. Additionally, standard $\mathcal{H}_\infty$ without preview has been used (Wang et al., 2016; De Roover and Bosgra, 2000) to design ILC filters, as well as $\mathcal{H}_\infty$ preview in feedforward (Hazell and Limebeer, 2008; Mirkin, 2003). Furthermore, optimization-based approaches include techniques based on LQ tracking control (Athans and Falb, 1966), also known as norm-optimal ILC (Gunnarsson and Norrlöf, 2001), where in addition to inversion a weight on the input signal can be imposed. In Wen and Potsaid (2004), ZPETC, ZMETC, and a model matching approach are compared. The model matching approach is similar to the $\mathcal{H}_\infty$-preview control presented in this chapter, yet without preview.

Although many algorithms and approaches are available for system inversion, the choice for a technique is sometimes made arbitrarily without a full understanding of the alternatives and their underlying mechanisms. For example, ZPETC is often used for the design of ILC filters, but requires an additional robustness filter at the cost of performance (Steinbuch and Van de Molengraft, 2000; Bristow et al., 2010). Alternatively, infinite preview (Chapter 10) or $\mathcal{H}_\infty$-based (Wang et al., 2016; De Roover and Bosgra, 2000) techniques can be used. However, Wang et al. (2016); De Roover and Bosgra (2000) lack the use of preview and are recently extended in Blanken et al. (2016b) towards preview/fixed lag smoothing situations.

This chapter provides guidelines on proper use of inversion techniques for both inverse model feedforward and learning control by addressing the application specific objective. The aim of this chapter is to compare existing approaches and provide several new approaches with clear benefits. In this regard, it extends Butterworth et al. (2012); Teng and Tsao (2015) with additional approaches by explicitly addressing the control goal, and investigating applicability to multivariable and time-varying systems. It also extends Chapter 10 in which technical results on several algorithms are presented by evaluating them in a broader perspective.

The outline of the chapter is as follows. In Section 3.2, the inverse model feedforward and ILC optimization problems are cast in a single general framework, and the associated challenges, optimization criteria, and properties are presented. In Section 3.3, the benchmark system used for assessing the inversion techniques is introduced. In Section 3.4, the inversion techniques are presented. First, the well-known approximate inverse techniques NPZ-Ignore, ZPETC, and ZMETC, and the stable inversion technique are recapitulated. Second, inversion techniques based on norm-optimal feedforward/ILC are presented. Third, $\mathcal{H}_\infty$-preview control and $\mathcal{H}_2$-preview control are presented. In Section 3.5, the

techniques are evaluated on the benchmark system of Section 3.3 in both a feedforward and an ILC setting. In Section 3.6, extensions of the techniques in Section 3.4 to multivariable and time-varying systems are considered. Section 3.7 contains conclusions and an outlook.

Notation. Apart from Section 3.6, discrete, single-input, single-output (SISO), linear, time-invariant (LTI) systems are considered. In Section 3.6, extensions to multi-input, multi-output (MIMO) and linear time-varying (LTV) systems are presented. Let $S = (1 + GC)^{-1}$ denote the sensitivity function and $\lambda_i(\cdot)$ the ith eigenvalue. A causal LTI system is referred to as stable (minimum phase) if and only if all poles (zeros) are inside the unit circle, otherwise the system is referred to as unstable (nonminimum phase). For ease of presentation, it is assumed that the inverted system is hyperbolic, i.e., contains no eigenvalues on the unit circle. Note that techniques as in Devasia (1997a) can be used to relax this condition.

3.2 Problem definition

In this section, the inverse model feedforward and ILC optimization problem are detailed, the common inversion problem is formulated, and the application specific criteria are defined.

3.2.1 Role of inversion for feedforward and ILC

Feedback and feedforward control are typically combined to achieve high performance. Feedback control can deal with uncertainty, but its performance is limited due to Bode's sensitivity integral. For known signals, feedforward control can be used to achieve excellent performance. In the feedforward scheme of Figure 3.1(a), the goal is to design feedforward f such that tracking error $e = r - y$ is minimized, where r is the desired trajectory for output y. If the system performs repetitive trajectories r, information of the previous task j can be used to enhance the performance of the next task $j + 1$ through iterative learning control (ILC). For the ILC scheme of Figure 3.1(b), f_{j+1} is designed based on data e_j, f_j such that $e_{j+1} = e_j - SG(f_{j+1} - f_j)$ is minimized.

Both the feedforward and the ILC design problem can be cast into the diagram of Figure 3.1(c). As shown by Table 3.1, both problems are equivalent to finding an input u such that error e is minimized. System H can be an open-loop system as in feedforward (G) or a closed-loop system as in ILC (SG) and repetitive control (SGC).

3.2.2 On inversion

Consider the general block diagram in Figure 3.1(c). Throughout this chapter, it is assumed that system H is proper with relative degree $d \in \mathbb{N}$, has $p \in \mathbb{N}$

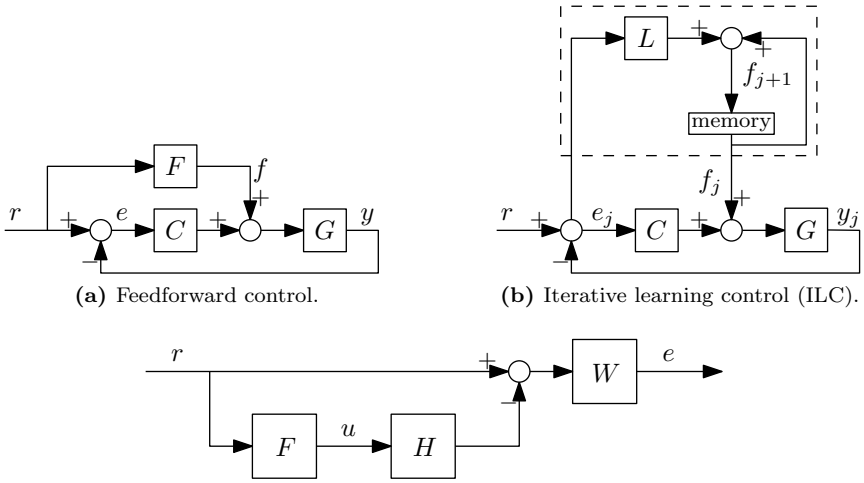

(a) Feedforward control.

(b) Iterative learning control (ILC).

(c) General block diagram.

Figure 3.1. The feedforward (a) and ILC (b) design problem are equivalent to finding u in (c) that minimizes e.

Table 3.1. Conversion from feedforward in Figure 3.1(a) and ILC in Figure 3.1(b) into the general diagram of Figure 3.1(c).

	r	F	u	H	W	e
Feedforward control	r	F	f	G	S	e
Iterative learning control (ILC)	e_j	L	$f_{j+1} - f_j$	SG	1	e_{j+1}

nonminimum-phase zeros, and has state-space realization (A, B, C, D). An immediate solution to minimize e is to select $F = H^{-1}$, where

$$H^{-1} \stackrel{z}{=} \left[\begin{array}{c|c} A - BD^{-1}C & BD^{-1} \\ \hline -D^{-1}C & D^{-1} \end{array}\right]. \tag{3.1}$$

At least three challenges are associated with the direct use of (3.1):

(i) Delay: for $d > 0$, H^{-1} does not exist since D is not invertible.

(ii) Non-square systems: systems with a different number of inputs and outputs cannot be directly inverted as in (3.1) since D is non-square.

(iii) Nonminimum-phase zeros: for $p > 0$, H^{-1} is unstable, which, when solved forward in time, yields unbounded u.

This chapter mainly focuses on the third challenge. The second challenge is addressed in Chapter 6.

Remark 3.1. *The first challenge can be overcome by inverting the bi-proper system $\bar{H} = z^d H$, where the acausal z^d is implemented as a time shift on the time-domain signal. Note that for an infinite-time horizon, filtering the time-shifted signal with $\bar{H}$ is equivalent to filtering the original signal with H, whereas for a finite-time horizon this might introduce boundary errors.*

3.2.3 Criteria

Depending on H, it might not be possible to achieve zero error $e = 0$. Therefore, the inversion techniques construct u given a certain criterion aimed at minimizing e. The criterion depends on the particular application.

In feedforward, generally high performance in terms of the error e is pursued. Typically, this is enforced by minimizing the energy in the error signal through minimizing $\|e\|_2$ (Van der Meulen et al., 2008; Boeren et al., 2015).

In ILC, the main concern is to guarantee convergence in the error to ensure stability over trails. Superior performance is obtained by executing several trials. For update $f_{j+1} = f_j + Le_j$, see also Figure 3.1(b), the error has trial dynamics $e_{j+1} = (1 - SGL)\, e_j$. Hence, to ensure convergence of $\|e_j\|_2$ over trials it should hold $\|1 - SGL\|_\infty < 1$ (Bristow et al., 2006). Note that this is equivalent to monotonic convergence of $\|e_j - e_\infty\|_2$. Assuming this is feasible, the fastest convergence for arbitrary e_j is found by minimizing $\|1 - SGL\|_\infty$. In the general block diagram of Figure 3.1(c), this is equivalent to minimizing $\|W(1 - HF)\|_\infty$. Optionally, if convergence cannot be guaranteed, a robustness filter Q can be added as $f_{j+1} = Q(f_j + Le_j)$ with corresponding convergence condition $\|Q(1 - SGL)\|_\infty < 1$. If the model is uncertain, the condition can be evaluated for the model with uncertainty or for the frequency response function of SG.

3.2.4 Properties

In Section 3.4, a variety of inversion techniques is presented. The main properties of these techniques are:

- Finite versus infinite horizon design;
- Finite versus infinite preview, i.e., the required amount of future input data;
- Applicability to SISO, MIMO, and non-square systems;
- Applicability to time-invariant and time-varying systems;
- Design objective.

An overview of these properties for the techniques in Section 3.4 is listed in Section 3.5.

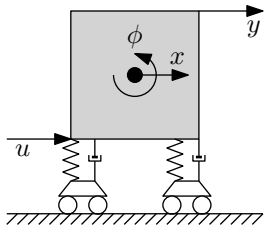

Figure 3.2. The benchmark system is a mass that can translate in x direction and rotate in ϕ direction. The system has input force u and output position y.

3.3 Benchmark system

To validate the inversion techniques of Section 3.4, the benchmark system shown in Figure 3.2 is used. The continuous-time open-loop system G from force u [N] to position y [m] is given by

$$G(s) = \frac{-0.0625(s - 131.9)(s + 56.87)}{s^2(s^2 + 37.5s + 3750)}. \tag{3.2}$$

The zero-order-hold discretized system with sample time $\delta = 0.001$ s is given by

$$G(z) = \frac{-3 \times 10^{-8}(z + 0.9632)(z - 0.9447)(z - 1.1410)}{(z - 1)^2(z^2 - 1.9595z + 0.9632)}. \tag{3.3}$$

The closed-loop system SG with feedback controller $C(z) = \frac{925(z-0.9979)}{z-0.9813}$ is given by

$$SG(z) = \frac{-3 \times 10^{-8}(z + 0.9632)(z - 0.9447)(z - 1.1410)(z - 0.9813)}{(z - 0.9901)(z^2 - 1.9903z + 0.9903)(z^2 - 1.9605z + 0.9640)}. \tag{3.4}$$

For both $H = G$ in feedforward and $H = SG$ in ILC, the following observations can be made:

- H is stable ($|\lambda_i(H)| \leq 1$, for all i);
- H has one nonminimum-phase zero $z = 1.1410$ ($p = 1$);
- H is strictly proper ($D = 0$) with relative degree $d = 1$, see also Remark 3.1.

The step response for SG is shown in Figure 3.3. Due to the single nonminimum-phase zero, the system initially moves in opposite direction (Vidyasagar, 1986).

The reference trajectory r is a fourth-order forward-backward motion of total length $N = 4201$ samples and depicted in Figure 3.4. Time $t = 0$ is defined as the start of the movement. The zero values at the start and end of the trajectory allow for pre-actuation and post-actuation, respectively.

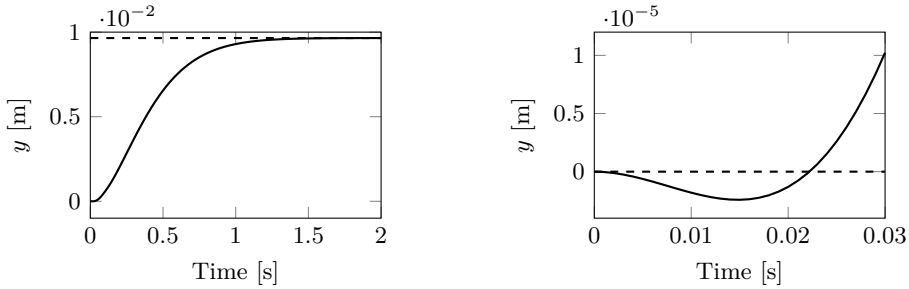

(a) Response to positive step.

(b) Initially, the system moves in negative direction.

Figure 3.3. Step response of SG. The nonminimum-phase character of the system is reflected in the system initially moving in opposite direction.

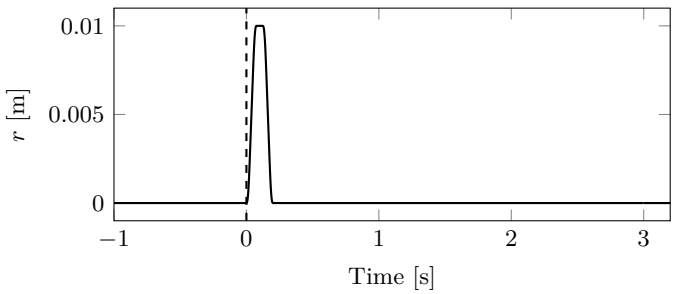

Figure 3.4. Reference trajectory r consists of a forward and backward movement and includes pre-actuation and post-actuation time.

3.4 Overview of techniques

In this section, inversion techniques are presented, developed, and implemented on the benchmark system of Section 3.3.

3.4.1 Approximate inverse (NPZ-Ignore, ZPETC, ZMETC)

3.4.1.1 Approach

As mentioned in Section 3.2.2, nonminimum-phase zeros and delays are key challenges for system inversion. Let H be decomposed as

$$H(z) = \frac{B_s(z)B_u(z)}{A(z)}, \tag{3.5}$$

Table 3.2. Overview of NPZ-Ignore, ZPETC and ZMETC for decomposition (3.5). The DC gain is compensated by $\beta = B_u(1)$, see also Appendix 3.A.

Technique	$F(z)$	Preview	$H(z)F(z)$
NPZ-Ignore	$\dfrac{A(z)}{\beta B_s(z)}$	$p+d$	$\dfrac{B_u(z)}{\beta}$
ZPETC	$\dfrac{z^{-p}A(z)B_u^*(z)}{\beta^2 B_s(z)}$	$p+d$	$\dfrac{z^{-p}B_u(z)B_u^*(z)}{\beta^2}$
ZMETC	$\dfrac{A(z)}{B_s(z)B_u^*(z)}$	d	$\dfrac{B_u(z)}{B_u^*(z)}$

with $B_s(z)$ containing all minimum-phase zeros and $B_u(z)$ the p nonminimum-phase zeros. A key issue is that $B_u^{-1}(z)$ is unstable. Several techniques have been proposed to approximate the inverse of $B_u(z)$, including NPZ-Ignore (Gross et al., 1994), zero phase error tracking control (ZPETC) (Tomizuka, 1987), and zero-magnitude-error tracking control (ZMETC). The results for these approaches are summarized in Table 3.2. If $H(z)$ is nonminimum phase, i.e., $p > 0$, then $H(z)F(z) \neq 1$ and stable. If $H(z)$ is minimum phase, i.e., $p = 0$, all three approaches are identical and exact: $H(z)F(z) = 1$. More background on these approaches can be found in Appendix 3.A. See, for example, Butterworth et al. (2012) for a comparison.

3.4.1.2 Application to benchmark system

To demonstrate the characteristics of these approaches, the approaches are applied to the benchmark system of Section 3.3 for $H = G$. The Bode diagram of HF for each technique is shown in Figure 3.5. Recalling that ideally $HF = 1$, it can observed that ZPETC indeed has zero phase error, ZMETC has zero magnitude error, and NPZ-Ignore has both a magnitude and phase error.

3.4.1.3 Summary

The techniques in Table 3.2 are based on an approximate infinite horizon design and have finite preview.

3.4.2 Stable inversion

In this section, the stable inversion approach for LTI systems is presented. For inversion of LTV systems see Chapter 10.

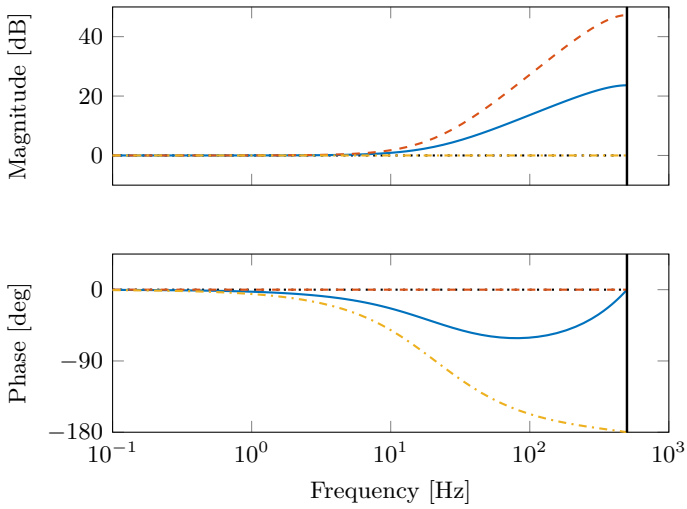

Figure 3.5. HF for NPZ-Ignore (——), ZPETC (- - -), and ZMETC (-·-·-). HF has zero phase for ZPETC and zero magnitude for ZMETC.

3.4.2.1 Approach

The techniques presented in the previous section are all based on approximations of the unstable part of the inverse system. In contrast, stable inversion regards the unstable part as a noncausal operation and generates signal u based on infinite preview. Consider LTI system $\bar{H}$ of Remark 3.1 in state-space form with state x. The state of the inverse $\bar{H}^{-1}$ is divided into a stable and unstable part by applying the state transformation $x[k] = T \begin{bmatrix} x_s[k] \\ x_u[k] \end{bmatrix}$, where T contains eigenvectors of $\bar{H}^{-1}$ such that

$$\begin{bmatrix} x_s[k+1] \\ x_u[k+1] \end{bmatrix} = \begin{bmatrix} A_s & 0 \\ 0 & A_u \end{bmatrix} \begin{bmatrix} x_s[k] \\ x_u[k] \end{bmatrix} + \begin{bmatrix} B_s \\ B_u \end{bmatrix} r[k], \tag{3.6}$$

$$u[k] = \begin{bmatrix} C_s & C_u \end{bmatrix} \begin{bmatrix} x_s[k] \\ x_u[k] \end{bmatrix} + Dr[k], \tag{3.7}$$

with $|\lambda(A_s)| < 1$ and $|\lambda(A_u)| > 1$, i.e., all stable poles are contained in A_s and all unstable poles in A_u. The bounded states are found through solving

$$x_s[k+1] = A_s x_s[k] + B_s r[k], \quad x_s[-\infty] = 0 \tag{3.8}$$

forward in time and

$$x_u[k+1] = A_u x_u[k] + B_u r[k], \quad x_u[\infty] = 0 \tag{3.9}$$

backward in time. The command signal u follows from

$$u[k] = C_s x_s[k] + C_u x_u[k] + Dr[k]. \tag{3.10}$$

In practice, the boundaries are finite, i.e., $x_s[0] = x_{s,0}$, $x_u[N] = x_{u,N}$, and introduce boundary errors.

The dichotomy in a stable and unstable part as in (3.6) is nontrivial for linear time-varying (LTV) systems. The dichotomy for a very general LTV case is presented in Chapter 4, namely for linear periodically time-varying (LPTV) systems. For the LTI benchmark system considered in this chapter the dichotomy can be found through an eigenvalue decomposition as shown above.

3.4.2.2 Application to benchmark system

To illustrate the influence of preview on the performance of the stable inversion approach, the approach is applied to $H = G$ with r the reference trajectory of Figure 3.4 in the time intervals $[-0.06, 0.2]$ and $[-0.08, 0.2]$, i.e., the pre-actuation is restricted to either 60 or 80 samples and the post-actuation to 0 samples. The results in Figure 3.6 show a considerable performance improvement when increasing the pre-actuation from 60 to 80 samples. For infinite pre-actuation and post-actuation, the results become exact.

3.4.2.3 Summary

Stable inversion is an infinite-time design that is exact on an infinite-time horizon and has infinite preview. A finite-time horizon introduces boundary errors.

3.4.3 Norm-optimal feedforward/ILC

In this section, norm-optimal inversion techniques based on norm-optimal ILC techniques are presented.

3.4.3.1 Approach

Within ILC there are two main classes (Bristow et al., 2006). The first class is frequency-domain ILC in which a learning filter $L \approx (SG)^{-1}$ is constructed. The filter is typically implemented using ZPETC or ZMETC, see Section 3.4.1. The second class is norm-optimal ILC in which the 2-norms of e_{j+1} and f_{j+1} are minimized. Here, subscript j denotes the current trial and $j+1$ the next trial. Common solution methods are adjoint ILC and lifted ILC. The reader is referred to Owens and Chu (2009); Owens et al. (2014) for adjoint ILC, including the effect of nonminimum-phase zeros. In this chapter, the focus is on lifted ILC. In lifted ILC, the solution is based on describing input-output relations in

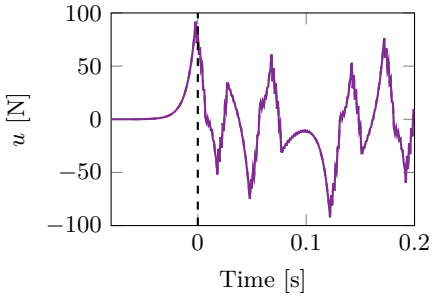

(a) Stable inversion generates identical u with 60 samples preview (- - -) and 80 samples preview (——) for $t \geq -0.06$, whereas for 80 samples preview u is non-zero for $-0.08 \leq t < -0.06$.

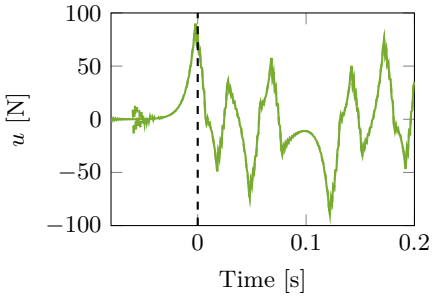

(b) Norm-optimal feedforward generates a non-zero input u at the begin of the task to compensate for boundary effects. The effect is larger for 60 samples preview (- - -) than for 80 samples preview (——).

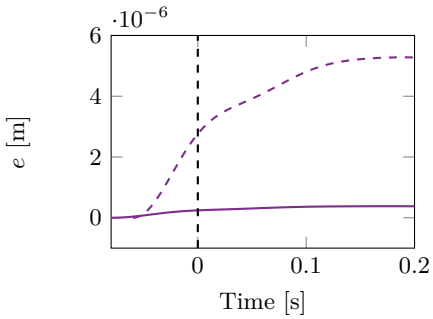

(c) The infinite-time design of stable inversion introduces significant boundary errors on a finite interval. The error is larger with 60 samples preview (- - -) than with 80 samples preview (——).

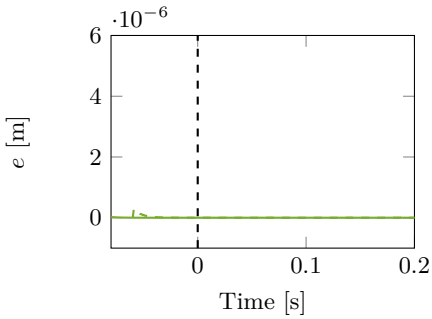

(d) The finite-time design of norm-optimal feedforward inversion introduces small boundary errors. The error is smaller with 80 samples preview (——) than with 60 samples preview (- - -).

Figure 3.6. The finite-time design of norm-optimal feedforward generates an input that compensates for boundary effects and thereby outperforms stable inversion on a finite horizon since the latter is an infinite-time design.

lifted/supervector notation (Moore, 1993). For example, the relation between y and u is described by

$$\underbrace{\begin{bmatrix} y[0] \\ y[1] \\ \vdots \\ y[N-1] \end{bmatrix}}_{\underline{y}} = \underbrace{\begin{bmatrix} h(0) & 0 & \dots & 0 \\ h(1) & h(0) & \dots & 0 \\ \vdots & \vdots & \ddots & \vdots \\ h(N-1) & h(N-2) & \dots & h(0) \end{bmatrix}}_{\underline{H}} \underbrace{\begin{bmatrix} u[0] \\ u[1] \\ \vdots \\ u[N-1] \end{bmatrix}}_{\underline{u}}, \tag{3.11}$$

where h is the impulse response of H given by

$$h(k) = \begin{cases} D, & k = 0, \\ CA^{k-1}B, & k = 1, 2, \dots, N-1, \end{cases} \tag{3.12}$$

with N the task length. A general performance criterion is

$$\|e_{j+1}\|^2_{\underline{W}_e} + \|f_{j+1}\|^2_{\underline{W}_f} + \|f_{j+1} - f_j\|^2_{\underline{W}_{\Delta f}}, \tag{3.13}$$

where $\|(\cdot)\|^2_W = (\cdot)^\top W(\cdot)$, with $\underline{W}_e = w_e \underline{I}_N$, $\underline{W}_f = w_f \underline{I}_N$, $\underline{W}_{\Delta f} = w_{\Delta f} \underline{I}_N$. The solution that minimizes this criterion is, see for example Theorem 10.2,

$$\underline{f}_{j+1} = \underline{Q}\,\underline{f}_j + \underline{L}\,\underline{e}_j, \tag{3.14}$$

$$\underline{Q} = \left(\underline{H}^\top w_e \underline{H} + w_f \underline{I} + w_{\Delta f} \underline{I}\right)^{-1} \left(\underline{H}^\top w_e \underline{H} + w_{\Delta f} \underline{I}\right), \tag{3.15}$$

$$\underline{L} = \left(\underline{H}^\top w_e \underline{H} + w_f \underline{I} + w_{\Delta f} \underline{I}\right)^{-1} \underline{H}^\top w_e. \tag{3.16}$$

The use of $N \times N$ matrix calculations results in extensive computation times growing as $\mathcal{O}(N^3)$, see Chapter 10. An alternative is to use Riccati equations to find the optimal solution as is done in Chapter 10. The approach yields exactly the same optimal solution, but the computation time is limited to $\mathcal{O}(N)$. Next, the resource-efficient approach based on Riccati equations is used for both ILC and feedforward design.

First, the approach for ILC is presented. Criterion (3.13) is equivalent to

$$\begin{aligned} \sum_{k=1}^{N-1} \Big(& (e_{j+1}[k])^\top w_e (e_{j+1}[k]) + (f_{j+1}[k])^\top w_f (f_{j+1}[k]) \\ & + (f_{j+1}[k] - f_j[k])^\top w_{\Delta f} (f_{j+1}[k] - f_j[k]) \Big). \end{aligned} \tag{3.17}$$

The optimal command signal f_{j+1} that minimizes (3.17) is the output of the state-space system

$$\left[\begin{array}{c|ccc} A - BL[k] & -BL_f[k] & BL_e[k] & BL_g[k] \\ \hline -L[k] & I_{n_i} - L_f[k] & L_e[k] & L_g[k] \end{array}\right], \tag{3.18}$$

with zero initial state for input $\begin{bmatrix} f_j[k] \\ e_j[k] \\ g_{j+1}[k+1] \end{bmatrix}$, where

$$L[k] = \left(\gamma^{-1}[k] + B^\top P[k+1]B\right)^{-1} \left(D^\top w_e C + B^\top P[k+1]A\right), \tag{3.19}$$

$$L_f[k] = \left(\gamma^{-1}[k] + B^\top P[k+1]B\right)^{-1} w_f, \tag{3.20}$$

$$L_e[k] = \left(\gamma^{-1}[k] + B^\top P[k+1]B\right)^{-1} D^\top w_e, \tag{3.21}$$

$$L_g[k] = \left(\gamma^{-1}[k] + B^\top P[k+1]B\right)^{-1} B^\top, \tag{3.22}$$

$$\gamma = \left(D^\top w_e D + w_f + w_{\Delta f}\right)^{-1}, \tag{3.23}$$

with

$$g_{j+1}[k] = \left(A^\top - K_g[k]B^\top\right) g_{j+1}[k+1] + C^\top w_e e_j[k] + K_g[k] w_f f_j[k], \tag{3.24a}$$

$$g_{j+1}[N] = 0_{n_x \times 1}, \tag{3.24b}$$

where

$$K_g[k] = \left(A^\top - C^\top w_e D \gamma B^\top\right) P[k+1] \left(I_{n_x} + B\gamma B^\top P[k+1]\right)^{-1} B\gamma, \tag{3.25}$$

and $P[k]$ the solution of the matrix difference Riccati equation

$$\begin{aligned} P[k] = {} & \left(A - B\gamma D^\top w_e C\right)^\top P[k+1] \\ & \times \left(I_{n_x} - B\left(\gamma^{-1}[k] + B^\top P[k+1]B\right)^{-1} B^\top P[k+1]\right) \\ & \times \left(A - B\gamma D^\top w_e C\right) \\ & + C^\top w_e C - (D^\top w_e C)^\top \gamma (D^\top w_e C), \end{aligned} \tag{3.26a}$$

$$P[N] = 0_{n_x \times n_x}. \tag{3.26b}$$

It can be shown that $\|e_j - e_\infty\|_2$ converges monotonically if $w_e > 0$, $w_f, w_{\Delta f} \geq 0$. If H is strictly proper, i.e., $D = 0$, then $w_f > 0$ or $w_{\Delta f} > 0$ is required to guarantee monotonic convergence. This inherently reduces the performance in terms of $\|e\|_2$ since input f_j or the convergence speed is penalized. To avoid this, H can be made bi-proper by applying time shifts, see Remark 3.1, such that $D \neq 0$ and hence $w_f = w_{\Delta f} = 0$ can be used.

Next, the approach for inverse model feedforward is presented. Feedforward can be seen as a special case of ILC in which there is only one trial and hence no input change weight $w_{\Delta f}$. In particular, if H is bi-proper and $w_f, w_{\Delta f} = 0$, the solution reduces to inverse model ILC. Without input change weight ($w_{\Delta f} = 0$), and $w_e = Q$, $w_f = R$, (3.17) reduces to the LQ criterion

$$\sum_{k=1}^{N-1} e^\top[k] Q e[k] + u^\top[k] R u[k]. \tag{3.27}$$

For the case without direct feedthrough ($D = 0$), the problem reduces further to the well-known LQ tracking problem (Athans and Falb, 1966), with solution

$$x[k+1] = (A - BL[k])x[k] + BL_g[k]g[k+1], \quad x[0] = 0, \tag{3.28}$$

$$u[k] = -L[k]x[k] + L_g[k]g[k+1], \tag{3.29}$$

where

$$L[k] = \left(R + B^\top P[k+1]B\right)^{-1} B^\top P[k+1]A, \tag{3.30}$$

$$L_g[k] = \left(R + B^\top P[k+1]B\right)^{-1} B^\top, \tag{3.31}$$

with

$$\begin{aligned} g[k] = {} & C^\top Q r[k] \\ & + A^\top \left(I - (P^{-1}[k+1] + BR^{-1}B^\top)^{-1} BR^{-1}B^\top\right) g[k+1], \end{aligned} \tag{3.32a}$$

$$g[N] = 0, \tag{3.32b}$$

and $P[k]$ the solution of the matrix difference Riccati equation

$$\begin{aligned} P[k] = {} & C^\top QC + A^\top P[k+1]A \\ & - A^\top P[k+1]B \left(R + B^\top P[k+1]B\right)^{-1} B^\top P[k+1]A, \end{aligned} \tag{3.33a}$$

$$P[N] = 0. \tag{3.33b}$$

3.4.3.2 Application to benchmark system

The norm-optimal feedforward approach is applied to the benchmark system $H = G$ under the same conditions as in Section 3.4.2, i.e., with reduced pre-actuation and post-actuation. The results are shown in Figure 3.6. The approach outperforms stable inversion since it takes the boundary effects into account using the linear time-varying (LTV) character of the solution. This behavior can be observed at the start of u in Figure 3.6(b).

3.4.3.3 Summary

Norm-optimal ILC/feedforward is a finite-time design and has infinite preview, i.e., equal to the task length. The approach is optimal in terms of minimizing $\|e\|_2$ if $w_f = 0$ in ILC or if $R = 0$ in feedforward.

3.4.4 Preview control

In preview control the inverse system is optimized for a specific infinite-time objective, with pre-defined preview.

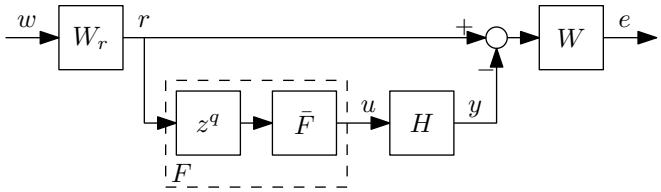

(a) In preview control, the objective is minimization of a certain norm on the transfer function $w \mapsto e$.

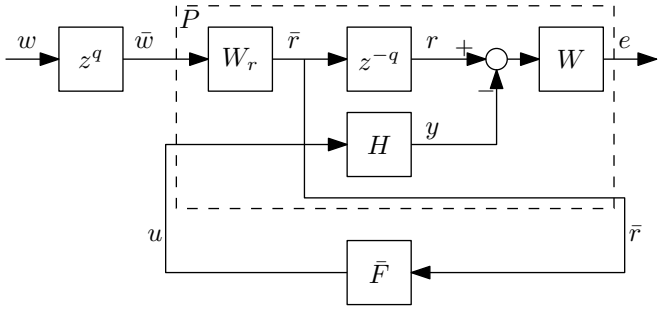

(b) General plant formulation.

Figure 3.7. In preview control, the preview q is fixed and $\bar{F}$ is optimized to minimize a certain norm on the transfer function $\bar{w} \mapsto e$.

3.4.4.1 Approach

A general formulation of preview control is shown in Figure 3.7(a) where F is decomposed into $F = \bar{F}z^q$, with preview $q \in \mathbb{N}$. Note that an input weighting W_r is added compared to Figure 3.1(c). For fixed q, $\bar{F}$ follows from

$$\bar{F} = \arg\min_{\bar{F}} \|W\left(z^{-q} - H\bar{F}\right)W_r\|_x, \tag{3.34}$$

where $\|\cdot\|_x$ is a certain norm. The problem cast into the general plant formulation is shown in Figure 3.7(b). Note that the pre-multiplication with the acausal part z^q is not part of generalized plant P to ensure $P \in \mathcal{RH}_\infty$. For the special case without preview, i.e., $q = 0$, the approach in Wen and Potsaid (2004) is recovered.

First, optimal ILC synthesis is presented in which the induced (worst-case) 2-norm of the error e is minimized by using $\mathcal{H}_\infty$-preview control, i.e., $x = \infty$ in (3.34). The input is set to $w = r$, i.e., $W_r = 1$. $\mathcal{H}_\infty$ synthesis on P minimizes $\|W\left(z^{-q} - H\bar{F}\right)\|_\infty = \|W\left(1 - HF\right)\|_\infty$ which is the ILC convergence criterion for $W = 1$, see also Section 3.2.3.

Second, optimal inverse model feedforward synthesis is presented in which $\|e\|_2$ is minimized for a specific reference r by using $\mathcal{H}_2$-preview control, i.e., $x = 2$ in (3.34). Input w is white noise of unity intensity and W_r is the power

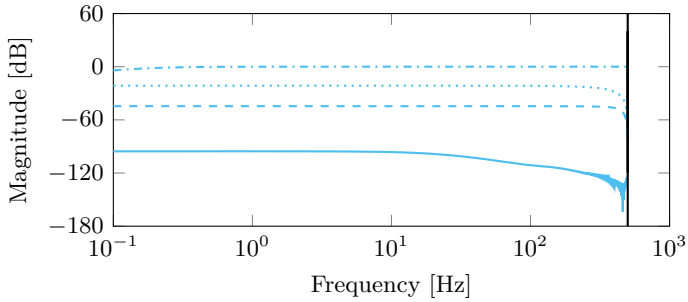

(a) $|W(1-HF)|$ for $\mathcal{H}_\infty$-preview control for $q = 0$ (-·-·-), $q = 20$ (·····), $q = 40$ (- - -), and $q = 90$ (——). For larger q, the maximum of $|W(1-HF)|$ is smaller

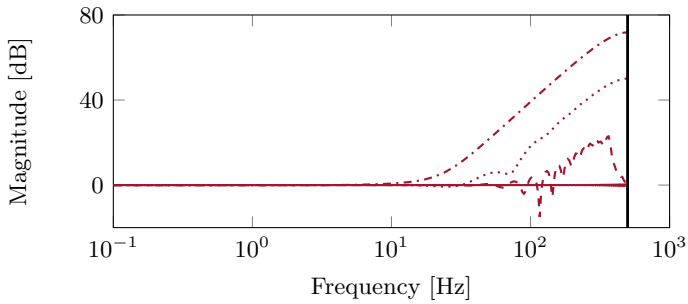

(b) $|HF|$ for $\mathcal{H}_2$-preview control for $q = 1$ (-·-·-), $q = 20$ (·····), $q = 40$ (- - -), and $q = 90$ (——). For larger q, $|HF|$ is closer to unity.

Figure 3.8. $\mathcal{H}_\infty$-preview control and $\mathcal{H}_2$-preview control for a range of preview values q. More preview yields better performance.

spectrum of r such that $\mathcal{H}_2$ synthesis on P minimizes $\|e\|_2$ for the spectrum of $r = W_r w$.

3.4.4.2 Application to benchmark system

For $\mathcal{H}_\infty$-preview control in a feedfoward setting, the results for a range of preview values q are shown in Figure 3.8(a). More preview q introduces more design freedom and hence $\|W(1-HF)\|_\infty$ decreases.

For $\mathcal{H}_2$-preview control in a feedforward setting with input weighting

$$W_r(z) = \left(\frac{2.0236(z+0.03295)}{z-0.9570}\right)^4, \tag{3.35}$$

the resulting filters HF for a range of preview values q are shown in Figure 3.8(b). For larger q, $|HF|$ is closer to unity.

Table 3.3. Overview of inversion techniques. *See Section 3.6.

Technique	Design	Preview	Dimensions*	Time varying*	Aim
NPZ-Ignore	Infinite	Finite	SISO	No	H^{-1} approx.
ZPETC	Infinite	Finite	SISO	No	H^{-1} approx.
ZMETC	Infinite	Finite	SISO	No	H^{-1} approx.
Stable inversion	Infinite	Infinite	Square	Yes	H^{-1} exact
Norm-optimal	Finite	Infinite	Non-square	Yes	$\min \|e\|_2$
$\mathcal{H}_\infty$-preview	Infinite	Finite	Non-square	No	$\min \|W(1-HF)\|_\infty$
$\mathcal{H}_2$-preview	Infinite	Finite	Non-square	No	$\min \|e\|_2$

Table 3.4. Design and performance in a feedforward setting.

Technique	Settings	$\|e\|_2$
NPZ-Ignore	-	0.0153
ZPETC	-	0.0050
ZMETC	-	0.0317
Stable inversion	-	3.5849×10^{-11}
Norm-optimal	$Q = 1$; $R = 0$	7.7392×10^{-11}
$\mathcal{H}_\infty$-preview	$q = 100$	3.6942×10^{-6}
$\mathcal{H}_2$-preview	W_r: (3.35); $q = 100$	6.6786×10^{-9}

3.4.4.3 Summary

Preview control is an infinite-time design with finite pre-defined preview. $\mathcal{H}_\infty$-preview control and $\mathcal{H}_2$-preview control address the control goal in ILC and feedforward, respectively.

3.5 A control goal perspective

A qualitative overview of the inversion techniques of the previous section is provided in Table 3.3. Extensions to multivariable and time-varying systems are presented in Section 3.6. In this section, the control goal is added to the inversion techniques of Section 3.4 and the results are validated on the benchmark system of Section 3.3.

3.5.1 Application to feedforward

Table 3.4 summarizes the results of the techniques in a feedforward setting on the benchmark system of Section 3.3. For norm-optimal feedforward the system is made bi-proper through shifting r such that $R = 0$ can be used, see also Section 3.4.3. For $\mathcal{H}_\infty$-preview control and $\mathcal{H}_2$-preview control, $q = 100$ samples preview are used. W_r for $\mathcal{H}_2$-preview control is given by (3.35).

The time signals u and e are shown in Figure 3.9 and Figure 3.10, respectively. Figure 3.9 shows $d = 1$ sample preview for ZMETC, $p+d = 2$ samples preview for NPZ-Ignore and ZPETC, $q = 100$ samples preview for $\mathcal{H}_\infty$-preview control and $\mathcal{H}_2$-preview control, and infinite preview for stable inversion and norm-optimal feedforward.

Figure 3.9(a) shows that the generated inputs of NPZ-Ignore and ZPETC are not very well suited for practical application, which is in line with the analysis in Butterworth et al. (2012, Section 6). Also the errors are considerably large as shown in Table 3.4 and Figure 3.10. Note that only part of the time axis is shown.

Figure 3.9(b) shows that the inputs of stable inversion, norm-optimal feedforward, $\mathcal{H}_\infty$-preview control, and $\mathcal{H}_2$-preview control are similar, whereas that of ZMETC is different. Table 3.4 and Figure 3.10 show a large error for the approximate inverse techniques. Stable inversion, norm-optimal feedforward, and $\mathcal{H}_2$-preview control achieve the lowest $\|e\|_2$, which is to be expected since these techniques are aimed at minimizing $\|e\|_2$, see also Table 3.3. $\mathcal{H}_\infty$-preview control achieves moderate performance since it aims at minimizing $\|W(1-HF)\|_\infty$ rather than $\|e\|_2$. The desired preview in preview control depends on the location of the nonminimum-phase zeros (Middleton et al., 2004), where higher preview enhances performance.

3.5.2 Application to ILC

3.5.2.1 Guaranteed convergence

In an ILC setting, there is guaranteed convergence in error norm $\|e_j\|_2$ over the trials if $\|W(1-HF)\|_\infty = \|1-SGF\|_\infty < 1$, see also Section 3.2.3. It might be possible that the condition cannot be satisfied at all, but if the condition can be satisfied, $\mathcal{H}_\infty$-preview control guarantees convergence since it minimizes $\|W(1-HF)\|_\infty$, see Section 3.4.4. Figure 3.11(a) shows the Bode magnitude $|W(1-HF)|$ for techniques with explicit design of F. Note that since the benchmark system is singlevariable, $\|W(1-HF)\|_\infty = \max_\omega |W(e^{j\omega\delta})(1-H(e^{j\omega\delta})F(e^{j\omega\delta}))|$. The figure reveals that both $\mathcal{H}_\infty$-preview control and $\mathcal{H}_2$-preview control are guaranteed to converge. The approximate inverse techniques require a robustness filter $W \neq 1$ to guarantee convergence, which goes at the expense of performance, i.e., $W(1-HF)$ for some possibly noncausal W.

On an infinite-time horizon, stable inversion is also guaranteed to converge since it is exact. However, on a finite-time interval truncation errors might deteriorate convergence. Finally, convergence can be guaranteed for norm-optimal ILC by proper weight selection, see Section 3.4.3.

In summary, convergence in $\|e_j\|_2$ can be guaranteed for $\mathcal{H}_\infty$-preview control, $\mathcal{H}_2$-preview control, norm-optimal ILC, and stable inversion (on an infinite horizon). For NPZ-Ignore, ZPETC and ZMETC an additional robustness filter $W \neq 1$ is required to enforce convergence, at the cost of performance.

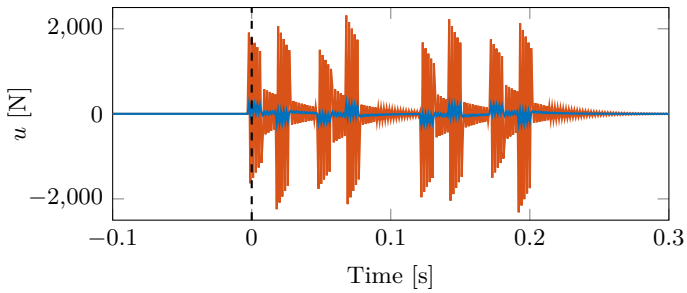

(a) NPZ-Ignore (——) and ZPETC (——).

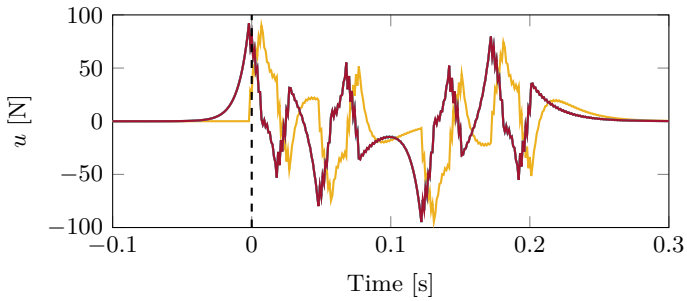

(b) ZMETC (——), stable inversion (——), norm-optimal feedforward (——), $\mathcal{H}_\infty$-preview control (——), and $\mathcal{H}_2$-preview control (——). All except ZMETC are overlapping.

Figure 3.9. Command signal u. The signals in (a) are unacceptably large. The signals in (b) are satisfactory.

3.5.2.2 Application to the benchmark system

The convergence on the benchmark system of Section 3.3 is investigated. Figure 3.11(b) shows $\|e_j\|_2$ over 11 trials. The results show that there is indeed convergence for $\mathcal{H}_\infty$-preview control, $\mathcal{H}_2$-preview control, and norm-optimal ILC, and also for stable inversion despite the boundary errors. For the approximate inverse techniques NPZ-Ignore, ZPETC, and ZMETC an additional robust filter W is used to guarantee convergence. The robustness filter is designed as $W = Q^*Q$ with Q^* the adjoint of Q to avoid phase distortion. A first-order low-pass filter is used for Q to reduce the high frequent magnitude, see also Figure 3.11(a).

Since the approximate inverse techniques NPZ-Ignore, ZPETC, and ZMETC require an additional robustness filter $W \neq 1$, the limit error is nonzero, i.e., $e_\infty \neq 0$. The consequence is a poor performance as shown by Figure 3.11(b) confirming statements in earlier sections.

Since there are no trial-varying disturbances, the theoretical limit error equals

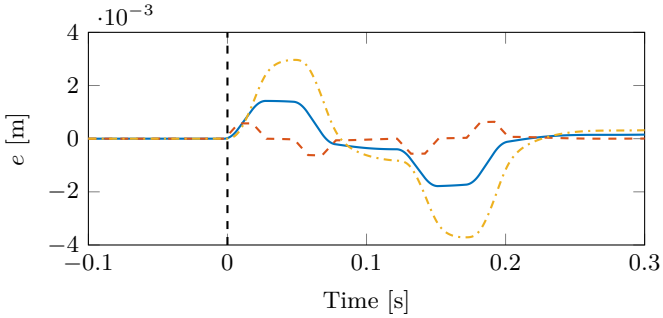

(a) NPZ-Ignore (——), ZPETC (- - -), and ZMETC (-·-·).

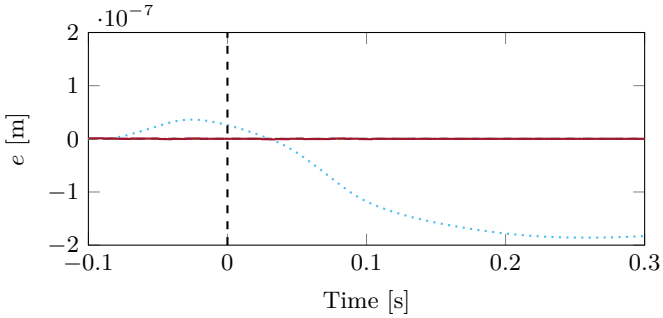

(b) Stable inversion (- - -), norm-optimal feedforward (-·-·), $\mathcal{H}_\infty$-preview control (·····), and $\mathcal{H}_2$-preview control (——). Norm-optimal feedforward, stable inversion, and $\mathcal{H}_2$-preview control are overlapping.

Figure 3.10. Error signal e. The errors in (a) are unacceptably large. The errors in (b) are close to zero as desired.

$e_\infty = 0$ for all methods without robustness filter, i.e., all except the approximate inverse techniques. However, due to numerical aspects, this value is not achieved exactly. Norm-optimal ILC converges in a single trial to e_∞ since $w_f = w_{\Delta f} = 0$. In contrast, $\mathcal{H}_\infty$-preview control, $\mathcal{H}_2$-preview control and stable inversion are not exact and therefore require multiple trials to converge. The number of preview samples q in $\mathcal{H}_\infty$-preview control ($q = 100$ in Figure 3.11) directly influences the convergence speed. Ideally, the $\mathcal{H}_2$-preview control filter F is updated every trial based on the spectrum of e_j. Figure 3.11 shows the results for fixed F based on the spectrum of $e_0 = Sr$ with $q = 100$.

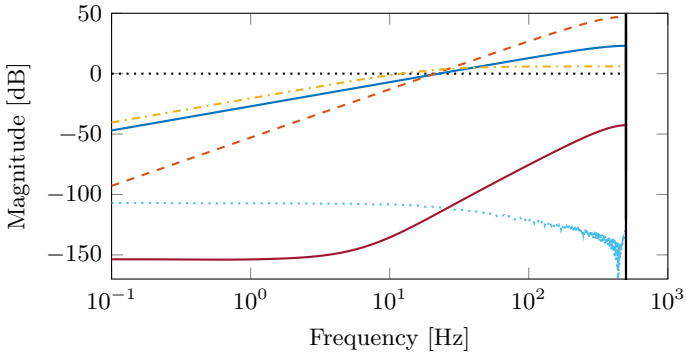

(a) ILC convergence is only guaranteed for $\mathcal{H}_\infty$-preview control (·····) and $\mathcal{H}_2$-preview control (——) since only for these approaches $|1 - SG(e^{j\omega\delta})F(e^{j\omega\delta})| < 1$, for all frequencies ω. The approximate inverse techniques NPZ-Ignore (——), ZPETC (- - -), and ZMETC (-·-·-) require an additional robustness to guarantee convergence (not shown).

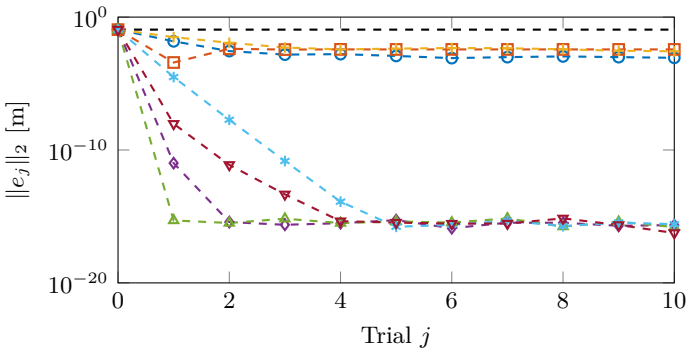

(b) For the approximate inverse techniques NPZ-Ignore (·⊖·), ZPETC (·⊟·), and ZMETC (·+·) convergence is enforced through a robustness filter $W = Q^*Q$ at the cost of performance $\|e_j\|_2$. All other techniques, i.e., stable inversion (·◇·), norm-optimal feedforward (·▲·), $\mathcal{H}_\infty$-preview control (·✱·), and $\mathcal{H}_2$-preview control (·▼·), converge to zero error up to numerical precision. Norm-optimal ILC is exact and therefore converges in a single trial.

Figure 3.11. Application in ILC with the convergence condition in (a) and the performance in (b).

3.6 Extensions: Multivariable, time varying, parameter varying, and nonlinear

The applicability of each technique to multivariable and time-varying systems is summarized in Table 3.3. For NPZ-Ignore, ZPETC, and ZMETC the extension to multivariable systems is nontrivial. In Blanken et al. (2016b), an approach for multivariable ZPETC is proposed, which applies multiple times SISO ZPETC to the Smith form of the system. Similarly, the Smith form can be used to construct NPZ-Ignore and ZMETC. However, in Blanken et al. (2016b) it is concluded that at present there are no numerically stable algorithms for finding Smith forms. Therefore, these techniques currently seem to be limited to SISO systems.

Techniques based on state-space descriptions, such as stable inversion and norm-optimal feedforward/ILC, can directly be extended to multivariable systems. Note, however, that stable inversion is only applicable to square systems since it requires the inverse system (3.1). Also $\mathcal{H}_\infty$-preview control and $\mathcal{H}_2$-preview control can directly be extended, but the exact implementation depends on the specific requirements. For example, in ILC convergence over trials of the error e_j is determined by $(I-(SG)F)$ whereas convergence of input u is determined by $(I-F(SG))$, and generally $(SG)F \neq F(SG)$ for multivariable systems. For underactuated systems, i.e., with more outputs than inputs, exact tracking is impossible. For overactuated systems, i.e., with more inputs than outputs, exact tracking is possible and the additional degrees of freedom can be exploited to satisfy additional requirements, see Chapter 6.

Application to time-varying systems is restricted to stable inversion and norm-optimal feedforward/ILC since others are based on time-invariant frequency-domain techniques. However, the dichotomy in stable inversion is nontrivial for general time-varying systems. For linear periodically time-varying (LPTV) systems this is solved in Chapter 4.

For stable inversion for nonlinear systems, the reader is referred to Devasia and Paden (1998); Pavlov and Pettersen (2008). For linear parameter-varying systems, the reader is referred to Sato (2008).

3.7 Conclusion and outlook

Inversion techniques are essential for achieving high performance in motion systems, either through inverse model feedforward or learning control. In this chapter, the criteria for inverse model feedforward and ILC are posed and several inversion techniques are investigated, developed, and compared on a nonminimum-phase benchmark system, resulting in the following guidelines.

For inverse model feedforward, norm-optimal feedforward in Section 3.4.3 has important advantages as it explicitly takes into account boundary effects. If

boundary effects are not critical, $\mathcal{H}_2$-preview control in Section 3.4.4 is recommended as infinite-time design.

For ILC, filter synthesis via $\mathcal{H}_\infty$-preview control in Section 3.4.4 is strongly recommended, since the optimization criterion is taken equal to the convergence condition of ILC. For non-optimal filter design, stable inversion in Section 3.4.2 is experienced to yield better results than the approximate inverse techniques NPZ-Ignore, ZPETC, and ZMETC in Section 3.4.1. Importantly, the approximate inverse techniques typically require an additional robustness filter at the cost of performance.

For applicability of the techniques to multivariable and time-varying systems the following conclusions are drawn. The approximate inverse techniques NPZ-Ignore, ZPETC, and ZMETC are currently limited to SISO systems. Stable inversion, norm-optimal feedforward/ILC, $\mathcal{H}_\infty$-preview control, and $\mathcal{H}_2$-preview control can directly be applied multivariable systems, although stable inversion is limited to square systems. Only stable inversion and norm-optimal feedforward/ILC are applicable to time-varying systems.

Ongoing research focuses on different system classes such as linear time varying (LTV), linear periodically time varying (LPTV), linear parameter varying (LPV), position dependent, and data-driven methods (Kim and Zou, 2008; Teng and Tsao, 2015; De Rozario and Oomen, 2018b; Bolder et al., 2016). Initial results can be found in Chapters 4, 5 and 10.

3.A Background approximate inverse techniques

In this appendix the approximate inverse techniques NPZ-Ignore, ZPETC, and ZMETC are derived for the decomposition in (3.5). The results are summarized in Table 3.2.

NPZ-Ignore ignores the nonminimum-phase dynamics by using

$$F(z) = \frac{A(z)}{\beta B_s(z)} \tag{3.36}$$

resulting in

$$H(z)F(z) = \frac{B_u(z)}{\beta}. \tag{3.37}$$

Parameter β is a tuning parameter and typically used to compensate for the DC gain by setting

$$\beta = B_u(1). \tag{3.38}$$

Note that (3.36) has $p+d$ samples preview. Recalling that ideally $H(z)F(z) = 1$, it follows that for $p > 0$ there is an error in both magnitude and phase.

Zero phase error tracking control (ZPETC) perfectly compensates for the phase using

$$F(z) = \frac{A(z)B_u(z^{-1})}{\beta^2 B_s(z)} = \frac{z^{-p}A(z)B_u^*(z)}{\beta^2 B_s(z)}, \tag{3.39}$$

with

$$B_u^*(z) = z^p B_u(z^{-1}). \tag{3.40}$$

For this choice it follows that

$$H(z)F(z) = \frac{B_u(z)B_u(z^{-1})}{\beta^2} = \frac{z^{-p}B_u(z)B_u^*(z)}{\beta^2} \tag{3.41}$$

has zero phase as desired. Note that with β in (3.38) the DC gain is compensated and that (3.39) has $p + d$ samples preview.

Zero-magnitude-error tracking control (ZMETC) perfectly compensates the magnitude by using

$$F(z) = \frac{A(z)}{z^p B_s(z)B_u(z^{-1})} = \frac{A(z)}{B_s(z)B_u^*(z)}, \tag{3.42}$$

resulting in

$$H(z)F(z) = \frac{B_u(z)}{z^p B_u(z^{-1})} = \frac{B_u(z)}{B_u^*(z)}. \tag{3.43}$$

Note that (3.43) indeed has zero magnitude error, i.e., unity magnitude, and that (3.42) has d preview samples.

Chapter 4

Stable inversion of LPTV systems

In Chapter 3, several approaches for system inversion of nonminimum-phase systems are presented. The results show that for linear time-invariant (LTI), nonminimum-phase systems, a bounded, noncausal inverse response can be obtained through stable inversion based on an exponential dichotomy. However, for generic linear time-varying (LTV) systems, such a dichotomy does not exist in general. The aim of this chapter is to develop an inversion approach for an important class of LTV systems, namely linear periodically time-varying (LPTV) systems, which occur in, e.g., position-dependent systems with periodic tasks and periodic, non-equidistantly sampled systems. The proposed methodology exploits the periodicity to determine a bounded inverse for general LPTV systems. Conditions for existence are provided. The method is successfully demonstrated in several application cases, including position-dependent and non-equidistantly sampled systems, and constitutes Contribution III.A.

4.1 Introduction

Inverses of dynamical systems are essential in many control applications, including feedforward and learning control. The early inversion approaches in Silverman (1969); Hirschorn (1979) are restricted to causal inverses of minimum-phase systems since they lead to unbounded responses for nonminimum-phase systems. See, for example, Butterworth et al. (2008) for the effect of nonminimum-phase zeros. Interestingly, in Section 3.4.2; Devasia and Paden 1994; Hunt et al. 1996;

The contents of this chapter are published in:
Jurgen van Zundert and Tom Oomen. Stable inversion of LPTV systems with application in position-dependent and non-equidistantly sampled systems. *International Journal of Control*, 2017. DOI: 10.1080/00207179.2017.1380315.

Devasia et al. 1996, an exact inverse for nonminimum-phase systems is obtained with bounded responses. This stable inversion approach is based on a dichotomy of the inverted system into a stable part and an unstable part. It essentially uses a bi-lateral Laplace or Z-transform (Sogo, 2010) by regarding the unstable part as an acausal operation and solving it backward in time. For linear time-invariant (LTI) systems such a dichotomy is trivial and successful applications in feedforward and learning control are reported in Boeren et al. (2015); Bolder and Oomen (2015); Clayton et al. (2009).

Linear time variance has a large impact on system inversion approaches. Such linear time-varying (LTV) applications occur frequently, e.g., (i) multirate systems with different sampling frequencies (Chen and Francis, 1995; Fujimoto and Hori, 2002; Ohnishi and Fujimoto, 2016b); (ii) non-equidistantly sampled systems with time-varying sampling intervals (Chapter 8); and (iii) position-dependent systems with periodic tasks (De Rozario et al. 2017; Chapter 10). Similar to LTI systems, inversion of LTV systems can lead to unbounded responses if a causal inverse is computed. For these applications, it is of direct interest to compute system inverses with bounded responses, similar to stable inversion techniques for LTI systems. However, an exponential dichotomy for LTV systems is nontrivial. In fact, such a dichotomy does not exist for the general class of LTV systems, as is shown in Coppel (1978) and Section 4.3.

Although stable inversion is a standard technique for LTI systems, it does not directly apply to LTV systems. The aim of this chapter is to provide a direct solution for linear periodically time-varying (LPTV) systems, which form an important subclass of LTV systems. In fact, the mentioned LTV applications (i)–(iii) typically satisfy the additional periodicity property. In this chapter, the periodicity of LPTV systems is exploited to establish the required exponential dichotomy, enabling the use of stable inversion for LPTV systems. The presented work relates to Devasia and Paden (1994); Hunt et al. (1996); Devasia et al. (1996); Devasia and Paden (1998); Pavlov and Pettersen (2008) where nonlinear systems are investigated and related conditions are imposed on the system, and to Devasia and Paden (1998); Zou and Devasia (1999); Zou and Devasia (2004); Zou (2009); Jetto et al. (2015) where perfect tracking is compromised for finite preview, with extension to nonlinear systems in Zou and Devasia (2007). For LTI systems, approaches related to stable inversion include inversion via lifting (Bayard, 1994), geometric approaches (Marro et al., 2002; Zattoni, 2014), and state-space reduction for non-square systems (Moylan, 1977). For continuous-time LTV systems with a time-varying state-to-output map, see Kasemsinsup et al. (2016).

The main contribution of this chapter is stable inversion for LPTV systems, with the following sub-contributions.

4.I It is shown that an exponential dichotomy does not always exist for general LTV systems.

4.II It is shown that an exponential dichotomy always exists for LPTV systems under mild conditions similar to those for LTI systems.

4.III Two computational procedures of the exponential dichotomy for LPTV systems are provided: one for reversible systems and one for non-reversible systems.

4.IV The proposed approach is demonstrated via three cases: (i) a reversible numerical example; (ii) a non-equidistantly sampled system; and (iii) a position-dependent system.

The outline of this chapter is as follows. In Section 4.2, the stable inversion problem for general LTV systems is formulated. The key issue lies in finding an exponential dichotomy. In Section 4.3, it is shown that such a dichotomy does not always exist for general LTV systems, which constitutes Contribution 4.I. In Section 4.4, the exponential dichotomy for LPTV systems is presented and shown to always exist, which constitutes Contribution 4.II. In Section 4.5, the stable inversion approach for LPTV systems is presented constituting Contribution 4.III. The approach is demonstrated using several cases in Sections 4.6 to 4.8 which constitutes Contribution 4.IV. Section 4.9 contains conclusions and an outlook.

Throughout this chapter, linear, single-input, single-output (SISO) systems are considered. Extensions to square multi-input, multi-output (MIMO) systems follow directly. The focus is on discrete-time systems, since this is natural for sampled systems. Results for continuous-time systems follow along similar lines.

4.2 Problem formulation

4.2.1 Application in mechatronics

In mechatronics, there is an ever increasing demand for lower cost and higher accuracy which introduces LPTV behavior, see also Chapter 1. At least three cases causing this behavior can be identified: (i) multirate systems, (ii) non-equidistant sampling, and (iii) position-dependent behavior with periodic tasks. These cases are detailed below.

To reduce cost, multiple applications are often embedded on a single platform. Scheduling of the different processes leads to non-equidistant sampling of the applications, which is observed as time variance of the system, see Figure 4.1(a). The scheduling is often periodic, leading to LPTV behavior. LTI control design for a lower equidistant rate is conservative in terms of performance since not all design freedom is exploited. To enhance the performance/cost trade-off, control design of the LPTV system is desired.

To reduce cost, the applications can also run on different dedicated control boards, depending on the performance requirement of the specific (control) loop.

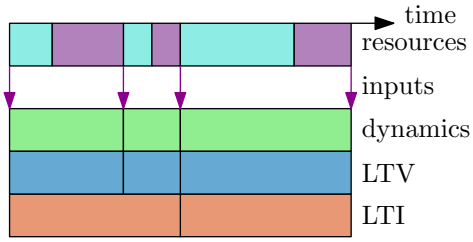

(a) Example of resource scheduling introducing non-equidistant sampling of the system. Periodic scheduling leads to LPTV behavior.

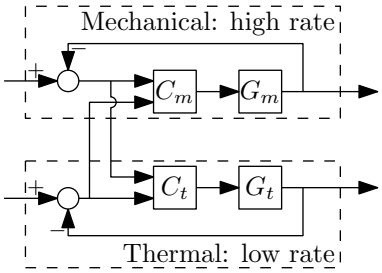

(b) Example of a thermomechanical control diagram (Evers et al., 2017; Evers et al., 2018). The different time scales lead to LPTV behavior.

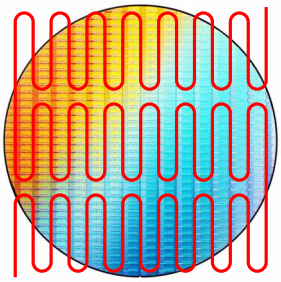

(c) Example of a meander pattern on a wafer stage. The periodic task on the position-dependent system leads to LPTV behavior.

Figure 4.1. LPTV behavior occurs in many mechatronic applications.

For example, fast dynamics are typically controlled with a higher sampling rate than slow dynamics, as is, for example, the case in thermomechanical systems, see Figure 4.1(b). The interconnection of the different loops forms a multirate system with LPTV behavior.

Accuracy is often limited by the inherent position-dependent behavior of mechatronic systems. However, most control is based on LTI designs, not taking into account the position-dependent behavior. For periodic motion tasks, as for example in Figure 4.1(c), the position-dependent behavior leads to LPTV behavior. Taking the LPTV behavior into account for control design can significantly improve the accuracy.

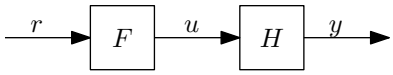

Figure 4.2. For nonminimum-phase system H, stable inversion yields bounded signal u such that $y = r$.

4.2.2 Problem setup

Consider the exponentially stable LTV system H given by

$$x[k+1] = A_H[k]x[k] + B_H[k]u[k], \tag{4.1a}$$
$$y[k] = C_H[k]x[k] + D_H[k]u[k], \tag{4.1b}$$

where $A_H[k] \in \mathbb{R}^{n_x \times n_x}$, $B_H[k] \in \mathbb{R}^{n_x \times 1}$, $C_H[k] \in \mathbb{R}^{1 \times n_x}$, $D_H[k] \in \mathbb{R}$, with time index k, $k_s \leq k \leq k_e$, $k_s, k, k_e \in \mathbb{Z}$, and $x[k_s] = 0$.

The problem considered in this chapter is to determine a bounded input u, such that $y = r$ in Figure 4.2. In particular, the main idea is to invert the system H, i.e., for square and invertible H use

$$F \stackrel{z}{=} \left[\begin{array}{c|c} A[k] & B[k] \\ \hline C[k] & D[k] \end{array}\right] \tag{4.2a}$$
$$= \left[\begin{array}{c|c} A_H[k] - B_H[k]D_H^{-1}[k]C_H[k] & B_H[k]D_H^{-1}[k] \\ \hline -D_H^{-1}[k]C_H[k] & D_H^{-1}[k] \end{array}\right]. \tag{4.2b}$$

The main point is that F in (4.2) does not need to be exponentially stable. The zeros of (4.1) can be immediately verified to be eigenvalues of $A_H[k] - B_H[k]D_H^{-1}[k]C_H[k]$, which in fact are the poles of (4.2). Hence, stability of F in (4.2) hinges on the zeros of H in (4.1). More on zero dynamics and stability of LTV systems can be found in, for example, Hill and Ilchmann (2011); Berger et al. (2015).

The following definition is adopted from Coppel (1978); Halanay and Ionescu (1994); Papaschinopoulos (1986).

Definition 4.1 (Exponential dichotomy)**.** *The system*

$$x[k+1] = A[k]x[k], \tag{4.3}$$

with $A[k] \in \mathbb{R}^{n_x \times n_x}$ and fundamental matrix solution $X[k] \in \mathbb{R}^{n_x \times n_x}$ satisfies an exponential dichotomy if there exist a projection $P = P^2 \in \mathbb{R}^{n_x \times n_x}$ and constants $K > 0$, $0 < p < 1$ such that

$$\|X[n]PX^{-1}[m]\| \leq Kp^{n-m}, \qquad n \geq m, \tag{4.4a}$$
$$\|X[n](I-P)X^{-1}[m]\| \leq Kp^{m-n}, \qquad m \geq n, \tag{4.4b}$$

where $\|(\cdot)\|$ is any convenient norm.

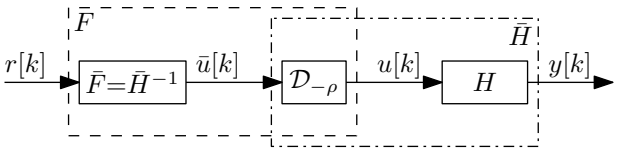

Figure 4.3. Input shift $\mathcal{D}_{-\rho}$ renders $\bar{H}$ bi-proper such that $\bar{H}$ is invertible. The shift is compensated through time-shifting output $\bar{u}[k]$ of $\bar{F} = \bar{H}^{-1}$ as $u[k] = \mathcal{D}_{-\rho}\bar{u}[k]$. The results are exact on an infinite horizon.

Essentially, P provides a projection onto the stable subspace (exponential decay for $k \to \infty$), and $I - P$ a projection onto the unstable subspace (exponential decay for $k \to -\infty$).

The main idea in stable inversion is to obtain an exponential dichotomy (Definition 4.1) through a nonsingular state transformation $T[k] \in \mathbb{C}^{n_x \times n_x}$:

$$x[k] = T[k] \begin{bmatrix} x_s[k] \\ x_u[k] \end{bmatrix}, \tag{4.5}$$

resulting in

$$\tilde{F} \stackrel{s}{=} \left[\begin{array}{c|c} \tilde{A}[k] & \tilde{B}[k] \\ \hline \tilde{C}[k] & \tilde{D}[k] \end{array}\right] = \left[\begin{array}{c|c} T^{-1}[k+1]A[k]T[k] & T^{-1}[k+1]B[k] \\ \hline C[k]T[k] & D[k] \end{array}\right]. \tag{4.6}$$

Note that the transformation into (4.6) is valid for inversion since the main interest is in the output u of (4.2), which is invariant under transformation (4.5). Instead of solving F completely forward in time, $\tilde{F}$ is solved with the stable part x_s forward in time and the unstable part x_u backward in time (Devasia et al., 1996), yielding a unique, bounded and noncausal solution. The key issue is determining this dichotomy for LTV systems, which is investigated next.

Remark 4.2. *Invertibility of H in* (4.1) *relates to invertibility of $D_H[k]$ in* (4.2) *and can be directly satisfied by applying input shifts to H as illustrated in Figure 4.3. Note that if $H = (A_H[k], B_H[k], C_H[k], 0)$, then $\bar{H} = H\mathcal{D}_{-1} = (A_H[k-1], B_H[k-1], C_H[k]A_H[k-1], C_H[k]B_H[k-1])$, with the delay operator defined as $(\mathcal{D}_\tau u)[k] = u[k-\tau]$.*

4.3 Exponential dichotomy for LTV systems

Stable inversion hinges on the existence of an exponential dichotomy (Definition 4.1). The following example shows that, for general LTV systems, there does not always exist such a dichotomy.

Example 4.3. *Consider the scalar LTV system*

$$x[k+1] = A[k]x[k], \quad A[k] = \begin{cases} \alpha, & k < 0, \\ \beta, & k \geq 0, \end{cases} \tag{4.7}$$

where $\alpha, \beta \in \mathbb{R}$, which has fundamental solution

$$X[k] = \begin{cases} \alpha^k, & k < 0, \\ \beta^k, & k \geq 0. \end{cases} \tag{4.8}$$

Whether the system admits an exponential dichotomy (Definition 4.1) depends on $|\alpha|, |\beta|$ as illustrated by the following cases:

1. $|\alpha|, |\beta| < 1$*: exponential dichotomy with $P = 1$, $K = 1$, and $p = \max\{|\alpha|, |\beta|\}$.*

2. $|\alpha|, |\beta| > 1$*: exponential dichotomy with $P = 0$, $K = 1$, and $p = \max\{|\alpha|^{-1}, |\beta|^{-1}\}$.*

3. $|\alpha| < 1$, $|\beta| > 1$*: no exponential dichotomy since there exists no constant P satisfying all conditions. Indeed, $P = P^2 \in \mathbb{R}$ implies $P = 0$ or $P = 1$. For $P = 0$, for example, $0 \geq m \geq n$ violates the condition. For $P = 1$, for example, $n \geq m \geq 0$ violates the condition.*

4. $|\alpha| = 1$ *or* $|\beta| = 1$*: no exponential dichotomy due to eigenvalues on the unit circle.*

Example 4.3 shows that an exponential dichotomy requires no eigenvalues on the unit circle, i.e., the system should be hyperbolic. This is a common condition (Coppel, 1978; Devasia and Paden, 1998) and also occurs for LTI systems (Devasia et al., 1996). If the system has eigenvalues on the unit circle, i.e., the system is non-hyperbolic, similar techniques as in Devasia (1997a) can be followed.

Importantly, also for hyperbolic systems, there does not always exist an exponential dichotomy, see case 3 of Example 4.3. Transformation $T[k]$ in (4.5) facilitates in finding suitable P to satisfy an exponential dichotomy. However, there does not always exist $T[k]$ such that the transformed system satisfies an exponential dichotomy. Indeed, for case 3, it can be directly observed that no such transformation exists.

4.4 Exponential dichotomy for LPTV systems

In this section, LPTV systems are considered, which are an important subclass of LTV systems, see also Section 4.2.1. It is shown that for LPTV systems,

there always exists an exponential dichotomy, under the mild condition of an hyperbolic system. Moreover, it is shown how to compute the dichotomy. To this end, two cases are distinguished: systems that are reversible and systems that are non-reversible.

4.4.1 Stability of LPTV systems

LPTV systems are a subclass of LTV systems also satisfying Definition 4.4.

Definition 4.4 (LPTV system)**.** *An LTV system H is LPTV with period $\tau \in \mathbb{N}$ if it commutes with the delay operator $\mathcal{D}_\tau$ defined by $(\mathcal{D}_\tau u)[k] = u[k-\tau]$, i.e., $\mathcal{D}_\tau H = H\mathcal{D}_\tau$.*

It is directly verified that if H in (4.1) and $T[k]$ in (4.5) are periodic with period τ, then F in (4.2) and $\tilde{F}$ in (4.6) are also periodic with period τ.

Exponential stability of LPTV systems directly relates to the monodromy matrix (Bittanti and Colaneri, 2009, Section 1.2), which for F in (4.2) is given by $\Psi[k] = \Phi_{k+\tau,k}$ with transition matrix

$$\Phi_{k_2,k_1} = \begin{cases} I, & k_2 = k_1, \\ A[k_2-1]A[k_2-2]\cdots A[k_1], & k_2 > k_1. \end{cases} \tag{4.9}$$

Importantly, the eigenvalues of $\Psi[k]$, and therefore stability, are independent of evaluation point k (Bittanti and Colaneri, 2009, Section 3.1). In particular, F in (4.2) with period τ is stable if and only if $|\lambda_i(\Psi)| < 1$, for all i (Bittanti and Colaneri, 2009, Section 1.2.3), where $\Psi := \Psi[0]$ is given by

$$\Psi = A[\tau-1]A[\tau-2]\cdots A[0]. \tag{4.10}$$

4.4.2 Exponential dichotomy

Theorem 4.5 provides conditions on $T[k]$ such that transformed system $\tilde{F}$ satisfies an exponential dichotomy. See Appendix 4.A for a proof.

Theorem 4.5 (Conditions $T[k]$)**.** *Let Ψ in (4.10) have no eigenvalues on the unit circle. Then, if there exists $T[k]$ in (4.5) such that the monodromy matrix of system $\tilde{F}$ in (4.6) with period τ (Definition 4.4) satisfies*

$$\tilde{\Psi} = \tilde{A}[\tau-1]\tilde{A}[\tau-2]\cdots\tilde{A}[0] = \begin{bmatrix} \tilde{\Psi}_s & 0 \\ 0 & \tilde{\Psi}_u \end{bmatrix}, \tag{4.11}$$

where $|\lambda_i(\tilde{\Psi}_s)| < 1$, for all i, and $|\lambda_i(\tilde{\Psi}_u)| > 1$, for all i, then $\tilde{F}$ in (4.6) satisfies an exponential dichotomy according to Definition 4.1.

The results in Theorem 4.5 directly lead to a possible choice of $T[k]$ such that $\tilde{F}$ satisfies an exponential dichotomy; see Theorem 4.6 and Appendix 4.B for a proof.

Theorem 4.6 (Dichotomy LPTV systems)**.** *If $T[k]$ is τ-periodic with $T[0]$ consisting of generalized eigenvectors of Ψ in* (4.10) *such that* (4.11) *is satisfied, then $\tilde{F}$ satisfies an exponential dichotomy according to Definition 4.1.*

The result of Theorem 4.6 essentially shows that only $T[0]$ is relevant for satisfying an exponential dichotomy. Next, the other entries of $T[k]$ are used to transform the LPTV system into one with time-invariant state matrix, which allows to completely separate the stable and unstable part. The separation will turn out to simplify the stable inversion approach in Section 4.5.

4.4.3 Reversible systems

Finding a transformation $T[k]$ such that the LPTV system F is transformed to $\tilde{F}$ with a time-invariant state matrix $\tilde{A}[k] = \hat{A}$, for all k, is known as the Floquet problem (Bittanti and Colaneri, 2009, Section 3.2). An important result is that such a transformation does not always exist, see Lemma 4.7 and Bittanti and Colaneri (2009, Section 3.2) for a proof.

Lemma 4.7. *Given F in* (4.2) *with period τ (Definition 4.4), there exists a τ-periodic invertible transformation $T[k]$ in* (4.5) *and a constant matrix $\hat{A}$ such that $\tilde{A}[k] = \hat{A}$, for all k, in* (4.6)*, if and only if* $\operatorname{rank}\{\Phi_{k+i,k}\}$ *is independent of k, for all $i \in [1, n_x]$, with $\Phi_{k+i,k}$ in* (4.9)*.*

The rank condition in Lemma 4.7 is automatically satisfied if F is reversible, see Definition 4.8. In fact, if F is reversible, there is a procedure (Bittanti and Colaneri, 2009, Section 3.2.1) to determine $T[k]$ such that $\tilde{A}[k]$ is constant for all k as provided by Lemma 4.9. See Appendix 4.C for a proof.

Definition 4.8 ((Non-)reversible system)**.** *A system $(A[k], B[k], C[k], D[k])$ is reversible if and only if $A[k]$ is non-singular for all k. If $A[k]$ is singular for some k, the system is non-reversible.*

Lemma 4.9. *Let F with period τ (Definition 4.4) be reversible (Definition 4.8) and given by* (4.2) *and let τ-periodic transformation $T[k]$ in* (4.5) *be given by*

$$T[k] = A[k-1]T[k-1]\hat{A}^{-1}, \quad k \in [1, \tau - 1], \tag{4.12}$$

with

$$\hat{A} = (T^{-1}[0]\Psi T[0])^{\frac{1}{\tau}}, \tag{4.13}$$

for some $T[0] \in \mathbb{C}^{n_x \times n_x}$. Then, transformed system $\tilde{F}$ in (4.6) *has constant state matrix $\tilde{A}[k] = T^{-1}[k+1]A[k]T[k] = \hat{A}$, for all k.*

The combination of Lemma 4.9 and Theorem 4.6 directly leads to the dichotomy for reversible systems in Theorem 4.10, see Appendix 4.D for a proof.

Theorem 4.10 (Dichotomy reversible systems)**.** *If F in* (4.2) *is LPTV with period τ (Definition 4.4) and reversible (Definition 4.8), and transformation $T[k]$ is given by Lemma 4.9 with $T[0]$ according to Theorem 4.6, then $\tilde{F}$ in* (4.6) *satisfies an exponential dichotomy according to Definition 4.1. Moreover, the stable and unstable parts are completely separated.*

4.4.4 Non-reversible systems

The transformation in Lemma 4.9 is only applicable to reversible systems. In practice, systems are often non-reversible. For instance, strictly proper systems that are made bi-proper to enable inversion through the procedure in Remark 4.2 which effectively introduces zeros at the origin in $\bar{H}$. These zeros become poles for the inverse system $\bar{H}^{-1}$ and consequently $A[k]$ in (4.2) has eigenvalues zero and is thus singular. Hence, for strictly proper H, F is non-reversible and Lemma 4.9 is not applicable.

For non-reversible systems, the transformation in Lemma 4.9 is thus not applicable. Since the system dynamics are often similar over time, a static transformation is used as provided by Corollary 4.11. The result follows directly from Theorem 4.6.

Corollary 4.11 (Dichotomy non-reversible systems)**.** *If F in* (4.2) *with period τ (Definition 4.4) is non-reversible (Definition 4.8) with transformation $T[k]$ in* (4.5) *given by*

$$T[k] = T[0], \quad \textit{for all } k, \tag{4.14}$$

with $T[0]$ according to Theorem 4.6, then $\tilde{F}$ in (4.6) *satisfies an exponential dichotomy according to Definition 4.1.*

In contrast to $T[k]$ in Lemma 4.9, $T[k]$ in Corollary 4.11 does generally not completely separate the stable and unstable parts. Indeed, this only holds if $A[k]$ has the same generalized eigenvectors for all k. A well-known class of such systems is the class of LTI systems.

4.5 Stable inversion

Based on the exponential dichotomy obtained in the previous section, the stable inversion approach for LPTV systems is presented. An overview over the complete approach is presented in Figure 4.4.

System (4.6), with $T[k]$ such that the conditions in Theorem 4.5 are satisfied, can be written as

$$x_s[k+1] = A_{ss}[k]x_s[k] + A_{su}[k]x_u[k] + B_s[k]r[k], \tag{4.15a}$$
$$x_u[k+1] = A_{us}[k]x_s[k] + A_{uu}[k]x_u[k] + B_u[k]r[k], \tag{4.15b}$$
$$u[k] = C_s[k]x_s[k] + C_u[k]x_u[k] + D[k]r[k], \tag{4.15c}$$

with $x_s[k_s], x_u[k_e] = 0$, where

$$\begin{bmatrix} A_{ss}[k] & A_{su}[k] \\ A_{us}[k] & A_{uu}[k] \end{bmatrix} = T^{-1}[k+1]A[k]T[k], \tag{4.16a}$$

$$\begin{bmatrix} B_s[k] \\ B_u[k] \end{bmatrix} = T^{-1}[k+1]B[k], \tag{4.16b}$$

$$\begin{bmatrix} C_s[k] & C_u[k] \end{bmatrix} = C[k]T[k]. \tag{4.16c}$$

The stable inversion approach yielding bounded u for discrete-time systems is provided in Theorem 4.12.

Theorem 4.12 (Stable inversion)**.** *Given that system* (4.15) *satisfies an exponential dichotomy with stable x_s and unstable x_u (Definition 4.1), output u* (4.15c) *is bounded for the solution*

$$x_s[k+1] = (A_{ss}[k] + A_{su}[k]S[k])\, x_s[k] + B_s[k]r[k] + A_{su}[k]g[k], \tag{4.17a}$$

$$x_u[k] = S[k]x_s[k] + g[k], \tag{4.17b}$$

$$S[k] = (A_{uu}[k] - S[k+1]A_{su}[k])^{-1} (S[k+1]A_{ss}[k] - A_{us}[k]), \tag{4.17c}$$

$$\begin{aligned} g[k] = {} & (S[k+1]A_{su}[k] - A_{uu}[k])^{-1} \\ & \times (B_u[k]r[k] - S[k+1]B_s[k]r[k] - g[k+1]), \end{aligned} \tag{4.17d}$$

with $x_s[k_s] = 0$, $S[k_e] = 0$, $g[k_e] = 0$.

For completeness, the derivation of Theorem 4.12 is included in Appendix 4.E. Stable inversion for continuous-time systems can be found in, e.g., Chen (1993) and follows along similar lines.

For reversible systems, Theorem 4.10 can be applied yielding constant

$$\tilde{A}[k] = \hat{A} = \begin{bmatrix} A_{ss} & 0 \\ 0 & A_{uu} \end{bmatrix}, \tag{4.18}$$

i.e., there is no coupling between x_s and x_u. This simplifies the expressions in Theorem 4.12 which are given in Corollary 4.13.

Corollary 4.13 (Stable inversion reversible systems)**.** *If F in* (4.2) *with period τ (Definition 4.4) is reversible (Definition 4.8), then $A_{su}[k] = 0$, $A_{us}[k] = 0$, $A_{ss}[k] = A_{ss}$, $A_{uu}[k] = A_{uu}$, for all k in* (4.15a), (4.15b)*, and Theorem 4.12 reduces to*

$$x_s[k+1] = A_{ss}x_s[k] + B_s[k]r[k], \tag{4.19a}$$

$$x_u[k] = A_{uu}^{-1}(x_u[k+1] - B_u[k]r[k]), \tag{4.19b}$$

with $x_s[k_s] = 0$, $x_u[k_e] = 0$.

If F is stable, the stable inversion solution reduces to the regular inverse solution $u = H^{-1}r$, see Corollary 4.14. The result follows directly from Theorem 4.12.

Corollary 4.14 (Stable inversion stable system)**.** *If system F in* (4.2) *is stable, then the stable inversion solution in Theorem 4.12 reduces to the causal inverse solution.*

The stable inversion procedure for LPTV systems is summarized in Figure 4.4.

Remark 4.15. *The results in Theorem 4.12 and Corollary 4.13 are exact for $k_s \to -\infty$, $k_e \to \infty$, as is also illustrated via an example in Section 4.8.*

4.6 Case 1: Numerical example of a reversible system

In this section, the stable inversion approach is applied step-by-step to a numerical example of a reversible system.

Consider the LPTV system F in (4.2) with period $\tau = 3$ defined by

$$A[0] = \begin{bmatrix} 0.3 & 2.0 \\ -0.9 & 0.8 \end{bmatrix}, \quad A[1] = \begin{bmatrix} 1.4 & 1.3 \\ 1.6 & 0.6 \end{bmatrix}, \quad A[2] = \begin{bmatrix} 0.4 & 3.0 \\ -0.2 & 0.7 \end{bmatrix}, \tag{4.20a}$$

$$B[k] = \begin{bmatrix} 1 \\ 1 \end{bmatrix}, \quad C[k] = \begin{bmatrix} 1 & 1 \end{bmatrix}, \quad D[k] = 1, \quad \text{for all } k. \tag{4.20b}$$

Since $A[0], A[1], A[2]$ are all full rank, the system is reversible, see Definition 4.8. The monodromy matrix (4.10) is given by

$$\Psi = A[2]A[1]A[0] = \begin{bmatrix} -0.318 & 2.640 \\ 0.192 & -3.344 \end{bmatrix}, \tag{4.21}$$

with eigenvalues and eigenvectors

$$\lambda_1 = -0.1589, \quad v_1 = \begin{bmatrix} 0.9982 \\ 0.0602 \end{bmatrix}, \tag{4.22a}$$

$$\lambda_2 = -3.5031, \quad v_2 = \begin{bmatrix} -0.6381 \\ 0.7699 \end{bmatrix}. \tag{4.22b}$$

Hence, F has one stable and one unstable state. Transforming F using $T[k]$ from Theorem 4.10 with $T[0] = \begin{bmatrix} v_1 & v_2 \end{bmatrix}$ yields $\tilde{F}$ in (4.6) with constant $\tilde{A}[k] = \hat{A}$,

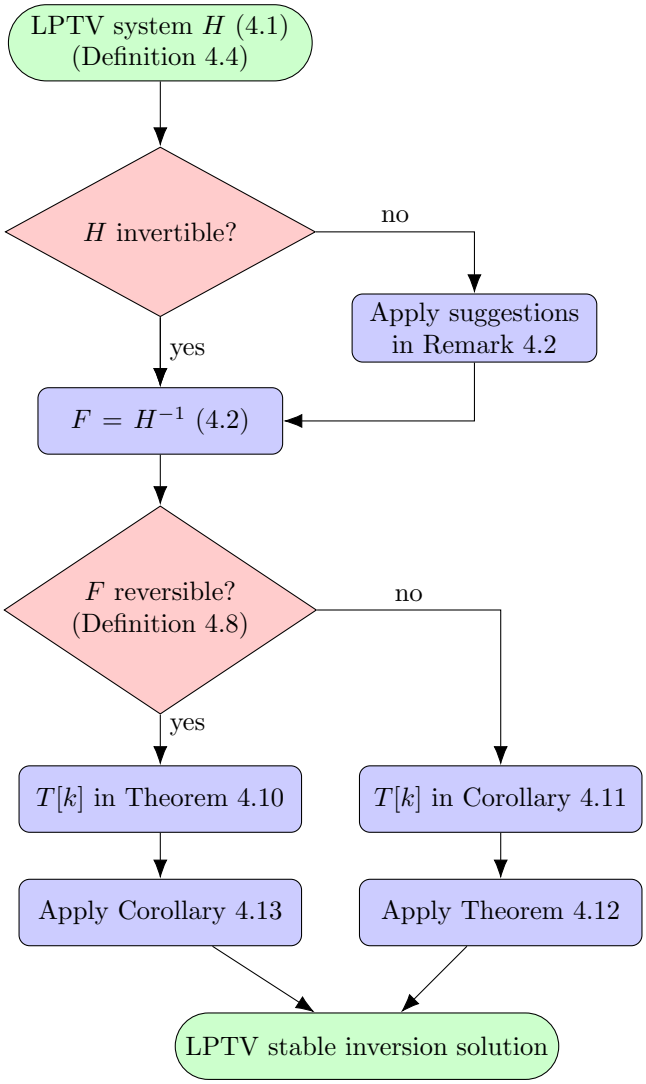

Figure 4.4. Stable inversion procedure for LPTV systems.

for all k:

$$\hat{A} = \begin{bmatrix} 0.2708 + 0.4690i & 0 \\ 0 & 0.7594 + 1.3153i \end{bmatrix}, \tag{4.23a}$$

$$\tilde{B}[0] = \begin{bmatrix} -0.0260 - 0.0451i \\ 0.5859 + 1.0148i \end{bmatrix}, \tag{4.23b}$$

$$\tilde{B}[1] = \begin{bmatrix} -0.0405 + 0.0701i \\ -0.3837 + 0.6646i \end{bmatrix}, \tag{4.23c}$$

$$\tilde{B}[2] = \begin{bmatrix} 1.7450 \\ 1.1625 \end{bmatrix}, \tag{4.23d}$$

$$\tilde{C}[0] = \begin{bmatrix} 1.0584 & 0.1318 \end{bmatrix}, \tag{4.23e}$$

$$\tilde{C}[1] = \begin{bmatrix} -0.3974 + 0.6883i & 0.8358 - 1.4476i \end{bmatrix}, \tag{4.23f}$$

$$\tilde{C}[2] = \begin{bmatrix} 0.6069 + 1.0512i & -1.3671 - 2.3679i \end{bmatrix}, \tag{4.23g}$$

$$\tilde{D}[k] = 1, \quad \text{for all } k. \tag{4.23h}$$

Note that, although the state-space of F is real-valued, the state-space of $\tilde{F}$ is complex-valued since $\Psi^{\frac{1}{\tau}}$ is complex.

By construction, $\tilde{F}$ satisfies an exponential dichotomy according to Theorem 4.5. Since the system is reversible, $A_{su}, A_{us} = 0$ in (4.15) and the stable inversion solution is found through Corollary 4.13.

For input

$$r[k] = \begin{cases} 1, & k = 2, \\ 0, & k \neq 2, \end{cases} \tag{4.24}$$

causal inversion and stable inversion yield

$$u_{CI} = \begin{bmatrix} 0 \\ 0 \\ 1 \\ 2 \\ 2.2 \\ 6.71 \\ -0.83 \\ -10.2188 \\ -25.5839 \end{bmatrix}, \quad u_{SI} = \begin{bmatrix} 0.0437 \\ 0.8424 \\ 3.0928 \\ 1.8468 \\ -0.7511 \\ -0.6213 \\ -0.2934 \\ 0.1193 \\ 0.0987 \end{bmatrix}. \tag{4.25}$$

As expected, u_{CI} grows unbounded since F is unstable. In contrast, u_{SI} remains bounded as desired. The noncausal character of stable inversion is visible in $u_{SI}[0], u_{SI}[1] \neq 0$ while $r[0], r[1] = 0$.

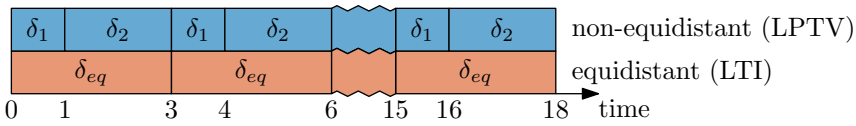

Figure 4.5. Time line of the non-equidistant sampling sequence. Control for the equidistant sampling sequence with period $\delta_{eq} = T\delta_b = \delta_1 + \delta_2 = 3$ is conservative since not all control points are exploited. To improve performance, control for the non-equidistant sampling sequence δ_1, δ_2 is pursued.

4.7 Case 2: Non-equidistant sampling

In this section, the potential of control under non-equidistant sampling is demonstrated. In particular, it is shown that the proposed stable inversion approach for LPTV systems enables exact tracking of the trajectory, whereas the tracking is non-exact for LTI control under non-equidistant sampling.

4.7.1 Sampling sequence

The non-equidistant sampling sequence is shown in Figure 4.5. It has periodicity $\tau = 2$, with $\delta_1 = \gamma_1\delta_b = 1$ and $\delta_2 = \gamma_2\delta_b = 2$.

4.7.2 System

Consider the continuous-time system of Example 2 in Åström et al. (1984):

$$H_c = \frac{1}{(s+1)^3} \stackrel{s}{=} \left[\begin{array}{c|c} A_c & B_c \\ \hline C_c & D_c \end{array}\right] = \left[\begin{array}{ccc|c} 0 & 1 & 0 & 0 \\ 0 & 0 & 1 & 0 \\ -1 & -3 & -3 & 1 \\ \hline 1 & 0 & 0 & 0 \end{array}\right], \tag{4.26}$$

with zero-order-hold discretization

$$H \stackrel{s}{=} \left[\begin{array}{c|c} A_H[k] & B_H[k] \\ \hline C_H & D_H \end{array}\right] = \left[\begin{array}{c|c} e^{A_c\delta_k} & A_c^{-1}(A_H[k] - I)B_c \\ \hline C_c & D_c \end{array}\right], \tag{4.27}$$

where δ_k is the sampling interval. Since $D_H = 0$, H is not directly invertible and the procedure in Remark 4.2 is followed. As a consequence, the inverse system F is non-reversible, see also Section 4.4.4.

As shown in Åström et al. (1984), for $0 < \delta_k < 1.8399$, there is one minimum-phase and one nonminimum-phase zero, and for $\delta_k \geq 1.8399$, both zeros are minimum phase. For the non-equidistant sampling sequence in Figure 4.5, one of the poles of LPTV system F alternates between stable and unstable.

It follows directly from Figure 4.5 that the smallest equidistant sampling sequence has period $\delta_{eq} = \delta_0 + \delta_1 = 3$. The corresponding LTI system is thus minimum phase. The reference trajectory r is shown in Figure 4.6(a).

4.7.3 Application in feedforward control

In this section, an application in inverse model feedforward control is considered. True system H is assumed to be exactly known and $F = H^{-1}$, with H in (4.27).

Regular inversion of the minimum-phase LTI system with period $\delta_{eq} = 3$ yields input u shown in Figure 4.6(b). Note that u is only updated after 3 time units, and constant in-between. Applying this input to the true LPTV system H yields the output in Figure 4.6(a). Due to the mismatch between the LTI system used for inversion and the true LPTV system, the output y differs from the reference r. The results show the importance of LPTV inversion techniques.

The results in Figure 4.6 show that causal inversion of LPTV system H through (4.2) yields perfect tracking $y = r$. However, input u is unbounded since F is unstable.

To obtain a bounded u and exact tracking, the stable inversion approach for LPTV systems as outlined in Figure 4.4 is used. Since F is non-reversible, Corollary 4.11 and Theorem 4.12 are used. The monodromy matrix Ψ in (4.10) has two eigenvalues inside and one outside the unit circle. A static transformation $T[k] = T[0]$, for all k, consisting of eigenvectors of Ψ is used, see Corollary 4.11. The stable inversion solution is obtained through Theorem 4.12. Figure 4.6(b) shows that stable inversion generates bounded u as desired.

The tracking in Figure 4.6(a) is non-exact due to finite-time effects (Middleton et al., 2004). To improve performance, the interval length is increased by starting at time -6, with $r[k] = 0$, $k = -6, \ldots, -1$. The results are shown in Figure 4.7. The addition of this preview time results in a performance improvement for stable inversion as desired. The addition of even more preview time further improves the performance.

4.7.4 Application in iterative learning control

In this section, an application in iterative learning control (ILC) is considered. In ILC, the same task is repeated and deterministic uncertainties are compensated by learning from past data using a system model; see also Bristow et al. (2006).

The ILC update law is based on the closed-loop model $\hat{H} = 0.8H$, with H in (4.27). The error dynamics are given by

$$e_{j+1} = e_j - H(u_{j+1} - u_j), \quad e_0 = r, \tag{4.28}$$

with trial number $j = 0, 1, \ldots$, and input u. The learning update is given by

$$u_{j+1} = u_j + \alpha F e_j, \quad u_0 = 0, \tag{4.29}$$

with learning filter $F = \hat{H}^{-1}$ and learning factor $\alpha = 0.5$. Note that if $\alpha F = H^{-1}$, error e_{j+1} is zero as desired.

The results for the reference signal r in Figure 4.7(a) are shown in Figure 4.8. Since $\alpha \neq 1$, it takes several trials for the algorithm to converge, as can be observed in the two-norm of the error shown in Figure 4.8(b). After approximately

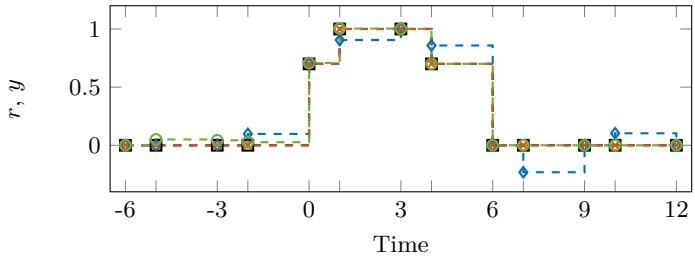

(a) Reference r (□) is perfectly tracked by output y using causal inversion (×). The tracking using stable inversion (○) is limited due to finite preview. Output y for the equidistantly sampled LTI system (◇) differs significantly from r.

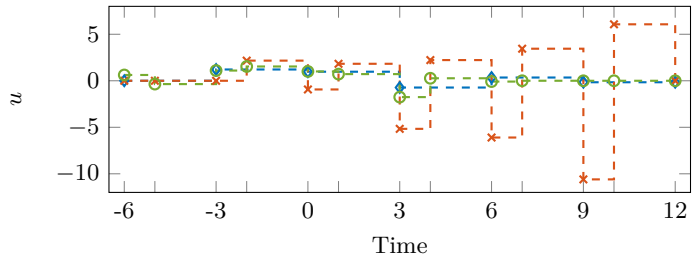

(b) Signal u is bounded for stable inversion (○), but not for causal inversion (×). For the equidistantly sampled LTI system (◇), u is bounded and only updated every 3 time steps.

Figure 4.6. Stable inversion generates bounded u, whereas causal inversion generates unbounded u. The performance of stable inversion is limited due to finite preview. The performance of the equidistant sampled LTI system is low due to an inexact inverse.

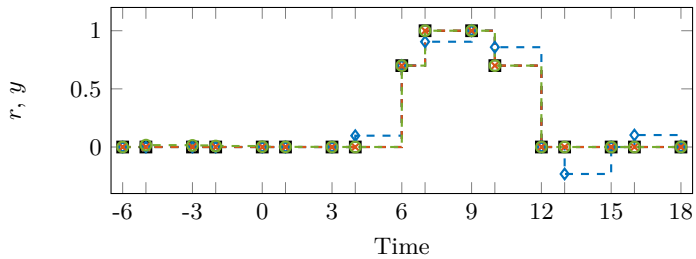

(a) The performance of stable inversion (○) is improved compared to Figure 4.6(a).

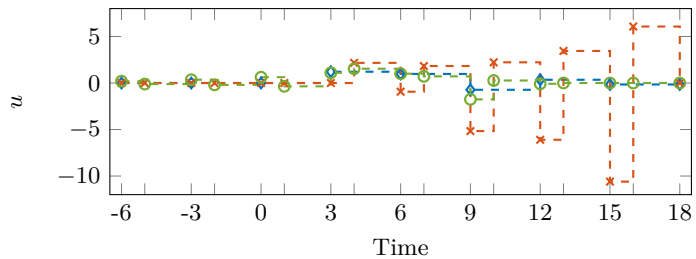

(b) Signal u is bounded for stable inversion (○), but not for causal inversion (×).

Figure 4.7. Additional preview improves the performance of stable inversion compared to Figure 4.6.

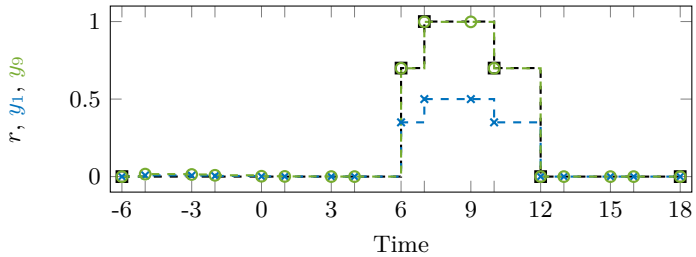

(a) After one trial the performance is poor (✕), but after ten trials the performance is excellent (○) and similar to that of inverse model feedforward in Figure 4.7.

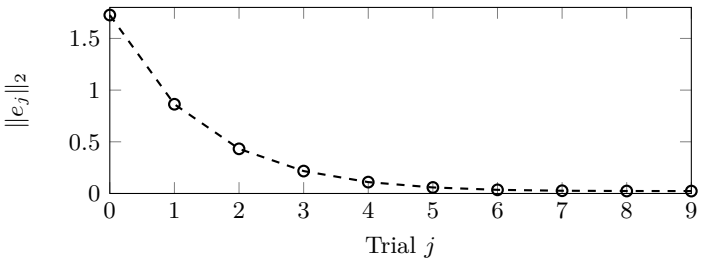

(b) The error norm converges in approximately ten trials to its final value.

Figure 4.8. Application of stable inversion in ILC enables high-performance tracking with a nonexact model.

ten trials, the update is converged to the same solution as with exact model inverse feedforward shown in Figure 4.7.

4.7.5 Summary

The case illustrates the use of stable inversion for non-equidistantly sampled systems, both in inverse model feedforward and ILC design. First of all, the case shows the advantage of LPTV control over LTI control for a non-equidistantly sampled system. Second, the case shows that causal inversion yields unbounded u whereas stable inversion generates bounded u. Third, the case shows that additional preview improves the performance of stable inversion. Indeed, stable inversion is exact for $k_s \to -\infty$. Finally, the application of LPTV stable inversion in ILC is demonstrated.

4.8 Case 3: Position-dependent system

One of the challenges in motion systems is position-dependent behavior, as present in, for example, wafer stages.

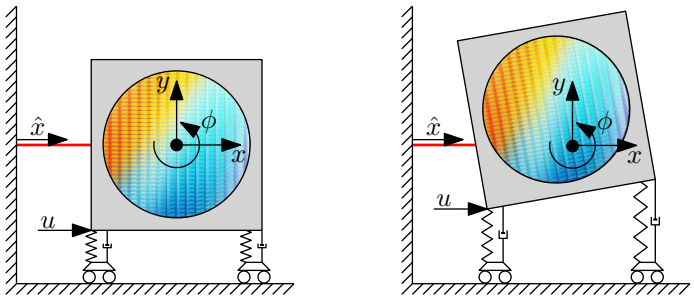

(a) Zero position. **(b)** Moved and rotated.

Figure 4.9. Top view of wafer stage. The interferometer is fixed on the metrology frame and measures distance $\hat{x}$ to the wafer stage, which has degrees of freedom x, y, ϕ. If $\phi \neq 0$, position y effects measurement $\hat{x}$.

Table 4.1. Parameter values of the wafer stage system.

Parameter	Symbol	Value	Unit
Mass	m	50	kg
Inertia	I	2.08	kgm^2
Spring constant	c	10^6	N/m
Damping constant	d	2500	Ns/m
Length	l	0.5	m

4.8.1 Wafer stage system

Wafer stages are key motion systems in wafer scanners used for the production of integrated circuits. A simplified 2D model of a wafer stage in the horizontal plane is considered as shown in Figure 4.9. The stage is actuated by force input u, can translate in x and y direction, and rotate in ϕ direction. The output is the distance $\hat{x}$ between the metrology frame and the wafer stage, measured through an interferometer located on the metrology frame. The parameters are listed in Table 4.1.

A typical wafer stage movement is a so-called meander pattern as illustrated in Figure 4.1(c); see also Van der Meulen et al. (2008). The position y is assumed to be prescribed by the periodic movement in Figure 4.11(a) and is controlled by a PD controller represented by the spring and damper in Figure 4.9. The desired trajectory $\hat{x}_d$ for $\hat{x}$ is also shown in Figure 4.11(a). The combination of y and $\hat{x}_d$ generates the meander pattern shown in Figure 4.10. A key observation is that the $\hat{x}$-dynamics are position dependent due to the influence of position y when $\phi \neq 0$.

A continuous-time state-space realization (A_c, B_c, C_c, D_c) of the $\hat{x}$-dynamics, linearized around $\phi, \dot{\phi} = 0$, with input u, state $\begin{bmatrix} x & \dot{x} & \phi & \dot{\phi} \end{bmatrix}^\top$,

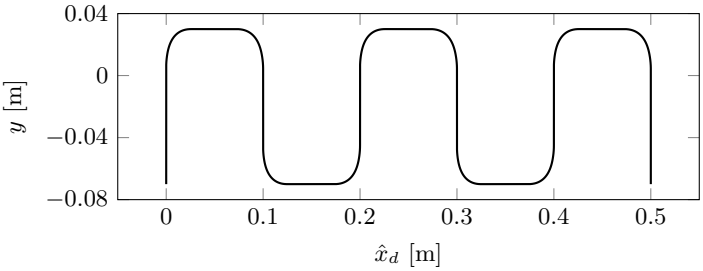

Figure 4.10. Part of meander pattern constructed by $\hat{x}_d, y$ in Figure 4.11(a).

and output $\hat{x}$ is

$$\left[\begin{array}{c|c} A_c & B_c \\ \hline C_c[k] & D_c \end{array}\right] = \left[\begin{array}{cccc|c} 0 & 1 & 0 & 0 & 0 \\ 0 & 0 & 0 & 0 & \frac{1}{m} \\ 0 & 0 & 0 & 1 & 0 \\ 0 & 0 & -\frac{1}{2}\frac{cl^2}{I} & -\frac{1}{2}\frac{dl^2}{I} & \frac{1}{2}\frac{l}{I} \\ \hline 1 & 0 & y[k] & 0 & 0 \end{array}\right]. \tag{4.30}$$

System H in (4.1) is the zero-order-hold discretized version of (4.30):

$$H \overset{s}{=} \left[\begin{array}{c|c} A_H & B_H \\ \hline C_H[k] & D_H \end{array}\right] = \left[\begin{array}{c|c} e^{A_c\delta} & A_c^{-1}(A-I)B_c \\ \hline C_c[k] & D_c \end{array}\right], \tag{4.31}$$

with sampling interval $\delta = 0.001$ s. Note that H is indeed position dependent through $C_H[k]$. Moreover, for the given parameters, the system is minimum phase if $y[k] \geq 0$, and nonminimum phase for $y[k] < 0$. Since $y[k]$ is periodic, H is LPTV. Also note that H is strictly proper since $D_H = 0$, and thus F being the inverse of time-shifted H is non-reversible. Finally, note that the time variance of $C_H[k]$ in H also introduces time variance in $A[k]$ of F in (4.2).

4.8.2 Nonminimum-phase system

Forward time simulation of F with reference $r = \hat{x}_d$ and trajectory y in Figure 4.11(a) yields the unbounded signal u shown in Figure 4.11(b). Since F is non-reversible, it follows from Figure 4.4 that Theorem 4.12 with static transformation $T[k] = T[0]$, for all k, in Corollary 4.11 yields the stable inversion solution with bounded u. The monodromy matrix Ψ reveals one unstable and three stable states. The resulting signal u is shown in Figure 4.11(b) and is indeed bounded. The output position $\hat{x}$ perfectly tracks the desired trajectory $\hat{x}_d$ as shown in Figure 4.11(a).

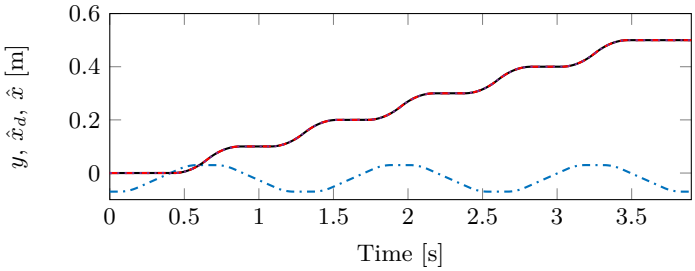

(a) Output $\hat{x}$ with forward simulation (——) and with stable inversion (- - -) perfectly tracks the desired trajectory $\hat{x}_d$ (·····) for the prescribed periodic position y (-·-·).

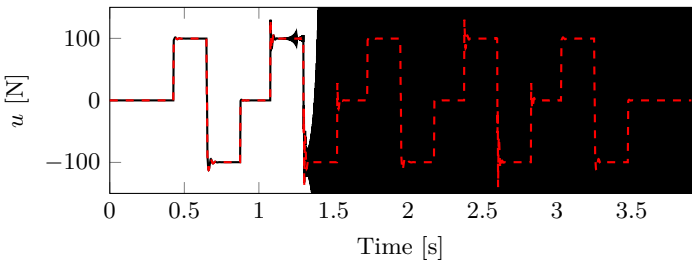

(b) Forward simulation (——) of F yields unbounded u, whereas stable inversion (- - -) yields bounded u.

Figure 4.11. Prescribed position y introduces position dependence resulting in an LPTV system that is unstable. With stable inversion, a bounded solution u resulting in perfect tracking is obtained.

4.8.3 Minimum-phase system

Consider the trajectory y in Figure 4.12(a). For this trajectory, the monodromy matrix Ψ indicates F is stable. Indeed, $y[k] < 0$ for some k, but this does not necessarily lead to unstable F. Since F is stable, the stable inversion solution reduces to forward simulation of F, see Corollary 4.14. The results are shown in Figure 4.12 and show exact tracking with bounded input.

4.8.4 Summary

The results show that if the LPTV system F is unstable, a bounded solution u is found, whereas if F is stable, the causal inversion result is recovered. The case demonstrates the application of the proposed LPTV stable inversion approach to position-dependent systems with periodic tasks.

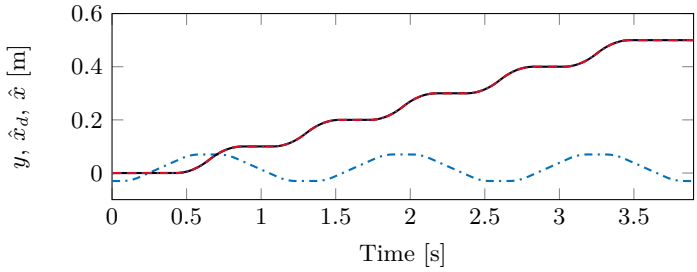

(a) Output $\hat{x}$ with forward simulation (——) and with stable inversion (- - -) perfectly tracks the desired trajectory $\hat{x}_d$ (·····) for the prescribed position y (-·-·).

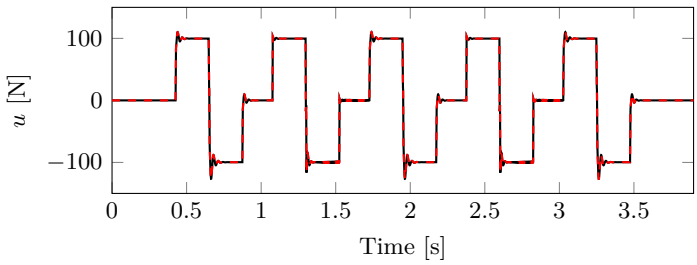

(b) Since LPTV system F is stable, the solutions of stable inversion (- - -) and forward simulation (——) of F are the same and bounded.

Figure 4.12. Prescribed position y introduces position dependence resulting in an LPTV system that is stable. The stable inversion solution reduces to that of forward simulation and yields perfect tracking.

4.9 Conclusion and outlook

In practice, many systems are LTV, yet exhibit periodicity, rendering them LPTV. Examples include, position-dependent systems with periodic tasks, multirate systems, and periodic, non-equidistantly sampled systems. System inversion is essential for tracking control applications, including feedforward and learning control. Perfect tracking of reference trajectories can be obtained via stable inversion. The stable inversion approach is based on a dichotomy of the system into a stable and unstable part. Such a dichotomy always exists for LTI systems (under mild conditions). In this chapter, it is shown that such a dichotomy may not exist for general LTV systems, hampering the use of stable inversion.

By exploiting the periodicity, a dichotomy for LPTV systems is established. In fact, there always exists a dichotomy for LPTV systems, under similar mild conditions as for LTI systems. In this chapter, this dichotomy is exploited to develop a stable inversion approach for LPTV systems, enabling perfect tracking of

general reference trajectories. The approach is demonstrated for reversible systems, in feedforward and learning control, and for position-dependent systems. For reversible systems, the stable inversion approach simplifies considerably. An overview of the complete approach can be found in Figure 4.4.

The presented stable inversion for LPTV systems enables feedforward and learning control design for an important class of systems.

The performance of stable inversion strongly depends on the amount of preview, as also observed in Section 4.7. Future research related to this focuses on the role of preview and in particular on deriving bounds similar as for the LTI case (Middleton et al., 2004). From a broader perspective, future research focuses on exploiting the structure associated with LPTV systems in general feedforward and ILC techniques, and their connection to zeros of such systems, see also, e.g., Zamani et al. (2016).

4.A Proof of Theorem 4.5

Proof. If Ψ has no eigenvalues on the unit circle, so does $\tilde{\Psi}$ and an exponential dichotomy exists. Let (4.11) be satisfied, then the autonomous system

$$\tilde{x}[k+1] = \tilde{\Psi}\tilde{x}[k] \tag{4.32}$$

has fundamental matrix solution

$$\tilde{X}[k] = \tilde{\Psi}^k = \begin{bmatrix} \tilde{\Psi}_s^k & 0 \\ 0 & \tilde{\Psi}_u^k \end{bmatrix}. \tag{4.33}$$

Since $|\lambda_i(\tilde{\Psi}_s)| < 1$, for all i, there exist constants $K_s > 0$ and $0 < p_s < 1$ such that

$$\|\tilde{\Psi}_s^k\| \leq K_s p_s^k. \tag{4.34}$$

Similarly, since $|\lambda_i(\tilde{\Psi}_u)| > 1$, for all i, there exist constants $K_u > 0$ and $0 < p_u < 1$ such that

$$\|\tilde{\Psi}_u^k\| \leq K_u p_u^{-k}. \tag{4.35}$$

Consequently, for

$$P = \begin{bmatrix} I_s & 0 \\ 0 & 0 \end{bmatrix}, \tag{4.36}$$

with I_s the identity matrix of size $\tilde{\Psi}_s$, it follows

$$\left\|X[n]PX^{-1}[m]\right\| \leq K_s p_s^{n-m}, \quad n \geq m, \tag{4.37}$$

$$\left\|X[n](I-P)X^{-1}[m]\right\| \leq K_u p_u^{m-n}, \quad m \geq n. \tag{4.38}$$

Hence, system (4.32) with $\tilde{\Psi}$ in (4.11) satisfies an exponential dichotomy according to Definition 4.1 for $K = \max\{K_s, K_u\}$, $p = \max\{p_s, p_u\}$, and P in (4.36). □

4.B Proof of Theorem 4.6

Proof. The transformed system $\tilde{F}$ has monodromy matrix $\tilde{\Psi} = \tilde{A}[\tau - 1]\tilde{A}[\tau - 2] \cdots \tilde{A}[0] = T^{-1}[\tau]\Psi T[0]$. For τ-periodic $T[k]$, it holds $T[\tau] = T[0]$ and hence $\tilde{\Psi} = T^{-1}[0]\Psi T[0]$. By selecting $T[0]$ as generalized eigenvectors of Ψ, condition (4.11) can be satisfied by proper ordering of the eigenvectors. It then directly follows from Theorem 4.5 that $\tilde{F}$ satisfies an exponential dichotomy according to Definition 4.1. □

4.C Proof of Lemma 4.9

For transformation $T[k]$ in (4.12), it follows using (4.6) that

$$\tilde{A}[k] = T^{-1}[k+1]A[k]T[k] \tag{4.39a}$$

$$= \left(A[k]T[k]\hat{A}^{-1}\right)^{-1} A[k]T[k] \tag{4.39b}$$

$$= \hat{A}\left(A[k]T[k]\right)^{-1}\left(A[k]T[k]\right) \tag{4.39c}$$

$$= \hat{A} \tag{4.39d}$$

for all k. Periodicity of $T[k]$ can be shown by successive substitution:

$$T_\tau = (A[\tau - 1]A[\tau - 2] \ldots A[0])T[0]\hat{A}^{-\tau} \tag{4.40a}$$

$$= \Psi T[0]\left(\left(T^{-1}[0]\Psi T[0]\right)^{\frac{1}{\tau}}\right)^{-\tau} \tag{4.40b}$$

$$= \Psi T[0]\left(T^{-1}[0]\Psi T[0]\right)^{-1} \tag{4.40c}$$

$$= \Psi T[0]T^{-1}[0]\Psi^{-1}T[0] \tag{4.40d}$$

$$= T[0]. \tag{4.40e}$$

Combining this result with (4.12) shows that $T[k]$ is periodic with period τ. Note that $\hat{A}^{-1}$ should exist, which is directly satisfied if $T[0]$ and Ψ are invertible. Indeed, the reversibility condition ensures $A[k]$, for all k, and thereby Ψ in (4.10) are invertible.

4.D Proof of Theorem 4.10

Proof. Lemma 4.9 yields $\tilde{A}[k] = \hat{A}$, for all k, such that by (4.11) it follows that $\tilde{\Psi} = \hat{A}^\tau = T^{-1}[0]\Psi T[0]$, for $\hat{A}$ in (4.13). With $T[0]$ given by Theorem 4.6, $\tilde{F}$

satisfies an exponential dichotomy. Moreover, condition (4.11) is satisfied and hence

$$\hat{A} = \tilde{\Psi}^{\frac{1}{\tau}} = \begin{bmatrix} \tilde{\Psi}_s^{\frac{1}{\tau}} & 0 \\ 0 & \tilde{\Psi}_u^{\frac{1}{\tau}} \end{bmatrix}, \tag{4.41}$$

which shows that the unstable and stable parts are separated. □

4.E Proof of Theorem 4.12

Proof. From (4.15a) and (4.15b) follows that there is an affine relation between x_s and x_u. Let this relation be given by (4.17b) for some $S[k], g[k]$. Substituting (4.17b) in (4.15a) yields (4.17a) which can be solved forward in time with $x_s[k_s] = 0$. Eliminating x_u from (4.15b) using (4.17b), substituting (4.17a), and rearranging terms yields

$$\begin{aligned} &S[k+1]x_s[k+1] + g[k+1] = \\ &\qquad A_{us}[k]x_s[k] + A_{uu}[k](S[k]x_s[k] + g[k]) + B_u[k]r[k], \end{aligned} \tag{4.42a}$$

$$\begin{aligned} &S[k+1]\big((A_{ss}[k] + A_{su}[k]S[k])x_s[k] + B_s[k]r[k] + A_{su}[k]g[k]\big) \\ &\quad + g[k+1] = \\ &\qquad A_{us}[k]x_s[k] + A_{uu}[k](S[k]x_s[k] + g[k]) + B_u[k]r[k], \end{aligned} \tag{4.42b}$$

$$\begin{aligned} &\big(S[k+1]A_{ss}[k] + S[k+1]A_{su}[k]S[k] - A_{us}[k] - A_{uu}[k]S[k]\big)x_s[k] = \\ &\qquad - S[k+1]B_s[k]r[k] - S[k+1]A_{su}[k]g[k] - g[k+1] \\ &\qquad + A_{uu}[k]g[k] + B_u[k]r[k], \end{aligned} \tag{4.42c}$$

which is of the form $\mathcal{A}[k]x_s[k] = \mathcal{B}[k]$. Since it holds for all $x_s[k]$, it follows that $\mathcal{A}[k] = 0$, for all k, which yields (4.17c), and $\mathcal{B}[k] = 0$, for all k, which yields (4.17d). Next, (4.17c) and (4.17d) are solved backward in time for some $S[k_e]$ and $g[k_e]$, respectively. Here, $S[k_e] = 0$ and $g[k_e] = 0$ are selected. □

Chapter 5

Discrete-time system inversion for intersample performance

Discrete-time system inversion for perfect tracking goes at the expense of intersample behavior. The aim of this chapter is the development of a discrete-time inversion approach that improves continuous-time performance by also addressing the intersample behavior. The proposed approach balances the on-sample and intersample behavior and provides a whole range of new solutions, with stable inversion and multirate inversion as special cases. Note that multirate inversion refers to using multirate techniques for inversion and differs from multirate control in Chapter 5. The approach is successfully applied to an LTI and an LPTV motion system. The proposed approach improves the intersample behavior through discrete-time system inversion and constitutes Contribution III.B.

5.1 Introduction

Physical systems evolve in continuous time and hence their performance is naturally defined in continuous time. Many approaches for tracking control, including inverse model feedforward and iterative learning control (ILC), are based on system inversion, see, for example Butterworth et al. (2012); Clayton et al. (2009); Kim and Zou (2013). For continuous-time systems, system inversion approaches such as, for example, Devasia et al. (1996) can be used. However, since

The contents of this chapter also appear in:
Jurgen van Zundert, Wataru Ohnishi, Hiroshi Fujimoto, and Tom Oomen. Improving Intersample Behavior in Discrete-Time System Inversion: With Application to LTI and LPTV Systems. *Submitted for journal publication*, 2018.

controllers are often implemented in a digital environment (Chen and Francis, 1995), discrete-time control is often used.

One of the main challenges in system inversion is nonminimum-phase behavior. Causal inversion of nonminimum-phase systems yields unbounded signals. To avoid unbounded signals, many discrete-time inversion approaches have been proposed, see, e.g., Chapter 3 for an overview. Approximate inversion approaches such as ZPETC, ZMETC, and NPZ-Ignore (Butterworth et al., 2012) are well-known, but yield limited performance due to the approximation. Optimal approaches, such as norm-optimal feedforward, $\mathcal{H}_2$-preview control, and $\mathcal{H}_\infty$-preview control (Section 3.4.3; Section 3.4.4), yield high performance in discrete time. Discrete-time stable inversion (Section 3.4.2) yields exact tracking at the discrete-time samples.

Discrete-time inversion approaches focus on the on-sample performance, i.e., at the discrete-time samples, resulting in poor intersample behavior, i.e., in between the samples. This holds in particular for zeros close to $z = -1$ (Moore et al., 1993), see, e.g., Oomen et al. (2009); Butterworth et al. (2008). As a consequence, the continuous-time behavior is poor. Indeed, the best on-sample performance does not necessarily lead to the best continuous-time performance.

Multirate inversion (Ohnishi et al., 2017; Ohnishi and Fujimoto, 2018; Fujimoto et al., 2001) provides an interesting alternative to improve intersample behavior by sacrificing on-sample performance. However, the approach does not take into account the system dynamics when balancing the intersample and on-sample performance. As a consequence, the continuous-time performance is generally suboptimal.

Although many discrete-time inversion approaches exist, the balance between on-sample performance and intersample behavior is not optimized. The main contribution of this chapter is a discrete-time inversion approach that finds the optimal balance between on-sample performance and intersample behavior for the purpose of continuous-time performance. The stable inversion and multirate inversion approaches are recovered as special cases. Related work includes Chen and Francis (1995); Yamamoto (1994); Bamieh and Pearson Jr. (1992) where synthesis-based approaches are presented. In contrast, the approach presented in this chapter does not require synthesis.

The outline of this chapter is as follows. In Section 5.2, the control objective is formulated. The concept of the proposed approach is presented in Section 5.3. Key ingredients to the approach are presented in Section 5.4 and Section 5.5. Based on these results, the approach is presented in Section 5.6. The advantages of the approach are demonstrated by application to an LTI motion system in Section 5.7 and to an LPTV motion system in Section 5.8. Conclusions are presented in Section 5.9.

Notation. For notational convenience, single-input, single-output (SISO) systems are considered. The results can directly be generalized to square multivariable systems. Let $s^{(i)} \triangleq \frac{\mathrm{d}^i}{\mathrm{d}t^i} s$ denote the ith time-derivative of s, ρ the

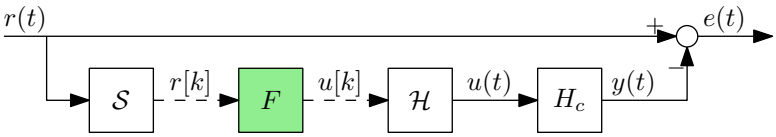

Figure 5.1. Tracking control diagram with continuous-time system H_c, sampler $\mathcal{S}$, and hold $\mathcal{H}$. Given continuous-time reference trajectory $r(t)$, the objective is to minimize continuous-time error $e(t)$ through design of discrete-time controller F, while control input $u[k]$ remains bounded.

Heaviside operator, $\mathcal{B}(\cdot)$ a bilinear transformation, and $\mathbb{R}^b_{>a} = \{x \in \mathbb{R}^b \mid x[k] > a \text{ for all } k = 0, 1, \ldots, b-1\}$. Let $\Sigma \overset{z}{=} (A, B, C, D)$ be a state-space model and define $\mathcal{T}(\Sigma, T) \overset{z}{=} (TAT^{-1}, TB, CT^{-1}, D)$.

5.2 Problem formulation

In this section, the control problem is formulated. The considered tracking control configuration is shown in Figure 5.1, with reference trajectory $r(t) \in \mathbb{R}$, control input $u(t) \in \mathbb{R}$, output $y(t) \in \mathbb{R}$, digital controller F, sampler $\mathcal{S}$, and zero-order hold $\mathcal{H}$. The continuous-time, linear time-invariant (LTI) system H_c is given by

$$\dot{x}(t) = A_c x(t) + B_c u(t), \tag{5.1a}$$
$$y(t) = C_c x(t), \tag{5.1b}$$

with $x(t) \in \mathbb{R}^n$, $n \in \mathbb{N}$ and can be either an open-loop or closed-loop system.

Conventional discrete-time control focuses on the on-sample performance. The discrete-time system $H = \mathcal{S} H_c \mathcal{H}$ with H_c in (5.1) and sampling time δ is given by

$$x[k+1] = Ax[k] + Bu[k], \tag{5.2a}$$
$$y[k] = Cx[k], \tag{5.2b}$$

with

$$A = e^{A_c \delta}, \qquad B = \int_0^\delta e^{A_c \tau} B_c \, \mathrm{d}\tau, \qquad C = C_c. \tag{5.2c}$$

In this setting, perfect on-sample tracking, i.e., $e[k] = 0$, for all k, is achieved for $F = H^{-1}$. However, this does not provide any guarantees for the intersample performance $e(t)$, $t \neq k\delta$. Hence, the continuous-time performance in terms of $e(t)$, for all t, may be poor as observed in, e.g., Oomen et al. (2009).

The control objective considered in this chapter is to minimize the continuous-time error $e(t)$. Note that this includes both on-sample ($t = k\delta$) and

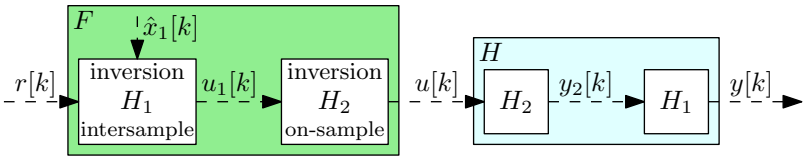

Figure 5.2. The discrete-time system H is decomposed into H_1 and H_2. System H_1 is inverted such that there is exact state tracking of the desired state $\hat{x}_1[k]$ every n_1 samples for the purpose of intersample behavior. System H_2 is inverted such that there is exact output tracking every sample for the purpose of on-sample behavior.

intersample ($t \neq k\delta$) performance. Importantly, $u[k]$ should remain bounded, even in the presence of nonminimum-phase behavior. Trajectory $r(t)$ is assumed to be known a priori.

In the next section, the concept of the proposed approach is presented.

5.3 Inversion for on-sample and intersample behavior

In the proposed approach, the system is decomposed into two parts and both parts are inverted separately as illustrated in Figure 5.2, where H is decomposed as $H = H_1H_2$. The inversion of system H_1 aims at the intersample behavior. More specific, let n_1 be the state dimension of H_1, then H_1 is inverted such that there is exact state tracking of a desired state $\hat{x}_1[k]$ every n_1 samples. The inversion of H_2 aims at the on-sample behavior through perfect output tracking for every sample.

Exact state tracking is experienced to yield good intersample behavior in multirate inversion (Ohnishi et al., 2017), whereas exact output tracking yields good on-sample behavior in stable inversion, see Chapter 3. Hence, the choice of the decomposition into H_1 and H_2 can be used to balance the on-sample behavior and the intersample behavior to the benefit of the continuous-time performance. The idea is conceptually illustrated in Figure 5.3. An important observation is that a small on-sample error does not necessarily yield a small continuous-time error. The figure shows that the approach provides a whole range of solutions that were non-existing before. The stable inversion and multirate inversion solution are recovered as the two extreme cases, see also Section 5.6.3.

The proposed approach requires the decomposition $H = H_1H_2$ in terms of state-space realizations and the desired state $\hat{x}_1[k]$ for H_1, see also Figure 5.2. In Section 5.4, the desired state for the continuous-time system H_c is presented. In Section 5.5, the state-space decomposition $H = H_1H_2$ is presented. Based on these results, the complete approach is presented in Section 5.6.

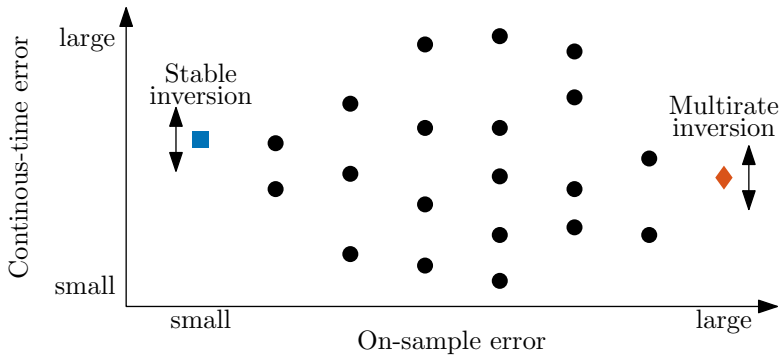

Figure 5.3. Qualitative plot of the continuous-time versus on-sample error. The proposed approach balances the intersample behavior and the on-sample behavior for the purpose of continuous-time performance. It provides a whole range of solutions that were non-existing before. Importantly, the smallest on-sample error does not necessarily yield the smallest continuous-time error as the intersample behavior may be poor. The relative performance depends on the particular settings, e.g., the system dynamics, and may vary. Stable inversion (■) and multirate inversion (♦) are recovered as special cases.

5.4 Desired state for continuous-time system

In this section, the desired state for the continuous-time system is presented. Given a continuous-time reference trajectory $r(t)$ together with its $n-1$ time derivatives and system H_c in (5.1), the objective is to determine a bounded state $\hat{x}(t)$ such that $y(t) = C_c\hat{x}(t)$ yields $y^{(i)}(t) = r^{(i)}(t)$, $i = 0, 1, \ldots, n-1$, where $(\cdot)^{(i)}$ denotes the ith time derivative of $(\cdot)$, i.e., such that $\bar{r}(t) = \bar{y}(t)$ where

$$\bar{r}(t) = \begin{bmatrix} r^{(0)}(t) \\ r^{(1)}(t) \\ \vdots \\ r^{(n-1)}(t) \end{bmatrix}, \qquad \bar{y}(t) = \begin{bmatrix} y^{(0)}(t) \\ y^{(1)}(t) \\ \vdots \\ y^{(n-1)}(t) \end{bmatrix}. \tag{5.3}$$

A similar approach as in Ohnishi and Fujimoto (2016a) is used based on the controllable canonical form given by Lemma 5.1, see also Goodwin et al. (2000, Section 17.6). The desired state is given by Theorem 5.2.

Lemma 5.1 (Controllable canonical form)**.** *Let the transfer function of H_c in* (5.1) *be given by*

$$H_c(s) = C_c(sI - A_c)^{-1}B_c = \frac{B(s)}{A(s)}, \tag{5.4a}$$

with

$$A(s) = \frac{s^n + a_{n-1}s^{n-1} + \ldots + a_0}{b_0}, \tag{5.4b}$$

$$B(s) = \frac{b_m s^m + b_{m-1}s^{m-1} + \ldots + b_0}{b_0}, \tag{5.4c}$$

$b_0 \neq 0$, *then the controllable canonical form* $H_{ccf}(s) = \mathcal{T}(H_c, T_{ccf})$ *is given by*

$$\dot{x}_{ccf}(t) = A_{ccf}x_{ccf}(t) + B_{ccf}u(t), \tag{5.5a}$$

$$y(t) = C_{ccf}x_{ccf}(t), \tag{5.5b}$$

where

$$\left[\begin{array}{c|c} A_{ccf} & B_{ccf} \\ \hline C_{ccf} & \end{array}\right] = \left[\begin{array}{ccccc|c} 0 & 1 & 0 & \cdots & 0 & 0 \\ 0 & 0 & 1 & \cdots & 0 & 0 \\ \vdots & \vdots & \vdots & \ddots & \vdots & \vdots \\ 0 & 0 & 0 & \cdots & 1 & 0 \\ -a_0 & -a_1 & -a_2 & \cdots & -a_{n-1} & b_0 \\ \hline 1 & \frac{b_1}{b_0} & \frac{b_2}{b_0} & \cdots & 0 & \end{array}\right] \tag{5.5c}$$

and

$$T_{ccf}^{-1} = \begin{bmatrix} B_c & A_cB_c & \cdots & A_c^{n-1}B_c \end{bmatrix} \begin{bmatrix} \frac{a_1}{b_0} & \frac{a_2}{b_0} & \cdots & \frac{1}{b_0} \\ \frac{a_2}{b_0} & \frac{a_3}{b_0} & \iddots & 0 \\ \vdots & \iddots & \iddots & \vdots \\ \frac{1}{b_0} & 0 & \cdots & 0 \end{bmatrix}. \tag{5.6}$$

Theorem 5.2 (Desired continuous-time state)**.** *Let* $B^{-1}(s)$ *in* (5.4) *be decomposed as*

$$B^{-1}(s) = F_s(s) + F_u(s), \tag{5.7}$$

with all poles $p_s \in \mathbb{C}$ *of* $F_s(s)$ *such that* $\Re(p_s) < 0$ *and all poles* $p_u \in \mathbb{C}$ *of* $F_u(s)$ *such that* $\Re(p_u) > 0$. *Let*

$$f_s(t) = \mathcal{L}^{-1}(F_s(s)), \qquad f_u(t) = \mathcal{L}^{-1}(F_u(-s)), \tag{5.8a}$$

$$\hat{x}_{ccf,s}(t) = \int_{-\infty}^{t} f_s(t-\tau)\bar{r}(\tau)\, d\tau, \tag{5.8b}$$

$$\hat{x}_{ccf,u}(t) = \int_{t}^{\infty} f_u(t-\tau)\bar{r}(\tau)\, d\tau, \tag{5.8c}$$

where $\mathcal{L}^{-1}(\cdot)$ *is the inverse uni-lateral Laplace transform (Oppenheim et al., 1997, Section 9.3). Let* H_c *in* (5.4) *have realization* (5.5), *then* $y(t) = C_c\hat{x}(t)$ *where*

$$\hat{x}(t) = T_{ccf}^{-1}(\hat{x}_{ccf,s}(t) + \hat{x}_{ccf,u}(t)), \tag{5.9}$$

is bounded and such that $\bar{y}(t) = \bar{r}(t)$, *with* $\bar{y}(t), \bar{r}(t)$ *in* (5.3).

Proof. See Appendix 5.A. □

Theorem 5.2 provides the desired bounded state for optimal state tracking. Together with the state-space decomposition presented in the next section, Theorem 5.2 forms the basis of the proposed approach presented in Section 5.6.

Remark 5.3. *If poles of $B^{-1}(s)$ have $\Re(p) = 0$, i.e., $B^{-1}(s)$ is non-hyperbolic, similar techniques as in Devasia (1997a) can be used.*

5.5 State-space decomposition

In this section, the multiplicative state-space decomposition is presented. Together with Theorem 5.2, the decomposition forms the basis of the proposed approach in Section 5.6.

Given the state-space system H in (5.2), the interest is in minimal realizations H_1, H_2 such that $H = H_1 H_2$ in terms of state-space realization, where the zeros and poles of H can be arbitrarily assigned to H_1 or H_2. The starting point is the multiplicative decomposition $H = H_1 H_2$ in terms of transfer functions as given by Lemma 5.4.

Lemma 5.4 (Transfer function decomposition)**.** *Let $H \overset{z}{=} (A, B, C, D)$ be a state-space realization with n states and invertible D. Let $V \in \mathbb{R}^{n \times n_1}$ be a column space of an invariant subspace of A and let $V_\times \in \mathbb{R}^{n \times n_2}$ be a column space of an invariant subspace of $A_\times = A - BD^{-1}C$, such that $S = \begin{bmatrix} V & V_\times \end{bmatrix}$ has full rank $n = n_1 + n_2$. Let*

$$\Pi = S \begin{bmatrix} I_{n_1} & 0_{n_1 \times n_2} \\ 0_{n_2 \times n_1} & 0_{n_2 \times n_2} \end{bmatrix} S^{-1}. \tag{5.10}$$

Then, the realizations

$$H_{1f} \overset{z}{=} \left[\begin{array}{c|c} A & \Pi B D^{-1} \\ \hline C & I \end{array}\right], \qquad H_{2f} \overset{z}{=} \left[\begin{array}{c|c} A & B \\ \hline C(I - \Pi) & D \end{array}\right] \tag{5.11}$$

are such that $H = H_{1f} H_{2f}$ in terms of transfer functions, i.e., $C(zI - A)^{-1}B + D = (C(zI - A)^{-1}\Pi B D^{-1} + I)(C(I - \Pi)(zI - A)^{-1}B + D)$.

Proof. Follows directly from extending Bart et al. (2005, Corrollary 11) to $D \neq I$. □

If the D matrix in Theorem 5.5 is singular, a bilinear transformation (Chen and Francis, 1995, Section 3.4; Oppenheim et al., 1997, Section 10.8.3) can possibly be employed to obtain an equivalent system with non-singular D matrix. A multiplicative decomposition for the transformed system is obtained through Lemma 5.4. Applying the inverse transformation on the decomposed system yields the decomposition for the original system since $\mathcal{B}(H_1 H_2) = \mathcal{B}(H_1)\mathcal{B}(H_2)$.

Importantly, Lemma 5.4 guarantees equivalence in terms of transfer functions, but not in terms of state-space realizations. Indeed, the decomposition of Lemma 5.4 yields nonminimal realizations of H_{1f}, H_{2f} as both have state dimension n. By exploiting the modal form and using a suitable state transformation, the desired state-space decomposition for the proposed approach is obtained as given by Theorem 5.5.

Theorem 5.5 (State-space decomposition)**.** *Let $T_{mod} \in \mathbb{C}^{n\times n}$ be such that $H_{mod} = \mathcal{T}(H, T_{mod}) = (A, B, C, D)$ is in modal form (Franklin et al., 2015, Section 7.4) with nonsingular D. Let $H_{1f}H_{2f} = H_{mod}$ be the decomposition given by Lemma 5.4. Let $T_{per} \in \mathbb{R}^{n\times n}$ be such that*

$$\mathcal{T}(H_{1f}, T_{per}) \overset{z}{=} \left[\begin{array}{cc|c} A_1 & 0 & B_1 \\ 0 & A_2 & 0 \\ \hline C_1 & C_{1r} & I \end{array}\right], \tag{5.12}$$

$$\mathcal{T}(H_{2f}, T_{per}) \overset{z}{=} \left[\begin{array}{cc|c} A_1 & 0 & B_{2r} \\ 0 & A_2 & B_2 \\ \hline 0 & C_2 & D \end{array}\right], \tag{5.13}$$

with $A_1 \in \mathbb{R}^{n_1\times n_1}$, $A_2 \in \mathbb{R}^{n_2\times n_2}$, $n_1 + n_2 = n$, and define

$$H_1 \overset{z}{=} \left[\begin{array}{c|c} A_1 & B_1 \\ \hline C_1 & I \end{array}\right], \qquad H_2 \overset{z}{=} \left[\begin{array}{c|c} A_2 & B_2 \\ \hline C_2 & D \end{array}\right]. \tag{5.14}$$

Furthermore, let $X \in \mathbb{R}^{n_1\times n_2}$ satisfy

$$A_1X - XA_2 = B_1C_2. \tag{5.15}$$

Then, the state-space realization of $\mathcal{T}(H_1H_2, T_{per}^{-1}T_{12})$ with

$$T_{12} = \begin{bmatrix} I_{n_1} & X \\ 0_{n_1\times n_2} & I_{n_2} \end{bmatrix}, \tag{5.16}$$

is identical to that of H_{mod}.

Proof. See Appendix 5.B. □

Theorem 5.5 yields a state-space decomposition $H = H_1H_2$ with identical state-space realizations. Note that such a decomposition always exists. Together with Theorem 5.2, Theorem 5.5 forms the basis for the proposed approach presented in the next section.

Remark 5.6. *Note that V in Lemma 5.4 is related to the poles of H, whereas $V_\times$ is related to the zeros of H. Hence, the selection of $V, V_\times$ enables to assign the poles and zeros to either H_1 or H_2.*

Remark 5.7. *The column spaces of the invariant subspaces in Lemma 5.4 can be constructed from eigenvectors. Note that for complex eigenvectors, the real and imaginary part should be used. For eigenvalues with multiplicity larger than* 1*, generalized eigenvectors obtained from the Jordan form can be used to ensure* S *has full rank.*

Remark 5.8. *Sylvester equation* (5.15) *has a unique solution* X *if the eigenvalues of* A_1 *and* $-A_2$ *are distinct (Bartels and Stewart, 1972).*

5.6 Approach

In the previous sections, preliminary results on the desired state and the state-space decomposition are presented. Based on these results, the proposed approach is presented in this section. First, the approach for LTI systems is presented. Second, the approach for LPTV systems is presented. Finally, special cases are recovered.

5.6.1 Approach for LTI systems

The proposed approach consists of two steps. First, stable inversion is applied to H_2 in (5.14) to obtain u such that $y_2[k] = u_1[k]$, for all k, see also Figure 5.2. The solution is given by Theorem 5.9 and provides exact output tracking every sample. See Section 3.4.2 for a proof.

Theorem 5.9 (Inversion of H_2)**.** *Consider Figure 5.2 and let* H_2^{-1} *be given by*

$$\begin{bmatrix} x_s[k+1] \\ x_u[k+1] \end{bmatrix} = \begin{bmatrix} A_s & 0 \\ 0 & A_u \end{bmatrix} \begin{bmatrix} x_s[k] \\ x_u[k] \end{bmatrix} + \begin{bmatrix} B_s \\ B_u \end{bmatrix} u_1[k], \tag{5.17a}$$

$$u[k] = \begin{bmatrix} C_s & C_u \end{bmatrix} \begin{bmatrix} x_s[k] \\ x_u[k] \end{bmatrix} + Du_1[k], \tag{5.17b}$$

with $|\lambda(A_s)| < 1$ *and* $|\lambda(A_u)| > 1$*. Then,* $y_2[k] = u_1[k]$*, for all* k*, if*

$$u[k] = C_s x_s[k] + C_u x_u[k] + Du_1[k], \tag{5.18}$$

which is bounded for bounded u_1*, where* x_s *follows from solving*

$$x_s[k+1] = A_s x_s[k] + B_s u_1[k], \quad x_s[-\infty] = 0 \tag{5.19}$$

forward in time and x_u *follows from solving*

$$x_u[k+1] = A_u x_u[k] + B_u u_1[k], \quad x_u[\infty] = 0 \tag{5.20}$$

backward in time.

If u_1 is bounded, u in Theorem 5.9 is bounded by construction of x_s, x_u, even if H_2 is nonminimum phase. The stable inversion solution in Theorem 5.9 achieves exact output tracking every sample and has infinite preactuation. Regular causal inversion is recovered as special case if the system is minimum phase, i.e., x_u is non-existing, see also Chapter 3.

Second, multirate inversion is applied to H_1 in (5.14) to obtain u_1. Note that by Theorem 5.9, $y_2[k] = u_1[k]$, for all k. The solution is based on lifting the state equation over n_1 samples. The solution is given by Theorem 5.10 and provides exact state tracking every n_1 samples.

Theorem 5.10 (Inversion of H_1)**.** *Consider Figure 5.2 with $y_2[k] = u_1[k]$, for all k, and let $\hat{x}_1$ be the desired state for system H_1 in* (5.14)*. Consider the state equation lifted over τ samples given by*

$$\underline{x}_1[q+1] = \underline{A}_1\, \underline{x}_1[q] + \underline{B}_1\, \underline{u}_1[q], \tag{5.21}$$

with $\underline{u}_1[q] = \begin{bmatrix} u_1[kn_1] & u_1[kn_1{+}1] & \dots & u_1[(k{+}1)n_1 - 1] \end{bmatrix}^\top$, $\underline{x}_1[q] = x_1[kn_1]$, $\underline{A}_1 = A_1^{n_1}$, *and* $\underline{B}_1 = \begin{bmatrix} A_1^{n_1-1}B_1 & A_1^{n_1-2}B_1 & \dots & B_1 \end{bmatrix}$. *Then,* $\underline{x}_1[q] = \underline{\hat{x}}_1[q]$, *for all q, if*

$$\underline{u}_1[q] = \underline{B}_1^{-1}\left(\underline{\hat{x}}_1[q+1] - \underline{A}_1\, \underline{\hat{x}}_1[q]\right), \tag{5.22}$$

which is bounded for bounded $\hat{x}_1$.

Proof. See Ohnishi et al. (2017, Section 3.3). □

Importantly, the inversion approach in Theorem 5.10 is based on the continuous-time system H_c, rather than the discrete-time system H. The approach yields exact state tracking, and hence exact output tracking, every n_1 samples and has n_1 samples preactuation. Note that u_1 is bounded if $\hat{x}_1$ is bounded, even if H_1 is nonminimum phase. More details can be found in, for example, Ohnishi et al. (2017); Fujimoto et al. (2001). The desired state $\hat{x}_1$ in Theorem 5.10 is obtained by Procedure 5.11 which follows from Section 5.4 and Section 5.5.

Procedure 5.11 (Desired state of H_1)**.** *Given H_c in* (5.5)*, H in* (5.2)*, and the decomposition $H = H_1H_2$ in Theorem 5.5, the following steps yields the desired state $\hat{x}_1[k]$ in Theorem 5.10.*

1. *Obtain the controllable canonical form $H_{ccf} = \mathcal{T}(H_c, T_{ccf})$ according to Lemma 5.1.*
2. *Obtain the desired state $\hat{x}(t)$ of H_c using Theorem 5.2.*
3. *Set the desired state of H to $\hat{x}[k] = \hat{x}(k\delta)$.*
4. *Obtain the desired state of H_{mod}: $\hat{x}_{mod}[k] = T_{mod}\hat{x}[k]$, with H_{mod}, T_{mod} in Theorem 5.5.*

5. *Given* H_1, H_2 *in* (5.14), *let*

$$H_{12} = H_1 H_2 \stackrel{z}{=} \left[\begin{array}{cc|c} A_1 & B_1C_2 & B_1D_2 \\ 0 & A_2 & B_2 \\ \hline C_1 & D_1C_2 & D_1D_2 \end{array}\right]. \tag{5.23}$$

6. *Obtain the desired state of* H_{12}*:* $\hat{x}_{12}[k] = T_{12}^{-1} T_{per} \hat{x}_{mod}[k]$*, with* T_{12} *in* (5.16) *and* T_{per} *satisfying* (5.12) *and* (5.13).

7. *Obtain the desired state for* H_1*:* $\hat{x}_1[k] = \begin{bmatrix} I_{n_1} & 0_{n_1 \times n_2} \end{bmatrix} \hat{x}_{12}[k]$.

The combination of the inversion of H_2 in Theorem 5.9 and the inversion of H_1 in Theorem 5.10 constitutes the control input u in Figure 5.2, which is bounded by design, also for nonminimum-phase systems. The design freedom is in the decomposition of H into H_1 and H_2 in Theorem 5.5. Equation (5.23) shows that the output is given by $y[k] = C_1x_1[k] + D_1C_2x_2[k]$ since either $D_1 = 0$ or $D_2 = 0$ as $D = 0$ in (5.2). If $D_1 = 0$, $y[k] = C_1x_1[k]$ and since inversion of H_1 in Theorem 5.9 ensures tracking of x_1 every n_1 samples, there is perfect output tracking every n_1 samples. If $D_1 \neq 0$, $y[k]$ also depends on $x_2[k]$ of H_2 and since inversion of H_2 in Theorem 5.10 does not provide perfect state tracking, there is no perfect output tracking for y every n_1 samples. Hence, to guarantee exact on-sample tracking every n_1 samples, $V, V_\times$ in Theorem 5.5 are preferably chosen such that $D_1 = 0$.

In summary, input $u[k]$ in Figure 5.1 that minimizes $e(t)$, in terms of both the intersample and on-sample behavior, is obtained by decomposing H as in Figure 5.2 using Theorem 5.5, followed by inversion of H_2 using Theorem 5.9 and inversion of H_1 using Theorem 5.10. In the next section, special cases are recovered.

Remark 5.12. *For strictly proper systems* H_2*, Theorem 5.9 can be applied to the bi-proper system* $\bar{H}_2$ *obtained through time shifts* $\bar{H}_2 = z^{d_2} H_2$*, where* d_2 *is the relative degree of* H_2*, see also Remark 3.1. If there are eigenvalues on the unit circle, i.e., there exist* λ_i *such that* $|\lambda_i(A)| = 1$*, then similar techniques as in Devasia (1997a) can be followed.*

Remark 5.13. *The decomposition of* H^{-1} *given by* (5.17) *can be obtained through an eigenvalue decomposition.*

Remark 5.14. *Note that* $\underline{B}_1$ *in Theorem 5.10 is the controllability matrix of* H_1 *and hence* $\underline{B}_1^{-1}$ *exists if* H_1 *is controllable.*

5.6.2 Approach for LPTV systems

In this section, the approach for LPTV systems is presented. Let the LPTV system H with period $\tau \in \mathbb{N}$ be given by

$$x[k+1] = A[k]x[k] + B[k]u[k], \tag{5.24a}$$
$$y[k] = C[k]x[k], \tag{5.24b}$$

with $A[k+\tau] = A[k]$, $B[k+\tau] = B[k]$, $C[k+\tau] = C[k]$, for all k. LPTV systems may result from non-equidistant sampling as in Example 5.15.

Example 5.15 (Non-equidistant sampling)**.** *Let the sampling in Figure 5.1 be non-equidistant in time and given by the sampling sequence $\Delta_{ne} \in \mathbb{R}^{\infty}_{>0}$ with periodicity $\tau \in \mathbb{N}$ defined as*

$$\Delta_{ne} = (\delta_1, \delta_2, \ldots, \delta_\gamma, \delta_1, \delta_2 \ldots), \tag{5.25}$$

with $\delta_i = \gamma_i \delta_b$, $\delta_b \in \mathbb{R}_{>0}$, $\gamma_i \in \mathbb{N}$, $i = 1, 2, \ldots, \tau$. Then, the discretized system $H = \mathcal{S} H_c \mathcal{H}$ is given by (5.24) *with*

$$A[i] = e^{A_c \delta_i}, \tag{5.26a}$$
$$B[i] = \int_0^{\delta_i} e^{A_c \tau} B_c \, d\tau, \qquad i = 1, 2, \ldots, \tau, \tag{5.26b}$$
$$C = C_c, \tag{5.26c}$$

where $A[k+\tau] = A[k], B[k+\tau] = B[k]$, for all k. By linearity of H_c and periodicity of Δ_{ne}, H is LPTV with period τ.

The approach for LPTV systems is similar to that for LTI systems, with the key difference that an additional lifting step is used. The lifting step turns the LPTV system into a (multivariable) LTI system as given by Lemma 5.16.

Lemma 5.16. *Lifting the input of H in* (5.24) *over τ samples yields the LTI system $\underline{H}$ given by*

$$\underline{x}[q+1] = \underline{A}\,\underline{x}[q] + \underline{B}\,\underline{u}[q], \tag{5.27a}$$
$$\underline{y}[q] = \underline{C}\,\underline{x}[q] + \underline{D}\,\underline{u}[q], \tag{5.27b}$$

where

$$\underline{x}[q] = x[k\tau], \tag{5.27c}$$

$$\underline{u}[q] = \begin{bmatrix} u[k\tau] \\ u[k\tau+1] \\ \vdots \\ u[(k+1)\tau-1] \end{bmatrix}, \tag{5.27d}$$

$$\underline{A} = \Phi_{\tau+1,1}, \tag{5.27e}$$

$$\underline{B} = \begin{bmatrix} \Phi_{\tau+1,2}B[1] & \Phi_{\tau+1,3}B[2] & \dots & B[\tau] \end{bmatrix}, \tag{5.27f}$$

$$\underline{C} = \begin{bmatrix} C[1] \\ C[2]\Phi_{2,1} \\ \vdots \\ C[\tau]\Phi_{\tau,1} \end{bmatrix}, \tag{5.27g}$$

$$\underline{D} = \begin{bmatrix} 0 & 0 & \cdots & 0 \\ C[2]B[1] & 0 & \cdots & 0 \\ \vdots & \vdots & \ddots & \vdots \\ C[\tau]\Phi_{\tau,2}B[1] & C[\tau]\Phi_{\tau,3}B[2] & \cdots & 0 \end{bmatrix}, \tag{5.27h}$$

with transition matrix

$$\Phi_{k_2,k_1} = \begin{cases} I, & k_2 = k_1, \\ A[k_2-1]A[k_2-2]\dots A[k_1], & k_2 > k_1. \end{cases} \tag{5.28}$$

For the lifted system $\underline{H}$ in (5.27), the same approach as for the LTI system illustrated in Figure 5.2 is used. The state-space decomposition $\underline{H} = \underline{H}_1\underline{H}_2$ is obtained using Theorem 5.5. System $\underline{H}_2$ is inverted using Theorem 5.9 and $\underline{H}_1$ is inverted using Theorem 5.10, where the desired state $\hat{\underline{x}}_1[q]$ follows along the same lines as in Procedure 5.11. The result is the lifted input signal $\underline{u}[q]$, which, after inverse lifting, yields input $u[k]$, for the LPTV system H in (5.24).

In the previous and present section, the approaches for LTI and LPTV are presented, respectively. Next, special cases are recovered.

5.6.3 Special cases

The proposed approach provides a whole range of solutions as illustrated in Figure 5.3. The stable inversion and multirate inversion solution are recovered as the two extreme cases and given by Corollary 5.17 and Corollary 5.18. The results hold for both LTI and LPTV systems.

Corollary 5.17 (Special case: stable inversion (Section 3.4.2; Chapter 4))**.** *The stable inversion solution for H is recovered from the proposed approach in Section 5.6 as special case when $H = H_2$, i.e., $H_1 = I$ and $n_1 = 0$.*

Corollary 5.18 (Special case: multirate inversion (Ohnishi et al., 2017; Fujimoto et al., 2001))**.** *The multirate inversion solution for H is recovered from the proposed approach in Section 5.6 as special case when $H = H_1$, i.e., $H_2 = I$ and $n_1 = n$.*

Importantly, although Theorem 5.9 yields exact output tracking of H_2 for every sample, the inversion of H_1 does not reduce to conventional multirate inversion of H_1 since the desired state $\hat{x}_1$ depends on the full system H_c and not only on H_1.

Finally, the approach for LTI systems is recovered from that for LPTV systems as given by Corollary 5.19. Indeed, for $\tau = 1$, (5.2) is recovered from (5.24).

Corollary 5.19. *The approach for LTI systems in Section 5.6.1 is recovered as a special case from the approach for LPTV systems in Section 5.6.2 for $\tau = 1$.*

The proposed approach provides a whole range of solutions that were non-existing before, see also Figure 5.3. The advantages of the approach are demonstrated by application to an LTI and an LPTV motion system in Section 5.7 and Section 5.8, respectively.

5.7 Application to an LTI motion system

In this section, the approach proposed in Section 5.6.1 is applied to a motion system. The results demonstrate the potential of the proposed approach.

5.7.1 Setup

The motion system is illustrated in Figure 5.4(a) and based on the benchmark system in Section 3.3. The continuous-time transfer function from input u to output y is given by

$$H_c = \frac{0.3125}{s^2} \frac{s^2 + 15s + 1500}{s^2 + 37.5s + 3750} \tag{5.29}$$

and is minimum phase. The discretized system (5.2) with sampling time $\delta = 0.02$ s has the transfer function

$$H = \frac{5.13 \times 10^{-5}(z + 0.842)}{(z-1)^2} \frac{z^2 - 1.249z + 0.742}{z^2 - 0.5415z + 0.4724} \tag{5.30}$$

and is also minimum phase. The Bode diagrams of H_c and H are shown in Figure 5.4(b). Reference trajectory r is shown in Figure 5.5.

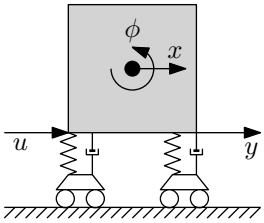

(a) The system is actuated by input force u, can translate in x direction, rotate in ϕ direction, and has output position y.

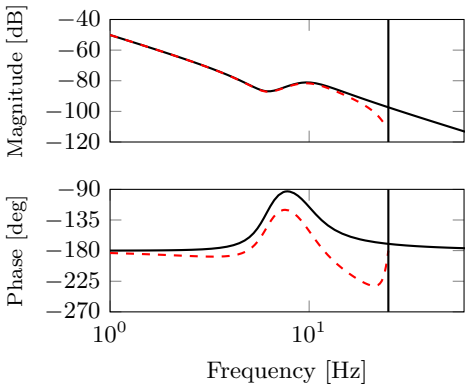

(b) Bode magnitude diagram of the continuous-time system H_c (——) and the discretized system H (- - -) from input u to output y in (a).

Figure 5.4. Motion system used for validation of the proposed approach.

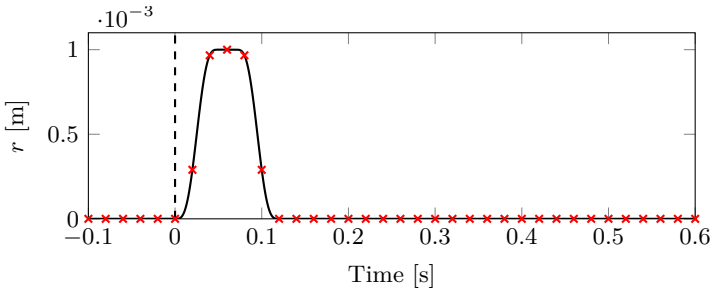

Figure 5.5. The reference trajectory $r(t)$ (——), with discretization $r[k]$ (×). The trajectory consists of a forward and backward movement.

5.7.2 Results

Three different solutions are compared in simulation: the proposed approach with $n_1 = 2$, the special case $n_1 = 0$, i.e., stable inversion in Corollary 5.18, and the special case $n_1 = 4$, i.e., multirate inversion in Corollary 5.17. The error signals for the three approaches are shown in Figure 5.6.

The results in Figure 5.6(a) show that the special case of stable inversion achieves exact tracking every sample, but poor intersample behavior. The results for the special case of multirate inversion in Figure 5.6(b) show good intersample behavior, but moderate on-sample behavior since the solution only yields exact tracking every $n = 4$ samples.

The results of the proposed approach are shown in Figure 5.6(c). The results show good intersample behavior with exact on-sample tracking every $n_1 = 2$ samples. Hence, it outperforms the special case of multirate inversion in terms of on-sample performance. At the same time, it outperforms the special case of stable inversion in terms of intersample performance.

The results demonstrate the potential of the proposed approach on a motion system as it outperforms the existing solutions. Next, the approach is demonstrated on an LPTV motion system.

5.8 Application to an LPTV motion system

In this section, the proposed approach is applied to an LPTV system resulting from non-equidistant sampling of an LTI motion system. The results show that many solutions of the proposed approach outperform the special cases of stable inversion and multirate inversion.

5.8.1 Setup

The considered motion system is the experimental high-precision positioning stage shown in Figure 5.7(a), with model in Figure 5.7(b). The Bode diagram of a frequency response function measurement is shown in Figure 5.7(c). The identified 8th order continuous-time system H_c ($n = 8$ and $m = 4$) is given by

$$\begin{aligned} H_c = &\frac{4.576 \cdot 10^6}{s(s+2.101)(s^2+10.89s+3.665 \cdot 10^4)} \\ &\times \frac{(s^2+8.132s+2.518 \cdot 10^4)(s^2+84.73s+8.497 \cdot 10^5)}{(s^2+45.4s+3.139 \cdot 10^5)(s^2+262.2s+3.507 \cdot 10^6)} \end{aligned} \tag{5.31}$$

and is stable and minimum phase. The Bode diagram of H_c is also shown in Figure 5.7(c).

The non-equidistant sampling sequence, see also Example 5.15, is set to $\gamma_1 = 1$, $\gamma_2 = 2$ ($\tau = 2$), with $\delta_b = 400$ µs. The lifted system $\underline{H}$ in (5.27) has one nonminimum-phase (transmission) zero due to discretization.

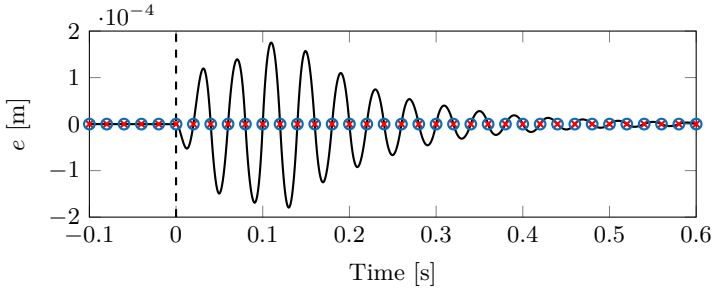

(a) Stable inversion yields exact on-sample tracking every sample (○), but poor intersample behavior (——).

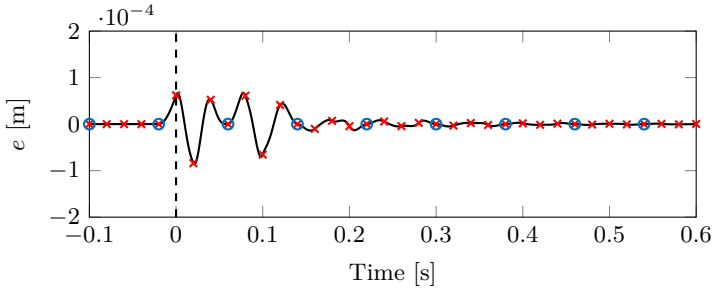

(b) Multirate inversion yields only exact on-sample tracking every $n = 4$ samples (○), but good intersample behavior (——).

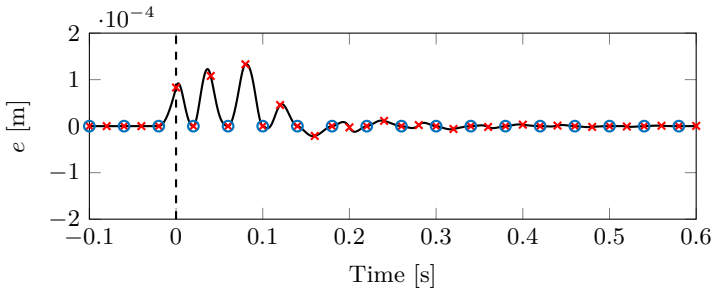

(c) The proposed approach yields exact on-sample tracking every $n_1 = 2$ samples (○) and good intersample behavior (——).

Figure 5.6. Error signals with on-sample error $e[k]$ (×) and continuous-time error $e(t)$ (——).

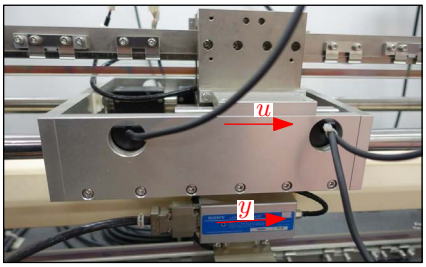

(a) Experimental high-precision positioning stage with input u and output y.

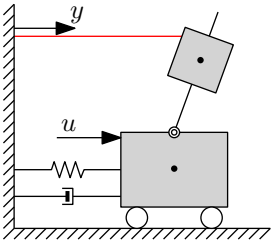

(b) Model of the experimental high-precision positioning in (a).

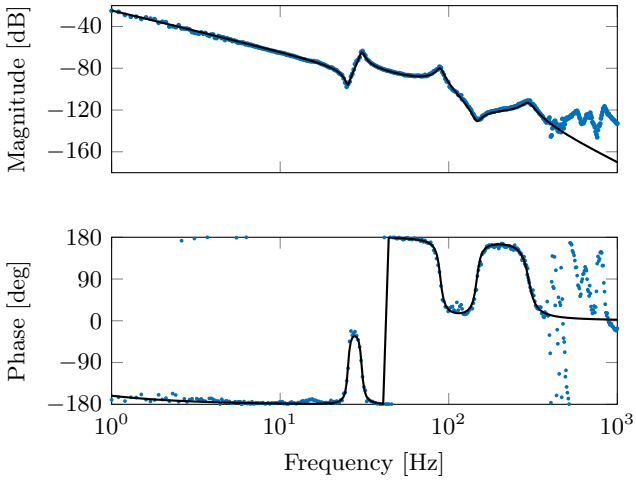

(c) Bode diagram of the frequency response function measurement (●) and identified continuous-time model H_c (——).

Figure 5.7. Motion system (Hara et al., 2008) used for validation of the proposed approach for LPTV systems in Section 5.8.

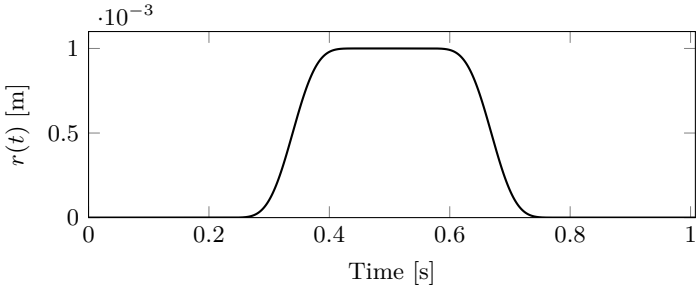

Figure 5.8. Reference trajectory $r(t)$ for the LPTV system in Figure 5.7 consisting of 8th order polynomials in t.

The trajectory $r(t)$ is given by the forward and backward motion shown in Figure 5.8. The profile consists of 8th order polynomials in t.

5.8.2 Simulation results

First, three different solutions are considered: the proposed approach with $n_1 = 4$, the special case $n_1 = 0$, i.e., multirate inversion in Corollary 5.18, and the special case $n_1 = 8$, i.e., stable inversion in Corollary 5.17. The continuous-time input signal $u(t)$ and error signal $e(t)$ for these solutions are shown in Figure 5.9.

The special case of stable inversion achieves perfect output tracking, see Figure 5.10(a). However, the intersample performance in Figure 5.9(b) is poor as a consequence of the erratic input, see Figure 5.9(a). The special case of multirate inversion yields a less erratic input, see Figure 5.9(a). Figure 5.10(b) shows perfect state tracking is achieved every $n = 8$ samples. The intersample performance shown in Figure 5.9(b) is reasonable.

The proposed approach yields good intersample performance as shown by Figure 5.9(b). Perfect state tracking is achieved every $n_1 = 4$ samples, see Figure 5.10(c). The proposed approach outperforms the special cases of stable inversion and multirate inversion in terms of the continuous-time error $e(t)$.

Second, the performance is evaluated for a variety of solutions. The results are shown in Figure 5.11 and quantify Figure 5.3. The results show that many of the solutions provided by the proposed approach outperform the special cases of stable inversion and multirate inversion. Figure 5.11 only shows results for even numbers n_1 due to the additional lifting step with $\tau = 2$ that is used.

In summary, in this simulation the intersample performance of the special case of stable inversion is poor due to an erratic input signal. The special case of multirate inversion yields a non-erratic input, but moderate intersample performance. The proposed approach offers a variety of options that outperform the two special cases of stable inversion and multirate inversion, and achieve superior performance.

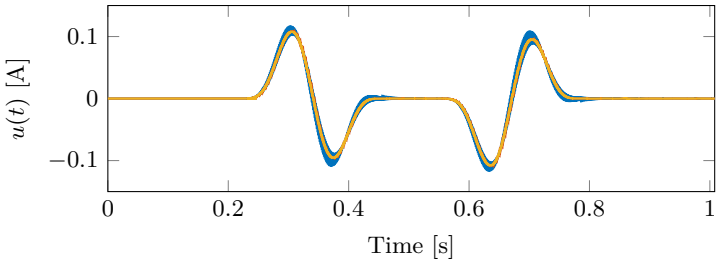

(a) The input signals $u(t)$ for multirate inversion and the proposed approach are overlapping. The input for the stable inversion approach is erratic.

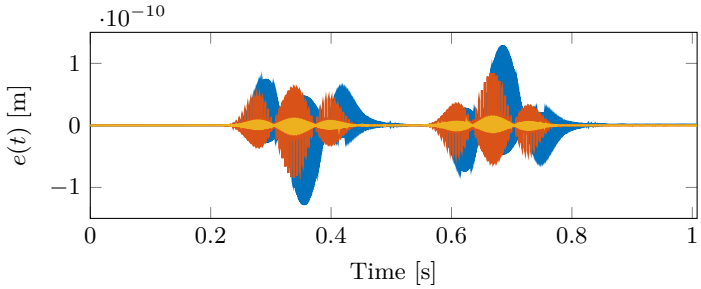

(b) The continuous-time error $e(t)$ is large for the stable inversion approach as a result of an erratic input. The proposed approach achieves the smallest error and outperforms the other approaches.

Figure 5.9. Results for the LPTV system in Section 5.8 with stable inversion (——), multirate inversion (——), and the proposed approach (——). The proposed approach achieves superior performance.

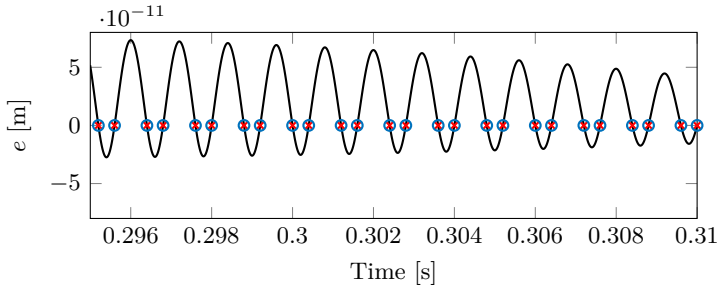

(a) The stable inversion approach achieves exact output tracking every sample (○).

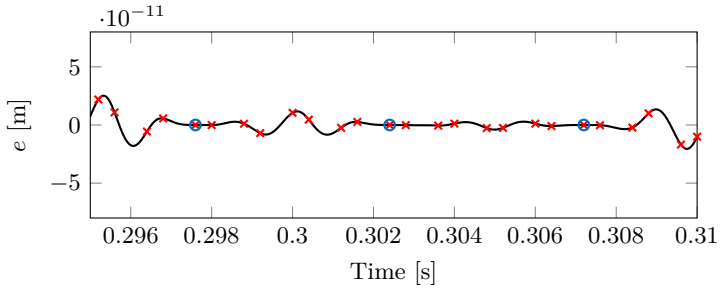

(b) The multirate inversion approach achieves exact state and output tracking every $n = 8$ samples (○).

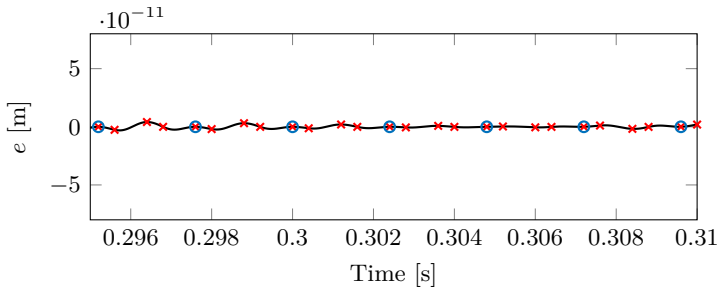

(c) The proposed approach achieves exact state and output tracking every $n_1 = 4$ samples (○).

Figure 5.10. Intersample error signal $e(t)$ (——) and on-sample error signal $e[k]$ (×) near $t = 0.30$ s for the LPTV system in Section 5.8. The proposed approach outperforms the other approaches.

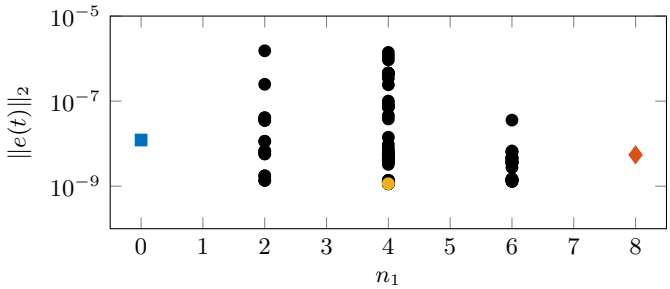

Figure 5.11. Quantification of Figure 5.3 for the LPTV system in Section 5.8. The number of states n_1 in $\underline{H}_1$ corresponds to the number of samples between exact on-sample tracking. The proposed approach ($n_1 = 4$, ●) outperforms the stable inversion approach ($n_1 = 0$, ■) and the multirate inversion approach ($n_1 = 8$, ♦).

5.9 Conclusion and outlook

A discrete-time inversion approach is developed that allows to balance the on-sample and intersample behavior for the purpose of continuous-time performance. The approach is applicable to both LTI and LPTV systems. The multirate inversion and stable inversion approaches are recovered as special cases. Application to two motion systems demonstrate the advantages of the proposed approach.

For LPTV systems, the proposed approach currently involves an additional lifting step, which limits applicability due to constraints on the input and state dimensions. In contrast, stable inversion and multirate inversion can be directly applied to LPTV systems. Future work focuses on an explicit state-space decomposition for LPTV systems to avoid the additional lifting step and thereby potentially increase the performance of the proposed approach.

5.A Proof of Theorem 5.2

Let $x_{ccf}(t)$ in (5.5) be given by $x_{ccf}(t) = \begin{bmatrix} x_0(t) & x_1(t) & \cdots & x_{n-1}(t) \end{bmatrix}^\top$ and ρ the Heaviside operator (Goodwin et al., 2000, Section 4.2), then

$$x_1(t) = \rho x_0(t), \tag{5.32a}$$

$$x_2(t) = \rho^2 x_0(t), \tag{5.32b}$$

$$\vdots$$

$$x_m(t) = \rho^m x_0(t), \tag{5.32c}$$

and

$$
\begin{aligned}
y(t) &= C_{ccf} x_{ccf}(t) && (5.33a)\\
&= x_0(t) + \tfrac{b_1}{b_0} x_1(t) + \ldots + \tfrac{b_m}{b_0} x_m(t) && (5.33b)\\
&= \frac{b_0 + b_1\rho + \ldots + b_m\rho^m}{b_0} x_0(t) && (5.33c)\\
&= B(\rho) x_0(t). && (5.33d)
\end{aligned}
$$

Hence, it holds

$$\bar{y}(t) = B(\rho) x_{ccf}(t). \tag{5.34}$$

For $y(t) = C_{ccf}\hat{x}_{ccf}(t)$, with

$$\hat{x}_{ccf}(t) = B^{-1}(\rho)\bar{r}(t), \tag{5.35}$$

it follows that $\bar{y}(t) = \bar{r}(t)$. Bounded $\hat{x}_{ccf}(t)$ is obtained through stable inversion for continuous-time systems, see, e.g., Devasia et al. (1996), as given by (5.8). State transformation (5.6) yields bounded $\hat{x}(t)$ in (5.9) which concludes the proof.

5.B Proof of Theorem 5.5

Due to the modal form of H_{mod}, the A matrix of H_{mod} is block diagonal and the states are decoupled per mode. The matrix T_{per} is a permutation matrix and follows directly from $V, V_\times$ and the state ordering of H_{mod}. The first n_1 states in (5.12) are uncontrollable and are redundant since the states are decoupled. Similarly, the last n_2 states in (5.13) are unobservable and are redundant since the states are decoupled. Hence, H_1, H_2 are minimal realizations such that $H_{mod} = H_1 H_2$ in terms of transfer functions. The product $H_1 H_2$ with H_1, H_2 in (5.14) is given by

$$H_1 H_2 = \left[\begin{array}{cc|c} A_1 & B_1 C_2 & B_1 D \\ 0 & A_2 & B_2 \\ \hline C_1 & C_2 & D \end{array}\right]. \tag{5.36}$$

Using (5.15),

$$
\begin{aligned}
\mathcal{T}(H_1 H_2, T_{12}) &= \left[\begin{array}{cc|c} A_1 & -A_1 X + B_1 C_2 + X A_2 & B_1 D + X B_2 \\ 0 & A_2 & B_2 \\ \hline C_1 & -C_1 X + C_2 & D \end{array}\right] && (5.37a)\\
&= \left[\begin{array}{cc|c} A_1 & 0 & B_{2r} \\ 0 & A_2 & B_2 \\ \hline C_1 & C_{1r} & D \end{array}\right]. && (5.37b)
\end{aligned}
$$

By definition of T_{per} in (5.12) and (5.13),

$$\mathcal{T}(H_1H_2, T_{per}^{-1}T_{12}) = \mathcal{T}(\mathcal{T}(H_1H_2, T_{12}), T_{per}^{-1}) = (A, B, C, D) = H_{mod} \tag{5.38}$$

which concludes the proof.

Chapter 6

Causal feedforward control for non-square systems

In Chapter 3, several approaches for system inversion of nonminimum-phase systems are presented. The key aspect to achieve perfect tracking for nonminimum-phase systems is the use of preview and pre-actuating the system. The aim of this chapter is to exploit the additional freedom in overactuated systems to avoid the use of pre-actuation and preview to enable causal and exact inversion of nonminimum-phase systems. In an either static or dynamic squaring-down step prior to inversion, the approach exploits the fact that non-square systems typically have no invariant zeros. The approach is successfully demonstrated on a benchmark system and through experiments on a motion system. The approach enables exact inversion for non-square systems without requiring preview or pre-actuation and constitutes Contribution III.C.

6.1 Introduction

System inversion is at the heart of achieving high performance in many control applications, including printing systems (Bolder et al., 2014), atomic force microscopes (Rios et al., 2018), and wafer stages (Blanken et al., 2017a). It is extensively used in, for example, inverse model feedforward (Boeren et al., 2015) and iterative learning control (ILC) (Bristow et al., 2006). See also Chapter 3 for an overview and comparison of system inversion approaches.

The contents of this chapter are published in:
Jurgen van Zundert, Fons Luijten, and Tom Oomen. Exact and Causal Inversion of Nonminimum-Phase Systems: A Squaring-Down Approach for Overactuated Systems. *Submitted for journal publication*, 2018.

Many systems have more actuators or sensors, for example flight control systems (Ma et al., 2012; Chen, 2016; Santamaria-Navarro et al., 2017), dual-stage actuators (Zheng et al., 2010), marine vessels (Fossen and Johansen, 2006; Tsopelakos and Papadopoulos, 2017), wafer stages (Van Herpen et al., 2014), ground vehicles (Wang et al., 2014; Knobel et al., 2006; Wang and Longoria, 2009), and many more (Johansen and Fossen, 2013). For such systems, system inversion is often performed after the system is cast in a square system, see, for example, Van de Wal et al. (2002). This can be done by, for example, choosing outputs such that they coincide with performance variables (Oomen et al., 2015) or choosing inputs such that the system is decoupled (Stoev et al., 2017). This facilitates the design of decentralized feedback control (Van de Wal et al., 2002; Oomen, 2018), as well as decentralized ILC (Blanken and Oomen, 2018).

One of the main challenges in system inversion is nonminimum-phase behavior, which is related to the invariant zeros of the system being "unstable". Indeed, causal inversion of nonminimum-phase systems yields unbounded signals. To avoid unbounded signals, inversion techniques have been developed, see also Chapter 3 for an overview. Traditionally, approximate inversion techniques such as ZPETC, ZMETC and NPZ-Ignore (Butterworth et al., 2012) are used, but such approaches inherently yield non-exact tracking. Stable inversion (Section 3.4.2) yields exact tracking, but for nonminimum-phase systems the approach requires preview, i.e., a priori knowledge of the reference trajectory, and pre-actuation, i.e., a non-zero input before the start of the trajectory. Furthermore, the approach is restricted to square systems. Optimization approaches such as norm-optimal feedforward (Athans and Falb, 1966) require preview, which is not always available. Synthesis approaches such as $\mathcal{H}_2$-preview control and $\mathcal{H}_\infty$-preview control (Section 3.4.4) are only optimal for trajectories with a specific frequency spectrum or address a control goal other than tracking error minimization, respectively.

Although there are many inversion techniques that yield bounded inputs for nonminimum-phase systems, they either require preview or pre-actuation. The aim of this chapter is to develop a new approach for system inversion that reconsiders traditional choices for squaring down, i.e., aiming to decouple systems as is outlined above. In particular, the approach considers new criteria for squaring down in view of system inversion, exploiting the additional design freedom available in overactuated systems.

The main contribution of this chapter is a causal inverse model feedforward solution for overactuated systems, also for systems with nonminimum-phase behavior. The approach exploits the design freedom at the input side to square down the non-square system to a square minimum-phase system, which enables exact causal inversion. A key aspect is that non-square systems generally do not have any invariant zeros. The following subcontributions are identified.

6.I Coordinate basis of non-square systems revealing key properties for squaring down.

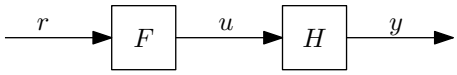

Figure 6.1. System inversion diagram. Given system H, the aim is to let output $y \in \mathbb{R}^{\bar{p}}$ track reference $r \in \mathbb{R}^{\bar{p}}$ through design of F such that $u \in \mathbb{R}^{\bar{m}}$ remains bounded.

6.II A squaring-down approach with a static compensator.

6.III A squaring-down approach with a dynamic compensator.

6.IV Systematic design framework for design of inverse model feedforward for overactuated systems.

6.V Validation of the design framework on a benchmark system.

6.VI Experimental validation of the design framework on an overactuated system with nonminimum-phase behavior.

Related work on overactuated systems addressing different aspects includes Duan and Okwudire (2018); Benosman et al. (2009), see also Johansen and Fossen (2013).

The outline of the chapter is as follows. In Section 6.2, the control problem is formulated. In Section 6.3, the main idea of the approach is presented together with preliminary results. The static squaring-down approach is presented in Section 6.4, with extension to dynamic squaring down in Section 6.5. An overview of the complete approach is presented in Section 6.6. Application to a benchmark system is presented in Section 6.7. In Section 6.8, the experimental validation on a motion system is presented. Conclusions are presented in Section 6.9.

6.2 Problem formulation

In this section, the challenges associated to inversion of (non-)square systems are illustrated through several examples, which leads to the problem considered in this chapter.

Consider the inversion diagram in Figure 6.1, where discrete-time system H has the minimal realization

$$H: \quad \begin{aligned} x[k+1] &= Ax[k] + Bu[k], \\ y[k] &= Cx[k] + Du[k], \end{aligned} \tag{6.1}$$

with $x \in \mathbb{R}^n$, $u \in \mathbb{R}^{\bar{m}}$, $y \in \mathbb{R}^{\bar{p}}$. Without loss of generality, it is assumed that $\operatorname{rank}\{\left[\begin{smallmatrix} B \\ D \end{smallmatrix}\right]\} = \bar{m}$ and $\operatorname{rank}\{\left[\begin{smallmatrix} C & D \end{smallmatrix}\right]\} = \bar{p}$. The system H is stable if and only if $|\lambda_i(A)| < 1$, for all i, where λ_i denotes the ith eigenvalue. The following definition is adopted.

Definition 6.1 (Invariant zeros (MacFarlane and Karcanias, 1976; Rosenbrock, 1970))**.** *The invariant zeros of H in* (6.1) *are given by*

$$z = \left\{ z_i \in \mathbb{C} \;\middle|\; \operatorname{rank}\{H_{RSM}(z_i)\} < \max_{z_j \in \mathbb{C}} \operatorname{rank}\{H_{RSM}(z_j)\} \right\}, \tag{6.2}$$

with $H_{RSM}(z) = \left[\begin{array}{c|c} zI_n - A & -B \\ \hline C & D \end{array}\right]$.

The system H in (6.1) is minimum phase if and only if all invariant zeros, see Definition 6.1, satisfy $|z_i| < 1$, for all i. System H is unstable (resp. nonminimum phase) if it is not stable (resp. minimum phase). If $|z_i| = 1$ for some i, techniques as in Devasia (1997a) can be used. It is assumed that H is right invertible as defined by Definition 6.2.

Definition 6.2 (Invertibility)**.** *System H in* (6.1) *is*

- *left invertible if and only if $r_n = \bar{m}$,*
- *right invertible if and only if $r_n = \bar{p}$,*
- *invertible if and only if $r_n = \bar{m} = \bar{p}$,*

with $r_n = \max_{z \in \mathbb{C}} \operatorname{rank}\{D + C(zI_n - A)^{-1}B\}$.

Given Figure 6.1 and H, the objective is to let output y track the reference trajectory r, while input u remains bounded. The following examples illustrate that the inversion of H is nontrivial.

Example 6.3. *Let H be scalar and given by*

$$H = \frac{(z - 0.6)(z + 2)}{(z - 0.1)(z + 0.8)(z - 0.4)}, \tag{6.3}$$

then

$$F = H^{-1} = \frac{(z - 0.1)(z + 0.8)(z - 0.4)}{(z - 0.6)(z + 2)} \tag{6.4}$$

is unique, but unstable (pole at $z = -2$) as a consequence of H being nonminimum phase. Hence, causal filtering with F leads to unbounded signals.

Example 6.3 shows the challenges associated with nonminimum-phase behavior. The following example illustrates the key concepts of this chapter.

Example 6.4. *Let H be non-square and given by*

$$H = \frac{1}{(z - 0.1)(z + 0.8)(z - 0.4)} \begin{bmatrix} (z - 0.6)(z + 2) & (z - 5) \end{bmatrix}, \tag{6.5}$$

then F such that $HF = 1$ is non-unique. The inverses

$$F_1 = \begin{bmatrix} \frac{1}{(z-0.6)(z+2)} \\ 0 \end{bmatrix} (z-0.1)(z+0.8)(z-0.4), \tag{6.6}$$

$$F_2 = \begin{bmatrix} 0 \\ \frac{1}{(z-5)} \end{bmatrix} (z-0.1)(z+0.8)(z-0.4) \tag{6.7}$$

may lead to unbounded responses since they are unstable. In contrast, the inverse

$$F = \begin{bmatrix} 1 \\ -0.3 \end{bmatrix} \frac{(z-0.1)(z+0.8)(z-0.4)}{(z+0.5)(z+0.6)}, \tag{6.8}$$

allows for bounded causal solutions since F is stable.

The main point of Example 6.4 is that for systems with nonminimum-phase behavior, selecting either one of the inputs may yield unstable inverses, see (6.6) and (6.7). Interestingly, a smart combination of inputs as in (6.8) yields a stable inverse. This is the main idea of this chapter and exploits the fact that in general non-square systems are minimum phase, regardless of the properties of the individual transfer functions. However, the solution is not always as straightforward as in Example 6.4, as shown by the following example.

Example 6.5. *Let H be non-square and given by*

$$H = \frac{1}{(z-0.1)(z+0.8)(z-0.4)} \begin{bmatrix} (z-0.6)(z+2) & (z-5)(z+0.9) \end{bmatrix}, \tag{6.9}$$

then F such that $HF = 1$ is non-unique. The only difference with Example 6.4 is one additional minimum-phase zero at the second input. For (6.9)*, the design of a stable F such that $HF = 1$ is not as straightforward as* (6.8) *in Example 6.4.*

The examples show that inversion of H is nontrivial if H is nonminimum phase or non-square. Example 6.4 shows that additional freedom in the inputs can be exploited to create a stable system that yields exact inversion. However, such a design is not straightforward as illustrated by Example 6.5. In the next sections, a systematic design framework for inversion of overactuated systems is presented. A design for Example 6.5 is presented later on.

Remark 6.6. *In this chapter, discrete-time systems are considered since this allows for a digital controller implementation. Results for continuous-time systems follow along the same lines.*

6.3 Causal and stable inversion for non-square systems

In this section, the main idea of the proposed approach is presented together with preliminary results.

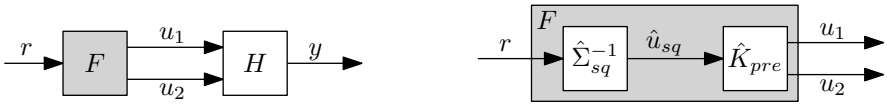

(a) Tracking control of $r \in \mathbb{R}^{\bar{p}}$ by H with more inputs $u_1 \in \mathbb{R}^{\bar{p}}$, $u_2 \in \mathbb{R}^{\bar{m}-\bar{p}}$ than outputs $y \in \mathbb{R}^{\bar{p}}$.

(b) Minimimum-phase, square $\hat{\Sigma}_{sq} = H\hat{K}_{pre}$ is created and inverted such that $HF = I$ and hence $y = r$.

Figure 6.2. Inverse model feedforward approach for a system H with more inputs than outputs. Perfect tracking is obtained without pre-actuation and preview through squaring down and direct inversion of the minimum-phase, square system.

6.3.1 Main idea: Squaring down in view of system inversion

Squaring down is a standard step in control applications. Typical considerations include decoupling. In this chapter, a systematic design approach is presented that exploits the additional freedom of overactuated systems H in Figure 6.1 in view of system inversion, i.e., with $\bar{m} > \bar{p}$, to obtain stable F such that $HF = I$ and hence $y = r$. A key aspect is that non-square systems generally have no invariant zeros. Hence, the invariant zeros of the squared-down system are determined by the squaring-down approach and can be affected.

The tracking control application of Figure 6.1 with more inputs than outputs ($\bar{m} > \bar{p}$) is shown in Figure 6.2(a), with input $u \in \mathbb{R}^{\bar{m}}$ divided into $u_1 \in \mathbb{R}^{\bar{p}}$ and $u_2 \in \mathbb{R}^{\bar{m}-\bar{p}}$. The design approach consists of two steps as shown in Figure 6.2(b). First, a precompensator $\hat{K}_{pre}$ is designed such that

$$\hat{\Sigma}_{sq} = H\hat{K}_{pre} \tag{6.10}$$

is square with dimensions $\bar{p} \times \bar{p}$. Second, F is selected as

$$F = \hat{K}_{pre}\hat{\Sigma}_{sq}^{-1} \tag{6.11}$$

such that perfect tracking is obtained since

$$y = HFr = H\hat{K}_{pre}\hat{\Sigma}_{sq}^{-1}r = H\hat{K}_{pre}(H\hat{K}_{pre})^{-1}r = r. \tag{6.12}$$

Note that the second step is straightforward once the first step is completed.

The proposed approach is also used in Example 6.4 in Section 6.2 where squaring down is performed by the static precompensator $\hat{K}_{pre} = \left[\begin{smallmatrix} 1 \\ -0.3 \end{smallmatrix}\right]$. The precompensator yields a minimum-phase, square system as desired. It is shown later on that there does not exist a static precompensator for the system in Example 6.5 such that the square system is minimum phase. However, there does always exist a dynamic compensator such that the square system is minimum phase. A dynamic compensator design for Example 6.5 is presented later on.

The precompensator design $\hat{K}_{pre}$ introduces additional invariant zeros in the square system $\hat{\Sigma}_{sq}$ in (6.10). The interest is in stable precompensator designs $\hat{K}_{pre}$ that yield minimum-phase, square systems $\hat{\Sigma}_{sq}$ as they result in stable F and thus bounded u when using the causal solution. If the compensator is stable, but the square system is nonminimum phase, then inversion techniques are required to compute bounded outputs of $\hat{\Sigma}_{sq}^{-1}$, since the invariant nonminimum-phase zeros become unstable poles in $\hat{\Sigma}_{sq}^{-1}$. Inversion techniques, such as stable inversion, are not preferred since they are noncausal and require pre-actuation and preview.

The critical step in the proposed approach is the design of the compensator $\hat{K}_{pre}$ in (6.10) which is presented in the subsequent sections based on the coordinate basis presented in the next section.

6.3.2 Coordinate basis for squaring down

In this section, a coordinate basis is presented to facilitate the design of the precompensator $\hat{K}_{pre}$ in (6.10). The basis is specifically developed for use in the squaring-down approach presented in Sections 6.4 and 6.5, in contrast to the more general special coordinate basis (s.c.b.) (Sannuti and Saberi, 1987; Saberi and Sannuti, 1990). The results in this section constitute Contribution 6.I.

The coordinate basis is developed for left-invertible systems. The right-invertible system $H \stackrel{z}{=} (A, B, C, D)$ in Figure 6.2(a) is transformed to a left-invertible system by considering its dual $\hat{\Sigma} = H_d$ given by

$$\hat{\Sigma}: \qquad \begin{aligned} \hat{x}[k+1] &= \hat{A}\hat{x}[k] + \hat{B}\hat{u}[k], \\ \hat{y}[k] &= \hat{C}\hat{x}[k] + \hat{D}\hat{u}[k], \end{aligned} \tag{6.13}$$

with $(\hat{A}, \hat{B}, \hat{C}, \hat{D}) = (A^\top, C^\top, B^\top, D^\top)$ and $\hat{x} \in \mathbb{R}^n$, $\hat{y} \in \mathbb{R}^p$, $\hat{u} \in \mathbb{R}^m$, where $p = \bar{m}$, $m = \bar{p}$. Note that since H is right invertible, $\hat{\Sigma} = H_d$ is left invertible, see also Definition 6.2.

In the related work Sannuti and Saberi (1987); Saberi and Sannuti (1990) the special coordinate basis (s.c.b.) is used. Existing algorithms to obtain this special structure, for example in Chen et al. (2004, Chapter 12), are experienced to be numerically inaccurate. Instead, an other structure is used which only enforces those features that are required for the squaring-down approach and thereby results in numerically more accurate results. The coordinate basis that is used is given by Theorem 6.7. See Appendix 6.A for the construction of the basis.

Theorem 6.7 (Coordinate basis)**.** *Let* $\Sigma = \Gamma_o^{-1}\hat{\Sigma}\Gamma_i$, *with* $\hat{\Sigma}$ *in* (6.13) *and*

$$\hat{y} = \Gamma_o \begin{bmatrix} y_f \\ y_s \end{bmatrix}, \quad \hat{u} = \Gamma_i u, \tag{6.14}$$

with non-singular $\Gamma_o \in \mathbb{R}^p$, $\Gamma_i \in \mathbb{R}^m$ *and* $y_f = \begin{bmatrix} y_{0f} \\ y_{xf} \end{bmatrix}$, $y_{0f} \in \mathbb{R}^{m_0}$, $y_{xf} \in \mathbb{R}^{m-m_0}$, $y_s \in \mathbb{R}^{p-m}$, *and* $u = \begin{bmatrix} u_0 \\ u_x \end{bmatrix}$, $u_0 \in \mathbb{R}^{m_0}, u_x \in \mathbb{R}^{m-m_0}$, *where* $m_0 = \text{rank}\{D\}$. *Then,* Σ *satisfies the coordinate basis*

$$x_a[k+1] = A_{aa}x_a[k] + A_{af}y_f[k], \tag{6.15a}$$
$$x_b[k+1] = A_{bb}x_b[k] + A_{bf}y_f[k], \tag{6.15b}$$
$$x_f[k+1] = A_{fa}x_a[k] + A_{fb}x_b[k] + B_{fx}u_x[k] + L_f y_f[k], \tag{6.15c}$$
$$y_{0f}[k] = C_{0fa}x_a[k] + C_{0fb}x_b[k] + C_{0ff}x_f[k] + u_0[k], \tag{6.15d}$$
$$y_{xf}[k] = x_f[k], \tag{6.15e}$$
$$y_s[k] = C_{sb}x_b[k]. \tag{6.15f}$$

The coordinate basis in Theorem 6.7 reveals several features that are used in the squaring-down approach in subsequent sections. For example, the invariant zeros, see Definition 6.1, of $\hat{\Sigma}$ in Theorem 6.7 are given by $\lambda(A_{aa})$. In the next section, the coordinate basis in Theorem 6.7 is exploited in the squaring-down approach to obtain the compensator $\hat{K}_{pre}$ in (6.10).

6.4 Causal feedforward through static squaring down

In this section, the static squaring-down approach is presented, which constitutes Contribution 6.II. The approach exploits properties of the coordinate basis presented in Section 6.3, and in particular Theorem 6.7. First, the static compensator design is presented. Second, the static compensator design is applied to the examples in Section 6.2. The extension to a dynamic compensator design is presented in Section 6.5. An overview of the complete feedforward design approach for H in Figure 6.2(a) is presented in Section 6.6.

6.4.1 Static compensator

The concept of squaring down a left-invertible system Σ in (6.15) is illustrated in Figure 6.3. The outputs $y_f \in \mathbb{R}^m, y_s \in \mathbb{R}^{p-m}$ are combined into a new output $\tilde{y} \in \mathbb{R}^m$ through a postcompensator as $\tilde{y} = K_{post}\begin{bmatrix} y_f \\ y_s \end{bmatrix}$, such that $\Sigma_{sq} = K_{post}\Sigma$ is square with dimensions $m \times m$. The main idea is to design K_{post} such that Σ_{sq} is invertible and nonminimum phase to enable direct inversion.

The precompensator K_{pre} for the right-invertible dual system system Σ_d is obtained as the dual of the postcompensator of Σ, i.e., $K_{pre} = K_{post,d}$. The

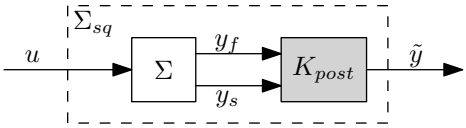

Figure 6.3. Postcompensator K_{post} combines outputs y_f, y_s of the left-invertible system Σ into a new output $\tilde{y}$ such that the combined system Σ_{sq} is square. The freedom in design of K_{post} is exploited to make Σ_{sq} minimum phase.

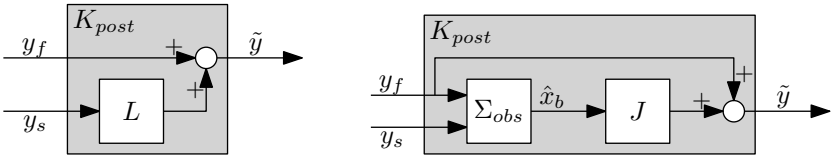

(a) Static postcompensator with static gain L.

(b) Dynamic postcompensator with observer Σ_{obs} to obtain $\hat{x}_b$ for use in state feedback.

Figure 6.4. Two proposed postcompensator designs for K_{post} in Figure 6.3.

precompensator $\hat{K}_{pre}$ for system H in Figure 6.2(b) is given by

$$\hat{K}_{pre} = \Gamma_o^{-\top} K_{pre} = \Gamma_o^{-\top} K_{post,d}. \tag{6.16}$$

The design of static compensator design K_{post} in Figure 6.3 is given by Theorem 6.8 and illustrated in Figure 6.4(a).

Theorem 6.8 (Static compensator)**.** *Given Figure 6.3 with Σ in* (6.15)*, the static compensator is given by*

$$K_{post} = \begin{bmatrix} I_m & L \end{bmatrix}, \tag{6.17}$$

i.e., $\tilde{y} = y_f + Ly_s$, with $L \in \mathbb{R}^{m\times(p-m)}$.

Proof. The proof follows along similar lines as for continuous-time systems based on the s.c.b. in Saberi and Sannuti (1988, III.A). □

Properties of the square system Σ_{sq} for the static compensator in Theorem 6.8 are provided by Theorem 6.9, where n_a, n_b are the dimensions of x_a, x_b in (6.15), respectively.

Theorem 6.9 (Properties Σ_{sq} static compensator)**.** *Given H in* (6.1) *and Σ in* (6.15)*, the square system Σ_{sq} in Figure 6.3 with K_{post} the static compensator of Theorem 6.8 has the following properties.*

- *Invertible;*

- $n_a + n_b$ *invariant zeros:* $\lambda(A_{aa}) \ + \ \lambda(A_{bb} - A_{bf}LC_{sb})$*;*
- n *poles:* $\lambda(\hat{A})$*.*

Proof. Substitution of $y_f = \tilde{y} - Ly_s = \tilde{y} - LC_{sb}x_b$ in (6.15) and obtaining the coordinate basis in Theorem 6.7 for the new system shows that $\tilde{x}_a = \begin{bmatrix} x_a \\ x_b \end{bmatrix}$ with $\tilde{A}_{aa} = \begin{bmatrix} A_{aa} & -A_{af}LC_{sb} \\ 0 & A_{bb} - A_{bf}LC_{sb} \end{bmatrix}$ from which the results follow directly. □

Theorem 6.9 shows that the static compensator introduces new invariant zeros in addition to the invariant zeros $\lambda(A_{aa})$ of Σ. When inverting the square system Σ_{sq}, these zeros become poles. Hence, these zeros are preferred to be minimum phase to avoid the use of inversion techniques which require pre-actuation. The zeros $\lambda(A_{aa})$ are fixed, but since Σ is non-square, there are typically no (nonminimum-phase) zeros. Theorem 6.10 shows how the additional zeros can possibly be placed through static output feedback.

Theorem 6.10 (Invariant zero placement static compensator)**.** *The invariant zeros introduced by the static compensator in Theorem 6.8 can possibly be placed by solving the static output feedback problem for the triplet* (A_{bb}, A_{bf}, C_{sb})*.*

Proof. By Theorem 6.9, the additional invariant zeros are given by $\lambda(A_{bb} - A_{bf}LC_{sb})$ and thus affected by L. These zeros are also the poles of the state-space system (A_{bb}, A_{bf}, C_{sb}) with static output feedback gain $-L$. □

Importantly, the static output feedback problem in Theorem 6.10 is not always solvable (Syrmos et al., 1997). This is also shown through examples in the next section.

6.4.2 Application of the static compensator

In this section, the static compensator design of Theorem 6.8 is applied to Example 6.4 and Example 6.5 in Section 6.2.

Example 6.4 (continued)**.** *The dual left-invertible system, see also Section 6.3.2, of* H *in* (6.5) *is given by*

$$H_d = \frac{1}{(z-0.1)(z+0.8)(z-0.4)} \begin{bmatrix} (z-0.6)(z+2) \\ (z-5) \end{bmatrix}, \tag{6.18}$$

with $m = 1$*,* $p = 2$*. System* $\Sigma = H_d$ *in the coordinate basis of Theorem 6.7 is*

given by

$$x_b[k+1] = \begin{bmatrix} 0.5935 & 0.1569 \\ 0.1069 & -1.9935 \end{bmatrix} x_b[k] + \begin{bmatrix} -1.9347 \\ 3.5010 \end{bmatrix} y_f[k], \tag{6.19a}$$

$$x_f[k+1] = \begin{bmatrix} 0.0580 & -0.6477 \end{bmatrix} x_b[k] + 1.1 y_f[k] \tag{6.19b}$$

$$y_f[k] = x_f[k], \tag{6.19c}$$

$$y_s[k] = \begin{bmatrix} 0.9512 & 0.8113 \end{bmatrix} x_b[k], \tag{6.19d}$$

with $\Gamma_o = \left[\begin{smallmatrix} 1 & 0 \\ 0 & 1 \end{smallmatrix}\right]$. *The coordinate basis confirms* Σ *has no invariant zeros since* x_a *is non-existing. Selecting* $L = -0.3$ *in Theorem 6.8 yields* $K_{post} = \begin{bmatrix} 1 & -0.3 \end{bmatrix}$ *and* $\lambda(A_{bb} - A_{bf}LC_{sb}) = \{-0.5, -0.6\}$. *Hence, by* (6.16), $\hat{K}_{pre} = \left[\begin{smallmatrix} 1 \\ -0.3 \end{smallmatrix}\right]$ *which yields controller* F *in* (6.8).

Example 6.5 (continued)**.** *The dual left-invertible system* H_d*, see Section 6.3.2, of* H *in* (6.9) *in the coordinate basis of Theorem 6.7 is given by*

$$x_b[k+1] = \begin{bmatrix} 0.5137 & 1.7257 \\ 0.1257 & -1.9137 \end{bmatrix} x_b[k] + \begin{bmatrix} -5.9323 \\ 5.3673 \end{bmatrix} y_f[k], \tag{6.20a}$$

$$x_f[k+1] = \begin{bmatrix} 0.0445 & -0.3942 \end{bmatrix} x_b[k] + 1.1 x_f[k] + u_x[k], \tag{6.20b}$$

$$y_f[k] = x_f[k], \tag{6.20c}$$

$$y_s[k] = \begin{bmatrix} 1.1556 & 0.2525 \end{bmatrix} x_b[k], \tag{6.20d}$$

with $\Gamma_o = \left[\begin{smallmatrix} 1 & 0 \\ 1 & 1 \end{smallmatrix}\right]$. *It can be verified that there does not exist an* $L \in \mathbb{R}$ *such that* $|\lambda(A_{bb} - A_{bf}LC_{sb})| < 1$. *Hence, for this system, there does not exist a static compensator that yields a square system which is minimum phase.*

Theorem 6.10 shows that the problem of designing a postcompensator reduces to solving a static output feedback problem. However, the static output feedback problem does not always have a solution, as also illustrated by Example 6.5 above. Therefore, in the next section a dynamic compensator is constructed for which the additional invariant zeros can always be placed arbitrarily.

6.5 Causal feedforward: Extension to dynamic squaring down

In the previous section, a static compensator design is presented that yields a square system. However, it is also shown that such a design may not suffice to obtain a minimum-phase square system, as is also illustrated through Example 6.5. In this section, the compensator design is extended to a dynamic compensator which enables to always obtain a minimum-phase square system. This section constitutes Contribution 6.III.

The minimum-phase square system is obtained by using an observer to reconstruct the full state x_b, followed by state feedback on this observed state $\hat{x}_b$. The resulting dynamic compensator is presented in Theorem 6.11 and illustrated in Figure 6.4(b). Note that the observer poles $\lambda(N)$ can be placed arbitrarily since (A_{bb}, A_{bf}) is controllable as Σ is a minimal realization. For minimal order observers, see, for example, O'Reilly (1983, Section 2.3).

Theorem 6.11 (Dynamic compensator)**.** *Given Figure 6.3 with* Σ *in* (6.15)*, the dynamic compensator* K_{post} *is given by*

$$K_{post} = \begin{bmatrix} I_m & 0 \end{bmatrix} + J\Sigma_{obs}, \tag{6.21}$$

i.e., $\tilde{y}[k] = y_f[k] + J\hat{x}_b[k]$, $\hat{x}_b[k] = \Sigma_{obs} \begin{bmatrix} y_f[k] \\ y_s[k] \end{bmatrix}$, *where* Σ_{obs} *denotes a minimal order observer with state matrix* N *for the matrix triplet* (A_{bb}, A_{bf}, C_{sb}).

Proof. The proof follows along similar lines as for continuous-time systems based on the s.c.b. in Saberi and Sannuti (1988, III.A). □

Properties of the square system Σ_{sq} for the dynamic compensator of Theorem 6.11 are provided by Theorem 6.12.

Theorem 6.12 (Properties Σ_{sq} dynamic compensator)**.** *Given* H *in* (6.1) *and* Σ *in* (6.15)*, the minimal realization of the square system* Σ_{sq} *in Figure 6.3 with* K_{post} *the dynamic compensator of Theorem 6.11 has the following properties.*

- *Invertible;*
- $n_a + n_b$ *invariant zeros:* $\lambda(A_{aa}) \ + \ \lambda(A_{bb} - A_{bf}J)$*;*
- n *poles:* $\lambda(\hat{A})$.

Proof. The proof follows along similar lines as for Theorem 6.9. □

The additional invariant zeros $\lambda(A_{bb} - A_{bf}J)$ are affected by J and can be arbitrarily placed through static state feedback of the pair (A_{bb}, A_{bf}). This requires that (A_{bb}, A_{bf}) is controllable which is satisfied since Σ is a minimal realization. Hence, if H is minimum phase, which typically holds, Σ_{sq} can be made minimum phase enabling the use of direct inversion without pre-actuation.

Next, the dynamic compensator design is applied to Example 6.5 in Section 6.4.2.

Example 6.5 (continued)**.** *The subsystem* (A_{bb}, A_{bf}, C_{sb}) *in* (6.20) *has two states and one output. Let the desired invariant zeros be* $\lambda(N) = 0.7$ *and* $\lambda(A_{bb} - A_{bf}J) = \{-0.5, -0.6\}$*, then pole placement on the pair* (A_{bb}, A_{bf}) *yields*

$J = \begin{bmatrix} -0.2188 & -0.2977 \end{bmatrix}$. *The dynamic postcompensator, see Theorem 6.11, is given by*

$$K_{post} = \frac{1}{(z-0.7)} \begin{bmatrix} (z+0.6) & 0.291(z-0.531) \end{bmatrix}, \tag{6.22}$$

which, by (6.11)*, yields*

$$F = \frac{(z-0.4)(z+0.8)(z-0.1)}{(z+0.6)(z+0.5)(z-0.7)} \begin{bmatrix} 0.709(z+1.064) \\ 0.291(z-0.531) \end{bmatrix}, \tag{6.23}$$

which is stable as desired. It can be verified that $HF = 1$ *and hence perfect tracking is obtained.*

In summary, the dynamic postcompensator design in Theorem 6.11 can always create a stable, minimum-phase, square system, if H in (6.1) is stable and has no nonminimum-phase invariant zeros, which typically holds for non-square systems. Next, the complete design framework is summarized, including both static and dynamic compensators.

6.6 Application in tracking control

In this section, the design framework is summarized which constitutes Contribution 6.IV.

The systematic design framework for design of F in Figure 6.2 given a right-invertible system H is shown in Figure 6.5. The result follows directly from combining the results of the previous sections. There are two main design types: static and dynamic squaring down. Properties of both are given by Lemma 6.13 and Lemma 6.14, respectively.

Lemma 6.13 (Properties controller with static compensator)**.** *Given* H *in* (6.1) *and* Σ *in* (6.15)*, the minimal realization of* F *in Figure 6.5 based on a static compensator has:*

- n *invariant zeros:* $\lambda(\hat{A})$*,*
- $n_a + n_b$ *poles:* $\lambda(A_{aa}) \; + \; \lambda(A_{bb} - A_{bf}LC_{sb})$*.*

Proof. The results follow from Theorem 6.9 and Figure 6.5. □

Lemma 6.14 (Properties controller with dynamic compensator)**.** *Given* H *in* (6.1) *and* Σ *in* (6.15)*, the minimal realization of* F *in Figure 6.5 based on a dynamic compensator has:*

- n *invariant zeros:* $\lambda(\hat{A})$*,*
- $n_a + 2n_b - p + m$ *poles:* $\lambda(A_{aa}) + \lambda(N) \; + \; \lambda(A_{bb} - A_{bf}J)$*.*

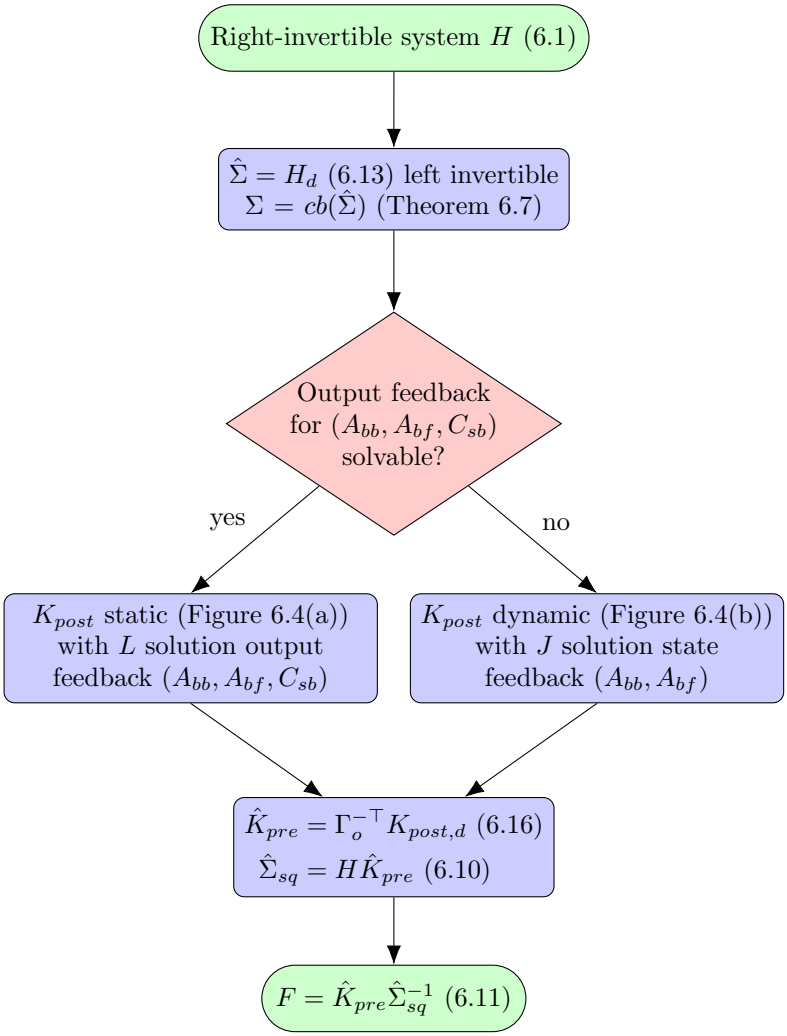

Figure 6.5. Inversion approach for overactuated systems in tracking control as shown in Figure 6.2. The precompensator $\hat{K}_{pre}$ is designed such that the square system $\hat{\Sigma}_{sq}$ has desired properties, for example, minimum-phase behavior. Perfect tracking is obtained through inversion of the square system.

Proof. The results follow from Theorem 6.12 and Figure 6.5. □

The locations of the invariant zeros of $\hat{\Sigma}_{sq}$ directly influence the dynamics and the resulting input signals u_1, u_2 in Figure 6.2. To avoid the use of pre-actuation, these invariant zeros can be made minimum phase.

In the next sections, the controller design framework presented in Figure 6.5 is validated through simulations and experiments.

6.7 Validation on a benchmark system

In this section, the static and dynamic squaring-down designs are applied to a benchmark system. The results demonstate the squaring-down approach outlined in Section 6.6 and constitute Contribution 6.V.

The non-square benchmark system is shown in Figure 6.6 and the reference trajectory r is shown in Figure 6.7. The system is an extended version of the benchmark system in Figure 3.2, with the addition of input u_2 located $0.1l$ from input u_1. The system H from $(u_1, u_2) \mapsto y$ is given by

$$\left[\begin{array}{c|cc} A & B_1 & B_2 \\ \hline C & D_1 & D_2 \end{array}\right] = \left[\begin{array}{cccc|cc} 1.0000 & 0.0010 & 0 & 0 & 0.0000 & 0.0000 \\ 0 & 1.0000 & 0 & 0 & 0.0001 & 0.0001 \\ 0 & 0 & 0.9981 & 0.0010 & 0.0000 & 0.0000 \\ 0 & 0 & -3.6783 & 0.9614 & 0.0037 & 0.0029 \\ \hline 1.0000 & 0 & -0.0500 & 0 & 0 & 0 \end{array}\right]. \tag{6.24}$$

By Definition 6.1 it follows that the transfer function $u_1 \mapsto y$, i.e., (A, B_1, C, D_1) has a nonminimum-phase zero at $z = 1.140$, see also Section 3.3, and that the transfer function $u_2 \mapsto y$, i.e., (A, B_2, C, D_2), has a nonminimum-phase zero at $z = 1.2965$. Since both transfer functions have a single nonminimum-phase zero, the step responses of both initially move in opposite direction (Vidyasagar, 1986), see Figure 6.6(b). Because the nonminimum-phase zeros are different, the non-square system H is minimum phase.

6.7.1 Static compensator design

In this section, a static compensator is designed for the system in Figure 6.6(a). First, a static precompensator is derived based on physical insights. From the dynamics follows that if the squared-down input acts above the center of mass, the transfer function is minimum phase. Therefore, the static transformation

$$\hat{K}_{pre,s1} = \begin{bmatrix} -1 \\ 1.1 \end{bmatrix} \tag{6.25}$$

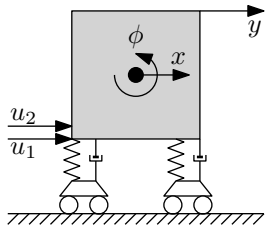

(a) System in Figure 3.2 extended with an additional input.

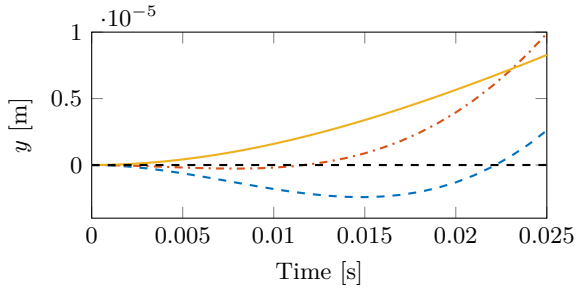

(b) The step responses of the transfer functionss $u_1 \mapsto y$ (- - -) and $u_2 \mapsto y$ (-·-·-) initially move in opposite direction of the final value, confirming nonminimum-phase behavior. The step response of the squared-down system (——) moves in the direction of the final value, confirming minimum-phase behavior.

Figure 6.6. The two-input, one-output system of which both individual transfer functions are nonminimum phase is squared down to a single-input, single-output, minimum-phase system.

is selected, which yields the scalar system $H\hat{K}_{pre,s1} \stackrel{z}{=} (A, \begin{bmatrix} B_1 & B_2 \end{bmatrix} \hat{K}_{pre,s1}, C, \begin{bmatrix} D_1 & D_2 \end{bmatrix} \hat{K}_{pre,s1})$, where

$$\begin{bmatrix} B_1 & B_2 \end{bmatrix} \hat{K}_{pre,s1} = 10^{-3} \times \begin{bmatrix} 0.0000 \\ 0.0125 \\ -0.0002 \\ -0.4414 \end{bmatrix}. \tag{6.26}$$

Using Definition 6.1, it can be shown that $H\hat{K}_{pre,s1}$ has no nonminimum-phase zeros as desired, which is confirmed by the step response in Figure 6.6(b). The resulting controller, see also (6.11), is denoted F_{s1} and the inputs u_1, u_2 are shown in Figure 6.8. Note that since $H\hat{K}_{pre,s1}$ is strictly proper with relative degree $d = 1$, one sample pre-actuation is required, see also Remark 3.1.

Next, the systematic design procedure illustrated in Figure 6.5 is used and compared with the design F_{s1} based on physical insights. The dual left-invertible system in the coordinates basis of Theorem 6.7 shows that the output feedback problem for (A_{bb}, A_{bf}, C_{sb}) is solvable, as is to be expected based on the previous results. In particular, for $6.99 \cdot 10^7 < L < 9.77 \cdot 10^7$ the square system is minimum phase. For $L = 7.99 \cdot 10^7$ the static precompensator is given by $\hat{K}_{pre,s2} = 5.77 \cdot 10^7 \left[\begin{smallmatrix} -1 \\ 1.1 \end{smallmatrix}\right]$. The compensator design matches the design based on physical insights $\hat{K}_{pre,s1}$ in (6.25), apart from a scaling factor. The scaling factor is canceled in F, see (6.11), and hence the same signals u_1, u_2 as in Figure 6.8 are obtained. The input signals are shown in Figure 6.9.

For comparison, the norm-optimal feedforward solution, see Section 3.4.3, is

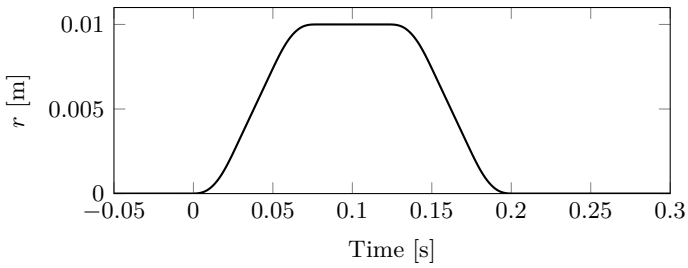

Figure 6.7. The reference trajectory consists of a forward and backward movement.

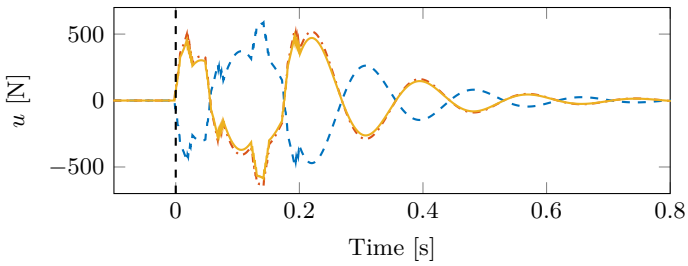

Figure 6.8. For the two-input, single-output system of Figure 6.6, the transformation (6.25) enables the use of exact and causal inversion yielding bounded inputs u_1 (- - -), u_2 (-·-·-), and combined input u (——).

also shown in Figure 6.9. Both the squaring down and norm-optimal feedforward solutions achieve exact tracking by design. The main difference is that the norm-optimal feedforward solution requires pre-actuation, whereas no pre-actuation is required for the proposed squaring-down approach. However, the input signals of the squaring-down approach are relatively large in magnitude. This is a consequence of the selected invariant zeros, which are design variables and can be used to "shape" the input signals, as is done for the experiments in Section 6.8.

6.7.2 Dynamic compensator design

In this section, a dynamic compensator is designed for the system in Figure 6.10 which includes actuator dynamics. The actuator dynamics for both inputs are modeled as identical mass-damper-spring systems with mass $m_a = 0.001$ kg, damping $d_a = 0.5$ Ns/m, and spring $k_a = 100$ N/m. Using Theorem 6.8, it can be shown that there does not exist a static compensator for the system in Figure 6.10 that yields a minimum-phase square system. It is possible to obtain a minimum-phase square system using a dynamic compensator. The dynamic compensator, see Theorem 6.11, is designed with $\lambda(N) = \{-0.8, 0.85, 0.9, 0.95\}$

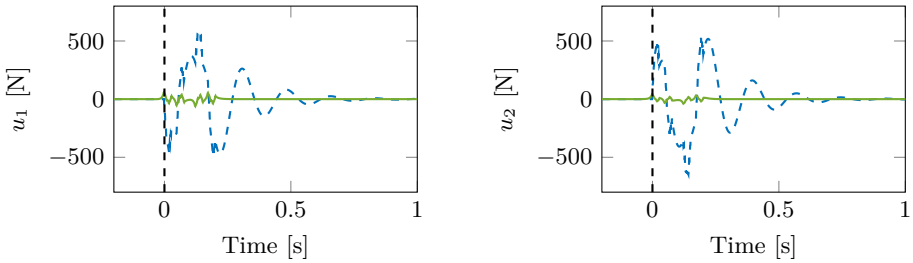

(a) Input signal u_1. **(b)** Input signal u_2.

Figure 6.9. Results for the system in Figure 6.6(a) with static squaring down (- - -), and norm-optimal feedforward (——). The squaring-down solution is also shown in Figure 6.8. The norm-optimal feedforward solution requires pre-actuation, whereas this is avoided in the squaring-down approach.

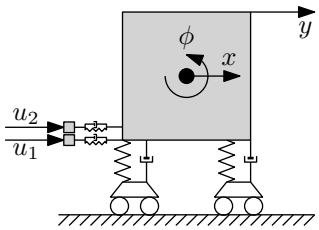

Figure 6.10. The system in Figure 6.6(a) extended with actuator dynamics.

and $\lambda(A_{bb} - A_{bf}J) = \{0.75, -0.8, 0.85, 0.9, 0.95\}$.

Figure 6.11 shows the input signals for the dynamic squaring-down approach and the norm-optimal feedforward solution, see Section 3.4.3. Both solutions yield exact tracking by design, with the key difference that the squaring-down approach avoids the use of pre-actuation. Similar as for static squaring-down, the input signals are relatively large in magnitude.

The results show how the additional design freedom at the inputs is exploited in the proposed approach to obtain exact tracking without pre-actuation. The results also show that a suitable static compensator may not always exist, as also observed in Example 6.5.

6.8 Experimental validation on an overactuated system

In this section, the squaring-down approach is validated in experiments by comparing it to traditional inversion approaches. The results demonstrate the high

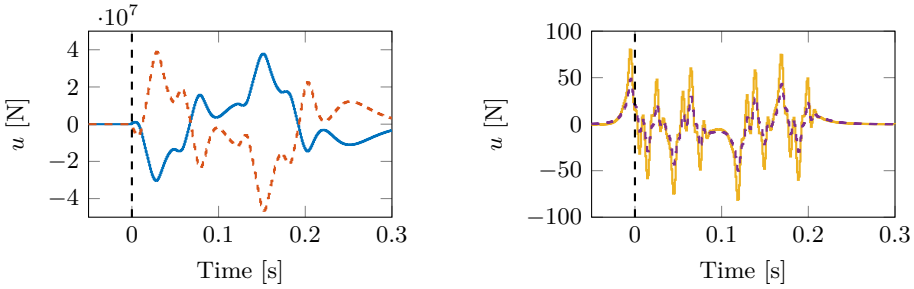

(a) Dynamic squaring down: u_1 (——) and u_2 (- - -).

(b) Norm-optimal feedforward: u_1 (——) and u_2 (- - -).

Figure 6.11. Input signals for the system in Figure 6.10. The dynamic squaring-down approach avoids the use of pre-actuation, but results in large input signals.

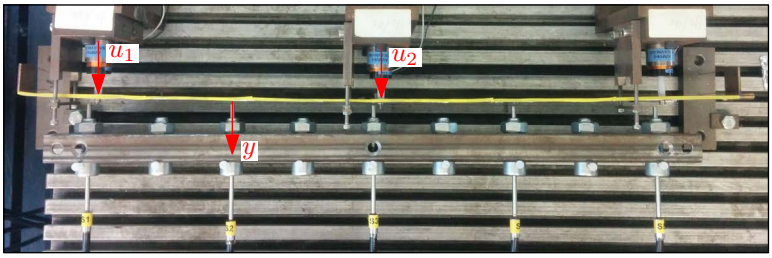

Figure 6.12. Top view of the experimental system. The system consists of the suspended beam in yellow with actuation in horizontal direction through actuators u_1, u_2 and position measurement through encoder y.

tracking performance of the squaring-down approach, without requiring pre-actuation or preview, and constitute Contribution 6.VI.

6.8.1 Experimental system

The motion system consists of a thin, suspended beam and is shown in Figure 6.12. For the experiments, the actuators u_1, u_2 and encoder y are used and the control architecture in Figure 6.2(a) is considered. The system has a stroke of 1 mm. The reference trajectory r is a forward and backward movement over 0.7 mm as shown in Figure 6.13.

The measured frequency response function of the system is shown in Figure 6.14 together with the identified 14th order parametric model H in (6.1) obtained using the procedure in Voorhoeve et al. (2018). Both transfer functions $u_1 \mapsto y$ and $u_2 \mapsto y$ are nonminimum phase and hence only using one

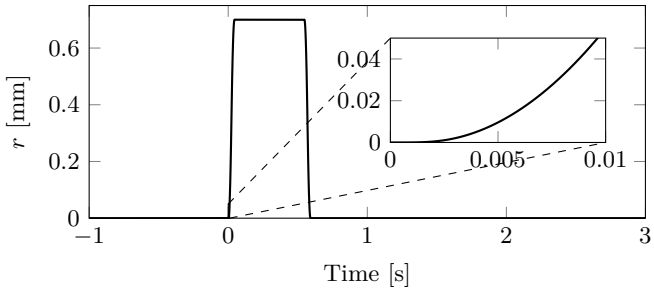

Figure 6.13. Reference trajectory r is a forward and backward movement constructed from fourth order polynomials.

input would require pre-actuation to ensure bounded signals, see also Example 6.4. The non-square system H is minimum phase, i.e., the x_a-dynamics in Theorem 6.7 are non-existing. Hence, the feedforward control design framework in Section 6.6 enables exact inversion with bounded inputs and without pre-actuation.

6.8.2 Controllers: Squaring down and norm optimal

The static and dynamic squaring-down solutions are compared with the commonly used norm-optimal feedforward solution. Table 6.1 provides an overview of the controllers. In this section, the controller designs are presented. The experimental results are presented in Section 6.8.3.

The inversion approach in Figure 6.5 is used to construct stable controllers to avoid the use of pre-actuation. A static compensator design, see Theorem 6.8, that satisfies this requirement is feasible. The poles of the static squaring-down controller F_{stat} are visualized in Figure 6.15. The input signals u_1, u_2 that are generated by the controller are shown in Figure 6.16. It turns out that, due to the limited design freedom of a static compensator in combination with the requirement of no pre-actuation, only oscillatory input signals can be generated. Moreover, there is a large difference in the magnitude of u_1 and u_2, which might be undesired in view of actuator constraints.

To avoid oscillatory input signals and better balance u_1 and u_2, a dynamic squaring-down controller F_{dyn} is designed. The oscillatory behavior in the inputs of F_{stat} is caused by low damping since the poles of F_{stat} are close to the unit circle, see Figure 6.15. Using the additional design freedom of a dynamic compensator compared to a static compensator, the poles of F_{dyn} are placed farther from the unit circle as shown in Figure 6.17. Similar to controller F_{stat}, controller F_{dyn} is stable and hence no pre-actuation is required. The input signals that are generated by the controller are shown in Figure 6.16 and, as desired, show less oscillatory behavior than those generated by F_{stat}.

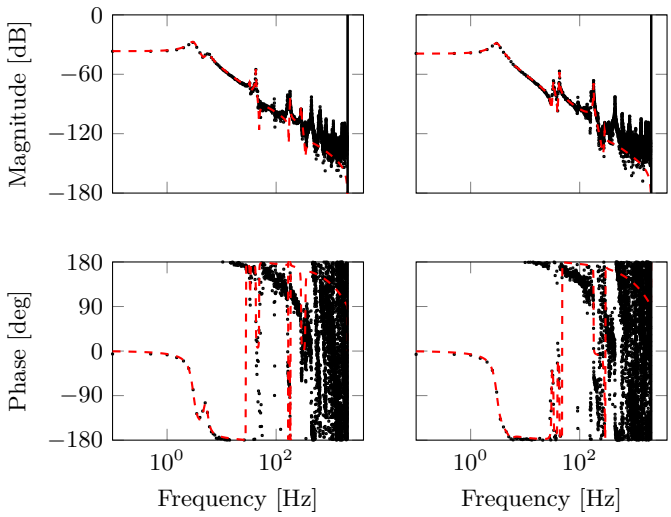

Figure 6.14. Frequency response function measurement (•) and identified 14th order model (- - -) of the experimental system in Figure 6.12 from inputs u_1, u_2 to output y.

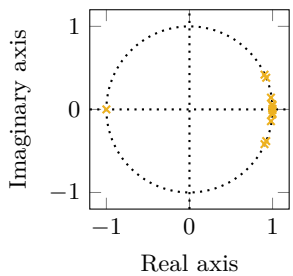

Figure 6.15. Pole locations of the static squaring-down controller F_{stat}, see also Lemma 6.13.

Table 6.1. Settings for the different controller designs. Controller F_{norm} uses preview and serves as a benchmark to compare the squaring-down controllers F_{stat}, F_{dyn}, which do not require preview.

Label	Type	Reference	Parameters	Preview
F_{norm}	Norm-optimal	Section 3.4.3	$Q = 1$; $R = \left[\begin{smallmatrix} 0 & 0 \\ 0 & 0 \end{smallmatrix}\right]$	Yes
F_{stat}	Static squaring-down	Theorem 6.8	Figure 6.15	No
F_{dyn}	Dynamic squaring-down	Theorem 6.11	Figure 6.17	No

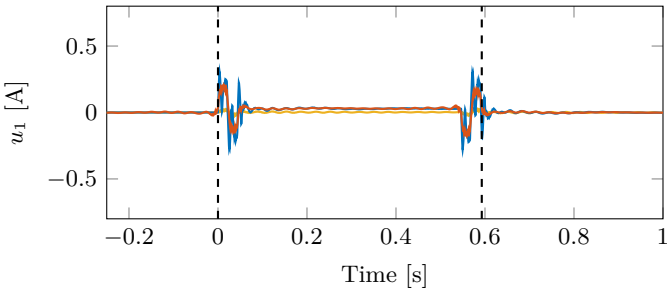

(a) Input signal u_1.

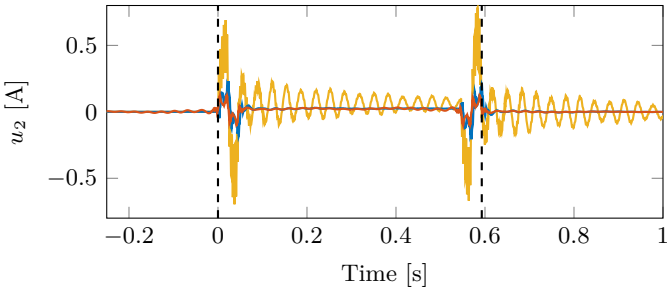

(b) Input signal u_2.

Figure 6.16. Input signals for the norm-optimal controller F_{norm} (——), the static squaring-down controller F_{stat} (——), and the dynamic squaring-down controller F_{dyn} (——). Input u_2 of F_{stat} has undesired oscillations. Controller F_{norm} yields pre-actuation, i.e., non-zero input before $t = 0$. Controller F_{dyn} yields smooth and causal inputs.

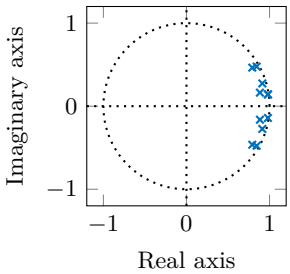

(a) Observer poles $\lambda(N)$.

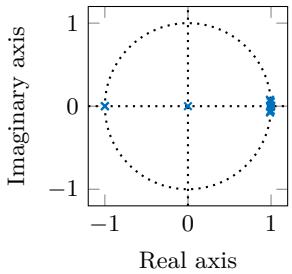

(b) Additional invariant zeros $\lambda(A_{bb} - A_{bf}J)$.

Figure 6.17. Pole locations of the dynamic squaring-down controller F_{dyn}, see also Lemma 6.14.

Table 6.2. Experimental results for the different controller designs in Table 6.1. The dynamic squaring-down controller F_{dyn} achieves superior performance in terms of both $\|e\|_\infty$ and $\|e\|_2$.

Label	$\|u_1\|_\infty$ [A]	$\|u_2\|_\infty$ [A]	$\|e\|_2$ [mm]	$\|e\|_\infty$ [mm]
F_{norm}	0.201	0.126	0.075	1.999
F_{stat}	0.028	0.785	0.080	2.025
F_{dyn}	0.308	0.231	0.064	1.774

The squaring-down approaches are compared with norm-optimal feedforward. Norm-optimal feedforward, see Section 3.4.3, is directly applicable to non-square systems, but requires preview, i.e., a priori knowledge of trajectory r. The weights of the performance criterion, i.e., Q for the error $e = r - y$ and R for the input $\left[\begin{smallmatrix} u_1 \\ u_2 \end{smallmatrix}\right]$, see also Section 3.4.3, are selected to minimize the error without restricting the input signals, see Table 6.1. The input signals are shown in Figure 6.16. Importantly, the controller requires preview of the entire reference trajectory r as well as pre-actuation, whereas this is not the case for the static and dynamic squaring-down controllers.

6.8.3 Experimental results

In simulation, all controllers achieve perfect tracking. However, in experiments the tracking is non-perfect due to model mismatches as shown by the tracking error signals $e = r - y$ for the different controllers in Figure 6.18. Due to pre-actuation and model mismatches, there is a non-zero error with F_{norm} for $t < 0$ in Figure 6.18(a), i.e., before any movement is required. Controller F_{stat} shows oscillatory behavior as a consequence of the oscillatory input in Figure 6.16 and model mismatches. The smallest error is achieved with the dynamic squaring-down controller F_{dyn}, see also Table 6.2.

The controller designs and experimental results are summarized in Table 6.1 and Table 6.2. The results show that the dynamic squaring-down controller outperforms the static squaring-down and the norm-optimal controllers. Importantly, both the static and dynamic squaring-down controllers do not require preview, i.e., they do not require a priori knowledge of the reference trajectory, in contrast to the norm-optimal controller.

6.9 Conclusion and outlook

In this chapter, system inversion is investigated and in particular from the perspective of squaring down. This leads to new insights that enable causal and exact feedforward for overactuated systems. An inversion approach is presented that does not require preview or pre-actuation for nonminimum-phase systems. The approach exploits the additional design freedom in overactuated systems

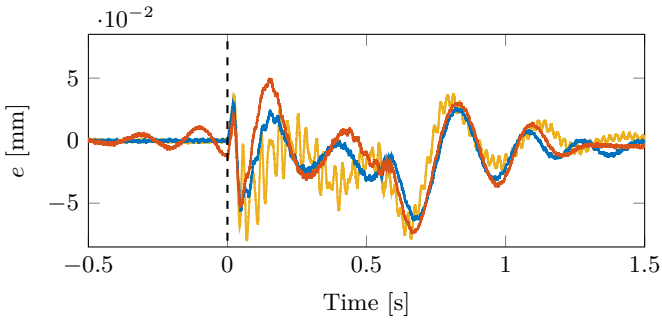

(a) Time domain signals.

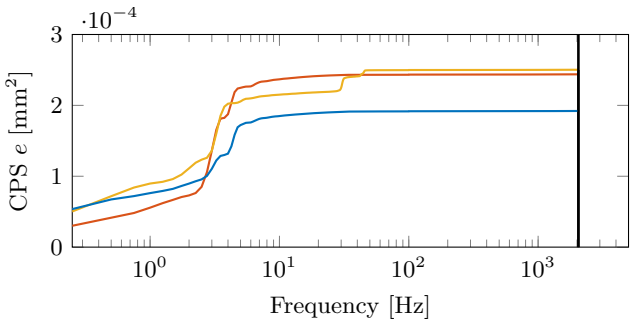

(b) Cumulative power spectra.

Figure 6.18. Error $e = r - y$ in the time and frequency domain for controllers F_{norm} (——), F_{stat} (——), and F_{dyn} (——). Due to model mismatches the tracking is non-perfect. The dynamic squaring-down controller F_{dyn} achieves the highest performance.

and the fact that non-square systems generally have no invariant zeros. Experimental results demonstrate superior tracking performance without requiring preview of pre-actuation.

The approach provides a systematic method to exploit overactuation to the benefit of control. Besides inverse model feedforward, the approach is also of interest to feedback control design by creating a square system with favorable properties, such as nonminimum-phase behavior.

Future research focuses on taking model uncertainty into account and using the available design freedom in overactuated systems to create robustness.

6.A Construction of coordinate basis

The coordinate basis in Theorem 6.7 is obtained through the following steps.

Step 1: Separate direct feedthrough

Let $\hat{D} = USV^\top$ be the singular value decomposition of $\hat{D}$, with $U \in \mathbb{R}^{p\times p}$, $V \in \mathbb{R}^{m\times m}$, and $S = \begin{bmatrix} S_{m_0} & 0 \\ 0 & 0 \end{bmatrix} \in \mathbb{R}^{p\times m}$, where $S_{m_0} \in \mathbb{R}^{m_o\times m_0}$ with $m_0 = \operatorname{rank}\{\hat{D}\}$ is a diagonal matrix with the singular values on the diagonal. Then $\Gamma_{o,1}^{-1}\hat{\Sigma}\Gamma_{i,1}$, with $\hat{\Sigma}$ in (6.13), $\Gamma_{o,1} = U$, and $\Gamma_{i,1} = V^{-\top}\begin{bmatrix} S_{m_0} & 0 \\ 0 & I_{m-m_0} \end{bmatrix}^{-1}$, admits the representation

$$x_1[k+1] = A_1 x_1[k] + B_{x,1}u_{x,1}[k] + B_{0,1}y_{0f,1}[k], \tag{6.27a}$$
$$y_{0f,1}[k] = C_{0f,1}x_1[k] + u_{0,1}[k], \tag{6.27b}$$
$$y_{xf,1}[k] = C_{xf,1}x_1[k], \tag{6.27c}$$
$$y_{s,1}[k] = C_{s,1}x_1[k], \tag{6.27d}$$

with $A_1 = \hat{A} - B_{0,1}C_{0f,1}$.

Step 2: Separate x_f

To separate x_f, find invertible $\Gamma_{s,2}$ such that $\Gamma_{s,2}^{-1}B_{x,1} = \begin{bmatrix} & 0 & \\ \times & \ddots & 0 \\ \vdots & & \\ \times & \cdots & \times \end{bmatrix}$ and $C_{xf,1}\Gamma_{s,2} = \begin{bmatrix} 0 & \begin{matrix} \times & \cdots & \times \\ & \ddots & \vdots \\ 0 & & \times \end{matrix} \end{bmatrix}$, where $\times$ are arbitrary elements. Such transformations can be found by considering the last row/column pairs in $C_{xf,1}$ and $B_{x,1}$, and working back as follows.

(i) Let the column/row pair be given by

$$\begin{bmatrix} b_1 \\ b_2 \\ b_3 \\ \vdots \end{bmatrix} \in \mathbb{R}^n, \qquad \begin{bmatrix} c_1 & c_2 & c_3 & \dots \end{bmatrix} \in \mathbb{R}^n. \tag{6.28}$$

(ii) Find matrices $P = Q^{-1} \in \mathbb{R}^{2\times 2}$, such that $P\begin{bmatrix} b_1 \\ b_2 \end{bmatrix} = \begin{bmatrix} 0 \\ \tilde{b}_2 \end{bmatrix}$ and $\begin{bmatrix} c_1 & c_2 \end{bmatrix} Q = \begin{bmatrix} 0 & \tilde{c}_2 \end{bmatrix}$. If P, Q exist, there exist unitary P, Q or P, Q such that $|\det(P)| = |\det(Q)| = 1$. If P, Q do not exist, a random (unitary) transformation may be applied and the procedure can be restarted.

(iii) Repeat the previous step for the pair $\begin{bmatrix} \tilde{b}_2 \\ b_3 \end{bmatrix}$, $\begin{bmatrix} \tilde{c}_2 & c_3 \end{bmatrix}$, and so on.

The process is repeated until all pairs and rows/columns are processed and the desired structure is obtained. The concatenation of all P, Q yields $\Gamma_{s,2}$.

Step 3: Separate x_a

The invariant zeros z_i, $i = 1, 2, \ldots, n_a$ are given by Definition 6.1. Let $A_2 = \Gamma_{s,2}^{-1} A_1 \Gamma_{s,2}$. To separate x_a, an eigenvalue decomposition can be used to obtain invertible $\Gamma_{s,3}$ such that

$$\Gamma_{s,3}^{-1} A_2 \Gamma_{s,3} = \begin{bmatrix} z_1 & & & & & \\ & \ddots & & & & \\ & & z_{n_a} & & & \\ & & & \times & \cdots & \times \\ & & & \vdots & \ddots & \vdots \\ & & & \times & \cdots & \times \end{bmatrix}, \tag{6.29}$$

where the structure related to x_f remains unaltered.

Step 4: Make y_s independent of x_f and $y_f = x_f$

Let the output matrix after step 3 be given by

$$C_3 = \begin{bmatrix} \begin{matrix} \times & \cdots & \times \\ \vdots & \ddots & \vdots \\ \times & \cdots & \times \end{matrix} & \begin{matrix} \times & \cdots & \times \\ \vdots & \ddots & \vdots \\ \times & \cdots & \times \end{matrix} & \begin{matrix} \times & \cdots & \times \\ \vdots & \ddots & \vdots \\ \times & \cdots & \times \end{matrix} \\ 0 & 0 & C_{xff,3} \\ 0 & \begin{matrix} \times & \cdots & \times \\ \vdots & \ddots & \vdots \\ \times & \cdots & \times \end{matrix} & C_{sd,3} \end{bmatrix}. \tag{6.30}$$

Then $\Gamma_{o,4} = \begin{bmatrix} I_{m_0} & 0 & 0 \\ 0 & C_{xff,3} & 0 \\ 0 & C_{sd,3} & I_{p-m} \end{bmatrix}$ yields

$$\Gamma_{o,4}^{-1} C_3 = \begin{bmatrix} \begin{matrix} \times & \cdots & \times \\ \vdots & \ddots & \vdots \\ \times & \cdots & \times \end{matrix} & \begin{matrix} \times & \cdots & \times \\ \vdots & \ddots & \vdots \\ \times & \cdots & \times \end{matrix} & \begin{matrix} \times & \cdots & \times \\ \vdots & \ddots & \vdots \\ \times & \cdots & \times \end{matrix} \\ 0 & 0 & I \\ 0 & \begin{matrix} \times & \cdots & \times \\ \vdots & \ddots & \vdots \\ \times & \cdots & \times \end{matrix} & 0 \end{bmatrix}. \tag{6.31}$$

which makes y_s independent of x_f and $y_f = x_f$.

This concludes the derivation of the coordinate basis in Theorem 6.7.

Chapter 7

Multirate control with basis functions

Motion systems with multiple control loops often run at a single sampling rate for simplicity of implementation and controller design. The achievable performance in terms of position accuracy is determined by the data acquisition hardware, such as sensors, actuators, and analog-to-digital/digital-to-analog converters, which is typically limited due to economic cost considerations. The aim of this chapter is to develop a multirate approach to go beyond this traditional performance/cost trade-off as illustrated in Figure 1.3. In particular, different sampling rates in different control loops are used to optimally use hardware resources. Note that such a multirate control approach is different from multirate inversion as used in Chapter 5. The multirate approach appropriately deals with the inherent time-varying behavior that is introduced by multirate sampling. A multirate feedforward control design framework with basis functions is presented to optimize tracking of a dual-stage multirate system. Application of the proposed approach to an industrial dual-stage wafer system demonstrates the advantages of multirate control, both in simulations and experiments. The results constitute Contribution IV.A.

The contents of this chapter also appear in:
Jurgen van Zundert, Tom Oomen, Jan Verhaegh, Wouter Aangenent, Duarte J. Antunes, and W.P.M.H. Heemels. Beyond Performance/Cost Trade-Offs in Motion Control: A Multirate Feedforward Design with Application to a Dual-Stage Wafer System. *Accepted for IEEE Transactions on Control Systems Technology*, 2018.

7.1 Introduction

Multivariable control systems, including those in motion systems, are often implemented digitally since it offers flexibility and directly connects to the digital supervisory layers. The digital implementation requires analog-to-digital and digital-to-analog conversion. For motion systems, these processes are often executed using fixed, single-rate sampling schemes (Chen and Francis, 1995; Åström and Wittenmark, 1997), i.e., homogeneous for all loops, since for linear time-invariant (LTI) systems it enables controller design using well-developed design approaches. In particular, it allows the use of frequency domain techniques such as Bode plots and Nyquist diagrams (Skogestad and Postlethwaite, 2005), which find application in various areas of controller design, including feedback control (Skogestad and Postlethwaite, 2005; Franklin et al., 2015), feedforward control (Steinbuch et al., 2010), and iterative learning control (Bristow et al., 2006).

Fixed, single-rate sampling is preferred from a controller design point of view, but not from a performance versus cost point of view. As an example, consider systems with multiple control loops, where only one limits the overall performance. The performance of a control loop can be increased by increasing the sampling frequency of that loop. For single-rate implementations this implies that if the performance of one of the loops is increased, the sampling frequency of all loops needs to be increased. Obviously, such an approach is expensive in terms of the required hardware, such as sensors, actuators, and analog-to-digital/digital-to-analog converters, since all loops are affected while only one is limiting performance.

From a performance versus cost point of view, flexible sampling is preferred over fixed sampling, see also Figure 7.1. Examples of flexible sampling include multirate control (Glasson, 1983; Salt and Tomizuka, 2014; Salt and Albertos, 2005; Lall and Dullerud, 2001; Ohnishi et al., 2017; Chen and Xiao, 2016; Ding et al., 2006; Lee, 2006; Fujimoto et al., 2001; Antunes and Heemels, 2016), sparse control (Oomen and Rojas, 2017), and non-equidistant sampling (Chapter 8; Valencia et al., 2016). Indeed, a multirate approach is more natural for multiloop systems with different performance requirements, but also for systems with different time scales such as thermomechanical systems (Fraser et al., 1999). Sparse control and non-equidistant sampling are used in, e.g., systems with limited resources and optimal resource allocation (Valencia et al., 2016; Aminifar et al., 2016).

Flexible sampling has a large potential, but its deployment is hampered by a lack of control design techniques. This is mainly caused by the fact that flexible sampling introduces time-varying behavior (Chen and Francis, 1995, Section 3.3). In particular, flexible sampling of a linear time-invariant (LTI) system yields a linear (periodically) time-varying (L(P)TV) system. Due to the time variance, the frequency domain control design techniques mentioned earlier are not (directly) applicable. Frequency domain design for linear time-varying

systems is investigated in Chapter 2; Lindgärde and Lennartson 1997; Cantoni and Glover 1997; Sandberg et al. 2005; Oomen et al. 2007 and linear time-varying feedforward design is investigated in Oomen et al. 2009; Chapter 8, but at present there is no systematic control design framework available.

Although flexible sampling has the potential to go beyond the traditional performance/cost trade-off for fixed sampling, as shown in Figure 7.1, at present its deployment is hampered by a lack of control design techniques for such sampling schemes. In this chapter, a framework to exploit multirate feedforward controller design is presented to overcome this restriction and thereby go beyond the traditional performance/cost trade-off. Application of the framework focuses on precision motion systems. In particular, the framework is demonstrated on an experimental dual-stage system, as standard in, e.g., wafer stages (Munnig Schmidt et al., 2011, Chapter 9).

The main contribution of this chapter is a framework to exploit multirate control for performance improvement. The following subcontributions are identified.

7.I Multirate controller design based on multirate system descriptions, including time variance.

7.II Controller optimization addressing non-perfect models.

7.III Performance improvement by exploiting time variance.

7.IV Application of the design framework in simulation.

7.V Experimental validation on a dual-stage system.

Related work on minimizing intersample behavior in digital control systems can be found in Bamieh et al. (1991); Chen and Francis (1995); Oomen et al. (2007). Related work on wafer stage control design includes feedback control (Van de Wal et al., 2002; Heertjes et al., 2016), feedforward control (Butler, 2013), LPV control (Groot Wassink et al., 2005), and sparse control (Oomen and Rojas, 2017). In the present work, previously unexplored freedom in sampling is exploited, which makes the approach complementary to other approaches.

This chapter is organized as follows. In Section 7.2, the main problem that is considered to improve the performance/cost trade-off through multirate control is presented. In Section 7.3, the multirate control system is modeled. The multirate controller design is presented in Section 7.4. Furthermore, the performance is further improved by exploiting properties of time-varying systems. The controller design is applied to an experimental setup resembling a dual-stage wafer system. The experimental setup is detailed in Section 7.5. Simulation results are presented in Section 7.6 and experimental results are presented in Section 7.7. Conclusions are given in Section 7.8.

Notation. Matrix variables are underlined, with $\underline{I}_n$ the $n \times n$ identity matrix, $\underline{0}_{m\times n}$ the $m \times n$ zero matrix, $\underline{1}_n$ the $n \times 1$ ones vector with all elements 1, and

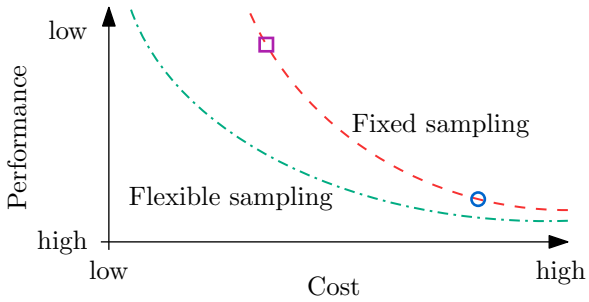

Figure 7.1. A low sampling frequency is inexpensive in terms of implementation cost, but yields low performance (□). A high sampling frequency yields high performance, but is expensive (○). This performance/cost trade-off is inherent to traditional fixed sampling (- - -). Flexible sampling goes beyond this trade-off through use of different sampling frequencies in different control loops. Essentially, the performance/cost trade-off can be decided upon per control loop, resulting in an improved overall trade-off (-·-·-).

$\underline{e}_n$ the $n \times 1$ unit vector with the first element 1 and others 0. Vector $\underline{\alpha} \in \mathbb{R}^N$, $N \in \mathbb{N}$, is given by $\underline{\alpha} = \begin{bmatrix}\alpha[0] & \alpha[1] & \dots & \alpha[N-1]\end{bmatrix}^\top$, with transpose $(\cdot)^\top$ and $\|\underline{\alpha}\|_2^2 = \underline{\alpha}^\top \underline{\alpha}$. The Kronecker product is denoted $\otimes$ and $\mathrm{diag}\{(\cdot)\}$ denotes a diagonal matrix with diagonal entries $(\cdot)$. The floor operator is given by $\lfloor x \rfloor = \max\{m \in \mathbb{Z} \mid m \leq x\}$. The discrete-time delay operator is denoted z^{-1}.

7.2 Problem definition

In this chapter, a framework is presented to enhance the performance/cost trade-off through multirate control. In this section, the main problem is presented.

7.2.1 Application motivation: Dual-stage motion systems with large differences in performance requirements

In many motion control applications, a high positioning accuracy is required over a large range. For such systems, a single-stage design may not suffice due to the large dynamic range. To achieve high precision over a large range, a dual-stage system can be used.

A dual-stage system, as illustrated in Figure 7.2, consists of two subsystems: a short stroke with a high positioning accuracy (and limited range) connected to a long stroke with a large range (and limited positioning accuracy). If designed properly, the dual-stage system is able to cover a large range with high positioning accuracy. Clearly, there is a large difference between the performance requirements of the two subsystems.

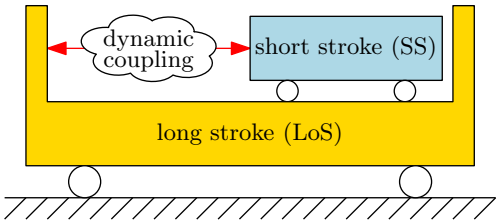

Figure 7.2. Dual-stage systems consist of two subsystems: a short stroke for high precision and a long stoke to cover large ranges. The combined system provides high positioning accuracy over a large range.

An example of a dual-stage system is a wafer stage in lithography machines (Munnig Schmidt et al., 2011, Chapter 9). Wafer stages require an accuracy up to nanometer level over a range of one meter (Butler, 2011; Munnig Schmidt et al., 2011, Section 9.3.1), resulting in a large dynamic range of $\mathcal{O}(10^9)$. Therefore, wafer stages are typically constructed as dual-stage systems. More details on the wafer stage application are presented in Section 7.5.

7.2.2 A performance/cost perspective on multivariable systems with large differences in performance requirements

In view of the performance/cost trade-off in Figure 7.1, the different (control) requirements for the subsystems of the dual-stage design provide an excellent opportunity to exploit multirate control to go beyond performance/cost trade-offs in motion control.

The considered multirate control architecture is shown in Figure 7.3 where a high sampling frequency f_h is used for the short stroke $G_{SS,h}$ (○ in Figure 7.1) and a low sampling frequency f_l is used for the long stroke $G_{LoS,l}$ to reduce cost (□ in Figure 7.1). The short-stroke system $G_{SS,h}$ tracks reference trajectory $\rho_{SS,h}$. The long-stroke system $G_{LoS,l}$ tracks the position of $G_{SS,h}$ to ensure the short stroke is within range and reaction forces are limited. The downsampler $\mathcal{D}_F$ facilitates the sampling rate conversion. The control design of both subsystems consists of feedback control (C_{FB}), feedforward control (C_{FF}), and input shaping (C_ψ).

For design of the long-stroke controllers, the interest is in the position error between the two stages during exposure, i.e., during the scanning motion, to limit reaction forces to the short stroke. This error measured at the highest possible sampling frequency f_* is denoted ε_* and not available for real-time control, but typically available afterwards for performance evaluation. The sampling

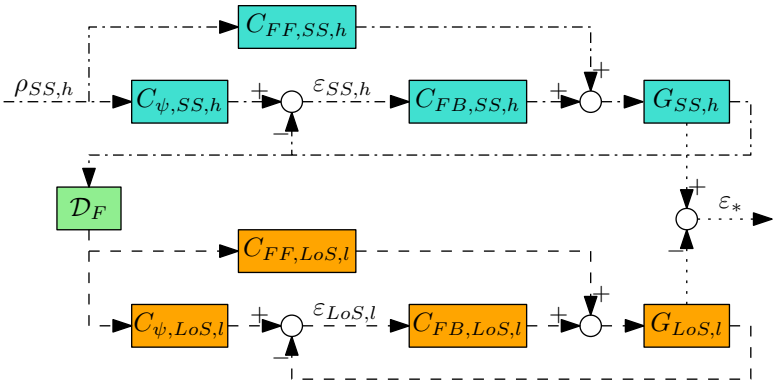

Figure 7.3. Multirate control configuration for a dual-stage system. The top part relates to the short stroke (SS) at high rate f_h. The bottom part relates to the long stroke (LoS) at low rate f_l. The long stroke tracks the output position of the short stroke, where downsampler $\mathcal{D}_F$ facilitates the sampling rate conversion. Dotted lines (·····) indicate extreme high sampling rates f_*, dashdotted lines (-·-·-) high sampling rates f_h, and dashed lines (- - -) low sampling rates f_l. Both control loops include a feedback controller C_{FB}, a feedforward controller C_{FF}, and an input shaper C_ψ. The objective is to minimize position difference ε_* through design of $C_{\psi,LoS,l}$ and $C_{FF,LoS,l}$.

frequencies are related by

$$f_* = F_h f_h = F_l f_l, \quad f_h = F f_l, \tag{7.1}$$

where $F_h \geq F_l \geq 1$, $F := \frac{F_l}{F_h}$, with $F_h, F_l, F \in \mathbb{N}$. In this chapter, finite-time signals are considered of which the signal lengths are related as

$$N_* = F_h N_h = F_l N_l, \quad N_h = F N_l \tag{7.2}$$

as directly follows from (7.1).

Remark 7.1. *The assumption of integer sampling rate factors in* (7.1) *is imposed for ease of notation, but can easily be relaxed if the factor is a rational number. The proposed approach is not applicable for irrational factors, although these can often be closely approximated with rational factors.*

7.2.3 Problem formulation: Framework for exploiting multirate sampling for enhanced control performance

In this chapter, the following problem is considered.

Main problem. *Given the multirate control configuration in Figure 7.3 with sampling frequencies admitting* (7.1)*, a given finite-time reference trajectory* $\underline{\rho}_{SS,h} \in \mathbb{R}^{N_h}$ *for* $\rho_{SS,h}$*, models* $G_{SS_*}, G_{LoS,*}$ *of* $G_{SS,h}, G_{LoS,l}$ *at sampling frequency* f_**, and controllers* $C_{FF,SS,h}$*,* $C_{\psi,SS,h}$*,* $C_{FB,SS,h}$*,* $C_{FB,LoS,l}$*, determine*

$$(C_{FF,LoS,l}, C_{\psi,LoS,l}) = \arg \min_{C_{FF,LoS,l}, C_{\psi,LoS,l}} \|\underline{\varepsilon}_*\|_2^2 , \tag{7.3}$$

where $\underline{\varepsilon}_* \in \mathbb{R}^{N_*}$ *denotes the position error* ε_* *over the considered interval.*

Controllers $C_{FF,SS,h}$, $C_{\psi,SS,h}$, $C_{FB,SS,h}$ are often available from earlier control designs based on the single-rate short-stroke system only, neglecting the long-stroke system and multirate aspects. A similar reasoning holds for $C_{FB,LoS,l}$. It is assumed that $C_{FB,SS,h}$ and $C_{FB,LoS,l}$ stabilize the short-stroke and long-stroke system, respectively. Note that stability is not affected by $C_{FF,LoS,l}$, $C_{\psi,LoS,l}$.

Importantly, control objective (7.3) incorporates the dynamics of the short stroke for design of the long-stroke controllers $C_{FF,LoS,l}, C_{\psi,LoS,l}$. Moreover, it considers $\underline{\varepsilon}_*$ rather than $\underline{\varepsilon}_{LoS,l}$ and thereby takes intersample behavior into account, which is an important aspect in multirate control (Oomen et al., 2007). Note that (7.3) is posed in terms of finite-time signals, rather than infinite-time signals, since, in practice, tasks have a finite length.

The presented framework allows to recover single-rate control as a special case of multirate control by setting $F_h = F_l$. In Section 7.6 and Section 7.7, multirate control is compared with single-rate control.

7.3 Multirate control system

In this section, the model-based multirate controller design is presented, which constitutes Contribution 7.I. In Section 7.3.1, the time-varying aspects of multirate systems are modeled. In Section 7.3.2, these models are used to describe the multirate control diagram in Figure 7.3. Based on these results, the multirate controller is presented in Section 7.4.

7.3.1 Modeling multirate systems: Time-varying aspects

In this section, building blocks to model the multirate system in Figure 7.3 are presented. The system is modeled over the finite-time length considered in the main problem in Section 7.2.3.

Consider a causal, single-input, single-output (SISO), discrete-time, linear time-invariant (LTI) system H with Markov parameters $h(k) \in \mathbb{R}$, $k = 0, 1, \ldots, N-1$. The mapping from the finite-time input $\underline{\alpha} \in \mathbb{R}^N$ to the finite-time output

$\underline{\beta} \in \mathbb{R}^N$ is given by $\underline{H} \in \mathbb{R}^{N\times N}$ via

$$\underline{\beta} = \underline{H}\underline{\alpha}, \tag{7.4}$$

$$\begin{bmatrix} \beta[0] \\ \beta[1] \\ \beta[2] \\ \vdots \\ \beta[N-1] \end{bmatrix} = \begin{bmatrix} h(0) & 0 & 0 & \cdots & 0 \\ h(1) & h(0) & 0 & \cdots & 0 \\ h(2) & h(1) & h(0) & \cdots & 0 \\ \vdots & \vdots & \vdots & \ddots & \vdots \\ h(N-1) & h(N-2) & h(N-3) & \cdots & h(0) \end{bmatrix} \begin{bmatrix} \alpha[0] \\ \alpha[1] \\ \alpha[2] \\ \vdots \\ \alpha[N-1] \end{bmatrix}. \tag{7.5}$$

Since $\underline{\alpha}, \underline{\beta}$ have the same sampling frequency, $\underline{H}$ is square. Moreover, since H is causal and time-invariant, $\underline{H}$ is lower triangular and Toeplitz, respectively (Chen and Francis, 1995).

The multirate system in Figure 7.3 involves different sampling frequencies. The conversions between the different sampling frequencies are given as follows, see also (Vaidyanathan, 1993, Section 4.1.1) and (Oomen et al., 2007, Definition 5). Let $\underline{\alpha} \in \mathbb{N}^{FN}$, $F, N \in \mathbb{N}$, then the downsampling operator $\mathcal{D}_F : \mathbb{R}^{FN} \mapsto \mathbb{R}^N$ with factor F yields $\underline{\beta} = \mathcal{D}_F(\underline{\alpha}) \in \mathbb{R}^N$ where

$$\beta[k] = \alpha[Fk], \quad k = 0, 1, \ldots, N-1. \tag{7.6}$$

Let $\underline{\alpha} \in \mathbb{R}^N$, $N \in \mathbb{N}$, then the upsampling operator $\mathcal{S}_{u,F} : \mathbb{R}^N \mapsto \mathbb{R}^{FN}$ with factor $F \in \mathbb{N}$ yields $\underline{\beta} = \mathcal{S}_{u,F}(\underline{\alpha}) \in \mathbb{R}^{FN}$ where

$$\beta[k] = \begin{cases} \alpha[\frac{k}{F}], & k = 0, F, 2F, \ldots, (N-1)F, \\ 0, & \text{otherwise.} \end{cases} \tag{7.7}$$

The upsampling operator inserts zeros in between the values of the low rate signal to create a high rate signal. The interpolation is performed using a zero-order-hold interpolator. In terms of discrete-time transfer functions, the zero-order-hold interpolator with factor $F \in \mathbb{N}$ is defined as

$$\mathcal{I}_{ZOH,F} = \sum_{f=0}^{F-1} z^{-f}. \tag{7.8}$$

The zero-order-hold interpolator is used in combination with the upsampling operator for upsampling. The resulting zero-order-hold upsampler is defined by $\mathcal{H}_F := \mathcal{I}_{ZOH,F}\,\mathcal{S}_{u,F}$, i.e., let $\underline{\alpha} \in \mathbb{R}^N$, $N \in \mathbb{N}$, then $\mathcal{H}_F$ with factor $F \in \mathbb{N}$ yields $\underline{\beta} = \mathcal{H}_F(\underline{\alpha}) \in \mathbb{R}^{FN}$ where

$$\beta[k] = \alpha[\lfloor \tfrac{k}{F} \rfloor], \quad k = 0, 1, \ldots, (N-1)F. \tag{7.9}$$

The system description and controller design are based on finite-time descriptions. The finite-time description of the downsampling operator $\mathcal{D}_F$ with factor $F \in \mathbb{N}$ is given by

$$\underline{\mathcal{D}}_F = \underline{I}_N \otimes \underline{e}_F^\top \in \mathbb{R}^{N\times FN}, \tag{7.10}$$

i.e., let $\underline{\alpha} \in \mathbb{R}^{FN}$, $N \in \mathbb{N}$ and let $\underline{\beta} \in \mathbb{R}^N$ be given by (7.6), then $\underline{\beta} = \underline{\mathcal{D}}_F \underline{\alpha}$ with $\underline{\mathcal{D}}_F$ in (7.10). The finite-time description of the zero-order-hold upsampling operator $\mathcal{H}_F$ with factor $F \in \mathbb{N}$ is given by

$$\underline{\mathcal{H}}_F = \underline{I}_N \otimes \underline{1}_F \in \mathbb{R}^{FN \times N}, \tag{7.11}$$

i.e., let $\underline{\alpha} \in \mathbb{R}^N$, $N \in \mathbb{N}$ and let $\underline{\beta} \in \mathbb{R}^{FN}$ be given by (7.9), then $\underline{\beta} = \underline{\mathcal{H}}_F \underline{\alpha}$ with $\underline{\mathcal{H}}_F$ in (7.11). Examples of $\underline{\mathcal{D}}_F$ and $\underline{\mathcal{H}}_F$ are provided by Example 7.2.

Example 7.2 (Downsampler and upsampler)**.** *Let $F = 2$, $N = 3$, then $\underline{\mathcal{D}}_F$ in* (7.10) *and $\underline{\mathcal{H}}_F$ in* (7.11) *are given by*

$$\underline{\mathcal{D}}_F = \begin{bmatrix} 1 & 0 & 0 & 0 & 0 & 0 \\ 0 & 0 & 1 & 0 & 0 & 0 \\ 0 & 0 & 0 & 0 & 1 & 0 \end{bmatrix}, \qquad \underline{\mathcal{H}}_F = \begin{bmatrix} 1 & 0 & 0 \\ 1 & 0 & 0 \\ 0 & 1 & 0 \\ 0 & 1 & 0 \\ 0 & 0 & 1 \\ 0 & 0 & 1 \end{bmatrix}. \tag{7.12}$$

Let $\underline{\alpha} = \begin{bmatrix} 1 & 2 & 3 & 4 & 5 & 6 \end{bmatrix}^\top$, then $\underline{\beta} := \mathcal{D}_F(\underline{\alpha}) = \underline{\mathcal{D}}_F \underline{\alpha} = \begin{bmatrix} 1 & 3 & 5 \end{bmatrix}^\top$ and $\underline{\gamma} := \mathcal{H}_F(\underline{\beta}) = \underline{\mathcal{H}}_F \underline{\beta} = \begin{bmatrix} 1 & 1 & 3 & 3 & 5 & 5 \end{bmatrix}^\top$. Note that $\underline{\gamma} = \underline{\mathcal{H}}_F \underline{\mathcal{D}}_F \underline{\alpha} \neq \underline{\alpha}$, since

$$\underline{\mathcal{H}}_F \underline{\mathcal{D}}_F = \begin{bmatrix} 1 & 0 & 0 & 0 & 0 & 0 \\ 1 & 0 & 0 & 0 & 0 & 0 \\ 0 & 0 & 1 & 0 & 0 & 0 \\ 0 & 0 & 1 & 0 & 0 & 0 \\ 0 & 0 & 0 & 0 & 1 & 0 \\ 0 & 0 & 0 & 0 & 1 & 0 \end{bmatrix} \neq \underline{I}_6. \tag{7.13}$$

Example 7.2 shows that down-up sampling affects the signal. More generally, using the Kronecker mixed-product property

$$(\underline{A} \otimes \underline{B})(\underline{C} \otimes \underline{D}) = (\underline{AC}) \otimes (\underline{BD}), \tag{7.14}$$

it can be shown that

$$\underline{\mathcal{D}}_F \underline{\mathcal{H}}_F = \underline{I}_N, \quad \underline{\mathcal{H}}_F \underline{\mathcal{D}}_F = \underline{I}_N \otimes (\underline{1}_F \underline{e}_F^\top) \neq \underline{I}_{FN}. \tag{7.15}$$

A key observation is that up-down sampling $\underline{\mathcal{D}}_F \underline{\mathcal{H}}_F$ has no effect on the signal, whereas down-up sampling $\underline{\mathcal{H}}_F \underline{\mathcal{D}}_F$ does affect the signal. In fact, $\underline{\mathcal{H}}_F \underline{\mathcal{D}}_F$ is block Toeplitz with block size F, see also Example 7.2, and hence the down-up sampling operation is not LTI, but linear periodically time-varying (LPTV) with period F. An important consequence is that if an input-output operation involves any sampling rate lower than the input sampling rate, then the operation

is LPTV. Indeed, this is the case for the multirate control diagram in Figure 7.3, which is thus LPTV. The presented finite-time descriptions enable to exactly describe this time-varying multirate system.

In the following section, the multirate control diagram is presented, based on the finite-time descriptions presented in this section.

Remark 7.3. *A more general definition of the downsampler $\mathcal{D}_F$ in* (7.6) *is obtained by considering $\alpha \in \mathbb{R}^M$, $\beta \in \mathbb{R}^{\lceil \frac{M}{F} \rceil}$, $F, M \in \mathbb{N}$. For ease of notation, it is assumed that $M = FN$.*

7.3.2 Multirate control diagram

The full control diagram of the architecture in Figure 7.3 is shown in Figure 7.4 and includes the modeling of systems $G_{SS,h}$ and $G_{LoS,l}$. The systems are modeled through $G_{SS,*}$ and $G_{LoS,*}$ operating at the extremely high rate f_*, which approximate the underlying continuous-time systems G_{SS} and G_{LoS}, respectively. Here, $\mathcal{H}_*, \mathcal{S}_*$ are the continuous-time hold (digital-to-analog) and sampling (analog-to-digital converter). Recall that signals at rate f_* are not available for real-time feedback control. However, this approach enables evaluation of the tracking error ε_* at rate f_*.

To determine the optimal controllers, the relation between $C_{FF,LoS,l}, C_{\psi,LoS,l}$ and ε_* is required. The dependence of finite-time $\underline{\varepsilon}_*$ on $\underline{\rho}_{SS,h}$, $\underline{\nu}_{FF,LoS,l}$, $\underline{\rho}_{\psi,LoS,l}$ is given by Lemma 7.4.

Lemma 7.4. *Given the finite-time descriptions in Section 7.3.1, $\underline{\varepsilon}_*$ in Figure 7.4 is given by*

$$\underline{\varepsilon}_* = \underline{\psi}_{SS,*} - \underline{\mathcal{A}} \begin{bmatrix} \underline{\nu}_{FF,LoS,l} \\ \underline{\rho}_{\psi,LoS,l} \end{bmatrix}, \tag{7.16}$$

with

$$\underline{\psi}_{SS,*} = \underline{G}_{SS,*}\underline{\mathcal{H}}_{F_h}\underline{S}_{SS,h}\left(\underline{C}_{FF,SS,h} + \underline{C}_{FB,SS,h}\underline{C}_{\psi,SS,h}\right)\underline{\rho}_{SS,h}, \tag{7.17}$$

$$\underline{\mathcal{A}} = \underline{G}_{LoS,*}\underline{\mathcal{H}}_{F_l}\underline{S}_{LoS,l}\begin{bmatrix}\underline{I}_{N_l} & \underline{C}_{FB,LoS,l}\end{bmatrix}, \tag{7.18}$$

$$\underline{S}_{SS,h} = (\underline{I}_{N_h} + \underline{C}_{FB,SS,h}\underline{G}_{SS,h})^{-1}, \tag{7.19}$$

$$\underline{S}_{LoS,l} = (\underline{I}_{N_l} + \underline{C}_{FB,LoS,l}\underline{G}_{LoS,l})^{-1}. \tag{7.20}$$

Proof. See Appendix 7.A. □

An important observation in Lemma 7.4 is that $\underline{\mathcal{A}}$ includes sampling rate changes and hence the transfer function from $\underline{\nu}_{FF,LoS,l}$, $\underline{\rho}_{\psi,LoS,l}$ to $\underline{\varepsilon}_*$ is LPTV and cannot be described using traditional frequency domain transfer functions. In the next section, the controllers are designed.

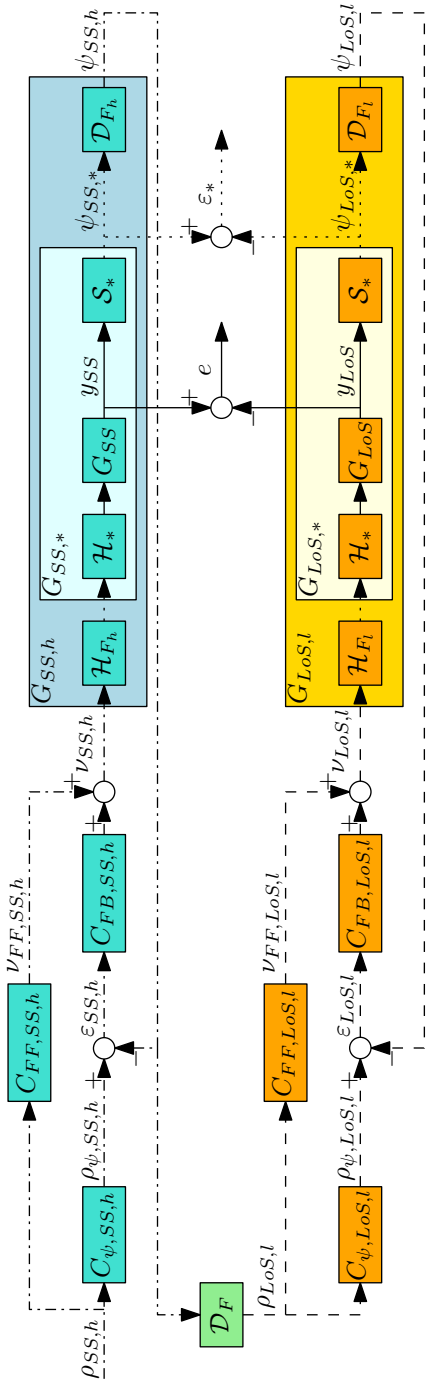

Figure 7.4. Multirate control architecture where the short-stroke (SS) loop (top part) runs at high rate f_h and the long-stroke (LoS) loop (bottom part) at low rate f_l. The interconnection is provided through downsampler $\mathcal{D}_F$. Error ε_* is an approximation of the continuous-time signal e at extreme high rate f_*. Solid lines (——) indicate continuous-time signals, dotted lines (·····) extreme high sampling rates f_*, dashdotted lines (-·-·-) high sampling rates f_h, and dashed lines (- - -) low sampling rates f_l. Both subsystems (G) are controlled through feedback (C_{FB}), feedforward (C_{FF}), and input shaping (C_ψ). The objective is to minimize ε_* through design of $C_{FF,LoS,l}$ and $C_{\psi,LoS,l}$ such that the long stroke tracks the short stroke. In this configuration, $C_{FF,LoS,l}$ and $C_{\psi,LoS,l}$ are implemented at the low rate, i.e., $f_c = f_l$.

7.4 Multirate controller design

In the previous section, the multirate system in Figure 7.4 was modeled. In this section, the controllers are parameterized and the optimal controller parameters are presented, constituting Contribution 7.II. Furthermore, the multirate system is further improved by modifying the controller implementation and design, which constitutes Contribution 7.III.

7.4.1 Controller parameterization

To address arbitrary reference trajectories, the feedforward and input shaping filters are parameterized in terms of basis functions, see, for example, Bolder et al. (2014); Bolder and Oomen (2015). Basis functions decouple the parameters from the reference trajectory, allowing variations in the reference trajectories without affecting the parameters. This is in contrast to standard learning approaches (Bristow et al., 2006) in which a command signal for one specific reference trajectory is learned.

Inspired by Boeren et al. (2014), controllers $C_{FF,LoS,l}, C_{\psi,LoS,l}$ are parameterized in terms of difference operators according to Definition 7.5. Note that $C_{FF,LoS,l}(\underline{0}) = 0$ and $C_{\psi,LoS,l}(\underline{0}) = 1$ such that if the parameters are zero, only feedback control is used.

Definition 7.5. *$C_{FF,LoS,l}$ and $C_{\psi,LoS,l}$ in Figure 7.4 are given by*

$$C_{FF,LoS,l}(\underline{\theta}_{FF}) = \sum_{i=0}^{n_{FF}-1} \theta_{FF}[i] \left(\frac{f_l(z-1)}{z}\right)^{i+1}, \tag{7.21}$$

$$C_{\psi,LoS,l}(\underline{\theta}_{\psi}) = 1 + \sum_{i=0}^{n_{\psi}-1} \theta_{\psi}[i] \left(\frac{f_l(z-1)}{z}\right)^{i+1}, \tag{7.22}$$

with design parameters $\underline{\theta}_{FF}$, $\underline{\theta}_{\psi}$.

Theorem 7.6 shows that $\underline{\nu}_{FF,LoS,l}$ and $\underline{\rho}_{\psi,LoS,l}$ depend affine on parameters $\underline{\theta}_{FF}$ and $\underline{\theta}_{\psi}$, respectively.

Theorem 7.6. *Given Definition 7.5, the finite-time descriptions of $\nu_{FF,LoS,l}$ and $\rho_{\psi,LoS,l}$ are given by*

$$\underline{\nu}_{FF,LoS,l} = \underline{C}_{FF,LoS,l}\underline{\mathcal{D}}_F\underline{\psi}_{SS,h} = \underline{\Phi}_{FF,l}\,\underline{\theta}_{FF}, \tag{7.23}$$

$$\underline{\rho}_{\psi,LoS,l} = \underline{C}_{\psi,LoS,l}\underline{\mathcal{D}}_F\underline{\psi}_{SS,h} \quad = \underline{\mathcal{D}}_F\underline{\psi}_{SS,h} + \underline{\Phi}_{\psi,l}\,\underline{\theta}_{\psi}, \tag{7.24}$$

with

$$\underline{\Phi}_{x,l} = \underline{\mathcal{D}}_F\underline{T}_{\psi_{SS,h}} \begin{bmatrix} \underline{I}_{n_x+1} \otimes \underline{e}_F \\ \underline{0}_{(N_h-F(n_x+1))\times(n_x+1)} \end{bmatrix} \underline{R}_{x,l}, \tag{7.25}$$

$$\underline{T}_{\psi_{SS,h}} = \begin{bmatrix} \psi_{SS,h}[0] & 0 & 0 & \cdots & 0 \\ \psi_{SS,h}[1] & \psi_{SS,h}[0] & 0 & \cdots & 0 \\ \psi_{SS,h}[2] & \psi_{SS,h}[1] & \psi_{SS,h}[0] & \cdots & 0 \\ \vdots & \vdots & \vdots & \ddots & \vdots \\ \psi_{SS,h}[N_h-1] & \psi_{SS,h}[N_h-2] & \psi_{SS,h}[N_h-3] & \cdots & \psi_{SS,h}[0] \end{bmatrix}, \tag{7.26}$$

$$\underline{R}_{x,l} = \begin{bmatrix} 1 & 1 & 1 & \dots & 1 \\ -1 & -2 & -3 & \dots & -n_x \\ 0 & 1 & 3 & \dots & * \\ 0 & 0 & -1 & \dots & * \\ \vdots & \vdots & \vdots & \ddots & \vdots \\ 0 & 0 & 0 & \dots & (-1)^{n_x} \end{bmatrix} \operatorname{diag}\{f_l^1, \dots, f_l^{n_x}\}, \tag{7.27}$$

where x refers to FF or ψ.

Proof. See Appendix 7.B. □

Combining Theorem 7.6 with Lemma 7.4 reveals an affine dependence of $\underline{\varepsilon}_*$ on $\underline{\theta}_{FF}$ and $\underline{\theta}_\psi$ as made explicit in Lemma 7.7.

Lemma 7.7. *Error $\underline{\varepsilon}_*$ is given by*

$$\underline{\varepsilon}_* = \underline{b} - \underline{\mathcal{A}\Phi\theta}, \tag{7.28}$$

with

$$\underline{b} = \underline{\psi}_{SS,*} - \underline{G}_{LoS,*}\underline{\mathcal{H}}_{F_l}\underline{S}_{LoS,l}\underline{C}_{FB,LoS,l}\underline{\mathcal{D}}_F\underline{\psi}_{SS,h}, \tag{7.29}$$

$$\underline{\Phi} = \begin{bmatrix} \underline{\Phi}_{FF,l} & 0 \\ 0 & \underline{\Phi}_{\psi,l} \end{bmatrix}, \tag{7.30}$$

$$\underline{\theta} = \begin{bmatrix} \underline{\theta}_{FF} \\ \underline{\theta}_\psi \end{bmatrix}. \tag{7.31}$$

Proof. See Appendix 7.C. □

Lemma 7.7 provides the dependence of $\underline{\varepsilon}_*$ on the controller parameters $\underline{\theta}$. In the next section, the parameters $\underline{\theta}$ are optimized.

7.4.2 Controller optimization

The optimal parameters for the control objective in (7.3) are given by the solution of the optimization problem

$$\min_{\underline{\theta}} \left\|\underline{\varepsilon}_*\right\|_2^2 \quad \text{s.t.} \quad \underline{\varepsilon}_* = \underline{b} - \underline{\mathcal{A}\Phi\theta}. \tag{7.32}$$

If $\underline{\mathcal{A}\Phi}$ is full rank, the solution to this quadratic optimization problem is given by the least-squares solution $\underline{\theta} = \underline{\theta}_0$, with

$$\underline{\theta}_0 = \left((\underline{\mathcal{A}\Phi})^\top(\underline{\mathcal{A}\Phi})\right)^{-1}(\underline{\mathcal{A}\Phi})^\top\underline{b}. \tag{7.33}$$

For perfect models, solution (7.33) provides the optimal solution.

In practice, there are always model mismatches for which the parameters are iteratively learned through an approach that closely resembles norm-optimal iterative learning control (ILC) (Bristow et al., 2006) based on the models and data of previous executions. A key observation is that the models are time-varying, which is in sharp contrast to standard learning techniques. One execution of the learning approach is referred to as a trial or task and indicated with subscript $j = 0, 1, 2, \ldots$. The parameters $\underline{\theta}_{j+1}$ for the next trial are determined as those minimizing the performance criterion in Definition 7.8 (Bristow et al., 2006) based on measured data from trial j.

Definition 7.8 (Performance criterion)**.** *The performance criterion for trial $j+1$, $j = 0, 1, 2, \ldots$ is given by*

$$\mathcal{J}(\underline{\theta}_{j+1}) = \left\|\underline{\varepsilon}_{j+1,*}\right\|^2_{\underline{W}_\varepsilon} + \left\|\underline{\xi}_{j+1,l}\right\|^2_{\underline{W}_\xi} + \left\|\underline{\xi}_{j+1,l} - \underline{\xi}_{j,l}\right\|^2_{\underline{W}_{\Delta\xi}} \tag{7.34}$$

where $\|(\cdot)\|^2_W = (\cdot)^\top W(\cdot)$, with $\underline{W}_\varepsilon \in \mathbb{R}^{N_* \times N_*}$ positive definite, $\underline{W}_\xi, \underline{W}_{\Delta\xi} \in \mathbb{R}^{2N_l \times 2N_l}$ semi-positive definite, and

$$\underline{\varepsilon}_{j+1,*} = \underline{\varepsilon}_{j,*} - \underline{\mathcal{A}\Phi}\left(\underline{\theta}_{j+1} - \underline{\theta}_j\right), \tag{7.35}$$

$$\underline{\xi}_{j,l} = \underline{\Phi}\underline{\theta}_j. \tag{7.36}$$

Performance criterion (7.34) can be used to address several control goals. For example, for $\underline{W}_\varepsilon = \underline{I}_{N_*}$ and $\underline{W}_\xi = \underline{W}_{\Delta\xi} = \underline{0}_{2N_l}$, the control goal in (7.3) is addressed, i.e., minimizing $\|\underline{\varepsilon}_*\|_2^2$. The optimal parameters for the general criterion are given by Theorem 7.9.

Theorem 7.9 (Iterative solution)**.** *The parameters $\underline{\theta}_{j+1}$, $j = 0, 1, 2, \ldots$, that minimize $\mathcal{J}(\underline{\theta}_{j+1})$ in Definition 7.8 are given by*

$$\underline{\theta}_{j+1} = \underline{Q}\underline{\theta}_j + \underline{L}\underline{\varepsilon}_{j,*}, \tag{7.37}$$

with

$$\begin{aligned}\underline{Q} = &\left((\underline{\mathcal{A}\Phi})^\top \underline{W}_\varepsilon (\underline{\mathcal{A}\Phi}) + \underline{\Phi}^\top \left(\underline{W}_\xi + \underline{W}_{\Delta\xi}\right)\underline{\Phi}\right)^{-1} \\ &\times \left((\underline{\mathcal{A}\Phi})^\top \underline{W}_\varepsilon (\underline{\mathcal{A}\Phi}) + \underline{\Phi}^\top \underline{W}_{\Delta\xi}\underline{\Phi}\right),\end{aligned} \tag{7.38}$$

$$\underline{L} = \left((\underline{\mathcal{A}\Phi})^\top \underline{W}_\varepsilon (\underline{\mathcal{A}\Phi}) + \underline{\Phi}^\top \left(\underline{W}_\xi + \underline{W}_{\Delta\xi}\right)\underline{\Phi}\right)^{-1} (\underline{\mathcal{A}\Phi})^\top \underline{W}_\varepsilon. \tag{7.39}$$

Theorem 7.9 directly follows from substitution of (7.35) and (7.36) in (7.34) and equating $\nabla\mathcal{J}(\underline{\theta}_{j+1}) = \underline{0}$, see also Bolder et al. (2014). Note that $\underline{W}_\varepsilon$, $\underline{W}_\xi$, $\underline{W}_{\Delta\xi}$ should be chosen such that the inverse in (7.38) and (7.39) exists. A step-by-step procedure for the iterative algorithm is provided in Algorithm 7.10, where (7.33) provides initial parameters based on models only.

Algorithm 7.10 (Iterative tuning procedure)**.** *Calculate* $\underline{Q}, \underline{L}$ *using* (7.38), (7.39)*, set* $j = 0$ *and determine* $\underline{\theta}_0$ *in* (7.33)*. Then, perform the following sequence of steps:*

1. *Execute task* j *and record data* $\underline{\varepsilon}_{j,*}$*.*
2. *Determine* $\underline{\theta}_{j+1}$ *through* (7.37)*.*
3. *Set* $j \to j+1$ *and repeat from step 1 until satisfactory convergence in* $\underline{\theta}_j$ *or a user-defined maximum number of trials is reached.*

Algorithm 7.10 provides the iterative tuning solution for the time-varying multirate system with controller design at the low rate. In the next section, the controllers are explicitly designed and implemented at the high rate to enhance the performance/cost trade-off in Figure 7.1.

7.4.3 Performance enhancement: High-rate control

In the previous sections, the optimal controller for the multirate system in Figure 7.4 is presented. In this section, the performance of the multirate system is further improved by modifying the controller implementation and design, which constitutes Contribution 7.III. The results of the previous section are recovered as a special case.

In contrast to time-invariant systems, time-varying systems do generally not commute, i.e., interchanging the order affects the output. One key advantage of the proposed approach is that this property can be directly exploited to enhance the performance/cost trade-off in Figure 7.1. In Figure 7.4, both the feedforward controller and input shaper of the long stroke are implemented at the low rate f_l. In this section, these controllers are implemented at high rate f_h as shown in Figure 7.5(a). This implementation has the potential to improve the performance since $\psi_{SS,h}$ contains more information than $\rho_{LoS,l} = \mathcal{D}_F \psi_{SS,h}$. This also follows from the noble identity $\mathcal{D}_F H(z^F) \equiv H(z)\mathcal{D}_F$, with H a discrete-time system rational in z (Vaidyanathan, 1993, Section 4.2). Indeed, since the frequency response of $C_{FF,LoS,h}$ is independent from that of $C_{FF,LoS,l}$, there is more design freedom as illustrated in Figure 7.5(b).

The additional cost of the high-rate implementation is negligible since it only involves a different controller design in software, without effecting hardware. In particular, it uses sensor information of the short-stroke loop at high rate, which is also required for feedback control on the short stroke. The new design does not require sensor information of the long-stroke loop at a higher rate. The actuation of the long-stroke loop remains at low rate.

The parameterization of the controllers at high rate is similar to that in Definition 7.5 and provided by Definition 7.11.

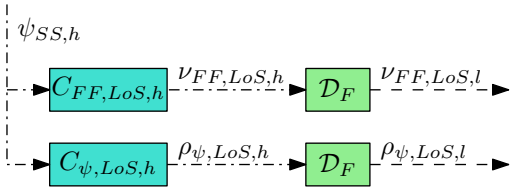

(a) Part of the control diagram in Figure 7.4 with the controllers implemented at high rate, i.e., $f_c = f_h$.

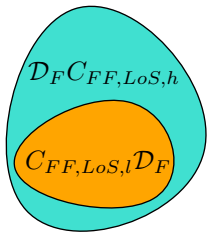

(b) The design space is larger for the controller design at high rate.

Figure 7.5. Designing and implementing the controllers at high rate allows to exploit all information in $\psi_{SS,h}$ and thereby improve performance.

Definition 7.11. *$C_{FF,LoS,h}$ and $C_{\psi,LoS,h}$ in Figure 7.5 are given by*

$$C_{FF,LoS,h}(\underline{\theta}_{FF}) = \sum_{i=0}^{n_{FF}-1} \theta_{FF}[i] \left(\frac{f_h(z-1)}{z}\right)^{i+1}, \tag{7.40}$$

$$C_{\psi,LoS,h}(\underline{\theta}_{\psi}) = 1 + \sum_{i=0}^{n_{\psi}-1} \theta_{\psi}[i] \left(\frac{f_h(z-1)}{z}\right)^{i+1}. \tag{7.41}$$

The finite-time descriptions for this parameterization are provided in Lemma 7.12. Using these results, the iterative approach outlined in Algorithm 7.10 is directly applicable.

Lemma 7.12. *Given Definition 7.11, the finite-time descriptions* (7.23), (7.24), *and* (7.30) *change to*

$$\underline{\nu}_{FF,LoS,l} = \underline{\mathcal{D}}_F \underline{C}_{FF,LoS,h} \underline{\psi}_{SS,h} = \underline{\mathcal{D}}_F \underline{\Phi}_{FF,h}\, \underline{\theta}_{FF}, \tag{7.42}$$

$$\underline{\rho}_{\psi,LoS,l} = \underline{\mathcal{D}}_F \underline{C}_{\psi,LoS,h} \underline{\psi}_{SS,h} = \underline{\mathcal{D}}_F \underline{\psi}_{SS,h} + \underline{\mathcal{D}}_F \underline{\Phi}_{\psi,h}\, \underline{\theta}_{\psi}, \tag{7.43}$$

$$\underline{\Phi} = \begin{bmatrix} \underline{\mathcal{D}}_F \underline{\Phi}_{FF,h} & 0 \\ 0 & \underline{\mathcal{D}}_F \underline{\Phi}_{\psi,h} \end{bmatrix}, \tag{7.44}$$

with

$$\underline{\Phi}_{x,h} = \underline{T}_{\psi_{SS,h}} \begin{bmatrix} \underline{I}_{n_x+1} \\ \underline{0}_{(N_h-(n_x+1))\times(n_x+1)} \end{bmatrix} \underline{R}_{x,h}, \tag{7.45}$$

$$\underline{R}_{x,h} = \begin{bmatrix} 1 & 1 & 1 & \dots & 1 \\ -1 & -2 & -3 & \dots & -n_x \\ 0 & 1 & 3 & \dots & * \\ 0 & 0 & -1 & \dots & * \\ \vdots & \vdots & \vdots & \ddots & \vdots \\ 0 & 0 & 0 & \dots & (-1)^{n_x} \end{bmatrix} \operatorname{diag}\{f_h^1, \dots, f_h^{n_x}\}, \tag{7.46}$$

where x refers to FF or ψ.

Proof. See Appendix 7.D. □

The controller design and implementation at high rate completes the multirate controller design. Next, the advantages of multirate control over single-rate control are demonstrated in both simulation and experiments.

7.5 Experimental setup: A dual-stage wafer stage system

In the remainder of this chapter, the multirate control design framework presented in the previous section is validated on a dual-stage system, both in simulations and experiments. In this section, the wafer stage system is introduced in more detail and the experimental setup of the dual-stage system is presented.

7.5.1 Wafer stages: Key components in lithography machines

Wafer stages are key components in wafer scanners. Wafer scanners are state-of-the-art lithography machines for the automated production of integrated circuits. In Figure 7.6, a schematic illustration of a wafer scanner system is depicted. Ultra-violet light from a light source ① passes through a reticle ②, which contains a blueprint of the integrated circuits to be manufactured. The reticle is clamped atop the reticle stage ③ which performs a scanning motion. The resulting image of the reticle is scaled down by a lens system ④ and projected onto the light sensitive layers of a wafer ⑤. The wafer is clamped on the wafer stage ⑥ and performs a synchronized scanning motion with the reticle stage.

During the scanning process, the wafer stage and reticle stage track reference signals with nanometer positioning accuracy. In this chapter, the focus is on control of the wafer stage, which has more stringent performance requirements than the reticle stage (Evers et al., 2017).

7.5.2 Experimental setup

The experimental setup is shown in Figure 7.7 and consists of two stages: a long stroke (LoS) and a short stroke (SS). Both stages can translate in one horizontal direction and are air guided. Each stage is actuated through a Lorentz actuator attached to the force frame. The position of each stage is measured through 1 nm resolution optical encoders attached to the metrology frame, which is separated from the force frame to reduce interaction. The total stroke is 16.0 mm.

The sampling rate of ε_* is $f_* = 10080$ Hz. The identified frequency response functions of both stages are shown in Figure 7.8. The stages are modeled as

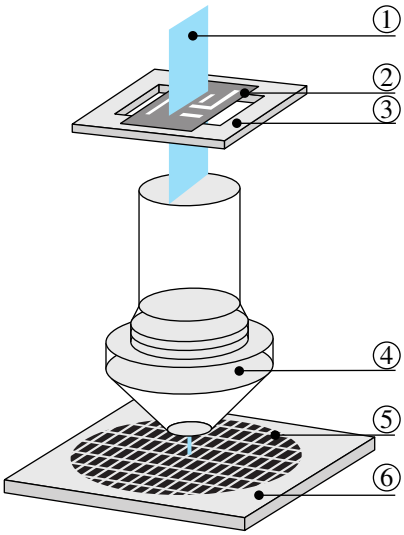

Figure 7.6. Schematic illustration of a wafer scanner system, consisting of light source ①, reticle ②, reticle stage ③, lens system ④, wafer ⑤, and wafer stage ⑥.

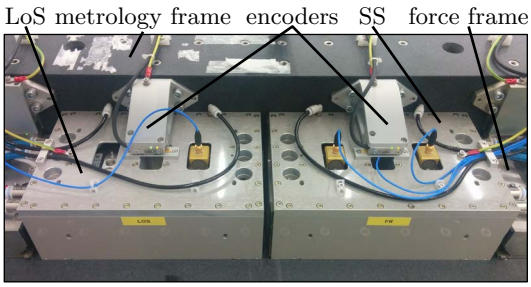

Figure 7.7. Experimental setup resembling a one degree-of-freedom wafer stage. The setup consists of two air-guided stages that can translate in one horizontal direction. The positions are measured through 1 nm resolution optical encoders.

freely moving masses with one sample I/O delay:

$$G_{x,*} = z^{-1}\frac{(z+1)}{2m_x f_*^2 (z-1)^2}, \tag{7.47}$$

with masses $m_{SS} = 4.70$ kg and $m_{LoS} = 4.33$ kg. The sampling rate factors F_h, F_l are varied and provided when relevant.

Reference trajectory $\underline{\rho}_{SS,h}$ consists of a forward and backward movement with a total duration of 0.25 s and is shown in Figure 7.9. The point-to-point profile is representative for the application in terms of distance, maximum acceleration, etc. A fourth-order profile is used to guarantee a smooth signal with limited high-frequency content to avoid excitation of higher-order dynamics, see also Figure 7.8 and, e.g., Lambrechts et al. (2005).

Experiments show that the measurement noise on both $\underline{\psi}_{SS,*}$ and $\underline{\psi}_{LoS,*}$ has a variance of $(45\text{ nm})^2$. This value is used during simulation to mimic experimental conditions.

7.5.3 Controller design

The fixed feedback controllers $C_{FB,SS,h}$ and $C_{FB,LoS,l}$ both consist of a lead filter, weak integrator, and second order lowpass filter based on loop-shaping techniques (Steinbuch et al., 2010). The controllers stabilize their respective closed-loop systems and yield a bandwidth (first 0 dB crossing of the open-loop) of 100 Hz for both loops. The feedforward controller and input shaper for the short stroke are given by

$$C_{FF,SS,h} = m_{SS}\frac{f_h^2(z-1)^2}{z^2}, \tag{7.48}$$

$$C_{\psi,SS,h} = G_{SS,h}C_{FF,SS,h}. \tag{7.49}$$

Hence, $C_{FF,SS,h}$ generates mass feedforward and the combination results in $\underline{\varepsilon}_{SS,h} = 0$, if $G_{SS,h}$ is exact.

The design of the long-stroke feedforward controller and input shaper aims to minimize $\|\underline{\varepsilon}_*\|_2^2$ by setting the weights in Definition 7.8 to

$$\underline{W}_\varepsilon = \underline{I}_{N_*}, \quad \underline{W}_\xi, \underline{W}_{\Delta\xi} = \underline{0}_{2N_l\times 2N_l}. \tag{7.50}$$

Note that these settings also facilitate fast convergence of the iterative procedure in Algorithm 7.10.

7.6 Simulation results

In this section, the simulation results are presented, which serve as a benchmark for the experimental results presented in Section 7.7. The simulations enable validation of the experimental results and constitute Contribution 7.IV.

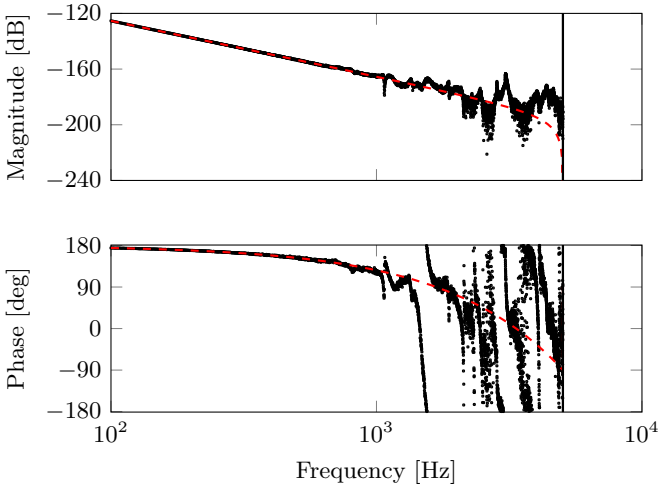

(a) Short-stroke (SS) stage.

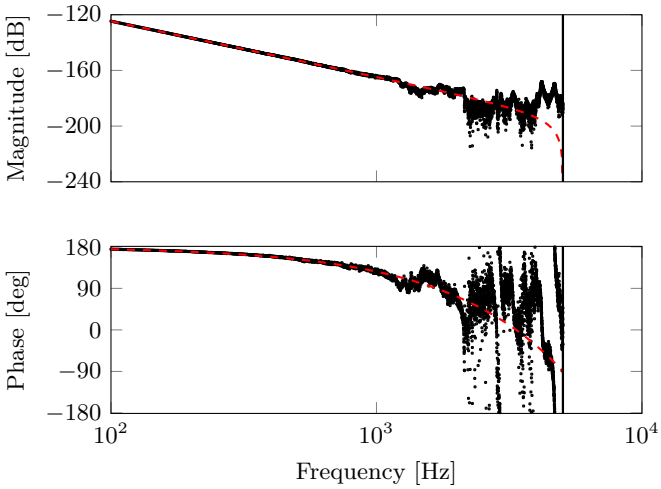

(b) Long-stroke (LoS) stage.

Figure 7.8. Measured frequency response functions (•) with sampling rate $f_* = 10080$ Hz and the identified models (- - -) in (7.47).

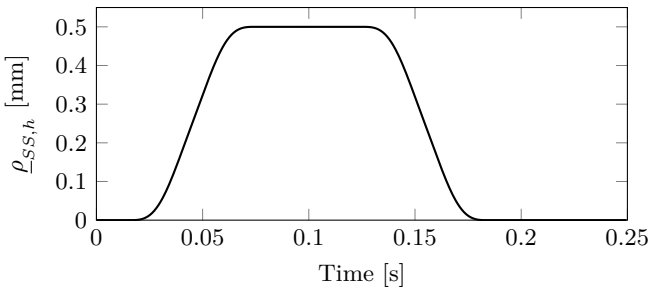

Figure 7.9. Reference trajectory $\underline{\rho}_{SS,h}$ is a forward and backward movement over 0.5 mm constructed from fourth-order polynomials.

Table 7.1. The four different control configurations that are evaluated.

Label	Symbol	f_* [Hz]	f_h [Hz]	f_l [Hz]	f_c [Hz]
Single-rate high	○	10080	2016	2016	2016
Single-rate low	△	10080	1008	1008	1008
Multirate high	×	10080	2016	1008	2016
Multirate low	◇	10080	2016	1008	1008

7.6.1 Comparing controllers at different rates

The considered control configurations are listed in Table 7.1, see also (7.1). Due to the difference in sampling rate between the controller parameterization on low rate (Definition 7.5) and high rate (Definition 7.11), the number of parameters n_{FF} and n_ψ alone does not provide a fair comparison between the controllers. Therefore, the controller buffer lengths

$$\tau_{FF} := \frac{n_{FF}}{f_c}, \qquad \tau_\psi := \frac{n_\psi}{f_c}, \tag{7.51}$$

are defined, where f_c is the sampling rate of the optimized controllers, see Table 7.1. These buffer lengths are an indication for the implementation cost of the controller.

7.6.2 Simulation setup

For comparison with the experimental results in Section 7.7, measurement noise is added to $\underline{\psi}_{SS,*}$ and $\underline{\psi}_{LoS,*}$. The noise is modeled as zero mean, Gaussian white noise with variance $\sigma^2 = (45\text{ nm})^2$ based on experimental data, see also Section 7.5.2.

In simulation, the models are exact and hence the initial parameters $\underline{\theta}_0$ in (7.33) provide the optimal solution. Note that the noise introduces trial-varying

disturbances, which cannot be compensated through the iterative tuning algorithm and thereby limits the achievable performance.

7.6.3 Results

The performance/cost trade-off curves for the configurations in Table 7.1 are shown in Figure 7.10. The figure shows the enhancement of the performance/cost trade-off through multirate control as illustrated in Figure 7.1. In particular, the figure shows I) increasing performance (decreasing $\mathcal{J}$) for increasing cost (increasing τ); and II) excellent performance through multirate control with design at high rate.

As a direct consequence of a higher sampling rate, single-rate high outperforms single-rate low. Multirate control is a trade-off between these two and hence the performance is somewhere in between. The performance improvement of multirate low is limited compared to single-rate low. In contrast, the performance of multirate high is close to that of single-rate high. The results show that multirate control can achieve high performance with limited cost, when designed and implemented at the high rate. Indeed, the long-stroke feedback control loop remains executed at the low rate.

The results in Figure 7.10(a) show the importance of adding the acceleration profile as basis function in terms of performance improvement, as is also apparent from the frequency response functions in Figure 7.8 and identified models in (7.47). Indeed, especially for low frequencies, the stages behave as a rigid body mass. Therefore, a mass feedforward controller $C_{FF,LoS} = \theta_{FF}[1]\frac{f_c^2(z-1)^2}{z^2}$ is used in Figure 7.10(b), where parameter $\theta_{FF}[1]$ is also optimized. Note that mass feedforward is also used for the short-stroke feedforward controller in (7.48).

Time-domain results for multirate high with $n_{FF} = 2$, $n_\psi = 0$ are shown in Figure 7.11. Compared to mass feedforward, there is an additional parameter in the feedforward filter as can be observed in $\underline{\nu}_{FF,LoS,l}$, resulting in improved performance.

The simulation results demonstrate the potential of multirate control, especially when the controllers are designed and implemented at the high rate. Next, the results are experimentally validated.

7.7 Experimental results

In this section, the simulation results of the previous section are experimentally validated on the setup described in Section 7.5. The results experimentally validate the advantages of multirate control and constitute Contribution 7.V.

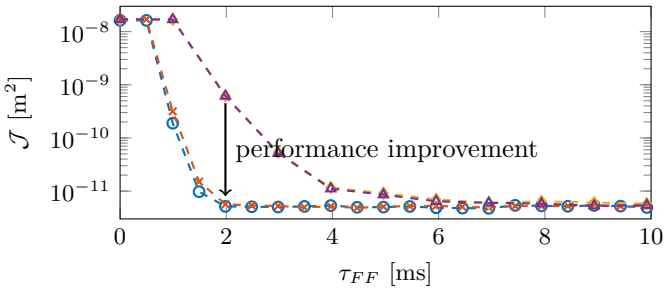

(a) Simulation results for varying τ_{FF} show that, due to more design freedom in terms of parameters n_{FF}, the performance increases ($\mathcal{J}$ decreases) for increasing cost (increasing buffer length τ_{FF}). The results shown are for fixed $C_{\psi,LoS} = 1$ and varying n_{FF}.

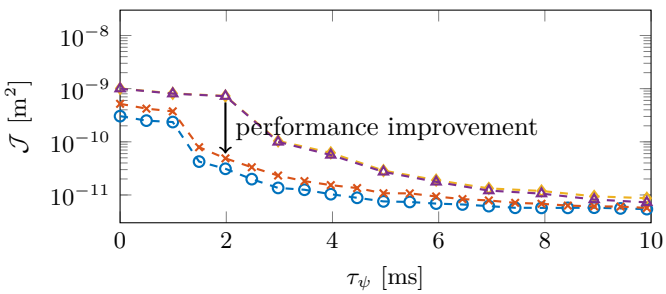

(b) Simulation results for varying τ_{ψ} show that larger cost (larger buffer length τ_{ψ}) yields better performance (lower $\mathcal{J}$). The results shown are for mass feedforward ($n_{FF} = 2$ and $\theta_{FF}[0] = 0$) and varying n_{ψ}.

Figure 7.10. Simulation results for the four control configurations in Table 7.1. As is expected, single-rate high (· ⊖ ·) outperforms single-rate low (· ▲ ·). The performance of multirate low (· ◆ ·) is similar to that of single-rate low (· ▲ ·). The performance of multirate high (· ✱ ·) is close to the performance of single-rate high (· ⊖ ·). The results demonstrate the advantages of multirate control. Indeed, a high level of performance is achievable with multirate control for limited cost since one of the feedback control loops is evaluated at a lower rate.

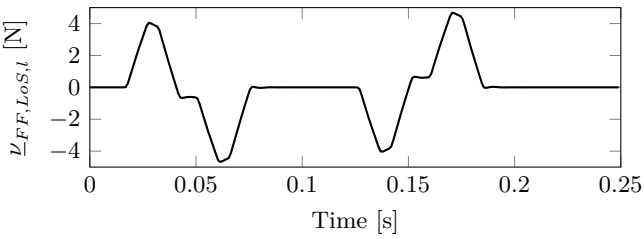

(a) Feedforward signal $\underline{\nu}_{FF,LoS,l}$.

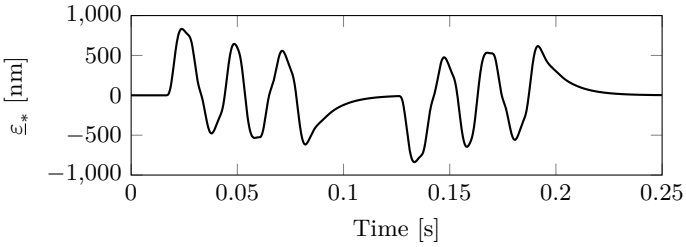

(b) Error signal $\underline{\varepsilon}_*$.

Figure 7.11. Time-domain simulation results for single-rate high with $n_{FF} = 2$, $n_\psi = 0$. The results show the importance of mass feedforward.

7.7.1 Application of iterative tuning

In contrast to simulation, the models do not exactly describe the system in experiments. Therefore, the iterative tuning procedure in Algorithm 7.10 is invoked to iteratively update the parameters based on measured data. The convergence of the iterative tuning algorithm is shown in Figure 7.12 for the various control configurations in Table 7.1 with a fixed buffer length $\tau_{FF} = 1$ ms ($\tau_\psi = 0$).

The results in Figure 7.12 show fast convergence (one trial) of the iterative algorithm as desired. Note that the deviations over the trials are caused by trial-varying disturbances for which the algorithm cannot compensate. In the remainder, five trials are used and only the results of the fifth trial are shown.

7.7.2 Results

The experimental results for the simulations in Figure 7.10 are shown in Figure 7.13. The results are in line with the simulation results and the conclusions in Section 7.6, i.e., higher performance (lower $\mathcal{J}$) for increasing number of parameters (increasing τ), and excellent performance for multirate control with control design at high rate (multirate high).

Time-domain signals for several parameterizations with multirate high are

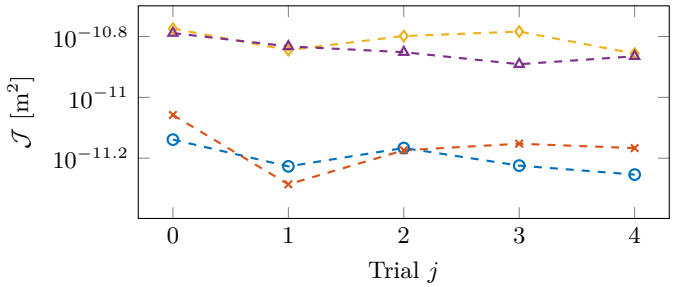

Figure 7.12. Experimental results of the performance criterion over trials for $\tau_{FF} = 1$ ms, $\tau_\psi = 0$ with single-rate high (○), multirate high (×), multirate low (◇), and single-rate low (△). The results show that all control configurations converge in one trial up to the level of trial-varying disturbances for which the iterative tuning algorithm cannot compensate.

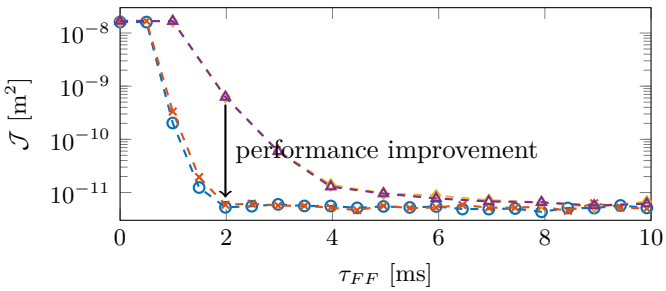

(a) Experimental validation of the simulation in Figure 7.10(a). The results are in line with the simulation results.

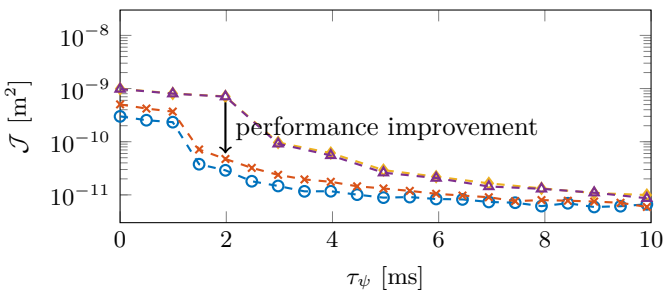

(b) Experimental validation of the simulation in Figure 7.10(b). The results are in line with the simulation results.

Figure 7.13. Experimental results for the four control configurations in Table 7.1. The results corroborate the simulations results in Figure 7.10.

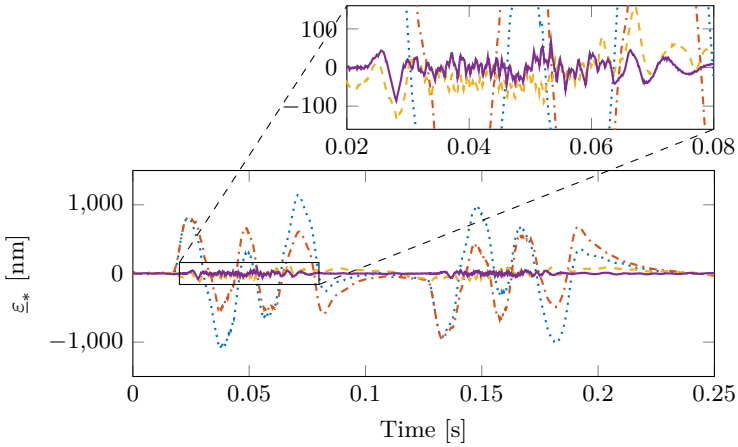

(a) Parameterizations with more design freedom yield a smaller error $\underline{\varepsilon}_*$ which is also apparent in the performance criterion $\mathcal{J}$ shown in Figure 7.10 and Figure 7.13.

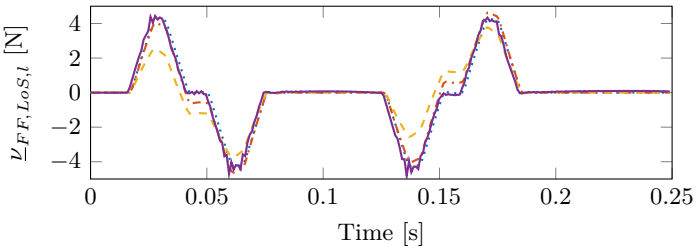

(b) The different feedforward signals $\underline{\nu}_{FF,LoS,l}$.

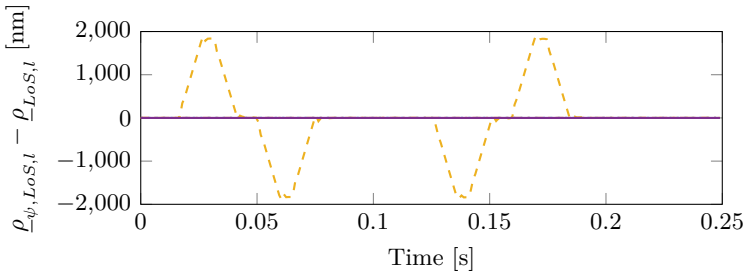

(c) The shaped input $\underline{\rho}_{\psi,LoS,l}$ is only different from $\underline{\rho}_{LoS,l}$ for the parameterization with $n_\psi = 4$ (- - -) since $n_\psi = 0$ for the other parameterizations.

Figure 7.14. Time-domain experimental results for multirate high for different parameterizations. In ascending order of design freedom: mass feedforward ($n_{FF} = 2$, $\theta_{FF}[0] = 0$, $n_\psi = 0$) (·····); $n_{FF} = 2$, $n_\psi = 0$ (-·-·); $n_{FF} = 2$, $n_\psi = 4$ (- - -); and full learning of $\underline{\nu}_{FF,LoS,h}$ ($n_{FF} = N_h$, $n_\psi = 0$) (——). More design freedom reduces the error $\underline{\varepsilon}_*$.

shown in Figure 7.14. Clearly, mass feedforward only ($n_{FF} = 2$, $\theta_{FF}[0] = 0$, $n_\psi = 0$) is restrictive and achieves moderate performance. When using $n_{FF} = 2$, $n_\psi = 0$ there is more design freedom resulting in better performance. Adding design freedom in the input shaper by using $n_{FF} = 2$, $n_\psi = 4$ yields even better performance. Most design freedom is obtained by fully parameterizing the feedforward signal as in traditional learning control with $n_{FF} = N_h$ ($n_\psi = 0$) and yields the best performance. Indeed, the performance of standard learning control in which the full signal is learned is superior for repeating tasks. However, the performance deteriorates drastically when the trajectory $\underline{\rho}_{SS,h}$ is changed, see for example Bolder et al. (2014); Bolder and Oomen (2015), which conflicts with the requirement on reference task flexibility in Section 7.2.3. Hence, there is a trade-off between performance and task flexibility, which can be balanced using basis functions.

7.7.3 Summary

The experimental results validate the simulation results and thereby demonstrate the potential of multirate control for dual-stage systems. Both the simulations and experiments show that a multirate design approach with control design at the high rate can significantly enhance the performance compared to traditional single-rate control on the low rate. In fact, the performance is similar to that of single-rate control at the high rate, but obtained with a lower cost since one of the control loops is executed at the low rate which reduces hardware cost.

7.8 Conclusion and outlook

In most motion systems, all control loops are operated on a single, fixed sampling rate since this allows the use of well-known control design techniques. However, for such a design, increasing the sampling rate to increase performance is costly in terms of required hardware since all control loops are affected.

In this chapter, a multirate approach is exploited to enhance the traditional performance/cost trade-off. In essence, this allows to allocate the performance and cost over the different control loops. The time variance introduced by multirate sampling complicates control design and constitutes the main challenge addressed in this chapter.

The main contribution of this chapter is a control design framework for multirate systems. The framework facilitates optimal feedforward control design through iterative tuning control. Through simulations and experiments on a dual-stage wafer stage system, the advantages of the multirate control approach are demonstrated. In particular, it is shown that by design of multirate control on the high rate excellent performance is achieved, with limited cost. The results demonstrate the potential of flexible sampling in motion systems.

Ongoing research focuses on feedback control design for multirate systems, see for example Chapter 2, and control design for other classes of flexible sampling.

7.A Proof Lemma 7.4

The following identity, known as the push-through rule, is exploited:

$$\left(\underline{I}_m + \underline{AB}\right)^{-1} \underline{A} = \underline{A}\left(\underline{I}_n + \underline{BA}\right)^{-1}, \tag{7.52}$$

with $\underline{A} \in \mathbb{R}^{m\times n}$, $\underline{B} \in \mathbb{R}^{n\times m}$, $n, m \in \mathbb{N}$.

Using Figure 7.4 and (7.52), $\underline{\psi}_{SS,*}$ is expressed in $\underline{\rho}_{SS,h}$:

$$\begin{aligned}
\underline{\psi}_{SS,*} &= \underline{G}_{SS,*}\underline{\mathcal{H}}_{F_h}\left(\underline{C}_{FF,SS,h} + \underline{C}_{FB,SS,h}\underline{C}_{\psi,SS,h}\right)\underline{\rho}_{SS,h} \\
&\qquad - \underline{G}_{SS,*}\underline{\mathcal{H}}_{F_h}\underline{C}_{FB,SS,h}\underline{\mathcal{D}}_{F_h}\underline{\psi}_{SS,*} && (7.53a)\\
&= \left(\underline{I}_{N_*} + \underline{G}_{SS,*}\underline{\mathcal{H}}_{F_h}\underline{C}_{FB,SS,h}\underline{\mathcal{D}}_{F_h}\right)^{-1}\underline{G}_{SS,*}\underline{\mathcal{H}}_{F_h} \\
&\qquad \times \left(\underline{C}_{FF,SS,h} + \underline{C}_{FB,SS,h}\underline{C}_{\psi,SS,h}\right)\underline{\rho}_{SS,h} && (7.53b)\\
&= \underline{G}_{SS,*}\underline{\mathcal{H}}_{F_h}\left(\underline{I}_{N_h} + \underline{C}_{FB,SS,h}\underline{\mathcal{D}}_{F_h}\underline{G}_{SS,*}\underline{\mathcal{H}}_{F_h}\right)^{-1} \\
&\qquad \times \left(\underline{C}_{FF,SS,h} + \underline{C}_{FB,SS,h}\underline{C}_{\psi,SS,h}\right)\underline{\rho}_{SS,h} && (7.53c)\\
&= \underline{G}_{SS,*}\underline{\mathcal{H}}_{F_h}\left(\underline{I}_{N_h} + \underline{C}_{FB,SS,h}\underline{G}_{SS,h}\right)^{-1} \\
&\qquad \times \left(\underline{C}_{FF,SS,h} + \underline{C}_{FB,SS,h}\underline{C}_{\psi,SS,h}\right)\underline{\rho}_{SS,h} && (7.53d)\\
&= \underline{G}_{SS,*}\underline{\mathcal{H}}_{F_h}\underline{S}_{SS,h}\left(\underline{C}_{FF,SS,h} + \underline{C}_{FB,SS,h}\underline{C}_{\psi,SS,h}\right)\underline{\rho}_{SS,h}, && (7.53e)
\end{aligned}$$

with

$$\underline{S}_{SS,h} = \left(\underline{I}_{N_h} + \underline{C}_{FB,SS,h}\underline{G}_{SS,h}\right)^{-1}. \tag{7.54}$$

Using Figure 7.4 and (7.52), $\underline{\psi}_{LoS,*}$ is expressed in $\underline{\rho}_{\psi,LoS,l}$, $\underline{\nu}_{FF,LoS,l}$:

$$\begin{aligned}
\underline{\psi}_{LoS,*} &= \underline{G}_{LoS,*}\underline{\mathcal{H}}_{F_l}\left(\underline{\nu}_{FF,LoS,l} + \underline{C}_{FB,LoS,l}\underline{\rho}_{\psi,LoS,l}\right) \\
&\qquad - \underline{G}_{LoS,*}\underline{\mathcal{H}}_{F_l}\underline{C}_{FB,LoS,l}\underline{\mathcal{D}}_{F_l}\underline{\psi}_{LoS,*} && (7.55a)\\
&= \left(\underline{I}_{N_*} + \underline{G}_{LoS,*}\underline{\mathcal{H}}_{F_l}\underline{C}_{FB,LoS,l}\underline{\mathcal{D}}_{F_l}\right)^{-1}\underline{G}_{LoS,*}\underline{\mathcal{H}}_{F_l} \\
&\qquad \times \left(\underline{\nu}_{FF,LoS,l} + \underline{C}_{FB,LoS,l}\underline{\rho}_{\psi,LoS,l}\right) && (7.55b)\\
&= \underline{G}_{LoS,*}\underline{\mathcal{H}}_{F_l}\left(\underline{I}_{N_l} + \underline{C}_{FB,LoS,l}\underline{\mathcal{D}}_{F_l}\underline{G}_{LoS,*}\underline{\mathcal{H}}_{F_l}\right)^{-1} \\
&\qquad \left(\underline{\nu}_{FF,LoS,l} + \underline{C}_{FB,LoS,l}\underline{\rho}_{\psi,LoS,l}\right) && (7.55c)
\end{aligned}$$

$$\begin{aligned}\underline{\psi}_{LoS,*} &= \underline{G}_{LoS,*}\underline{\mathcal{H}}_{F_l}\left(\underline{I}_{N_l}+\underline{C}_{FB,LoS,l}\underline{G}_{LoS,l}\right)^{-1} \\ &\qquad \times\left(\underline{\nu}_{FF,LoS,l}+\underline{C}_{FB,LoS,l}\underline{\rho}_{\psi,LoS,l}\right) && (7.55d)\\ &= \underline{G}_{LoS,*}\underline{\mathcal{H}}_{F_l}\underline{S}_{LoS,l}\begin{bmatrix}\underline{I}_{N_l} & \underline{C}_{FB,LoS,l}\end{bmatrix}\begin{bmatrix}\underline{\nu}_{FF,LoS,l}\\ \underline{\rho}_{\psi,LoS,l}\end{bmatrix} && (7.55e)\\ &= \underline{\mathcal{A}}\begin{bmatrix}\underline{\nu}_{FF,LoS,l}\\ \underline{\rho}_{\psi,LoS,l}\end{bmatrix}, && (7.55f)\end{aligned}$$

with

$$\underline{S}_{LoS,l} = \left(\underline{I}_{N_l}+\underline{C}_{FB,LoS,l}\underline{G}_{LoS,l}\right)^{-1}, \tag{7.56}$$

$$\underline{\mathcal{A}} = \underline{G}_{LoS,*}\underline{\mathcal{H}}_{F_l}\underline{S}_{LoS,l}\begin{bmatrix}\underline{I}_{N_l} & \underline{C}_{FB,LoS,l}\end{bmatrix}. \tag{7.57}$$

The result follows from

$$\underline{\varepsilon}_* = \underline{\psi}_{SS,*} - \underline{\psi}_{LoS,*} = \underline{\psi}_{SS,*} - \underline{\mathcal{A}}\begin{bmatrix}\underline{\nu}_{FF,LoS,l}\\ \underline{\rho}_{\psi,LoS,l}\end{bmatrix}. \tag{7.58}$$

7.B Proof Theorem 7.6

It is shown that for the parameterization

$$C_l(\underline{\theta}) = \sum_{i=0}^{n-1}\theta[i]\left(\frac{f_l(z-1)}{z}\right)^{i+1} \tag{7.59}$$

it holds

$$\underline{\xi}_l = \underline{C}_l\underline{\mathcal{D}}_F\underline{\rho}_{SS,h} = \underline{\Phi}_l\underline{\theta}. \tag{7.60}$$

Relations (7.23) and (7.24) directly follow from this result.

Parameterization (7.59) can equivalently be written as a finite impulse response (FIR) structure of order $n_\alpha = n+1$:

$$C_l(\underline{\theta}) = \sum_{i=0}^{n-1}\theta[i]\left(\frac{f_l(z-1)}{z}\right)^{i+1} = \sum_{i=0}^{n_\alpha-1}\alpha[i]z^{-i}. \tag{7.61}$$

By equating coefficients, it directly follows that the relation between parameters is given by $\underline{\alpha} = \underline{R}_l\underline{\theta}$ with $\underline{R}_l \in \mathbb{R}^{n_\alpha\times n}$ as in (7.27). Note that $\underline{R}_l$ is the product of a truncated transposed (lower triangular Cholesky factor of the) Pascal matrix of order n_α, with a diagonal scaling matrix depending on f_l.

The finite-time description of C_l in terms of $\underline{\alpha}$ is given by

$$\underline{C}_l = \begin{bmatrix} \alpha[0] & 0 & 0 & \cdots \\ \alpha[1] & \alpha[0] & 0 & \cdots \\ \vdots & \alpha[1] & \alpha[0] & \cdots \\ \alpha[n_\alpha-1] & \vdots & \alpha[1] & \ddots \\ 0 & \alpha[n_\alpha-1] & \vdots & \ddots \\ 0 & 0 & \alpha[n_\alpha-1] & \ddots \\ \vdots & \vdots & \vdots & \ddots \end{bmatrix}. \tag{7.62}$$

Using the Kronecker mixed-product property rule (7.14) the order of $\underline{C}_l$ and $\underline{\mathcal{D}}_F$, see (7.10), is interchanged:

$$\begin{aligned}
\underline{C}_l\underline{\mathcal{D}}_F &= (\underline{C}_l \otimes 1)\left(\underline{I}_{N_l} \otimes \underline{e}_F^\top\right) && (7.63a)\\
&= \left(\underline{C}_l\underline{I}_{N_l}\right) \otimes \left(1\underline{e}_F^\top\right) && (7.63b)\\
&= \left(\underline{I}_{N_l}\underline{C,l}\right) \otimes \left((\underline{e}_F^\top\underline{e}_F)\underline{e}_F^\top\right) && (7.63c)\\
&= \left(\underline{I}_{N_l}\underline{C,l}\right) \otimes \left(\underline{e}_F^\top(\underline{e}_F\underline{e}_F^\top)\right) && (7.63d)\\
&= \left(\underline{I}_{N_l} \otimes \underline{e}_F^\top\right)\left(\underline{C}_l \otimes (\underline{e}_F\underline{e}_F^\top)\right) && (7.63e)\\
&= \underline{\mathcal{D}}_F\left(\underline{C}_l \otimes (\underline{e}_F\underline{e}_F^\top)\right). && (7.63f)
\end{aligned}$$

Note that $\underline{C}_l \otimes (\underline{e}_F\underline{e}_F^\top)$ is a lower triangular matrix and that $\underline{\psi}_{SS,h} = \underline{T}_{\psi_{SS,h}}\underline{e}_{N_h}$, with $\underline{T}_{\psi_{SS,h}}$ in (7.26) is also a lower triangular matrix.

Next, the commutative property of lower triangular matrices is exploited to express $\underline{\xi}_l$ in $\underline{\theta}$. To this end, the Kronecker product rule and the relation $\underline{\alpha} = \underline{R}_l\underline{\theta}$ are used:

$$\begin{aligned}
\underline{\xi}_l &= \underline{C}_l\underline{\mathcal{D}}_F\underline{\psi}_{SS,h} && (7.64a)\\
&= \underline{\mathcal{D}}_F\left(\underline{C}_l \otimes (\underline{e}_F\underline{e}_F^\top)\right)\underline{\psi}_{SS,h} && (7.64b)\\
&= \underline{\mathcal{D}}_F\left(\underline{C}_l \otimes (\underline{e}_F\underline{e}_F^\top)\right)\underline{T}_{\psi_{SS,h}}\underline{e}_{N_h} && (7.64c)\\
&= \underline{\mathcal{D}}_F\underline{T}_{\psi_{SS,h}}\left(\underline{C}_l \otimes (\underline{e}_F\underline{e}_F^\top)\right)\underline{e}_{N_h} && (7.64d)\\
&= \underline{\mathcal{D}}_F\underline{T}_{\psi_{SS,h}}\begin{bmatrix} \underline{\alpha} \otimes \underline{e}_F \\ \underline{0}_{(N_h-Fn_\alpha)\times 1}\end{bmatrix} && (7.64e)\\
&= \underline{\mathcal{D}}_F\underline{T}_{\psi_{SS,h}}\begin{bmatrix} \left(\underline{I}_{n_\alpha}\underline{\alpha}\right) \otimes (\underline{e}_F 1) \\ \underline{0}_{(N_h-Fn_\alpha)\times 1}\end{bmatrix} && (7.64f)\\
&= \underline{\mathcal{D}}_F\underline{T}_{\psi_{SS,h}}\begin{bmatrix} \left(\underline{I}_{n_\alpha} \otimes \underline{e}_F\right)(\underline{\alpha} \otimes 1) \\ \underline{0}_{(N_h-Fn_\alpha)\times 1}\end{bmatrix} && (7.64g)\\
&= \underline{\mathcal{D}}_F\underline{T}_{\psi_{SS,h}}\begin{bmatrix} \left(\underline{I}_{n_\alpha} \otimes \underline{e}_F\right)\underline{\alpha} \\ \underline{0}_{(N_h-Fn_\alpha)\times 1}\end{bmatrix} && (7.64h)
\end{aligned}$$

$$\underline{\xi}_l = \underline{\mathcal{D}}_F \underline{T}_{\psi_{SS,h}} \begin{bmatrix} \underline{I}_{n_\alpha} \otimes \underline{e}_F \\ \underline{0}_{(N_h - F n_\alpha)\times n_\alpha} \end{bmatrix} \underline{\alpha} \tag{7.64i}$$

$$= \underline{\mathcal{D}}_F \underline{T}_{\psi_{SS,h}} \begin{bmatrix} \underline{I}_{n_\alpha} \otimes \underline{e}_F \\ \underline{0}_{(N_h - F n_\alpha)\times n_\alpha} \end{bmatrix} \underline{R}_l \underline{\theta} \tag{7.64j}$$

$$= \underline{\Phi}_l \underline{\theta}, \tag{7.64k}$$

which concludes the proof of (7.59). Relations (7.23) and (7.24) directly follow from this result.

7.C Proof Lemma 7.7

Substitution of (7.23) and (7.24) in (7.16) and using (7.18) yields

$$\underline{\varepsilon}_* = \underline{\psi}_{SS,*} - \underline{\mathcal{A}} \begin{bmatrix} \underline{\nu}_{FF,LoS,l} \\ \underline{\rho}_{\psi,LoS,l} \end{bmatrix} \tag{7.65a}$$

$$= \underline{\psi}_{SS,*} - \underline{\mathcal{A}} \begin{bmatrix} \underline{\Phi}_{FF,l} \underline{\theta}_{FF} \\ \underline{\mathcal{D}}_F \underline{\psi}_{SS,h} + \underline{\Phi}_{\psi,l} \underline{\theta}_\psi \end{bmatrix} \tag{7.65b}$$

$$= \underline{\psi}_{SS,*} - \underline{\mathcal{A}} \begin{bmatrix} \underline{0}_{N_l} \\ \underline{\mathcal{D}}_F \underline{\psi}_{SS,h} \end{bmatrix} - \underline{\mathcal{A}} \begin{bmatrix} \underline{\Phi}_{FF,l} \underline{\theta}_{FF} \\ \underline{\Phi}_{\psi,l} \underline{\theta}_\psi \end{bmatrix} \tag{7.65c}$$

$$\begin{aligned} = \underline{\psi}_{SS,*} &- \underline{G}_{LoS,*} \underline{\mathcal{H}}_{F_l} \underline{S}_{LoS,l} \begin{bmatrix} \underline{I}_{N_l} & \underline{C}_{FB,LoS,l} \end{bmatrix} \begin{bmatrix} \underline{0}_{N_l} \\ \underline{\mathcal{D}}_F \underline{\psi}_{SS,h} \end{bmatrix} \\ &- \underline{\mathcal{A}} \begin{bmatrix} \underline{\Phi}_{FF,l} \underline{\theta}_{FF} \\ \underline{\Phi}_{\psi,l} \underline{\theta}_\psi \end{bmatrix} \end{aligned} \tag{7.65d}$$

$$\begin{aligned} = \underline{\psi}_{SS,*} &- \underline{G}_{LoS,*} \underline{\mathcal{H}}_{F_l} \underline{S}_{LoS,l} \underline{C}_{FB,LoS,l} \underline{\mathcal{D}}_F \underline{\psi}_{SS,h} \\ &- \underline{\mathcal{A}} \begin{bmatrix} \underline{\Phi}_{FF,l} & 0 \\ 0 & \underline{\Phi}_{\psi,l} \end{bmatrix} \begin{bmatrix} \underline{\theta}_{FF} \\ \underline{\theta}_\psi \end{bmatrix} \end{aligned} \tag{7.65e}$$

$$= \underline{b} - \underline{\mathcal{A}} \Phi \theta, \tag{7.65f}$$

with $\underline{b}, \underline{\Phi}, \underline{\theta}$ as given in Lemma 7.7.

7.D Proof Lemma 7.12

It is shown that for the general parameterization

$$C_h(\underline{\theta}) = \sum_{i=0}^{n-1} \theta[i] \left(\frac{f_h(z-1)}{z} \right)^{i+1} \tag{7.66}$$

it holds

$$\underline{\xi}_l = \underline{\mathcal{D}}_F \underline{C}_h \underline{\psi}_{SS,h} = \underline{\mathcal{D}}_F \underline{\Phi}_h \, \underline{\theta}. \tag{7.67}$$

Relations (7.42) and (7.43) directly follow from this result.

The proof is similar to that of Theorem 7.6. First, C_h is expressed in terms of FIR parameters $\underline{\alpha}$:

$$C_h(\underline{\theta}) = \sum_{i=0}^{n-1} \theta[i] \left(\frac{f_h(z-1)}{z} \right)^{i+1} = \sum_{i=0}^{n_\alpha - 1} \alpha[i] z^{-i}, \tag{7.68}$$

where $\underline{\alpha} = \underline{R}_h \underline{\theta}$ with $\underline{R}_h \in \mathbb{R}^{n_\alpha \times n}$ as in (7.46) and $n_\alpha = n+1$. The finite-time description of C_h in terms of $\underline{\alpha}$ is given by

$$\underline{C}_h = \begin{bmatrix} \alpha[0] & 0 & 0 & \cdots \\ \alpha[1] & \alpha[0] & 0 & \cdots \\ \vdots & \alpha[1] & \alpha[0] & \cdots \\ \alpha[n_\alpha - 1] & \vdots & \alpha[1] & \ddots \\ 0 & \alpha[n_\alpha - 1] & \vdots & \ddots \\ 0 & 0 & \alpha[n_\alpha - 1] & \ddots \\ \vdots & \vdots & \vdots & \ddots \end{bmatrix}. \tag{7.69}$$

Next, it is exploited that the lower triangular matrices $\underline{C}_h$ and $\underline{T}_{\psi_{SS,h}}$ commute:

$$\begin{aligned}
\underline{\xi}_l &= \underline{\mathcal{D}}_F \underline{C}_h \underline{\psi}_{SS,h} && (7.70a)\\
&= \underline{\mathcal{D}}_F \underline{C}_h \underline{T}_{\psi_{SS,h}} \underline{e}_{N_h} && (7.70b)\\
&= \underline{\mathcal{D}}_F \underline{T}_{\psi_{SS,h}} \underline{C}_h \underline{e}_{N_h} && (7.70c)\\
&= \underline{\mathcal{D}}_F \underline{T}_{\psi_{SS,h}} \begin{bmatrix} \underline{\alpha} \\ \underline{0}_{(N_h - n_\alpha)\times 1} \end{bmatrix} && (7.70d)\\
&= \underline{\mathcal{D}}_F \underline{T}_{\psi_{SS,h}} \begin{bmatrix} \underline{I}_{n_\alpha} \\ \underline{0}_{(N_h - n_\alpha)\times n_\alpha} \end{bmatrix} \underline{\alpha} && (7.70e)\\
&= \underline{\mathcal{D}}_F \underline{T}_{\psi_{SS,h}} \begin{bmatrix} \underline{I}_{n_\alpha} \\ \underline{0}_{(N_h - n_\alpha)\times n_\alpha} \end{bmatrix} \underline{R}_h \underline{\theta} && (7.70f)\\
&= \underline{\mathcal{D}}_F \underline{\Phi}_h \underline{\theta}. && (7.70g)
\end{aligned}$$

Relations (7.42) and (7.43) directly follow from this result.

Chapter 8

Task flexibility for LPTV systems: A basis functions approach

Motion control applications traditionally operate with a single-rate, equidistant sampling scheme. For cost reasons, a current trend in industry is consolidating multiple applications on a single embedded platform, see also Figure 1.3. Generally, to deal with inter-application interference, a predictable scheduling policy allocates resources to the applications in these platforms. Realizing an equidistant sampling scheme on such shared platform is inflexible and often turns out to be expensive in terms of resources or conservative in terms of performance. The aim of this chapter is to investigate the possibilities to relax the equidistant sampling convention. To this end, recent results show that platform timing properties can be represented by a known, precise, and periodically varying set of sampling periods. In view of such predictable platforms, a framework is presented for analysis and synthesis of lifted domain feedforward controllers for non-equidistantly sampled closed-loop systems. Through simulations the potential of non-equidistant sampling over conservative equidistant sampling schemes is demonstrated. The results constitute Contribution IV.B.

The contents of this chapter are published in:
Jurgen van Zundert, Tom Oomen, Dip Goswami, and W.P.M.H. Heemels. On the Potential of Lifted Domain Feedforward Controllers with a Periodic Sampling Sequence. In *Proceedings of the 2016 American Control Conference*, pages 4227–4232. Boston, Massachusetts, 2016.

8.1 Introduction

Traditional motion controllers are often designed and implemented using a single sampling frequency under equidistant sampling, either in a continuous-time setting with a posterior discretization, a discrete-time setting, or a sampled-data setting (Chen and Francis, 1995). Hence, it is tacitly assumed that resources, such as computation, communication, and memory, are sufficiently available.

In certain applications, increasing performance requirements and enhanced functionality lead to a situation where resources are scarce. To deal with these resource limitations, platforms are commonly shared by multiple applications. For example, visual servoing (Chaumette and Hutchinson, 2006) uses feedback information from visual sensors in motion control, where both image processing and control computation tasks are executed on the same processor. In such shared platforms, a scheduler statically/dynamically decides the availability of a resource to an application, and the order of execution of various tasks or applications. Realizing an equidistant sampling scheme in such shared embedded implementation imposes inflexibility and often leads to unnecessary expensive design solutions.

Recently, a potentially promising embedded platform candidate, Composable and Predictable System on Chip (CompSOC), was introduced (Goossens et al., 2017). Composability allows for independent development of multiple applications, while predictability provides precise temporal behavior of the platform. The CompSOC platform is suitable for independent development and interference-free execution of (control) applications. In Valencia et al. (2015), it is shown that a resource-efficient implementation of a control algorithm in such composable platform leads to a set of known, precise, and periodically varying sampling periods. Whereas the majority of control design techniques aims at a single sampling frequency, the aim of this chapter is to develop a control design framework that exploits the periodicity knowledge from the platform for analyzing and synthesizing motion controllers. In particular, the focus is on feedforward controllers, since they constitute the largest part of the motion system's control input (De Gelder et al., 2006).

The design of controllers for linear periodically time-varying (LPTV) systems has been investigated in Bamieh et al. (1991); Yamamoto and Khargonekar (1996) and has been mainly applied to sampled-data designs with an equidistant sample frequency (Bamieh and Pearson Jr., 1992; Chen and Francis, 1995). These approaches have been further developed towards multirate sampling, where different actuator/sensor channels have different rates, see Lall and Dullerud (2001); Fujimoto and Hori (2002); Salt and Albertos (2005) for feedback designs, Oomen et al. (2007) for motion feedback control, and Chapter 7 for multirate feedforward design.

Although important developments for periodically time-varying systems have occurred, they are not directly applicable to feedforward design for a periodic

sampling sequence. The main contribution of this chapter is a framework for the design of feedforward controllers under non-equidistant sampling. This combines the analysis of data-based feedforward design (Van de Wijdeven and Bosgra, 2010; Van der Meulen et al., 2008; Boeren et al., 2015) with non-equidistant sampling, where the main technical step involves a specific lifting step.

The outline of this chapter is as follows. First, the problem and control goal are formulated in Section 8.2. The model of the non-equidistantly sampled system is developed in Section 8.3. This model is used for feedforward controller design in Section 8.4. In Section 8.5, the advantages of describing and controlling the system as a non-equidistantly sampled system instead of a conservative time-invariant sampled system are demonstrated through a simulation example. Finally, conclusions and an outlook are given in Section 8.6.

Notation. Finite dimensional, linear, single-input, single-output, discrete-time systems are considered. Extension to multi-input, multi-output systems is straightforward, since the theory is based on state-space descriptions. Dotted lines indicate a high equidistant sampling rate, dashed lines a low equidistant sampling rate, and dash-dotted lines a non-equidistant sampling rate. Underlined variables indicate finite-time matrix descriptions. $\underline{I}_n$ denotes the $n \times n$ identity matrix, $\otimes$ the Kronecker product, and $\circ$ the Hadamard product. The superscript 0 refers to the base period, subscript i refers to subperiod δ_i.

8.2 Problem formulation

In this section, the objective is formulated by defining the periodic sampling sequence, the control configuration, and the control goal.

8.2.1 Periodic sampling sequence

In this section, the periodic timing behavior observed in platforms as Goossens et al. (2017); Valencia et al. (2015) is described. Such a platform runs under a time division multiplexing (TDM) policy where the TDM wheel of length $T\delta_b$ is divided into a fixed number of time slots. Depending on the allocation of slots to the applications, the timing behavior of an application can be abstracted as shown in Figure 8.1. The motion control task is only allocated and executed in the ■ slots. Other applications run on the ■ slots. The composable nature of the platform allows for independent analysis of the control application.

Assumption 8.1 is imposed throughout this chapter.

Assumption 8.1. *In a period $T\delta_b$ there are τ subperiods of length δ_i, $i = 1, 2, \ldots, \tau$, which are an integer multiple of base period δ_b, i.e., $\delta_i = \gamma_i \delta_b$, $\gamma_i \in \mathbb{N}$, indicated by*

$$\Gamma_{ne} := \begin{bmatrix} \gamma_1 & \gamma_2 & \ldots & \gamma_\tau \end{bmatrix}. \tag{8.1}$$

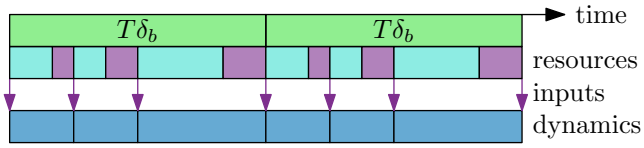

Figure 8.1. Example timeline where the processor is allocated to either motion control tasks (■) or to non-motion control tasks (■).

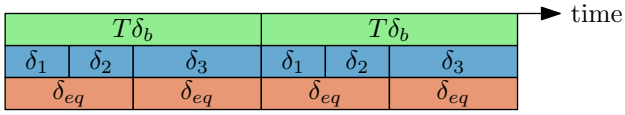

Figure 8.2. Example of periodic non-equidistant sampling where a period $T\delta_b$ consists of three subperiods ($\tau = 3$) with $\Gamma_{ne} = \begin{bmatrix}1 & 1 & 2\end{bmatrix}$.

An example of two periods $T\delta_b$ is provided by Example 8.2.

Example 8.2. *Consider Figure 8.2 with the sampling sequence given by* $\Gamma_{ne} = \begin{bmatrix}1 & 1 & 2\end{bmatrix}$. *There is more design freedom with the non-equidistant sequence (■) than with the conservative equidistant sampling sequence (■).*

Remark 8.3. *Assumption 8.1 can directly be relaxed at the expense of more involved derivations.*

8.2.2 Control configuration

The motion system is controlled via the feedback/feedforward control architecture depicted in Figure 8.3. The selected configuration is common in motion control, but the results can readily be extended to other configurations. In Figure 8.3, G is the motion system, and C the feedback controller acting on the error error ε between the output ψ and the reference signal ρ. F is the feedforward controller to be designed, see also Section 8.2.3.

Including the periodic non-equidistant sampling into the control diagram of Figure 8.3 yields Figure 8.4. Here, $G = \mathcal{D}G_b\mathcal{H}$ is a sampled version of the (linear) plant G_b at the base rate δ_b, with $\mathcal{D}$ and $\mathcal{H}$ the downsampler and upsampler, respectively, that are defined in Section 8.3.4.

8.2.3 Control goal

The control goal is to design the feedforward controller F such that error ε is minimized according to a certain performance criterion. To provide a fair comparison, the feedback controller C is designed at a conservative, equidistant sampling rate, see also Figure 8.2. This is by no means restrictive and can

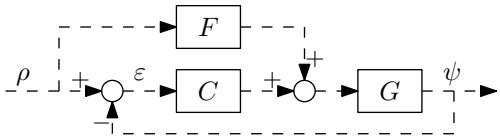

Figure 8.3. Closed-loop control configuration.

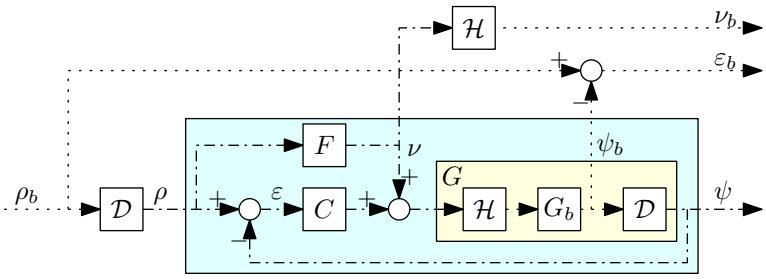

Figure 8.4. Control diagram including the sample rate conversion between the equidistant base rate δ_b (- - -) and the non-equidistant rate (-·-·). Only the □ part is implemented on the actual system.

directly be relaxed. The feedforward controller is explicitly designed and implemented at the non-equidistantly sampled rate. To enable a fair comparison, the tracking error ε_b at equidistant rate δ_b is used for performance evaluation. This data is often available off-line and can be used in batch-to-batch feedforward control (Gorinevsky, 2002; Boeren et al., 2015). The framework can easily be adapted for evaluation of the tracking error at other rates.

With the definition of the non-equidistant sampling sequence and the control configuration, the main problem can be formulated.

Main problem. *Given the closed-loop configuration in Figure 8.4, with stabilizing C, and a periodic, non-equidistant sampling sequence, see for example Figure 8.2, determine the optimal feedforward controller*

$$F_{opt} := \arg\min_{F \in \mathcal{F}} V_b(F), \tag{8.2}$$

where

$$V_b(F) = \|\underline{\varepsilon}_b\|^2_{\underline{W}_\varepsilon} + \|\underline{\nu}_b\|^2_{\underline{W}_\nu}, \tag{8.3}$$

with $\|(\cdot)\|^2_W = (\cdot)^\top W(\cdot)$, $\underline{W}_\varepsilon{}^\top = \underline{W}_\varepsilon \succ 0$, $\underline{W}_\nu{}^\top = \underline{W}_\nu \succeq 0$, *and where* $\underline{\varepsilon}_b, \underline{\nu}_b \in \mathbb{R}^{N_b}$, $N_b \in \mathbb{N}$, *are the lifted domain equivalents of* ε_b *and* ν_b, *respectively.*

In Section 8.4, the feedforward class $\mathcal{F}$ is defined and the optimal feedforward controller F_{opt} is derived. The latter requires the relation between $\underline{\nu}$ and $\underline{\varepsilon}_b$ which is derived next.

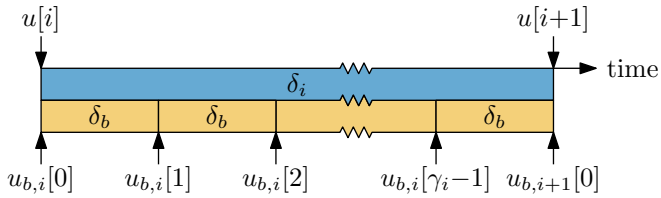

Figure 8.5. A single period δ_i consists of γ_i base periods δ_b where the input $u_{b,i}$ remains constant.

8.3 System description

In this section, the non-equidistantly sampled system G and feedback controller C are described in order to express $\underline{\varepsilon}_b$ in terms of $\underline{\nu}$. The design of F is presented separately in Section 8.4. In the following sections, a systematic framework for describing these systems using finite-time descriptions is presented. In succession, the dynamics during a subperiod δ_i, during a period $T\delta_b$, and during a finite length N are described. Finally, finite-time descriptions of the downsampler and upsampler are derived, and the system interconnection is derived, providing the relation between $\underline{\varepsilon}_b$ and $\underline{\nu}$.

8.3.1 Dynamics during a subperiod

Due to the periodic nature, the system dynamics are identical for every period $T\delta_b$. In order to describe the dynamics during a period $T\delta_b$, a description of the dynamics during subperiods δ_i is required. In Theorem 8.4, the dynamics over a subperiod are provided at rate δ_b. In Corollary 8.5, the equivalent dynamics at rate δ_i are presented.

Theorem 8.4. *Let the dynamics of a discrete-time system with equidistant sampling time δ_b have state-space representation (A_b, B_b, C_b, D_b) and let the sampling periods δ_i satisfy Assumption 8.1, see also Figure 8.5. If a zero-order-hold of period δ_i is applied to the input of this system, i.e., $u_{b,i}[k] = u[i]$, $k = 0, 1, \ldots, \gamma_i - 1$, then the dynamics during the interval δ_i are given by*

$$x_{b,i}[n] = A_b^n x_{b,i}[0] + \sum_{j=0}^{n-1} A_b^j B_b u_{b,i}[0], \quad n \leq \gamma_i, \tag{8.4a}$$

$$y_{b,i}[0] = C_b x_{b,i}[0] + D_b u_{b,i}[0]. \tag{8.4b}$$

Proof. Follows from successive substitution. □

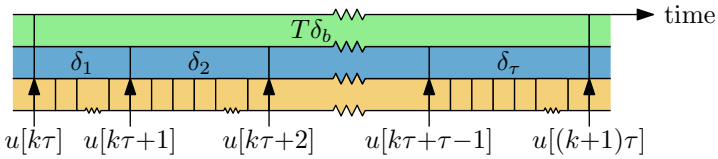

Figure 8.6. The dynamics over a period $T\delta_b$ is determined by the dynamics of the τ subperiods δ_i, $i = 1, 2, \ldots, \tau$.

Corollary 8.5. *The equivalent dynamics of the system in Theorem 8.4 for sampling time δ_i has state-space representation*

$$\left[\begin{array}{c|c} A[i] & B[i] \\ \hline C[i] & D[i] \end{array}\right] = \left[\begin{array}{c|c} A_b^{\gamma_i} & \sum_{j=0}^{\gamma_i-1} A_b^j B_b \\ \hline C_b & D_b \end{array}\right]. \tag{8.5}$$

Corollary 8.5 shows that downsampling the system of Theorem 8.4 from sampling time δ_b to δ_i is equivalent to considering $n = \gamma_i$ steps as a single step, see also Example 8.6.

Example 8.6. *Consider the discrete-time system with transfer function $\frac{5z}{z-2}$ at equidistant sampling rate δ_b. A state-space realization of this system is*

$$(A_b, B_b, C_b, D_b) = (2, 4, 2.5, 5). \tag{8.6}$$

Then, by Corollary 8.5, the dynamics over a subperiod $\delta_i = 2\delta_b$, admit the state-space realization

$$(A[i], B[i], C[i], D[i]) = \left(A_b^2, B_b + A_b B_b, C_b, D_b\right) = (4, 12, 2.5, 5) \tag{8.7}$$

and has transfer function

$$C[i](z - A[i])^{-1}B[i] + D[i] = \frac{5z + 10}{z - 4}. \tag{8.8}$$

8.3.2 Dynamics during a period

The dynamics during a subperiod at rate δ_i are described by Corollary 8.5. By combining the dynamics of the τ subperiods δ_i, $i = 1, 2, \ldots, \tau$, see Figure 8.6, the dynamics during a period $T\delta_b$ are obtained as provided by Theorem 8.7. Downsampling this system to rate $T\delta_b$ yields a multi-input, multi-output system as shown by Theorem 8.8.

Theorem 8.7. *During the kth period $T\delta_b$, consisting of τ periods δ_i, the dynamics at non-equidistant rate δ_i evolve according to*

$$x[k\tau+n] = \prod_{j=0}^{n-1} A[n-j]\,x[k\tau] + \sum_{i=0}^{n-1}\prod_{j=0}^{n-i-2} A[n-j]B[i+1]u[k\tau+i], \tag{8.9a}$$

$$y[k\tau+n] = C[n]x[k\tau+n] + D[n]u[k\tau+n], \quad n \leq \tau, \tag{8.9b}$$

with $\prod_{j=0}^{n} A[j] = I$ *for* $n \leq 0$.

Proof. Follows from successive substitution of the dynamics in (8.5) according to Figure 8.6. □

Theorem 8.8. *The dynamics of Theorem 8.7 at non-equidistant rate δ_i have a τ-input, τ-output equivalent at equidistant rate $T\delta_b$ with state-space realization*

$$\left[\begin{array}{c|cccc} \prod_{j=0}^{\tau-1} A[\tau-j] & \prod_{j=0}^{\tau-2} A[\tau-j]B[1] & \prod_{j=0}^{\tau-3} A[n-j]B[2] & \cdots & B[\tau] \\ \hline C_b & D_b & 0 & \cdots & 0 \\ C_bA[1] & C_bB[1] & D_b & \ddots & \vdots \\ \vdots & \vdots & \ddots & \ddots & 0 \\ C_b\prod_{j=0}^{\tau-1} A[\tau-j] & C_b\sum_{j=0}^{\tau-2} A[\tau-j]B[1] & \cdots & C_bB[\tau-1] & D_b \end{array}\right], \tag{8.10}$$

with state $\underline{x}$, $\underline{x}[k] = x[k\tau]$, $k \in \mathbb{N}$, and input $\underline{u}$ and output $\underline{y}$ given by

$$\underline{u}[k] = \begin{bmatrix} u[k\tau] \\ u[k\tau+1] \\ \vdots \\ u[(k+1)\tau-1] \end{bmatrix}, \qquad \underline{y}[k] = \begin{bmatrix} y[k\tau] \\ \underline{y}[k\tau+1] \\ \vdots \\ \underline{y}[(k+1)\tau-1] \end{bmatrix}. \tag{8.11}$$

Proof. Follows from successive substitution of the relations in Theorem 8.7 and Corollary 8.5. □

Since the system is perceived at non-equidistant rate δ_i, Theorem 8.7 is used for deriving finite-time expressions in Section 8.3.3. Theorem 8.8 is used for feedforward controller design in Section 8.4.

8.3.3 Finite-time description of the system

The dynamics over the finite signal length are described using finite-time descriptions. First, finite-time descriptions for LTI systems are recapitulated. Second, finite-time expressions for the LPTV system are derived.

Let the single-rate discrete-time system $G \overset{z}{=} (A, B, C, D)$ be operating over a finite-time interval $[0, N-1]$. Then, the input-to-output behavior is given by

$$\underline{\psi} = \underline{G}\underline{\nu}, \qquad \underline{G} = \begin{bmatrix} h(0) & 0 & 0 & \cdots & 0 \\ h(1) & h(0) & 0 & \cdots & 0 \\ h(2) & h(1) & h(0) & \cdots & 0 \\ \vdots & \vdots & \vdots & \ddots & \vdots \\ h(N-1) & h(N-2) & h(N-3) & \cdots & h(0) \end{bmatrix}, \tag{8.12}$$

with Markov parameters $h(0) = D$ and $h(k) = CA^{k-1}B$, $k = 1, 2, \ldots, N-1$. For causal singlevariable LTI systems, $\underline{G} \in \mathbb{R}^{N \times N}$ is a square lower triangular Toeplitz matrix that maps input vector $\underline{\nu} = \begin{bmatrix} \nu[0] & \nu[1] & \nu[2] & \ldots & \nu[N-1] \end{bmatrix}^\top \in \mathbb{R}^N$ to output vector $\Psi = \begin{bmatrix} \psi[0] & \psi[1] & \psi[2] & \ldots & \psi[N-1] \end{bmatrix}^\top \in \mathbb{R}^N$.

Finite-time descriptions can also be used for LPTV systems. For time-invariant systems, entries in the finite-time description correspond to equidistant points in time. This property is lost for non-equidistantly sampled systems where the entries correspond to non-equidistant points in time determined by the sampling sequence Γ_{ne}. The finite-time description for the LPTV system of Theorem 8.7 is provided by Theorem 8.9.

Theorem 8.9. *Given a state space realization (A_b, B_b, C_b, D_b) of the system G_b at equidistant rate δ_b, and a periodic, non-equidistant sampling sequence of τ subperiods per period $T\delta_b$, the finite-time description of G, given the periodic, non-equidistant sampling sequence Γ_{ne}, is given by*

$$\underline{G} = \left[\begin{array}{ccccc|c} D_b & 0 & 0 & \cdots & 0 & \cdots \\ C_b B[1] & D_b & 0 & \cdots & 0 & \cdots \\ C_b A[2] B[1] & C_b B[2] & D_b & \cdots & 0 & \cdots \\ \vdots & \ddots & \ddots & \ddots & \vdots & \ddots \\ C_b \prod_{j=0}^{\tau-2} A[\tau-j] B[1] & \cdots & \cdots & C_b B[\tau-1] & D_b & \cdots \\ \hline \vdots & \ddots & \vdots & \vdots & \vdots & \ddots \end{array}\right], \tag{8.13}$$

where $A[i] = A_b^{\gamma_i}$, $B[i] = \sum_{j=0}^{\gamma_i - 1} A_b^j B_b$, and $\underline{G} \in \mathbb{R}^{N \times N}$.

Proof. The finite-time description of the dynamics of Theorem 8.7 is given by

$$\underline{G} = \begin{bmatrix} D[1] & 0 & 0 & \cdots & 0 \\ C[2]B[1] & D[2] & 0 & \cdots & 0 \\ C[3]A[2]B[1] & C[2]B[2] & D[3] & \cdots & 0 \\ \vdots & \ddots & \ddots & \ddots & \vdots \\ C[N] \prod_{j=0}^{N-2} A[N-j] B[1] & \cdots & \cdots & C[N]B[N-1] & D[N] \end{bmatrix}. \tag{8.14}$$

Since the system is periodic with period T consisting of τ subperiods, it holds that $A[i+k\tau] = A[i]$ and $B[i+k\tau] = B[i]$, for all $k \in \mathbb{N}$, with $(A[i], B[i], C[i], D[i])$ given by Corollary 8.5. □

Note that $\underline{G}$ in Theorem 8.9 is block-Toeplitz with block size $\tau \times \tau$. The equidistant sampling case is a special case of Theorem 8.9, see Corollary 8.10.

Corollary 8.10. *If $\gamma_i = \gamma$, for all i, then $(A[i], B[i], C[i], D[i]) = (A, B, C, D)$, for all i, and the equidistant sampling case is recovered as a special case.*

8.3.4 Finite-time descriptions of rate conversions

In Theorem 8.9, the finite-time description for the LPTV system is provided. To describe the full system of Figure 8.4 in a finite-time framework, the finite-time descriptions of the downsampler $\mathcal{D}$ and zero-order-hold upsampler $\mathcal{H}$ are required. These are provided by Theorem 8.11 where it should be noted that these results can readily be extended to the situation when there is not an integer number of periods T present in N.

Theorem 8.11. *For the purpose of exposition, let the time span of N samples consist of an integer number of periods T, and define the vectors*

$$\mu_T[i] := i - 1, \quad i = 1, 2, \ldots, T, \tag{8.15}$$

$$\mu_\tau[i] := \begin{cases} 0, & n = 1, \\ \sum_{j=1}^{i-1} \gamma_i, & n = 2, 3, \ldots, \tau + 1. \end{cases} \tag{8.16}$$

The finite-time expression of the downsampler $\mathcal{D}$ is

$$\underline{\mathcal{D}} := \underline{I}_{\frac{N}{T}} \otimes \underline{\mathcal{D}}_{T,\tau}, \tag{8.17}$$

with $\underline{\mathcal{D}}_{T,\tau} \in \mathbb{R}^{\tau \times T}$ given by

$$\underline{\mathcal{D}}_{T,\tau}[i,j] := \begin{cases} 1, & \mu_\tau[i] = \mu_T[j], \\ 0, & \textit{otherwise}. \end{cases} \tag{8.18}$$

The finite-time expression of the zero-order-hold upsampler $\mathcal{H}$ is

$$\underline{\mathcal{H}}_{\tau,T} := \underline{I}_{\frac{N_b}{T}} \otimes \underline{\mathcal{H}}_T, \tag{8.19}$$

with $\underline{\mathcal{H}}_{\tau,T} \in \mathbb{R}^{T \times \tau}$ given by

$$\underline{\mathcal{H}}_{\tau,T}[i,j] := \begin{cases} 1, & \mu_\tau[j] \leq \mu_T[i] < \mu_\tau[j+1], \\ 0, & \textit{otherwise}. \end{cases} \tag{8.20}$$

Proof. See, for example, Oomen et al. (2009). □

Note that both $\underline{\mathcal{H}}$ and $\underline{\mathcal{D}}$ are block-Toeplitz matrices. Furthermore, note that up-down conversion does not affect the signal ($\underline{\mathcal{D}}\underline{\mathcal{H}} = \underline{I}_N$), whereas down-up conversion does affect the signal ($\underline{\mathcal{H}}\underline{\mathcal{D}} \neq \underline{I}_{N_b}$).

8.3.5 System interconnection

By combining Theorem 8.9 and Theorem 8.11, the finite-time description of the system in Figure 8.4 is complete and the system interconnection can be described. The error $\underline{\varepsilon}_b$ as function of the feedforward $\underline{\nu}$ is provided by Theorem 8.12.

Theorem 8.12. *The finite-time error $\underline{\varepsilon}_b$ in Figure 8.4 for the equidistant rate δ_b is given by*

$$\underline{\varepsilon}_b = \underline{S}_b\underline{\rho}_b - \underline{S}_b\underline{G}_b\underline{\mathcal{H}}\underline{\nu}, \tag{8.21}$$

with $\underline{S}_b = \left(\underline{I}_{N_b} + \underline{G}_b\underline{\mathcal{H}}\underline{C}\underline{\mathcal{D}}\right)^{-1}$.

Proof. The output at the base rate is given by

$$\underline{\psi}_b = \underline{S}_b\underline{G}_b\underline{\mathcal{H}}\underline{\nu} + \underline{S}_b\underline{G}_b\underline{\mathcal{H}}\underline{C}\underline{\mathcal{D}}\underline{\rho}_b. \tag{8.22}$$

The result follows from substituting this expression in $\underline{\varepsilon}_b = \underline{\rho}_b - \underline{\psi}_b$ and rearranging terms. □

In this section, finite-time descriptions for the system interconnection of Figure 8.4 are presented. Next, these expressions are used for designing the feedforward filter F.

8.4 Lifted domain feedforward optimization

The class $\mathcal{F}$ to which the feedforward controller F in the main problem in Section 8.2.3 belongs to is parameterized according to Definition 8.13. Parameter $\underline{\beta} \in \mathbb{R}^{n_\beta\tau^2}$ contains all parameters in $\underline{\beta}_i$, $i = 0, 1, \ldots, n_\beta - 1$.

Definition 8.13. *The feedforward class $\mathcal{F}$ is given by*

$$\mathcal{F} = \left\{ \sum_{i=0}^{n_\beta-1} \underline{\beta}_i \circ \vartheta_i(z) \;\middle|\; \underline{\beta}_i \in \mathbb{R}^{\tau\times\tau} \right\}, \tag{8.23}$$

with $\vartheta_i(z)$ an τ-input, τ-output system of basis functions.

Note that the class $\mathcal{F}$ in Definition 8.13 consists of multivariable transfer functions in the so-called lifted domain (Bamieh and Pearson Jr., 1992). In the physical time domain, after reversal of the lifting operator, it becomes a singlevariable yet LPTV operator, due to the periodic sampling sequence, hence the name lifted feedforward controller.

The finite-time description of F, denoted $\underline{F}(\underline{\beta})$, depends on the particular choice of Γ_{ne}. Since by Definition 8.13 it is linear in $\underline{\beta}$, there exists a matrix $\underline{T}_{\rho,\beta} \in \mathbb{R}^{N \times n_\beta \tau^2}$ satisfying

$$\underline{F}(\underline{\beta})\underline{\rho} = \underline{T}_{\rho,\beta}\underline{\beta}. \tag{8.24}$$

Using (8.24) and combining the results of the previous sections, the optimal feedforward filter can be computed, see Theorem 8.14.

Theorem 8.14. *The optimal solution to the main problem in Section 8.2.3 with $\mathcal{F}$ according to Definition 8.13 is given by*

$$\underline{\beta}_{opt} = \left(\underline{\mathcal{M}}^\top \underline{W}_\varepsilon \underline{\mathcal{M}} + \underline{T}_{\rho,\beta}^\top \underline{W}_\nu \underline{T}_{\rho,\beta}\right)^{-1} \underline{\mathcal{M}}^\top \underline{W}_\varepsilon \underline{b}, \tag{8.25}$$

with

$$\underline{b} = \underline{S}_b \underline{\rho}_b, \tag{8.26}$$

$$\underline{\mathcal{M}} = \underline{S}_b \underline{G}_b \underline{\mathcal{H}} \underline{T}_{\rho,\beta}. \tag{8.27}$$

Proof. Substitution of $\underline{\nu} = \underline{F}(\underline{\beta})\underline{\rho} = \underline{T}_{\rho,\beta}\underline{\beta}$, see (8.24), in Theorem 8.12 yields $\underline{\varepsilon}_b = \underline{b} - \underline{\mathcal{M}}\underline{\beta}$. Hence, V_b is quadratic in $\underline{\beta}$ and thus the minimum follows from $\nabla_{\underline{\beta}} V_b = 0$ which yields $\underline{\beta}_{opt}$. □

Theorem 8.14 is used in the simulation case study of the next section.

8.5 Simulation case study

In this section, the advantages of the periodic, non-equidistant sampling framework introduced in this chapter over conservative equidistant sampling are shown through a simulation case study.

8.5.1 System definition

The system is based on the rotational two-mass-spring-damper system shown in Figure 8.7. The feedback controller C is a lead filter yielding a closed-loop bandwidth (first 0 dB crossing of the open-loop) of 10 Hz. In order to have the same feedback controller for each sampling sequence, the feedback controller is designed at the lowest rate. The reference signal ρ_b is selected as the fourth order point-to-point trajectory depicted in Figure 8.8.

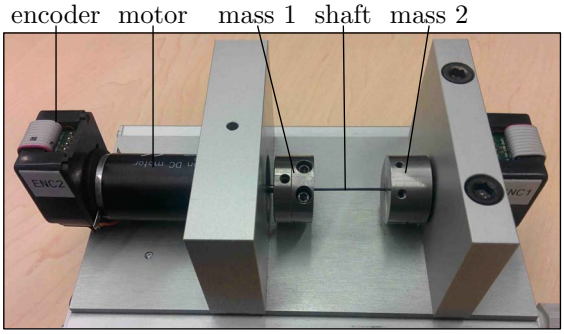

(a) Photograph of the mechanical setup consisting of two masses interconnected by a flexible shaft.

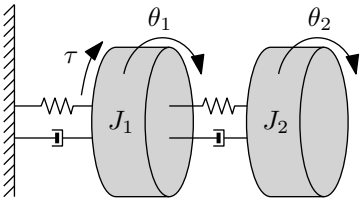

(b) Model of the mechanical setup in (a).

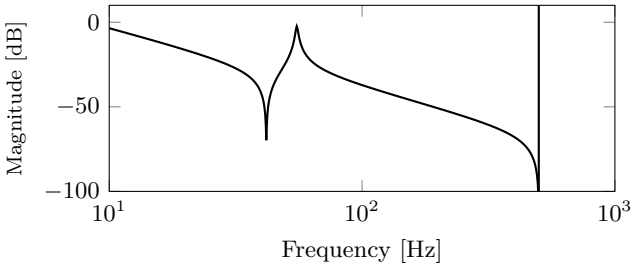

(c) Bode magnitude plot of the model for sampling time $\delta_b = 1$ ms.

Figure 8.7. The system G is the model of the collocated control loop from the motor to the encoder.

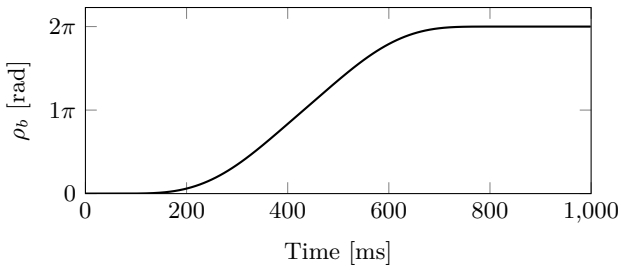

Figure 8.8. The reference trajectory is a fourth order point-to-point profile.

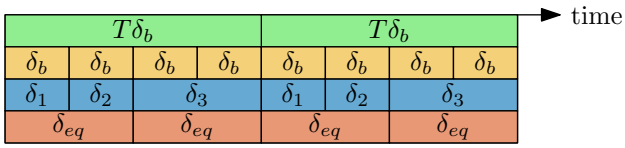

Figure 8.9. Two periods $T\delta_b$ of the case study's timeline with the base rate δ_b (■), non-equidistant sampling (■), and equidistant sampling (■).

8.5.2 Sampling sequences

In this case study, the sampling sequence of Figure 8.2 is used, i.e., $\Gamma_{ne} = \begin{bmatrix}1 & 1 & 2\end{bmatrix}$, see also Figure 8.9. The highest possible equidistant sampling rate is $2\delta_b$, i.e., $\Gamma_{eq} = \begin{bmatrix}2 & 2\end{bmatrix}$, which is conservative since in each period $T\delta_b$ a control point is neglected. The proposed framework allows to exploit all possible control points. Since this increases the freedom of the feedforward signal, an increase in performance can be expected.

The basis functions $\vartheta_i(z)$ in Definition 8.13 are selected as

$$\vartheta_i(z) = z^{-i} \begin{bmatrix} 1 & 1 & \cdots & 1 \\ 1 & 1 & \cdots & 1 \\ \vdots & \vdots & \ddots & \vdots \\ 1 & 1 & \cdots & 1 \end{bmatrix}. \tag{8.28}$$

In the simulation $\delta_b = 0.001$ s, $N_b = 1000$, and the weights in (8.3) are selected as $\underline{W}_\varepsilon = 10^{12}\underline{I}_{N_b}$ and $\underline{W}_\nu = 0_{N_b}$ in order to minimize $\underline{\varepsilon}_b$.

8.5.3 Results

For comparison, the results for sampling at the base rate δ_b are also presented. Note that this is typically not possible in practice, but included here as benchmark. The results are shown in Figure 8.10.

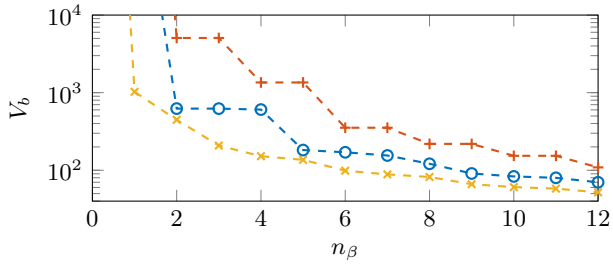

(a) Performance metric V_b versus number of parameterized periods n_β.

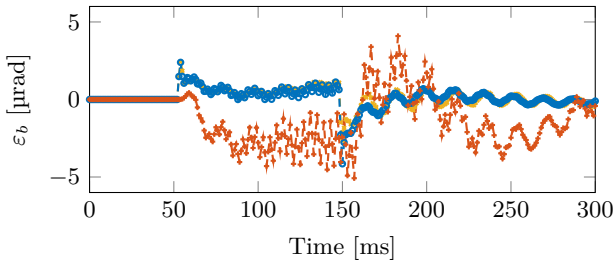

(b) Error signal ε_b at the start of the motion for $n_\beta = 3$.

Figure 8.10. Results of the case study for $\Gamma_b = \begin{bmatrix}1 & 1 & 1 & 1\end{bmatrix}$ (·✱·), $\Gamma_{ne} = \begin{bmatrix}1 & 1 & 2\end{bmatrix}$ (·⊖·), and $\Gamma_{eq} = \begin{bmatrix}2 & 2\end{bmatrix}$ (·+·).

The performance metric V_b as function of n_β for the three sampling sequences is shown in Figure 8.10(a). A higher n_β means a larger operating time span of the feedforward controller and therefore an improved performance. This is indeed observed for all three cases: V_b decreases for increasing n_β. As expected, the performance of the sampling sequence $\Gamma_{ne} = \begin{bmatrix}1 & 1 & 2\end{bmatrix}$ is worse than for $\Gamma_b = \begin{bmatrix}1 & 1 & 1 & 1\end{bmatrix}$ (less control points per period) and higher than for $\Gamma_{eq} = \begin{bmatrix}2 & 2\end{bmatrix}$ (more control points per period). The time-domain error signal $\underline{\varepsilon}_b$ near the start of the motion is provided in Figure 8.10(b) for $n_\beta = 3$.

8.6 Conclusion and outlook

A resource-efficient implementation on a class of predictable platforms leads to a periodically switched system due to periodic, non-equidistant sampling. The analysis and controller design of such systems can be done by (i) settling with slower equidistant sampling of the system and using standard LTI techniques; or (ii) controlling the system as a non-equidistantly sampled system and exploiting all possible control points. The first option is often conservative in terms of performance since not all measurement and actuation points are exploited. In

this chapter, a framework is introduced that allows to describe the periodic, non-equidistantly sampled systems of option (ii). Moreover, the framework allows for optimal feedforward design incorporating the non-equidistant sampling of the system. As a case study, a motion control application is considered and through simulation it is shown that non-equidistant sampling control of option (ii) is indeed superior to conservative equidistant sampling of option (i).

Ongoing work focuses on experimental validation of the presented work. Future work aims at optimal selection of the sampling sequence.

Chapter 9

Task flexibility in ILC: A rational basis functions approach

Iterative Learning Control (ILC) can significantly enhance the performance of systems that perform repeating tasks, see also Section 1.5. However, small variations in the performed task may lead to a large performance deterioration. The aim of this chapter is to develop a novel ILC approach, by exploiting rational basis functions, that enables performance enhancement through iterative learning, while providing flexibility with respect to task variations. The proposed approach involves an iterative optimization procedure after each task that exploits recent developments in instrumental variable-based system identification. Enhanced performance compared to pre-existing results is proven theoretically and illustrated through simulation examples. The results constitute Contribution IV.C.

9.1 Introduction

ILC enables a significant performance enhancement of batch-repetitive processes. In ILC, the command signal is iteratively updated from one experiment (trial) to the next. Typical ILC algorithms generate a control signal that exactly compensates for the trial-invariant exogenous disturbances during a specific task. ILC has been thoroughly researched, including convergence analysis (Norrlöf and Gunnarsson, 2002; Moore, 1993), multivariable systems (Blanken et al., 2016a), and robustness to model uncertainty (Ahn et al., 2007; Li et al., 2016;

The contents of this chapter are published in:
Jurgen van Zundert, Joost Bolder, and Tom Oomen. Optimality and flexibility in Iterative Learning Control for varying tasks. *Automatica*, 67:295–302, 2016.

Bristow and Alleyne, 2008) and disturbances (Ghosh and Paden, 2002; Saab, 2005). In addition, many successful applications have been reported, including wafer scanners (Mishra et al., 2007; De Roover and Bosgra, 2000), rehabilitation (Xu et al., 2014), and printing systems (Bolder et al., 2014).

ILC can perfectly compensate for non-varying disturbances, but is consequently very sensitive to varying disturbances. These varying disturbances include measurement noise and also changing reference trajectories. As a result, a learned signal corresponds to a specific reference signal and a change in this signal potentially leads to performance deterioration (Gao and Mishra, 2014; Phan and Frueh, 1996; Heertjes and Van de Molengraft, 2009; Hoelzle et al., 2011). To overcome this drawback, several solutions to enhance the extrapolation properties of ILC have been developed. In Hoelzle et al. (2011), the extrapolation properties are enhanced by constructing the task such that it consists of a set of basis tasks. This provides extrapolation to tasks consisting of a finite set of elementary tasks. A more general approach is to parameterize the command signal in a set of basis functions (Phan and Frueh, 1996; Oh et al., 1997). Such an approach allows for arbitrary tasks. Examples include polynomial basis functions (Van de Wijdeven and Bosgra, 2010; Bolder et al., 2014; Heertjes and Van de Molengraft, 2009; Gao and Mishra, 2014) for which the associated optimization problem has an explicit analytic solution (Gunnarsson and Norrlöf, 2001). These polynomial approaches have clear advantages from an optimization perspective, since global optimality can be guaranteed and the implementation and computation is generally inexpensive and fast.

Recently, rational basis functions have been introduced in ILC in Bolder and Oomen (2015). These rational basis functions are more general than polynomial basis functions. In fact, polynomial basis functions are recovered as a special case of rational basis functions. In the rational case, an analytic solution can be retained if the poles are pre-specified (Heuberger et al., 2005). Alternatively, the poles can be updated while maintaining a convex optimization problem (Blanken et al., 2017b; Blanken et al., 2018). In Bolder and Oomen (2015), the poles are also optimized to enable enhanced performance by solving the non-convex optimization problem using a similar algorithm as in Steiglitz and McBride (1965). In Bolder and Oomen (2015), fast convergence to a stationary point and increased performance is reported. In addition, the algorithm is reported to be less sensitive to local minima when compared to a Gauss-Newton type of algorithm as shown in, for example, Bohn and Unbehauen (1998). However, in this chapter both a theoretical and numerical analysis are presented that reveal that the stationary point of the iteration is not necessarily a minimum of the objective function, which in fact has also been observed in related system identification algorithms (Whitfield, 1987).

Although important contributions have been made to enhance extrapolation capabilities of ILC through basis functions, presently available optimization algorithms suffer from the problem of non-optimality or poor convergence prop-

erties. The aim of this chapter is to develop a new approach that guarantees that the stationary point of the iterative solution is always an optimum. As a consequence, increased performance is achieved compared to pre-existing approaches. The proposed approach is related to instrumental variable system identification. Note that the instrumental variable approach in Boeren et al. (2015) is essentially different in that it deals with an estimation problem and not an ILC problem.

The contributions of this chapter are threefold. First, a new iterative solution algorithm for rational basis functions in ILC is proposed, which constitutes the main contribution of this chapter. Second, non-optimality of the pre-existing approach for rational basis functions in ILC is established. Third, it is shown by two simulation examples that (i) the proposed approach outperforms the pre-existing approach, and (ii) ILC with basis functions outperforms standard ILC for varying reference tasks. Since the proposed approach has close connections to instrumental variable-based system identification, the simulation study may be of interest to instrumental variable based system identification. In Bolder and Oomen (2015), a different iterative solution for rational basis functions in ILC is provided. In this chapter, it is theoretically proven and illustrated through simulation examples that this pre-existing approach is non-optimal by construction and is outperformed by the proposed approach.

The outline of this chapter is as follows. In Section 9.2, the problem considered in this chapter is introduced. The proposed approach is presented in Section 9.3. In Section 9.4, the proposed approach is compared with the pre-existing approach in Bolder and Oomen (2015). Moreover, non-optimality of the pre-existing approach is established. The two iterative approaches are compared by use of a simulation example in Section 9.5, demonstrating that the proposed approach outperforms the pre-existing approach on a complex industrial system. In Section 9.6, a simulation example is presented revealing the benefit of using basis functions in ILC. Section 9.7 contains conclusions and an outlook.

Notation. In this chapter, systems are discrete-time, linear, time-invariant (LTI), single-input, single-output (SISO). Systems are generally rational in complex indeterminate z and indicated with the argument z, for example $H(z)$. Let $x[k]$ denote a signal x at time k. Let h be the impulse response of the system $H(z)$. The output $y[k]$ of the response of $H(z)$ to input u is given by $y[k] = \sum_{l=-\infty}^{\infty} h(l)u[k-l]$. Let $N \in \mathbb{Z}^+$ denote the trial length, i.e., the number of samples per trial. Assuming $u[k] = 0$ for $k < 0$ and $k > N-1$, then the input-output relation can be recast as

$$\underbrace{\begin{bmatrix} y[0] \\ y[1] \\ \vdots \\ y[N-1] \end{bmatrix}}_{y} = \underbrace{\begin{bmatrix} h(0) & h(-1) & \dots & h(1-N) \\ h(1) & h(0) & \dots & h(2-N) \\ \vdots & \vdots & \ddots & \vdots \\ h(N-1) & h(N-2) & \dots & h(0) \end{bmatrix}}_{H} \underbrace{\begin{bmatrix} u[0] \\ u[1] \\ \vdots \\ u[N-1] \end{bmatrix}}_{u}, \tag{9.1}$$

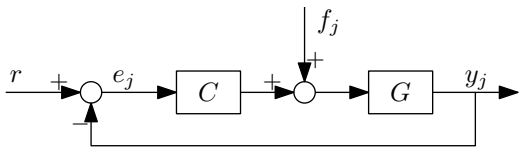

Figure 9.1. Block diagram of closed-loop system under consideration.

with $u, y \in \mathbb{R}^N$ the input and output, respectively. Let $\|x\|_W^2 := x^\top W x$, where $x \in \mathbb{R}^N$ and $W = W^\top \in \mathbb{R}^{N\times N}$. W is positive definite ($W \succ 0$) if and only if $x^\top W x > 0$, for all $x \neq 0$, and positive semi-definite ($W \succeq 0$) if and only if $x^\top W x \geq 0$, for all x.

To facilitate presentation, occasionally transfer functions are assumed causal to enable a direct relation between infinite and finite time. This is standard in ILC (Norrlöf and Gunnarsson, 2002) and not a restriction on the presented results. For instance, the approach in Boeren et al. (2015, Appendix A) may be adopted.

9.2 Problem formulation

In this section, the considered problem is defined by describing the system, introducing norm-optimal ILC, and highlighting the limitations of standard norm-optimal ILC. Finally, the contributions are listed explicitly.

9.2.1 System description

The control setup is shown in Figure 9.1. Here $G = \frac{B_0}{A_0}$, $B_0, A_0 \in \mathcal{R}[z]$, is the rational system and C an internally stabilizing feedback controller. The closed-loop system is assumed to operate batch-repetitive, i.e., the same process of fixed length N is repeated over and over. A single execution is referred to as a trial. The aim is to determine the feedforward f_{j+1} for trial $j+1$ such that the output y_{j+1} follows the trial-invariant reference r, i.e., minimizes the error $e_{j+1} = r - y_{j+1}$.

The error for trial j is given by

$$e_j = Sr - SGf_j \tag{9.2a}$$
$$= Sr - Jf_j, \tag{9.2b}$$

with sensitivity $S := (I + GC)^{-1}$, and process sensitivity $J := SG$. The error for trial $j+1$ is given by

$$e_{j+1} = Sr - Jf_{j+1}. \tag{9.3}$$

Eliminating Sr from (9.3) by using (9.2b) yields the trial-to-trial dynamics

$$e_{j+1} = e_j + J\left(f_j - f_{j+1}\right), \tag{9.4}$$

which are optimized in norm-optimal ILC.

9.2.2 Norm-optimal ILC

Norm-optimal ILC is an important class of ILC in which the feedforward signal f_{j+1} for the next trial is determined by minimizing a performance criterion as in Definition 9.1.

Definition 9.1. *The performance criterion for norm-optimal ILC is given by*

$$\mathcal{J}(f_{j+1}) := \|e_{j+1}\|^2_{W_e} + \|f_{j+1}\|^2_{W_f} + \|f_{j+1} - f_j\|^2_{W_{\Delta f}} \tag{9.5}$$

with $W_e, W_f, W_{\Delta f} \succeq 0$ *and* e_{j+1} *given by* (9.4).

Since $\mathcal{J}(f_{j+1})$ is quadratic in f_{j+1}, the optimal feedforward signal $f_{j+1,opt}$ can be computed analytically (Gunnarsson and Norrlöf, 2001) from

$$\left.\frac{\mathrm{d}\mathcal{J}(f_{j+1})}{\mathrm{d}f_{j+1}}\right|_{f_{j+1}=f_{j+1,opt}} = 0 \tag{9.6}$$

and is provided by Theorem 9.2.

Theorem 9.2. *Given* $J^\top W_e J + W_f + W_{\Delta f} \succ 0$*, model* J*, and measurement data* r, f_j, e_j*, optimal* $f_{j+1,opt}$ *for norm-optimal ILC with the performance criterion of Definition 9.1 is*

$$f_{j+1,opt} = Qf_j + Le_j, \tag{9.7}$$

$$Q = \left(J^\top W_e J + W_f + W_{\Delta f}\right)^{-1}\left(J^\top W_e J + W_{\Delta f}\right), \tag{9.8}$$

$$L = \left(J^\top W_e J + W_f + W_{\Delta f}\right)^{-1} J^\top W_e. \tag{9.9}$$

Proof. Substitute (9.4) in (9.5) and solve (9.6) for $f_{j+1,opt}$. □

With norm-optimal ILC excellent performance is achieved for exactly repeating tasks. Indeed, if G is invertible, $W_e \succ 0$, and $W_f = W_{\Delta f} = 0$, convergent ILC with a perfect model results in $f_{j+1,opt} = G^{-1}r$ and hence $e_{j+1} = Sr - SGf_{j+1,opt} = 0$, for all r. However, this result does not hold when r varies as shown next. Let the reference signal at trail j be denoted by r_j. Then, under the same conditions as before, $f_{j+1,opt} = G^{-1}r_j$ and hence $e_{j+1} = Sr_{j+1} - SGf_{j+1,opt} = S\left(r_{j+1} - r_j\right)$. Consequently, $e_{j+1} \neq 0$ if $r_{j+1} \neq r_j$, i.e., for a trial-varying reference signal.

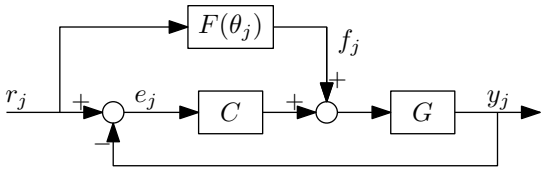

Figure 9.2. Implementation of basis functions in $f_j = F(\theta_j)r_j$.

Ideally $f_{j+1,opt} = G^{-1}r_{j+1}$, which corresponds to inverse model feedforward and shows that the optimal feedforward signal is a function of the applied reference signal. A key observation for norm-optimal ILC is that only information of previous trials is exploited. Hence, the learned signal will only be optimal for one specific constant reference signal and non-optimal for varying reference signals, i.e., extrapolation properties are poor. To enhance extrapolation properties, basis functions are exploited in this chapter.

9.2.3 Problem formulation

Inspired by inverse model feedforward, extrapolation properties are introduced in ILC by use of basis functions as

$$f_j = F(\theta_j)r_j, \tag{9.10}$$

where $F(\theta_j) \in \mathbb{R}^{N\times N}$ denotes the matrix notation of the feedforward filter parameterized in parameters $\theta_j \in \mathbb{R}^{n_\theta}$. Similar parameterizations are used in, for example, Hätönen et al. (2006); Van de Wijdeven and Bosgra (2010). The implementation in the control scheme of Figure 9.1 is depicted in Figure 9.2. Note that f_{j+1} is a function of r_{j+1}, which is in sharp contrast to standard norm-optimal ILC where it is implicitly only a function of r_j. Substitution of (9.10) in (9.2a) yields $e_j = Sr_j - SGF(\theta_j)r_j = S(I - GF(\theta_j))r_j = 0$, for all r_j, if $F(\theta_j) = G^{-1}$. Hence, by proper selection of $F(\theta_j)$ and learning θ_j, zero error may be achieved for arbitrary reference signals.

The basic idea is that if instead of learning f_j, the ILC algorithm optimizes θ_j, then e_j is invariant under r if $F(\theta_j) = G^{-1} = \frac{A_0}{B_0}$. Note that a standard model-based feedforward is recovered from (9.10) if θ_j is pre-specified. In this chapter, rational basis functions are used for parameterizing the feedforward filter $F(\theta_j)$, see Definition 9.3, which enables optimization of both zeros and poles.

Definition 9.3. *Rational basis functions in the parameters $\theta_j \in \mathbb{R}^{n_\theta}$ with reference r_j as basis are defined as in* (9.10) *with $F(\theta_j)$ the matrix representation of $F(\theta_j, z) \in \mathcal{F}$,*

$$\mathcal{F} = \left\{ \frac{A(\theta_j, z)}{B(\theta_j, z)} \middle| \theta_j \in \mathbb{R}^{n_\theta} \right\}, \tag{9.11}$$

with

$$A(\theta_j, z) = \xi_{A,0}(z) + \sum_{i=1}^{n_\theta} \xi_{A,i}(z)\theta_j[i-1], \tag{9.12}$$

$$B(\theta_j, z) = \xi_{B,0}(z) + \sum_{i=1}^{n_\theta} \xi_{B,i}(z)\theta_j[i-1], \tag{9.13}$$

where $\xi_{A,i}(z), \xi_{B,i}(z) \in \mathcal{R}[z]$, $i = 0, 1, \ldots, n_\theta$ *are polynomials in* z.

Note that for $B(\theta_j, z) = \xi_{B,0}(z)$ the pole locations of $F(\theta_j, z)$ are prespecified. Polynomial basis functions are the special case of rational basis functions with $B(\theta_j, z) = 1$.

Substitution of (9.10) in (9.5) yields Definition 9.4, which reveals that $\mathcal{J}(f_{j+1})$ is a function of θ_{j+1} by the fixed structure of (9.10). Instead of determining $f_{j+1,opt}$, $\theta_{j+1,opt}$ is to be determined.

Definition 9.4. *The performance criterion for norm-optimal ILC with basis functions is given by*

$$\begin{aligned}\mathcal{J}(\theta_{j+1}) := \|e_{j+1}(\theta_{j+1})\|^2_{W_e} + \|f_{j+1}(\theta_{j+1})\|^2_{W_f} \\ + \|f_{j+1}(\theta_{j+1}) - f_j\|^2_{W_{\Delta f}},\end{aligned} \tag{9.14}$$

with $W_e, W_f, W_{\Delta f} \succeq 0$, *and using Definition 9.3 and* (9.4),

$$f_{j+1} = B^{-1}(\theta_{j+1})A(\theta_{j+1})r_j, \tag{9.15}$$

$$e_{j+1} = e_j + Jf_j - JB^{-1}(\theta_{j+1})A(\theta_{j+1})r_j. \tag{9.16}$$

The goal in this chapter is to solve the following problem.

Main problem. *Given Definition 9.3, a model of* J, *parameters* θ_j, *and measurement data* r_j, f_j, e_j, *determine*

$$\theta_{j+1,opt} = \arg\min_{\theta_{j+1}} \mathcal{J}(\theta_{j+1}), \tag{9.17}$$

with $\mathcal{J}(\theta_{j+1})$ *given by Definition 9.4.*

The contributions of this chapter are as follows.

9.I An iterative approach to solve the main problem in Section 9.2.3 is proposed and its optimality is shown.

9.II By analysis of the approach it is shown that the solution in Bolder and Oomen (2015) solves the main problem in Section 9.2.3 non-optimally.

9.III The results of Contribution 9.I and Contribution 9.II are confirmed by use of simulation examples. In particular, it is validated that the proposed approach outperforms the pre-existing approach, and the benefits of ILC with basis functions in terms of extrapolation properties are demonstrated.

Experimental validation of the results can be found in Bolder et al. (2017).

9.3 Proposed approach

In this section, the main problem in Section 9.2.3 is analyzed and the proposed approach is introduced, forming Contribution 9.I. Finally, polynomial basis functions and standard norm-optimal ILC are recovered as special cases.

9.3.1 Analysis

In standard norm-optimal ILC, see Section 9.2.2, the optimal feedforward is found through (9.6). Similarly, $\theta_{j+1,opt}$ satisfies

$$\left.\frac{\mathrm{d}\mathcal{J}(\theta_{j+1})}{\mathrm{d}\theta_{j+1}}\right|_{\theta_{j+1}=\theta_{j+1,opt}} = 0, \tag{9.18}$$

with the gradient given by Lemma 9.5.

Lemma 9.5. *Given Definition 9.3, the gradient of $\mathcal{J}(\theta_{j+1})$ with respect to θ_{j+1} is given by*

$$\begin{aligned}\left(\frac{d\mathcal{J}(\theta_{j+1})}{d\theta_{j+1}}\right)^\top = 2\left(\frac{df_{j+1}}{d\theta_{j+1}}\right)^\top \Big[&\left(-J^\top W_e J - W_{\Delta f}\right) f_j + J^\top W_e e_j \\ &+ \left(J^\top W_e J + W_f + W_{\Delta f}\right) B^{-1}(\theta_{j+1}) A(\theta_{j+1}) r_j\Big].\end{aligned} \tag{9.19}$$

Proof. Follows from substituting (9.4) in (9.14) and using that for $x, b \in \mathbb{R}^N$, $A \in \mathbb{R}^{N\times N}$, and $W = W^\top \in \mathbb{R}^{N\times N}$,

$$\frac{\mathrm{d}\left(\|Ax+b\|_W^2\right)}{\mathrm{d}x} = 2(Ax+b)^\top WA. \tag{9.20}$$

The stated result is found by substitution of (9.15). □

Lemma 9.5 reveals that $\frac{\mathrm{d}\mathcal{J}(\theta_{j+1})}{\mathrm{d}\theta_{j+1}}$ is nonlinear in θ_{j+1} because of the terms $\frac{\mathrm{d}f_{j+1}}{\mathrm{d}\theta_{j+1}}$ and $B^{-1}(\theta_{j+1})$. Consequently, there is no general analytic solution available and there may exist multiple optima. To solve this optimization problem, an iterative solution is proposed in the following subsection.

9.3.2 Optimal solution

In this subsection the proposed approach to solve the main problem in Section 9.2.3 is introduced, which forms the main contribution of this chapter. The idea is to iteratively solve a sequence of convex optimization problems, which are also a solution of the non-convex optimization problem if the iterative procedure converges. A weighted version of (9.18) is considered, which is affine in the parameters and enables an analytic solution. Upon convergence, the gradient in Lemma 9.5 is recovered and a solution to the main problem in Section 9.2.3 is obtained.

First, an auxiliary iteration index q is introduced and a weighting is applied to (9.19) as given by Definition 9.6.

Definition 9.6. *The weighted gradient of the performance criterion is defined as*

$$\begin{aligned}\left(\overline{\frac{d\mathcal{J}(\theta_{j+1,q})}{\theta_{j+1,q}}}\right)^{\top} = 2\zeta_q\Big[&-\left(J^{\top}W_eJ+W_{\Delta f}\right)B(\theta_{j+1,q})f_j\\ &-J^{\top}W_eB(\theta_{j+1,q})e_j\\ &+\left(J^{\top}W_eJ+W_f+W_{\Delta f}\right)A(\theta_{j+1,q})r_j\Big]\in\mathbb{R}^{n_\theta},\end{aligned} \tag{9.21}$$

with

$$\zeta_q=\left(\overline{\frac{df_{j+1,q-1}}{d\theta_{j+1,q-1}}}\right)^{\top}B^{-1}(\theta_{j+1,q-1})\in\mathbb{R}^{n_\theta\times N}. \tag{9.22}$$

Note that the expression in Lemma 9.5 is recovered from Definition 9.6 upon convergence, i.e., $\theta_{j+1,q}=\theta_{j+1,q-1}=\theta_{j+1}$.

Second, it is observed that (9.21) is affine in $A(\theta_{j+1,q})$ and $B(\theta_{j+1,q})$. Since both $A(\theta_{j+1,q})$ and $B(\theta_{j+1,q})$ are affine in $\theta_{j+1,q}$, see Definition 9.3, (9.21) is affine in $\theta_{j+1,q}$. This is exploited in Theorem 9.7.

Theorem 9.7. *Given $r_j, f_j, e_j, \theta_{j+1,q-1}$, the solution to $\overline{\frac{d\mathcal{J}(\theta_{j+1,q})}{\theta_{j+1,q}}}=0$ is given by*

$$\theta_{j+1,q,opt}=-\left(\zeta_qQ\right)^{-1}\zeta_qR, \tag{9.23}$$

with

$$\begin{aligned}Q=&\left(J^{\top}W_eJ+W_f+W_{\Delta f}\right)\Psi_{A,r_j}-J^{\top}W_e\Psi_{B,e_j}\\ &-\left(J^{\top}W_eJ+W_{\Delta f}\right)\Psi_{B,f_j},\end{aligned} \tag{9.24}$$

$$\begin{aligned}R=&\left(J^{\top}W_eJ+W_f+W_{\Delta f}\right)\xi_{A,0}r_j-J^{\top}W_e\xi_{B,0}e_j\\ &-\left(J^{\top}W_eJ+W_{\Delta f}\right)\xi_{B,0}f_j.\end{aligned} \tag{9.25}$$

Proof. Using the notation defined in Section 9.1:

$$A(\theta_{j+1,q})r_j = \xi_{A,0}r_j + \Psi_{A,r_j}\theta_{j+1,q}, \tag{9.26}$$
$$B(\theta_{j+1,q})e_j = \xi_{B,0}e_j + \Psi_{B,e_j}\theta_{j+1,q}, \tag{9.27}$$
$$B(\theta_{j+1,q})f_j = \xi_{B,0}f_j + \Psi_{B,f_j}\theta_{j+1,q}. \tag{9.28}$$

Substituting these expressions into (9.21), equating to zero, and solving for $\theta_{j+1,q} = \theta_{j+1,q,opt}$ completes the proof. □

Note that (9.23) only depends on data of trial j (r_j, f_j, e_j) and the previous parameter estimate $\theta_{j+1,q-1}$.

In the previous steps two key elements are derived, which are briefly summarized as follows. First, a weighted gradient is introduced in Definition 9.6, from which the gradient in Lemma 9.5 is recovered for $\theta_{j+1,q} = \theta_{j+1,q-1} = \theta_{j+1}$. Second, an analytic solution for $\theta_{j+1,q,opt} = \theta_{j+1,q}$ is obtained for which the weighted gradient in Definition 9.6 is zero. Hence, upon convergence, the actual gradient also converges to zero and optimal performance is achieved. Combining these two elements, there is an optimal analytic solution to the main problem in Section 9.2.3 when there is convergence in the parameters, i.e., $\theta_{j+1,q} \to \theta_{j+1,q-1}$. The iterative algorithm to obtain this solution is given by Algorithm 9.8.

Algorithm 9.8. *The proposed algorithm for solving the main problem in Section 9.2.3 is given by the following sequence of steps.*

1. *Given r_j, f_j, e_j, θ_j, set $q = 1$, initialize $\theta_{j+1,q-1} = \theta_j$.*
2. *Compute $\theta_{j+1,q,opt}$ in* (9.23).
3. *Set $q \to q+1$ and go back to step 2 until an appropriate stopping criterion is satisfied.*

Note that the iteration in q is performed off-line and hence does not require additional experiments in the usual ILC sense.

The convergence of similar type of algorithms is experienced to be good in well-established related algorithms in instrumental variable system identification (Gilson et al., 2011; Blom and Van den Hof, 2010), yet at present global convergence has only been proved under certain assumptions (Stoica and Söderström, 1981).

9.3.3 Recovering pre-existing results as special cases

For polynomial basis functions the optimization problem is convex and convergence is achieved in a single step. Indeed, $\zeta_q = \left(\frac{\mathrm{d}A(\theta_{j+1,q-1})r_j}{\mathrm{d}\theta_{j+1,q-1}}\right)^\top = \Psi_{A,r_j}^\top$ in Algorithm 9.8 is constant for all q and hence the procedure yields the single-step solution provided by Corollary 9.9, which recovers the well-known results

in Van de Wijdeven and Bosgra (2010) and Bolder and Oomen (2015). Moreover, for standard norm-optimal ILC, i.e., $f_j = \theta_j$, Theorem 9.2 is recovered from Theorem 9.7, see Corollary 9.9.

Corollary 9.9. *For polynomial basis functions, the solution in* (9.23) *reduces to the analytic solution*

$$\begin{aligned}\theta_{j+1,opt} = \Big(\Psi_{A,r_j}^\top \left(J^\top W_e J + W_f + W_{\Delta f}\right) \Psi_{A,r_j}\Big)^{-1} \Psi_{A,r_j}^\top \\ \times \left(-\left(J^\top W_e J + W_f + W_{\Delta f}\right) \xi_{A,0} r_j \right. \\ \left. + J^\top W_e e_j + \left(J^\top W_e J + W_{\Delta f}\right) f_j\right).\end{aligned} \tag{9.29}$$

If in addition $\xi_{A,0}(z) = 0$, then

$$\theta_{j+1,opt} = Q f_j + L e_j, \tag{9.30}$$

with

$$Q = \Big(\Psi_{A,r_j}^\top \left(J^\top W_e J + W_f + W_{\Delta f}\right) \Psi_{A,r_j}\Big)^{-1} \Psi_{A,r_j}^\top \left(J^\top W_e J + W_{\Delta f}\right), \tag{9.31}$$

$$L = \Big(\Psi_{A,r_j}^\top \left(J^\top W_e J + W_f + W_{\Delta f}\right) \Psi_{A,r_j}\Big)^{-1} \Psi_{A,r_j}^\top J^\top W_e. \tag{9.32}$$

If $f_j = \theta_j$, then Theorem 9.2 is recovered.

Proof. Substitute $\zeta_q = \Psi_{A,r_j}^\top$, $\xi_{B,0} = I$, and $\Psi_{B,e_j} = \Psi_{B,f_j} = 0$ in (9.23). If in addition $\xi_{A,0}(z) = 0$, then $\xi_{A,0} = 0$ and $f_j = \Psi_{A,r_j}\theta_j$. For $f_j = \theta_j$, $\Psi_{A,r_j} = I$ which substituted in (9.30) yields (9.7). □

9.4 Non-optimality of pre-existing approach

In Bolder and Oomen (2015), an alternative solution to the main problem in Section 9.2.3 is proposed. In this section, it is demonstrated that this iterative procedure generally converges to a non-optimal stationary point. As a result, the proposed approach potentially yields better performance. This section forms Contribution 9.II.

9.4.1 Pre-existing approach

In the proposed approach, the gradient of the performance criterion is weighted. In contrast, in the pre-existing approach of Bolder and Oomen (2015) the performance criterion is weighted, see Definition 9.10.

Definition 9.10. *The weighted performance criterion is defined as*

$$\begin{aligned}\hat{\mathcal{J}}(\theta_{j+1,q}) := &\left\|B^{-1}(\theta_{j+1,q-1})B(\theta_{j+1,q})e_{j+1,q}\right\|_{W_e}^2 \\ &+ \left\|B^{-1}(\theta_{j+1,q-1})B(\theta_{j+1,q})f_{j+1,q}\right\|_{W_f}^2 \\ &+ \left\|B^{-1}(\theta_{j+1,q-1})B(\theta_{j+1,q})f_{j+1,q} - f_j\right\|_{W_{\Delta f}}^2 .\end{aligned} \tag{9.33}$$

Note that if $\theta_{j+1,q} = \theta_{j+1,q-1} = \theta_{j+1}$, then $\hat{\mathcal{J}}(\theta_{j+1,q}) = \mathcal{J}(\theta_{j+1})$, i.e., the unweighted performance criterion is recovered.

The weighted signals are affine in $\theta_{j+1,q}$ since the term $B^{-1}(\theta_{j+1,q})$ is canceled. As a result, $\hat{\mathcal{J}}(\theta_{j+1,q})$ is quadratic in $\theta_{j+1,q}$ and there is a unique solution for $\theta_{j+1,q,opt}$, which can be determined analytically from

$$\left(\frac{\mathrm{d}\hat{\mathcal{J}}(\theta_{j+1,q})}{\mathrm{d}\theta_{j+1,q}}\right)^\top\Bigg|_{\theta_{j+1,q}=\theta_{j+1,q,opt}} = 0. \tag{9.34}$$

The idea is to iteratively determine $\theta_{j+1,q,opt}$ for $\hat{\mathcal{J}}(\theta_{j+1,q})$ in Definition 9.10 using (9.34). The reasoning is that upon convergence of the parameters, i.e., $\theta_{j+1,q} \to \theta_{j+1,q-1}$, $\theta_{j+1,q,opt}$ are also the optimal parameters for the main problem in Section 9.2.3, because $\mathcal{J}(\theta_{j+1})$ is recovered from $\hat{\mathcal{J}}(\theta_{j+1,q})$ for $\theta_{j+1,q} = \theta_{j+1,q-1} = \theta_{j+1}$. However, in the next section it is demonstrated that this reasoning is incorrect, i.e., the stationary point of the iteration is not necessarily a minimum of $\mathcal{J}(\theta_{j+1})$.

9.4.2 Non-optimality

In the approach outlined in Section 9.4.1, (9.34) is solved, which yields the minimum of $\hat{\mathcal{J}}(\theta_{j+1,q})$. However, this is not necessarily a minimum of $\mathcal{J}(\theta_{j+1})$. As a consequence, the parameters do not necessarily provide the solution to the main problem in Section 9.2.3. The non-optimality of this approach is highlighted in Theorem 9.11.

Theorem 9.11. *For the purpose of exposition let $W_f = W_{\Delta f} = 0$ and assume that the pre-existing iterative procedure described in Section 9.4.1 converges to a stationary point, and let $\theta_{j+1,pre} = \lim_{q\to\infty} \theta_{j+1,q,opt}$ with $\theta_{j+1,q,opt}$ the solution to* (9.34)*. Then non-optimal performance is achieved if*

$$\left(B^{-1}(\theta_{j+1,pre})\frac{dB(\theta_{j+1,pre})}{d\theta_{j+1,pre}}e_{j+1,pre}\right)^\top W_e e_{j+1,pre} \neq 0. \tag{9.35}$$

Proof. Substitution of $W_f = W_{\Delta f} = 0$ in (9.19) and using $\frac{\mathrm{d}f_{j+1}}{\mathrm{d}\theta_{j+1}} = \frac{\mathrm{d}F_{j+1}}{\mathrm{d}\theta_{j+1}}r_j$ it follows

$$\left(\frac{\mathrm{d}\mathcal{J}(\theta_{j+1})}{\mathrm{d}\theta_{j+1}}\right)^\top = -2\left(J\frac{\mathrm{d}F(\theta_{j+1})}{\mathrm{d}\theta_{j+1}}r_j\right)^\top W_e e_{j+1}, \tag{9.36}$$

with e_{j+1} given by (9.4). The gradient of (9.33) for $W_f = W_{\Delta f} = 0$ is given by

$$\left(\frac{\mathrm{d}\tilde{\mathcal{J}}(\theta_{j+1,q})}{\mathrm{d}\theta_{j+1,q}}\right)^\top = 2\left(B^{-1}(\theta_{j+1,q-1})\frac{\mathrm{d}B(\theta_{j+1,q})e_{j+1,q}}{\mathrm{d}\theta_{j+1}}\right)^\top \times W_e B^{-1}(\theta_{j+1,q-1})B(\theta_{j+1,q})e_{j+1,q}, \tag{9.37}$$

$$\frac{\mathrm{d}B(\theta_{j+1,q})e_{j+1,q}}{\mathrm{d}\theta_{j+1}} = \frac{\mathrm{d}B(\theta_{j+1,q})}{\mathrm{d}\theta_{j+1,q}}e_{j+1,q} - B(\theta_{j+1,q})J\frac{\mathrm{d}F(\theta_{j+1,q})}{\mathrm{d}\theta_{j+1,q}}r_j. \tag{9.38}$$

Evaluating this gradient after convergence, i.e., $\theta_{j+1,q-1} = \theta_{j+1,q} = \theta_{j+1,pre}$, yields

$$2\left(B^{-1}(\theta_{j+1,pre})\frac{\mathrm{d}B(\theta_{j+1,pre})}{\mathrm{d}\theta_{j+1,pre}}e_{j+1,pre} - J\frac{\mathrm{d}F(\theta_{j+1,pre})}{\mathrm{d}\theta_{j+1,pre}}r_j\right)^\top W_e e_{j+1,pre} \tag{9.39}$$

which is zero by definition of $\theta_{j+1,pre}$. Hence, if

$$\left(B^{-1}(\theta_{j+1,pre})\frac{\mathrm{d}B(\theta_{j+1,pre})}{\mathrm{d}\theta_{j+1,pre}}e_{j+1,pre}\right)^\top W_e e_{j+1,pre} \neq 0, \tag{9.40}$$

then, by (9.36), $\left.\frac{\mathrm{d}\mathcal{J}(\theta_{j+1})}{\mathrm{d}\theta_{j+1}}\right|_{\theta_{j+1}=\theta_{j+1,pre}} \neq 0$, indicating non-optimality which concludes the proof. □

Theorem 9.11 implies that the pre-existing approach solves the main problem in Section 9.2.3 if $e_{j+1} = 0$. This requires there exists θ_{j+1} such that $F(\theta_{j+1}) = G^{-1}$, see Section 9.2.2. This is, however, generally not the case due to unmodeled dynamics and therefore non-optimal performance is achieved. Moreover, the non-optimality of the pre-existing approach may be more severe under stochastic disturbances, see for example Whitfield (1987).

The key difference between the two approaches is the level at which the weight is applied. In the pre-existing approach this is at the level of the performance criterion, whereas with the proposed approach this is at the level of the gradient of the performance criterion. Since the parameters are determined at the level of the gradient, the proposed approach is optimal, whereas this is generally not the case for the pre-existing approach. The non-optimality of the pre-existing approach is illustrated in a simulation example in Section 9.5.

9.5 Example: Convergence

In this section, a simulation example is presented to demonstrate the optimality of the proposed approach in Section 9.3 and the non-optimality of the pre-existing approach in Section 9.4. In addition, the convergence behavior of both approaches is analyzed and compared to the Gauss-Newton algorithm. This section forms the first part of Contribution 9.III.

9.5.1 Setup

The parameter update over a single trial is considered and therefore the subscript j is omitted throughout this section. An open-loop system is considered, i.e., $C = 0$, with the system defined as

$$G = \frac{(1 + 2\beta_{1,1} + \omega_1)\, z^2 - 2(1 - \beta_{1,1})z + 1}{(1 + 2\beta_{1,2} + \omega_1)\, z^2 - 2(1 - \beta_{1,2})z + 1} \times \frac{(1 + 2\beta_{2,1} + \omega_2)\, z^2 - 2(1 - \beta_{2,1})z + 1}{(1 + 2\beta_{2,2} + \omega_2)\, z^2 - 2(1 - \beta_{2,2})z + 1}, \tag{9.41}$$

where $\beta_{1,1} = 0.12$, $\beta_{1,2} = 0.01$, $\omega_1 = 0.0005 \cdot 2\pi$, $\beta_{2,1} = 1.2$, $\beta_{2,2} = 0.1$, and $\omega_2 = 0.01 \cdot 2\pi$.

The reference signal is defined as

$$r[k] = 40 \sin(\omega_1 k) + \sin(\omega_2 k), \quad k = 0, 1, \ldots N - 1, \tag{9.42}$$

with trial length $N = 1000$. The weighting filters in Definition 9.4 are set to $W_e = 10^{-4} I$ and $W_f = W_{\Delta f} = 0$ in order to only weigh the error.

The feedforward filter is parameterized as

$$F(\theta) = \frac{(z-1)^2 + (2\beta_1(z-1) + \omega_n)\,\theta}{(z-1)^2 + (2\beta_2(z-1) + \omega_n)\,\theta}, \tag{9.43}$$

with $\beta_1 = 0.001$, $\beta_2 = 2$, $\omega_n = 0.02 \cdot 2\pi$. Note that $F(\theta)$ can be written in the form of Definition 9.3 with $n_\theta = 1$ and

$$\xi_{A,0}(z) = (z-1)^2, \quad \xi_{A,1}(z) = 2\beta_1(z-1) + \omega_n, \tag{9.44}$$

$$\xi_{B,0}(z) = (z-1)^2, \quad \xi_{B,1}(z) = 2\beta_2(z-1) + \omega_n. \tag{9.45}$$

The Bode plot of $F(\theta)$ is depicted in Figure 9.3 for various values θ, together with the system inverse. The figure shows that there exists θ such that $F(\theta)$ resembles (part of) the system inverse. However, by design, $F(\theta)$ is only able to (partially) compensate one of the two system resonances. Assuming minor influence of transient behavior, it is to be expected that there are two optima: compensation of either the resonance at 0.0005 Hz or the resonance at 0.01 Hz.

9.5.2 Results

The results are shown in Figure 9.4, Figure 9.5, Table 9.1, and Table 9.2.

First, the performance criterion is analyzed. In Figure 9.4, $\mathcal{J}(\theta)$ is depicted for a grid of values for θ. As expected, there are two minima: $\theta_{opt,1} = 1.5959 \times 10^{-4}$ and $\theta_{opt,2} = 0.0315$, of which the feedforward filters are depicted in Figure 9.5. Visual inspection reveals that for $\theta = \theta_{opt,1}$ the first resonance of the system is (partially) compensated, whereas for $\theta = \theta_{opt,2}$ the second system

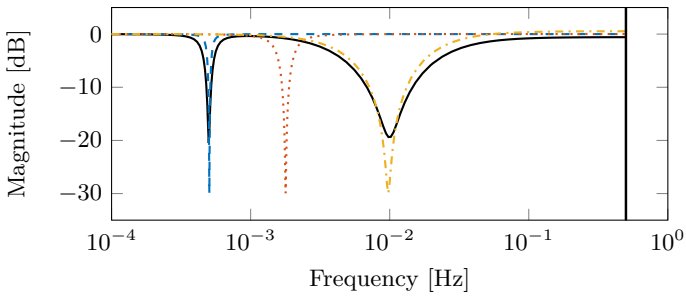

Figure 9.3. The inverse system G^{-1} (——) and feedforward filters $F(\theta = 10^{-5})$ (- - -), $F(\theta = 10^{-3})$ (·····), and $F(\theta = 10^{-1})$ (-·-·). By design, $F(\theta)$ is only able to (partially) compensate one of the resonances.

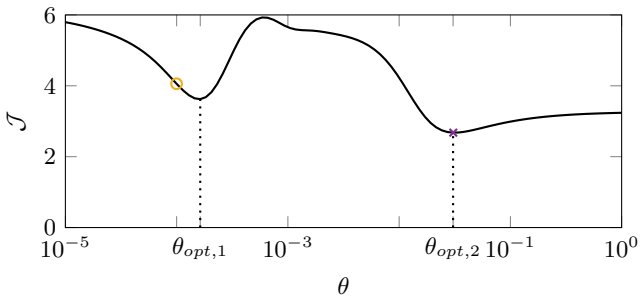

Figure 9.4. $\mathcal{J}$ for a grid in θ and the corresponding optimal parameters. For $\theta_0 = 10^{-3}$, the pre-existing approach (○) converges to the point near the local minimum, whereas the proposed approach (×) converges to the global minimum.

resonance is (partially) compensated. Note that the difference in resonance frequency between $F(\theta_{opt,1})$ and the first resonance frequency of G appears to be large due to the logarithmic scale, but is small and in the same order as the difference between the resonance frequency of $F(\theta_{opt,2})$ and the second resonance frequency of G.

Second, non-optimality of the pre-existing approach and optimality of the proposed approach are demonstrated. In Figure 9.4, the stationary point of the pre-existing approach $\theta = 9.7249 \times 10^{-5}$ for an initial value $\theta_0 = 10^{-3}$ is indicated after ten iterations. The stationary point is located near local minimum $\theta_{opt,1}$. Clearly, this stationary point yields non-optimal performance since there exists θ for which $\mathcal{J}(\theta)$ is lower. Indeed, since $\tilde{\mathcal{J}}$ instead of $\mathcal{J}$ is minimized, non-optimal performance is obtained in terms of $\mathcal{J}$, see also Table 9.1. The results confirm Theorem 9.11 since the stationary point of the pre-existing approach is not a local minimum of $\mathcal{J}$. In contrast to the pre-existing approach, the gradient

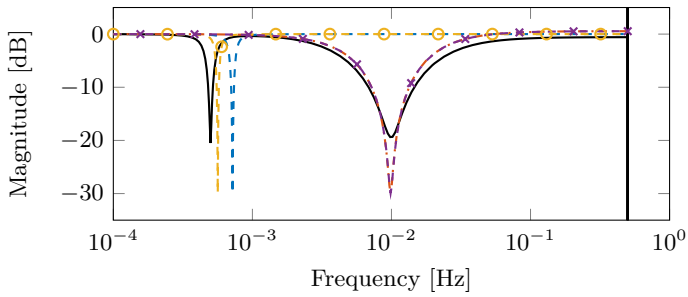

Figure 9.5. $F(\theta)$ for $\theta_{opt,1}$ (- - -), $\theta_{opt,2}$ (-·-·-), and pre-existing (· ⊖ ·) and proposed (· ✱ ·) approach (both after ten iterations) partially compensate different resonances of G^{-1} (——).

Table 9.1. Convergence properties of the pre-existing and proposed approach after ten iterations.

	θ_{opt}	$\mathcal{J}$	$\left\lvert\frac{\mathrm{d}\mathcal{J}}{\mathrm{d}\theta}\right\rvert$
$\theta_{opt,1}$	1.5950×10^{-4}	3.6226	−0.5151
$\theta_{opt,2}$	0.0315	2.6776	0.0001
Pre-existing	9.9856×10^{-5}	4.0573	14556
Proposed	0.0307	2.6781	1.3158

of $\mathcal{J}$ converges to zero for the proposed approach. Indeed, Table 9.1 shows a small value $\frac{\mathrm{d}\mathcal{J}}{\mathrm{d}\theta}$ for the proposed approach. As a result, optimal performance is achieved and the value of $\mathcal{J}$ is the lowest for the proposed approach.

Finally, convergence is considered. In Table 9.2, the stationary point of the approaches is indicated for a range of θ_0. From the table it is observed that the pre-existing approach always converges to the same stationary point located closely to the local minimum, independent of the initial parameter. In contrast, for this case the stationary point of the proposed approach is always the global optimum. Hence, the proposed approach outperforms both the pre-existing and Gauss-Newton approach.

Table 9.2. Converged parameters. For the given interval, the stationary point of the pre-existing approach is always near $\theta_{opt,1}$, whereas the stationary point of Gauss-Newton depends on the initial parameter.

Initial value θ_0	Gauss-Newton	Pre-existing	Proposed
$10^{-5} < \theta_0 \leq 6 \times 10^{-4}$	$\theta_{opt,1}$	near $\theta_{opt,1}$	$\theta_{opt,2}$
$6 \times 10^{-4} < \theta_0 \leq 10^{0}$	$\theta_{opt,2}$	near $\theta_{opt,1}$	$\theta_{opt,2}$

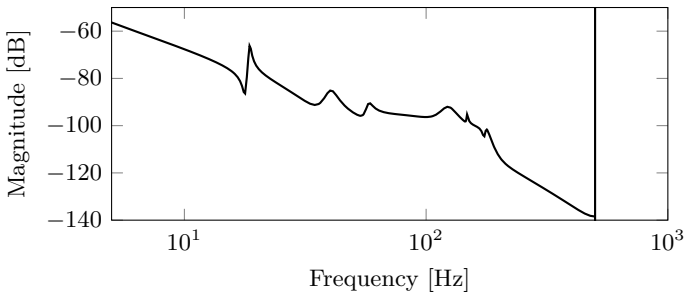

Figure 9.6. Bode magnitude plot of the printer model.

9.6 Example: Performance

In this section, the pre-existing and proposed approach for ILC with rational basis functions are compared with standard ILC and ILC with polynomial basis functions. Varying reference signals and a model of a complex industrial printer are considered. The simulation demonstrates the excellent extrapolation properties of ILC with basis functions compared to standard ILC. Moreover, the simulation highlights the difference in performance for the three variants of ILC with basis functions. This section forms the second part of Contribution 9.III.

9.6.1 System description

The system is a model of the carriage position of an Océ Arizona 550 GT flatbed printer of which the Bode magnitude plot is depicted in Figure 9.6. The system operates in closed-loop with a bandwidth of 25 Hz.

9.6.2 Simulation setup

Nine trials are considered with a trial-varying reference signal according to Figure 9.7. All trials have a length of $N = 4000$ samples.

Rational basis functions with $\theta_j \in \mathbb{R}^4$ are defined according to Definition 9.3 and Lambrechts et al. (2005) as follows

$$A(\theta_j, z) = \left(1 + \left(\tfrac{z-1}{z\delta}\right)\theta_j[0] + \left(\tfrac{z-1}{z\delta}\right)^2 \theta_j[1]\right)\left(\tfrac{z-1}{z\delta}\right)^2, \tag{9.46}$$

$$B(\theta_j, z) = \left(1 + \left(\tfrac{z-1}{z\delta}\right)\theta_j[2] + \left(\tfrac{z-1}{z\delta}\right)^2 \theta_j[3]\right), \tag{9.47}$$

with sampling time δ and where the choice of basis functions is in part based on Lambrechts et al. (2005). Recall that polynomial basis functions are the special case of rational basis functions with $B(\theta_j, z) = 1$, i.e., $\theta_j[2] = \theta_j[3] = 0$, for all j. The initial parameters θ_0 are set to zero. To simulate noise, white noise with

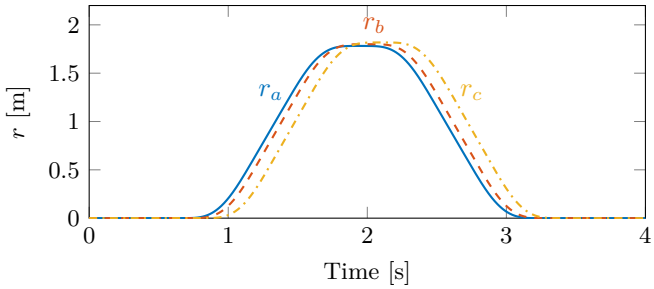

Figure 9.7. A trial-varying reference signal is considered. Reference signal r_a (——) is active during trial $j = 0, 1, 2$; r_b (- - -) during $j = 3, 4, 5$; and r_c (-·-·-) during $j = 6, 7, 8$.

a variance of 10^{-4} µm^2 is injected on the error signal. The weighting filters in Definition 9.4 are set to $W_e = I$, $W_f = W_{\Delta f} = 0$ in order to only penalize the error.

9.6.3 Simulation results

In Figure 9.8, $\mathcal{J}_j$ is shown as function of the trial index j. The following observations are made. First, the proposed approach outperforms the pre-existing approach for rational basis functions by a factor 40. Second, rational basis functions outperform polynomial basis functions; even the pre-existing approach is a factor 480 better. Third, ILC with basis functions outperforms standard ILC after a change in reference signal by at least a factor 9. The error signal after such a change is depicted in Figure 9.9. The results (i) clearly highlight the problem encountered in standard ILC with respect to extrapolation, (ii) demonstrate the excellent extrapolation properties of ILC with basis functions, and (iii) confirm the analysis in Section 9.2.2.

9.7 Conclusion and outlook

For systems operating repetitively, high performance can be achieved by use of ILC. However, standard norm-optimal ILC has poor extrapolation properties with respect to varying reference signals. In this chapter, rational basis functions are used to enhance these extrapolation properties. The associated optimization problem is significantly more complex than for polynomial basis functions, but can be solved iteratively. The main contribution of this chapter is a new iterative algorithm for rational basis functions. The algorithm relates to techniques from system identification and is guaranteed to converge to a minimum. The algorithm is compared with the pre-existing iterative algorithm in

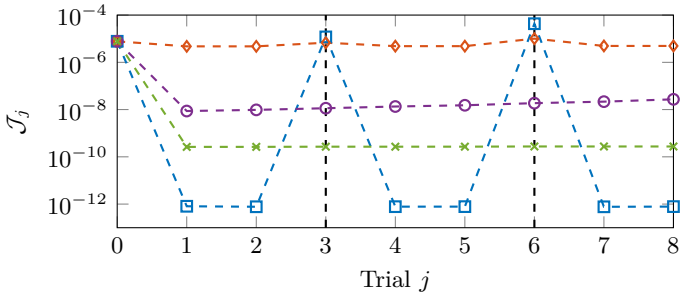

Figure 9.8. For rational basis functions the proposed approach (×) outperforms the pre-existing approach (○), which both outperform polynomial basis functions (◇). At reference signal changes (trial $j = 3$ and $j = 6$) basis functions outperform standard ILC (□).

Bolder and Oomen (2015) which is shown to be non-optimal. As a consequence, the proposed approach outperforms the pre-existing results.

The results are supported using simulation examples. It is shown that, even for simple systems, the difference in performance between the pre-existing and proposed approach can be significant. The excellent extrapolation properties of ILC with basis functions are demonstrated in a simulation of a complex industrial system. Also for this simulation, the proposed approach is superior to the pre-existing approach.

Experimental validation of the simulation results can be found in Bolder et al. (2017). Ongoing research focuses on the selection of basis functions, robustness analysis, and numerical aspects along the lines of Van Herpen et al. (2013) and Blanken et al. (2017b); Blanken et al. (2018). Finally, an interesting extension could be to investigate convergence to the global minimum along the lines of Eckhard et al. (2012).

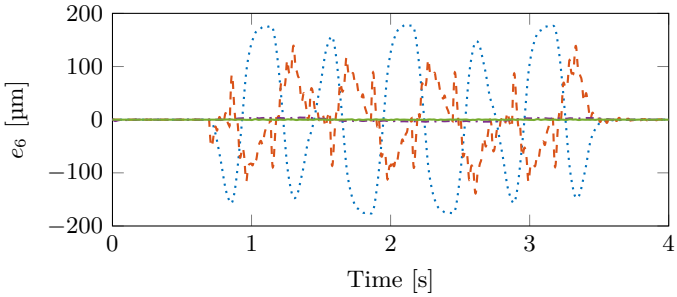

(a) Error signals.

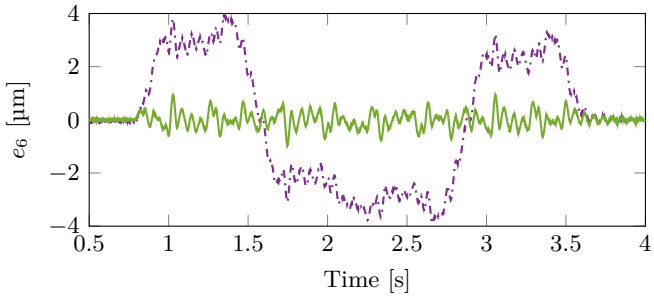

(b) The performance difference between the pre-existing and proposed approach is significant.

Figure 9.9. Time-domain error signals after a change in reference signal ($j = 6$) for standard ILC (·····), polynomial basis functions (- - -), and rational basis functions using the pre-existing (-·-·) and the proposed (——) approach. The change in reference signal has significant impact on the performance of standard ILC, whereas the effect on ILC with basis functions is significantly smaller, especially for rational basis functions.

Chapter 10

Resource-efficient ILC

Iterative learning control (ILC) enables high performance for systems that execute repeating tasks, see also Section 1.5. Norm-optimal ILC based on lifted system representations provides an analytic expression for the optimal feedforward signal. However, for large tasks the computational load increases rapidly for increasing task lengths, compared to the low computational load associated with so-called frequency-domain ILC designs. The aim of this chapter is to solve norm-optimal ILC through a Riccati-based approach for a general performance criterion. The approach leads to exactly the same solution as found through lifted ILC, but at a much smaller computational load: $\mathcal{O}(N)$ versus $\mathcal{O}(N^3)$ for both linear time-invariant (LTI) and linear time-varying (LTV) systems. Interestingly, the approach involves solving a two-point boundary value problem (TPBVP). This is shown to have close connections to stable inversion presented in Section 3.4.2, which is central in typical frequency-domain ILC designs. The proposed approach is implemented on an industrial flatbed printer with large tasks, which cannot be implemented using traditional lifted ILC solutions. The proposed methodologies and results are applicable to both ILC and rational feedforward techniques by applying them to suitable closed-loop or open-loop system representations. In addition, they are applied to a position-dependent system, revealing necessity of addressing position-dependent dynamics and confirming the potential of LTV approaches in this situation. The results constitute Contribution IV.D.

The contents of this chapter are published in:
Jurgen van Zundert, Joost Bolder, Sjirk Koekebakker, and Tom Oomen. Resource-efficient ILC for LTI/LTV systems through LQ tracking and stable inversion: Enabling large feedforward tasks on a position-dependent printer. *IFAC Mechatronics*, 38:76–90, 2016.

10.1 Introduction

10.1.1 Iterative learning control in mechatronic applications

Mechatronic systems can be accurately positioned using control. With feedback control the command signal is updated based on past errors, namely the difference between the measured and desired output. With feedforward control information of the desired output is used to anticipate on future errors, which enables accurate positioning. In this chapter, the main focus is on learning such a feedforward command signal from data via iterative learning control (ILC).

ILC algorithms often achieve exceptional performance for systems that operate repetitively, i.e., systems that perform the same task over and over again. ILC exploits the repetitive behavior of the system by learning from past executions (Bristow et al., 2006; Moore, 1993). Many successful ILC applications in mechatronics have been reported, including wafer scanners (Mishra et al., 2007; De Roover and Bosgra, 2000), H-drive pick and place machines (Steinbuch and Van de Molengraft, 2000), and printing systems (Sutanto and Alleyne, 2015; Bolder et al., 2014).

An important class in ILC is norm-optimal ILC (Norrlöf and Gunnarsson, 2002; Owens et al., 2013), where the optimal feedforward is determined on the basis of a performance criterion. When representing the system in the lifted framework (Tousain et al., 2001), an analytic expression can be directly obtained for the optimal ILC controller (Gunnarsson and Norrlöf, 2001). However, the implementation of lifted ILC involves multiplication and inversion of $N \times N$-matrices, with N the task length. Since the matrices scale with the task length, lifted ILC is impractical for large tasks. The need for computationally efficient techniques is well-recognized, see, for example, Barton et al. (2010). In addition, efficient techniques for the computation of the ILC convergence condition are developed, see, for example, Rice and Van Wingerden (2013).

10.1.2 Iterative learning control for large tasks

Several approaches in ILC have been used that have a significantly smaller computational burden compared to standard norm-optimal ILC algorithms. On the one hand, norm-optimal ILC has been extended in several ways. Basis functions in lifted ILC (Chapter 9; Bolder and Oomen, 2015) lead to smaller computational burden. However, these basis functions are typically used to enhance extrapolation properties of ILC, at expense of performance. Alternatively, the Toeplitz/Hankel structure of the involved matrices can be exploited, see Vandebril et al. (2008), as is done in Haber et al. (2012).

On the other hand, alternative approaches to ILC are typically based on (non-optimal) two-step approaches. These approaches include a learning filter

obtained via typically noncausal plant inversion techniques and is completed by a robustness filter to guarantee convergence of the iteration. For instance, preview based control approaches such as zero phase error tracking control (ZPETC) are often applied in ILC. ZPETC was originally developed for noncausal feedforward compensation of nonminimum-phase systems (Tomizuka, 1987). See Blanken et al. (2016b) for a multivariable extension and Butterworth et al. (2012) for related methods. Such ZPETC-related algorithms enable the design of noncausal filters and have computationally complexity $\mathcal{O}(N)$. However, they typically introduce approximation errors and are only applicable to linear time-invariant (LTI) systems.

Interestingly, stable inversion (Tien et al., 2005; Hunt et al., 1996; Zou and Devasia, 1999) has been abundantly used in ILC and feedforward, see, for example, Chapter 9; Boeren et al. (2015); Bolder et al. (2017); Blanken et al. (2016b) for high-tech motion control applications, and Marro et al. (2002); Blanken et al. (2016a) for multivariable extensions. Such inversion methods enable noncausal inverses for square multivariable systems and some immediately generalize to linear time-varying (LTV) systems. These methods essentially provide an exact inverse over a bi-infinite time horizon, but still introduce approximation errors for finite tasks. These errors are caused by incompatible initial conditions in the finite-time case as a result of mixed causal/noncausal filtering.

10.1.3 Contributions

Although several frameworks and associated algorithms have been developed for ILC, there seems to be a trade-off between computational requirements and accuracy. One either has to accept a large computational time or approximation errors for non-optimal approaches. The aim of this chapter is to develop an optimal design algorithm for joint design of the learning and robustness filter. The algorithm exploits noncausality, is directly applicable to LTV systems, and addresses the finite-time interval behavior through LTV designs for both LTI and LTV systems, while providing computational complexity $\mathcal{O}(N)$. In addition, the underlying solution involves solving a two-point boundary value problem (TPBVP). This is shown to have a direct connection to LTI/LTV stable inversion techniques, revealing very similar underlying mechanisms and proving a unified framework for both approaches.

The main contribution of this chapter is to provide a systematic resource-efficient norm-optimal ILC framework, which is implementable for large tasks, and is applicable to both LTI and LTV systems. The following five subcontributions are identified.

10.I The resource-efficient ILC approach is presented for LTI and LTV systems with general performance criteria, including derivations and proofs.

10.II Connections to stable inversion are established, revealing very similar un-

derlying mechanisms. These inversion techniques have recently received significant attention in ILC and feedforward. This in turn leads to a unified framework of norm-optimal ILC and stable inversion. Hence the techniques in this chapter apply to a large class of LTI/LTV ILC algorithms.

10.III Through application of the resource-efficient ILC approach on an industrial flatbed printer with large tasks, the practical relevance is demonstrated as lifting techniques are unsuitable.

10.IV The relevance of LTV feedforward and ILC is demonstrated on a position-dependent printing system, confirming the necessity to address position-dependent effects in this situation.

10.V The computational load of the lifted ILC and the resource-efficient ILC approach are compared, revealing the significant advantages of the proposed approach.

The proposed approach is foreseen to facilitate the resource-efficient implementation of optimal ILC for LTI/LTV systems. Due to its inherent connection with stable inversion, it also enables the direct implementation of both square and non-square rational feedforward controllers (Boeren et al., 2014; Blanken et al., 2017a). Finally, it is foreseen for use as system inversion technique in frequency-domain ILC designs.

10.1.4 Related results

Several results related to the ones presented here have appeared in the literature. As in typical ILC designs, the proposed approach is based on noncausal feedforward techniques for reference tracking, but then applied iteratively and on a closed-loop system transfer function. This is similar to applying ZPETC and stable inversion. In this chapter, the approach is based on the classical linear quadratic (LQ) tracking controller (Athans and Falb, 1966, Chapter 9), which is well-known to be noncausal. It builds on the ILC approaches in Amann et al. (1996); Oomen et al. (2011) and exploits optimal control theory for computing the optimal feedforward signal. Since the state-space instead of the lifting framework is used for describing the system, the computational burden is much smaller. In particular, it extends the result in Amann et al. (1996) for a more general performance criterion, including input weighting, and LTV systems. In Oomen et al. (2011), a related theoretical development is presented, linked to sampled-data ILC with intersample behavior. Finally, related results are developed in Dijkstra and Bosgra (2002), where a different LQ criterion is posed and in Van de Wijdeven et al. (2011), where an H_∞-type criterion is employed.

The LTV case is of particular importance for certain systems, including the position-dependent printer considered here, but also in very different applica-

tions, including nuclear fusion (Felici and Oomen, 2015) and rehabilitation (Xu et al., 2014). More general criteria with dedicated optimizations can be found in Zou and Liu (2016). Finally, in Brinkerhoff and Devasia (2000), stable inversion is extended to deal with non-square systems to address non-square systems with more actuators using infinite horizon LQ theory. In this chapter, possible truncation effects for finite-time implementations are explicitly addressed. It thereby possibly extends the results in Brinkerhoff and Devasia (2000) for situations where these boundary effects have a significant influence on the performance, as occasionally occurs in ILC.

10.1.5 Outline

The outline of this chapter is as follows. In Section 10.2, ILC and norm-optimal ILC are formulated and the well-known analytic solution of lifted norm-optimal ILC is presented. Analysis of this solution reveals the computational challenges that come with actual implementation and motivates the development of a resource-efficient ILC approach. In Section 10.3, the resource-efficient ILC approach for LTI and LTV systems is presented based on LQ tracking, which constitutes Contribution 10.I. Also, in Section 10.3, connections to stable inversion and a simulation case study of both approaches are presented, leading to Contribution 10.II. Many systems, including the position-dependent flatbed printer considered in this chapter, can be modeled as LTV systems. The experimental setup of the flatbed printer is described in Section 10.4. The developed resource-efficient ILC approach can directly be applied on LTV models, which significantly enhances the performance for LTV systems, as shown in Section 10.5, which constitutes Contribution 10.III. In Section 10.6, the potential of resource-efficient ILC is demonstrated on the industrial flatbed printer involving large tasks ($N = 100\,000$), constituting Contribution 10.IV. Finally, the computational load of resource-efficient ILC is compared with that of lifted ILC in Section 10.7 to illustrate the significant saving in computational time, leading to Contribution 10.V. Conclusions and an outlook are given in Section 10.8.

Notation. The considered systems are linear, in discrete time, have n_i inputs and n_o outputs. Let $x[k]$ denote a signal x at time k. Let $h_{ij}(k,l) \in \mathbb{R}^{n_o \times n_i}$ be the impulse response of the time-varying system $H_{ij}[k]$ from the jth input $u_j[l]$ at time l, to the ith output $y_i[k]$ at time k. The output $y_i[k]$ of the response of $H_{ij}[k]$ to input u_j is given by $y_i[k] = \sum_{l=-\infty}^{\infty} h_{ij}(k,l)u_j[l]$. Let $N \in \mathbb{Z}^+$ denote the trial length, i.e., the number of samples per trial. Many results directly generalize to the continuous-time case. Variables related to the lifted framework, also called supervector notation (Moore, 1993), are underlined. Define the stacked input

signal

$$\underline{u}[k] = \begin{bmatrix} u_1[k] \\ u_2[k] \\ \vdots \\ u_{n_i}[k] \end{bmatrix} \in \mathbb{R}^{n_i \times 1} \tag{10.1}$$

and similarly $\underline{y}[k] \in \mathbb{R}^{n_o \times 1}$ and $\underline{h}(k,l) \in \mathbb{R}^{n_o \times n_i}$. Assuming $\underline{u}[l] = \underline{0}$ for $l < 0$ and $l > N-1$, then the input-output relation in lifted notation is given by

$$\underbrace{\begin{bmatrix} \underline{y}[0] \\ \underline{y}[1] \\ \vdots \\ \underline{y}[N-1] \end{bmatrix}}_{\underline{y}} = \underbrace{\begin{bmatrix} \underline{h}(0,0) & \underline{h}(0,1) & \dots & \underline{h}(0,N-1) \\ \underline{h}(1,0) & \underline{h}(1,1) & \dots & \underline{h}(1,N-1) \\ \vdots & \vdots & \ddots & \vdots \\ \underline{h}(N-1,0) & \underline{h}(N-1,1) & \dots & \underline{h}(N-1,N-1) \end{bmatrix}}_{\underline{H}} \underbrace{\begin{bmatrix} \underline{u}[0] \\ \underline{u}[1] \\ \vdots \\ \underline{u}[N-1] \end{bmatrix}}_{\underline{u}}. \tag{10.2}$$

If system H is LTI, then $h_{ij}(k,l)$ reduces to $h_{ij}(k-l)$, i.e., only depends on the relative time, and in which case $\underline{H}$ is Toeplitz. Let $\|\underline{x}\|_{\underline{W}}^2 := \underline{x}^\top \underline{W}\underline{x}$, where $\underline{x} \in \mathbb{R}^{Nn_x}$ and $\underline{W} = \underline{W}^\top \in \mathbb{R}^{Nn_x \times Nn_x}$. $\underline{W}$ is positive definite ($\underline{W} \succ 0$) if and only if $\underline{x}^\top \underline{W}\underline{x} > 0$, for all $\underline{x} \neq \underline{0}$, and positive semi-definite ($\underline{W} \succeq 0$) if and only if $\underline{x}^\top \underline{W}\underline{x} \geq 0$, for all $\underline{x}$.

10.2 Problem formulation

In this section, the problem is formulated by defining the ILC design problem and the norm-optimal performance criterion, and deriving and analyzing the analytic optimal solution for lifted ILC. This reveals the computational challenges of this solution, which in turn motivates the development of the resource-efficient ILC approach.

10.2.1 ILC and norm-optimal ILC

Consider the closed-loop configuration depicted in Figure 10.1, with G the n_i-input, n_o-output system to control with outputs y_{j+1}, C a stabilizing feedback controller, and $e_{j+1} = r - y_{j+1}$ the error signal to be minimized. For repetitive tasks, the reference signal r has finite length and is independent of j. Each repetition/execution is called a trial and indicated with a subscript $j = 0, 1, 2, \dots$. In ILC, the goal is to minimize error e_{j+1} by design of the n_i-dimensional feedforward f_{j+1} based on data of previous trials, i.e., e_j, f_j. Typically, approximate models G and C are used.

In lifted notation, see Section 10.1, the error at trial j is

$$\underline{e}_j = \underline{S}\underline{r} - \underline{S}\underline{G}\underline{f}_j \tag{10.3a}$$

$$= \underline{S}\underline{r} - \underline{J}\underline{f}_j, \tag{10.3b}$$

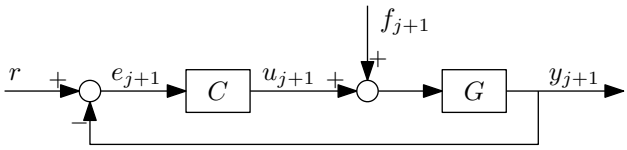

Figure 10.1. ILC control diagram. The goal for trial $j+1$ is to minimize the error e_{j+1} by design of feedforward f_{j+1}.

with (output) sensitivity $\underline{S} = \left(\underline{I}_{Nn_o} + \underline{GC}\right)^{-1}$ and (output) process sensitivity $\underline{J} = \underline{SG}$. Since $\underline{r}$ is trial-invariant, it follows that

$$\underline{e}_{j+1} = \underline{Sr} - \underline{J}\underline{f}_{j+1} \tag{10.4a}$$

$$= \underline{e}_j - \underline{J}(\underline{f}_{j+1} - \underline{f}_j). \tag{10.4b}$$

Hence, to minimize $\underline{e}_{j+1}$, $\underline{f}_{j+1}$ can be based on a model $\underline{J}$ and data $\underline{e}_j, \underline{f}_j$.

10.2.2 Lifted norm-optimal ILC

An important class of ILC is norm-optimal ILC in which $\underline{f}_{j+1}$ follows from minimizing a performance criterion as given in Definition 10.1.

Definition 10.1 (Performance criterion)**.** *A general performance criterion in norm-optimal ILC is given by*

$$\mathcal{J}(\underline{f}_{j+1}) = \|\underline{e}_{j+1}\|^2_{\underline{W}_e} + \|\underline{f}_{j+1}\|^2_{\underline{W}_f} + \|\underline{f}_{j+1} - \underline{f}_j\|^2_{\underline{W}_{\Delta f}}, \tag{10.5}$$

with $\underline{W}_e \succ 0$, $\underline{W}_f, \underline{W}_{\Delta f} \succeq 0$, *and* $\underline{e}_{j+1}$ *given by* (10.4b).

Since $\underline{e}_{j+1}$ is affine in $\underline{f}_{j+1}$, $\mathcal{J}(\underline{f}_{j+1})$ is quadratic in $\underline{f}_{j+1}$ and hence the optimal feedforward signal $\underline{f}_{j+1,opt}$ can be computed analytically, as in, e.g., Gunnarsson and Norrlöf (2001), from

$$\left.\frac{d\mathcal{J}(\underline{f}_{j+1})}{d\underline{f}_{j+1}}\right|_{\underline{f}_{j+1}=\underline{f}_{j+1,opt}} = 0 \tag{10.6}$$

with solution provided by Theorem 10.2.

Theorem 10.2 (Solution lifted ILC)**.** *Given* $\underline{J}^\top \underline{W}_e \underline{J} + \underline{W}_f + \underline{W}_{\Delta f} \succ 0$, *an LTI or LTV model* $\underline{J}$, *and measurement data* $\underline{f}_j, \underline{e}_j$, *the optimal* $\underline{f}_{j+1,opt}$ *for the performance criterion of Definition 10.1 is*

$$\underline{f}_{j+1,opt} = \underline{Q}\underline{f}_j + \underline{L}\underline{e}_j, \tag{10.7}$$

with

$$\underline{\Gamma} = \left(\underline{J}^\top \underline{W}_e \underline{J} + \underline{W}_f + \underline{W}_{\Delta f}\right)^{-1}, \tag{10.8a}$$

$$\underline{Q} = \underline{\Gamma}\left(\underline{J}^\top \underline{W}_e \underline{J} + \underline{W}_{\Delta f}\right), \tag{10.8b}$$

$$\underline{L} = \underline{\Gamma}\underline{J}^\top \underline{W}_e. \tag{10.8c}$$

Proof. Substitute (10.4b) in (10.5) and solve (10.6) for $\underline{f}_{j+1,opt} = \underline{f}_{j+1}$. □

Two key observations can be made from Theorem 10.2. First, the solution of Theorem 10.2 is time-varying, i.e., $\underline{Q}$, $\underline{L}$ are not Toeplitz, even if model J is LTI, i.e., $\underline{J}$ is Toeplitz. This is caused by the transpose $\underline{J}^\top$ and the inverse $\underline{\Gamma}$. Second, the solution in Theorem 10.2 is noncausal, i.e., $\underline{Q}$, $\underline{L}$ are not necessarily lower triangular, even if the model J is causal, i.e., $\underline{J}$ is lower triangular.

10.2.3 Computational challenges in lifted ILC

The derivation and calculation of $\underline{f}_{j+1,opt}$ in Theorem 10.2 is elementary and involves straightforward matrix algebra. However, its direct implementation may be challenging from a computational perspective. For instance, the $Nn_i \times Nn_i$ matrix inversion in $\underline{\Gamma}$ via the Gauss-Jordan method has time complexity $w = 3$, i.e., the computational time grows as $\mathcal{O}(N^3)$, see Sharma et al. (2013). Although many methods have been developed to reduce the computational time, currently a time complexity of $w = 2.4$ seems to be the limit (Sharma et al., 2013). Also the matrix multiplications via Schoolbook matrix multiplication grow as $\mathcal{O}(N^3)$. Even when pre-computing $\underline{Q}$ and $\underline{L}$ off-line, a direct implementation of Theorem 10.2 is impractical when $\overline{N}$ becomes large since matrix-vector multiplication, via Schoolbook matrix multiplication, grows as $\mathcal{O}(N^2)$. These observations are experimentally demonstrated in Section 10.6, and intensively analyzed in Section 10.7.

In lifted ILC, matrices with dimensions in the order of $N \times N$ are used to describe the system J and the fact that a resource-efficient system with McMillan degree n_x underlies this input-output system is not recognized. Since typically $n_x \ll N$, lifted ILC is a resource-inefficient norm-optimal ILC approach, as will be shown in Section 10.7. In the following section, an alternative to Theorem 10.2 is presented that builds on well-known results in optimal control. The approach exploits state-space descriptions and provides a resource-efficient norm-optimal ILC approach.

10.3 Resource-efficient ILC

In this section, the resource-efficient ILC approach is presented, i.e., Contribution 10.I. The approach is an alternative to the lifted ILC approach, see Theorem 10.2, providing identical optimal performance, but at significantly smaller computational load. This makes resource-efficient ILC practical for experimental implementation of large tasks, as is demonstrated in Section 10.6. The difference in computational load is analyzed and demonstrated in Section 10.7. In the current section, also connections and a simulation comparison to stable inversion techniques are presented, constituting Contribution 10.II.

Remark 10.3. *In the remainder of this chapter, the argument $[k]$ is suppressed for the system matrices. This is done to emphasize that the optimal ILC controller for an LTI system is LTV, which is an important property of such finite-time optimal ILC controllers.*

10.3.1 State-space description

In resource-efficient ILC, the system J is described using a state-space description as provided by Lemma 10.4.

Lemma 10.4. *Let the LTV system G and the feedback controller C in Figure 10.1 be described by the state-space realizations*

$$G \overset{z}{=} \left[\begin{array}{c|c} A_G & B_G \\ \hline C_G & D_G \end{array}\right] \quad \text{and} \quad C \overset{z}{=} \left[\begin{array}{c|c} A_C & B_C \\ \hline C_C & D_C \end{array}\right]. \tag{10.9}$$

Then, a state-space realization of the process sensitivity J is given by

$$J \overset{z}{=} \left[\begin{array}{c|c} A & B \\ \hline C & D \end{array}\right], \tag{10.10a}$$

with

$$A = \begin{bmatrix} A_G - B_G\left(I_{n_i} + D_C D_G\right)^{-1} D_C C_G & B_G\left(I_{n_i} + D_C D_G\right)^{-1} C_C \\ -B_C\left(I_{n_o} + D_G D_C\right)^{-1} C_G & A_C - B_C\left(I_{n_o} + D_G D_C\right)^{-1} D_G C_C \end{bmatrix}, \tag{10.10b}$$

$$B = \begin{bmatrix} B_G\left(I_{n_i} + D_C D_G\right)^{-1} \\ -B_C\left(I_{n_o} + D_G D_C\right)^{-1} D_G \end{bmatrix}, \tag{10.10c}$$

$$C = \begin{bmatrix} \left(I_{n_o} + D_G D_C\right)^{-1} C_G & \left(I_{n_o} + D_G D_C\right)^{-1} D_G C_C \end{bmatrix}, \tag{10.10d}$$

$$D = \left(I_{n_o} + D_G D_C\right)^{-1} D_G, \tag{10.10e}$$

and for $D_G = 0$

$$J \overset{z}{=} \left[\begin{array}{c|c} A & B \\ \hline C & D \end{array}\right] = \left[\begin{array}{cc|c} A_G - B_G D_C C_G & B_G C_C & B_G \\ -B_C C_G & A_C & 0 \\ \hline C_G & 0 & 0 \end{array}\right]. \tag{10.11}$$

Proof. See Appendix 10.A. □

10.3.2 Optimal solution

Typically, diagonal performance weights are chosen in Definition 10.1, see, e.g., Bolder and Oomen (2015); Gunnarsson and Norrlöf (2001), i.e., $W_e = \text{diag}\{w_e[k]\}$ with $w_e[k] \in \mathbb{R}^{n_o \times n_o}$, $W_f = \text{diag}\{w_f[k]\}$ with $w_f[k] \in \mathbb{R}^{n_i \times n_i}$, and $W_{\Delta f} = \text{diag}\{w_{\Delta f}[k]\}$ with $w_{\Delta f}[k] \in \mathbb{R}^{n_i \times n_i}$. For this choice, Definition 10.1 is equivalent to Definition 10.5.

Definition 10.5 (Performance criterion diagonal weights)**.** *The performance criterion with diagonal weights is given by*

$$\begin{aligned} \mathcal{J}(f_{j+1}) = \sum_{k=0}^{N-1} & e_{j+1}^\top[k] w_e[k] e_{j+1}[k] + f_{j+1}^\top[k] w_f[k] f_{j+1}[k] \\ & + \left(f_{j+1}[k] - f_j[k]\right)^\top w_{\Delta f}[k] \left(f_{j+1}[k] - f_j[k]\right), \end{aligned} \tag{10.12}$$

with $w_e[k] > 0$, $w_f[k] \geq 0$, $w_{\Delta f}[k] \geq 0$, *for all* k.

Resource-efficient ILC determines the optimal feedforward for the performance criterion of Definition 10.5 and is provided by Theorem 10.6.

Theorem 10.6 (Solution resource-efficient LTI/LTV ILC)**.** *Let the model* J *of the process sensitivity have the LTI/LTV state-space realization* (A, B, C, D)*, with* n_i *inputs,* n_o *outputs, and state dimension* n_x*, see also Lemma 10.4. Then, for the performance criterion of Definition 10.5,* $f_{j+1,opt}$ *is the output of the state-space system*

$$\left[\begin{array}{c|ccc} A - BL[k] & -BL_f[k] & BL_e[k] & BL_g[k] \\ \hline -L[k] & I_{n_i} - L_f[k] & L_e[k] & L_g[k] \end{array}\right], \tag{10.13}$$

with zero initial state for input $\begin{bmatrix} f_j[k] \\ e_j[k] \\ g_{j+1}[k+1] \end{bmatrix}$*, where*

$$L[k] = \left(\gamma^{-1}[k] + B^\top P[k+1]B\right)^{-1} \left(D^\top w_e[k] C + B^\top P[k+1] A\right), \tag{10.14a}$$

$$L_f[k] = \left(\gamma^{-1}[k] + B^\top P[k+1]B\right)^{-1} w_f[k], \tag{10.14b}$$

$$L_e[k] = \left(\gamma^{-1}[k] + B^\top P[k+1]B\right)^{-1} D^\top w_e[k], \tag{10.14c}$$

$$L_g[k] = \left(\gamma^{-1}[k] + B^\top P[k+1]B\right)^{-1} B^\top, \tag{10.14d}$$

$$\gamma[k] = \left(D^\top w_e[k] D + w_f[k] + w_{\Delta f}[k]\right)^{-1}, \tag{10.14e}$$

with

$$\begin{aligned} g_{j+1}[k] &= \left(A^\top - K_g[k]B^\top\right) g_{j+1}[k+1] \\ &\qquad + C^\top w_e[k]e_j[k] + K_g[k]w_f[k]f_j[k], \end{aligned} \tag{10.15a}$$

$$g_{j+1}[N] = 0_{n_x \times 1}, \tag{10.15b}$$

where

$$\begin{aligned} K_g[k] &= \left(A^\top - C^\top w_e[k]D\gamma[k]B^\top\right) P[k+1] \\ &\qquad \times \left(I_{n_x} + B\gamma[k]B^\top P[k+1]\right)^{-1} B\gamma[k], \end{aligned} \tag{10.16}$$

and $P[k]$ the solution of the matrix difference Riccati equation

$$\begin{aligned} P[k] &= \left(A^\top - C^\top w_e[k]D\gamma[k]B^\top\right) P[k+1] \\ &\qquad \times \left(I_{n_x} - B\left(\gamma^{-1}[k] + B^\top P[k+1]B\right)^{-1} B^\top P[k+1]\right) \\ &\qquad \times \left(A - B\gamma[k]D^\top w_e[k]C\right) \\ &\qquad + C^\top w_e[k]C - C^\top w_e[k]D\gamma[k]D^\top w_e[k]C, \end{aligned} \tag{10.17a}$$

$$P[N] = 0_{n_x \times n_x}. \tag{10.17b}$$

Proof. See Appendix 10.B. □

Note that time index k is explicitly indicated only for some elements in (10.13), while it is suppressed for others. The main reason is to illustrate the following interesting aspects, see also Remark 10.3. If G and C are LTI, then optimal ILC in (10.13) is LTV, and time variance of any of the matrices in (10.9) affects all elements in (10.13) through $L[k], L_f[k], L_e[k], L_g[k]$. Note that LTV designs are a key advantage for LTI systems, since these essentially handle the boundary effects for finite-time trials (Wallén et al., 2013). To see this, by definition of the optimal feedforward, the result of Theorem 10.6 is the same as the result of Theorem 10.2, computed using a different approach. It is well-known that lifted ILC allows for time-varying and noncausal feedforward signals. This is reflected in the matrices $\underline{Q}$ and $\underline{L}$ of (10.8) being not Toeplitz and not lower-triangular, respectively. These aspects can also be observed in the results of Theorem 10.6: the dependence on k of the state-space matrices (10.13) reflects time variance, whereas solving part of the equations backwards in time reflects noncausality and is closely related to stable inversion techniques.

Algorithm 10.7 provides a step-by-step procedure for implementing the results of Theorem 10.6. Note that step 1 can be performed off-line whereas step 2 and step 3 form the trial update.

Algorithm 10.7 (Resource-efficient approach)**.** *The resource-efficient $f_{j+1,opt}$ is calculated by the following steps.*

1. *Solve the matrix difference Riccati equation* (10.17a) *backwards in time.*
2. *Calculate* $g_{j+1}[k]$ *by solving* (10.15a) *backward in time.*
3. *Calculate* $f_{j+1,opt}[k]$ *forward in time as the output of state-space system* (10.13).

It should be noted that the solutions of Theorem 10.2 and Theorem 10.6 are exactly the same. Hence, no performance is sacrificed, however the computational approaches do differ. In particular, the calculations in Theorem 10.6 scale with N instead of N^3 as in Theorem 10.2, see also Section 10.2.3. Therefore the resource-efficient ILC approach delivers a significant reduction in computational cost at a small expense of diagonal time-varying weighting filters, see Definition 10.5. As a result, resource-efficient ILC is well-suited for large tasks as will be demonstrated in Section 10.6 by implementing the approach on an industrial setup. Next, connections to stable inversion are highlighted.

Remark 10.8. *For* $D = 0$ *and* $w_f[k] + w_{\Delta f}[k] = R$, (10.17a) *reduces to*

$$\begin{aligned} P[k] = C^\top w_e[k]C + A^\top P[k+1]A \\ - A^\top P[k+1]B\left(B^\top P[k+1]B + R\right)^{-1} B^\top P[k+1]A, \end{aligned} \tag{10.18}$$

which is the well-known discrete-time dynamic Riccati equation.

10.3.3 Stable inversion

Theorem 10.6 reveals that resource-efficient ILC solution for both LTI and LTV systems grows as $\mathcal{O}(N)$. Interestingly, the results and proof of Theorem 10.6 have a very close connection to algorithms used in, i.a., frequency-domain ILC designs and rational feedforward control (Blanken et al., 2017a). In particular, in both cases a rational model H has to be inverted as $F = H^{-1}$, where $H = G$ for rational feedforward and $H = J^{-1} = (SG)^{-1}$ for the ILC structure in Section 10.2. Let H be square, invertible, and have state-space realization $(A_H[k], B_H[k], C_H[k], D_H[k])$, then,

$$F \stackrel{z}{=} \left[\begin{array}{c|c} A_H[k] - B_H[k]D_H^{-1}[k]C_H[k] & B_H[k]D_H^{-1}[k] \\ \hline -D_H^{-1}[k]C_H[k] & D_H^{-1}[k] \end{array}\right]. \tag{10.19}$$

Note that the system F in (10.19) may be unstable. For instance, in the case where H is LTI and has nonminimum-phase zeros, then F has unstable poles.

A traditional solution in feedforward and ILC to deal with such unstable poles is ZPETC (Tomizuka, 1987), which leads to an approximate inverse that is noncausal with a certain finite preview. However, it is by definition an approximation, see also Butterworth et al. (2012) where different approximations

are evaluated, and does not address the finite-time aspect of practical feedforward and ILC implementations. In addition, extension to multivariable systems is practically not trivial, see Blanken et al. (2016b) for results in this direction. See Chapter 3 for a complete overview.

In stable inversion, the unstable part is seen as a noncausal operator and solved backwards in time as a stable system. For the general time-varying system (10.19), this means that the system has to be split in a stable and unstable part, which is not trivial for time-varying systems (Devasia and Paden, 1998; Halanay and Ionescu, 1994). If such a split is found, Theorem 10.9 can be applied. When poles are on the unit circle, the techniques in Devasia (1997b); Jetto et al. (2014) can be exploited. Note that if the state matrix of F in (10.19) is independent of k, then such a split follows directly from an eigenvalue decomposition as in Corollary 10.10.

Theorem 10.9. *Let an LTV system be split as*

$$x_s[k+1] = A_{ss}[k]x_s[k] + A_{su}[k]x_u[k] + B_s u[k], \tag{10.20a}$$

$$x_u[k+1] = A_{us}[k]x_s[k] + A_{uu}[k]x_u[k] + B_u u[k], \tag{10.20b}$$

$$y[k] = \begin{bmatrix} C_s[k] & C_u[k] \end{bmatrix} \begin{bmatrix} x_s[k] \\ x_u[k] \end{bmatrix} + D[k]u[k], \tag{10.20c}$$

where $x_s[k]$ is picking up the stable part with $x_s[0] = x_{s,0}$ and $x_u[k]$ the unstable part with $x_u[N] = 0$. Then, to find the bounded solution $y[k]$, solve for $P[k]$ backward in time using

$$P[k] = \left(A_{uu}[k] - P[k+1]A_{su}[k]\right)^{-1} \left(P[k+1]A_{ss}[k] - A_{us}[k]\right), \tag{10.21a}$$

$$P[N] = 0, \tag{10.21b}$$

and for $g[k]$ backward in time using

$$\begin{aligned} g[k] = {} & \left(P[k+1]A_{su}[k] - A_{uu}[k]\right)^{-1} \\ & \times \left(B_u[k]u[k] - P[k+1]B_s[k]u[k] - g[k+1]\right), \end{aligned} \tag{10.22a}$$

$$g[N] = 0. \tag{10.22b}$$

Then, $x_s[k]$ can be solved forward in time from

$$x_s[k+1] = \left(A_{ss}[k] + A_{su}[k]P[k]\right) x_s[k] + B_s[k]u[k] + A_{su}[k]g[k] \tag{10.23a}$$

$$x_s[0] = x_{s,0}, \tag{10.23b}$$

and $x_u[k]$ follows from

$$x_u[k] = P[k]x_s[k] + g[k]. \tag{10.24}$$

Output $y[k]$ follows directly from

$$y[k] = \begin{bmatrix} C_s[k] & C_u[k] \end{bmatrix} \begin{bmatrix} x_s[k] \\ x_u[k] \end{bmatrix} + D[k]u[k]. \tag{10.25}$$

Proof. See Appendix 10.C. □

Corollary 10.10. *For systems F with time-invariant state matrix, the following procedure can be followed.*

1. *Let F have the state-space realization*

$$x[k+1] = Ax[k] + B[k]u[k], \tag{10.26a}$$
$$y[k] = C[k]x[k] + D[k]u[k], \tag{10.26b}$$

   with $x[k] = x_0$.

2. *Introduce the state transformation*

$$x[k] = T \begin{bmatrix} x_s[k] \\ x_u[k] \end{bmatrix}, \tag{10.27}$$

   where T contains eigenvectors of A as columns such that

$$\begin{bmatrix} x_s[k+1] \\ x_u[k+1] \end{bmatrix} = \begin{bmatrix} A_s & 0 \\ 0 & A_u \end{bmatrix} \begin{bmatrix} x_s[k] \\ x_u[k] \end{bmatrix} + \begin{bmatrix} B_s[k] \\ B_u[k] \end{bmatrix} u[k], \tag{10.28a}$$
$$y[k] = \begin{bmatrix} C_s[k] & C_u[k] \end{bmatrix} \begin{bmatrix} x_s[k] \\ x_u[k] \end{bmatrix} + D[k]u[k], \tag{10.28b}$$

   with $\lambda(A_s) \subset \bar{\mathbb{D}}$ and $\lambda(A_u) \cap \bar{\mathbb{D}} = \emptyset$, where $\bar{\mathbb{D}}$ is the closed unit disk and $\lambda(\cdot)$ the set of eigenvalues, i.e., all stable poles are contained in A_s and all unstable poles in A_u.

3. *Solve*

$$x_s[k+1] = A_s x_s[k] + B_s[k]u[k], \quad x_s[0] = x_{s,0} \tag{10.29}$$

   forward in time,

$$x_u[k+1] = A_u x_u[k] + B_u[k]u[k], \quad x_u[N] = x_{u,N} \tag{10.30}$$

   backward in time via

$$x_u[k] = A_u^{-1} x_u[k+1] - A_u^{-1} B_u[k]u[k]. \tag{10.31}$$

   Then, $y[k]$ follows directly from

$$y[k] = \begin{bmatrix} C_s[k] & C_u[k] \end{bmatrix} \begin{bmatrix} x_s[k] \\ x_u[k] \end{bmatrix} + D[k]u[k]. \tag{10.32}$$

A key observation is that both the results in Theorem 10.6, Theorem 10.9, and Corollary 10.10 involve a two-point boundary value problem. In addition, a very similar sweep method is used for the actual solution, albeit applied to a system with smaller dimension in case of Theorem 10.9 and Corollary 10.10. The following remarks are appropriate.

(i) The stable inversion approach provides an exact inverse in the case where the initial conditions are taken at $x_s[-\infty]$ and $x_u[\infty]$ in Theorem 10.9. In the case where they are finite, as is specified in Theorem 10.9 and Corollary 10.10, then this may lead to an incorrect initial state, leading to an inexact inverse and boundary effects. These boundary effects depend on the location of the nonminimum-phase zeros and can be mitigated if the preview length is extended, i.e., by preceding the input with zeros, see, e.g., Middleton et al. (2004), or by using an approach as in Theorem 10.6.

(ii) The stable inversion technique yields an LTI inverse in case the system is LTI, whereas the approach in Theorem 10.6, i.e., LQ tracking based, generally yields an LTV solution, even if the original system is LTI.

(iii) In case the original system is LTV, then notice that time variance of any of the entries, i.e., A, B, C, or D, implies that the inverse has a time-dependent state matrix, see F in (10.19), in which case Theorem 10.9 has to be used instead of the simpler version in Corollary 10.10. This in turn necessitates the dichotomic split in stable and unstable dynamics in (10.20). This split is not necessary in case Theorem 10.6 is applied, which may be preferred in practical applications, e.g., systems with varying sensor locations or actuators, such as the moving-mass mechatronic stage in Oomen et al. (2014).

(iv) Both Theorem 10.9 and Corollary 10.10 require that D_H is invertible. This requires that H is square. In the case that D_H is non-invertible, additional steps of preview can be added, i.e., forward shift operators, as is done in, e.g., ZPETC (Tomizuka, 1987).

(v) In contrast to stable inversion in Theorem 10.9 and Corollary 10.10, the optimal approach in Theorem 10.6 does not require the system to be square or strictly proper due to the input weighting. As a result, it also applies to next-generation motion systems where additional sensors and actuators will be exploited (Oomen et al., 2014, Section I; Van Herpen et al., 2014).

(vi) Theorem 10.6 is very closely related to LQ optimal control, for which it is well-known that the LQ solution mirrors the unstable poles with respect to the unit disc, see also Anderson and Moore (1989, Section 6.1) for vanishing input weight. As a result, it is very closely related to the solution of the stable inversion approach in Theorem 10.9, where essentially a slightly different split is made. Notice that in this case, the TPBVP in Theorem 10.6 is twice the size of the one in Theorem 10.9. In this case, both solutions are present in the TPBVP, where a suitable selection is made in standard feedback control. Interestingly, the solution to the stable inversion problem is thus contained in the LQ tracking solution, where a different selection is made.

(vii) Stable inversion can also be directly seen in an input-output setting. In the LTI case, H is decomposed as H_{stab}, H_{unstab}, which essentially can be solved using a bi-lateral instead of a uni-lateral Laplace/Z-transform (Sogo, 2010), see also Vinnicombe (2001, Section 1.5).

Remark 10.11. *The result of Corollary 10.10 is a special case of Theorem 10.9 with $A_{ss}[k] = A_s$, $A_{su}[k] = 0$, $A_{us}[k] = 0$, $A_{uu}[k] = A_u$, yielding $P[k] = 0$, for all k, and $x_u[k] = g[k]$.*

Remark 10.12. *For motion control systems, the states typically represent time-derivatives of the position such as velocity and acceleration. Hence, if the system is initially at rest, then $x_{s,0} = 0$. The terminal condition $x_{u,N}$ should ideally be chosen such that $x_u[0]$ matches with $x[0]$. It can, however, not be derived a priori from $x_u[0]$ since this requires forward simulation of the unstable system.*

10.3.4 Resource-efficient ILC and stable inversion

The stable inversion techniques presented in the previous section can be used to determine an exact bounded inverse of a nonminimum-phase system. In the previous section, it is highlighted that these techniques are very similar to those used in the proposed resource-efficient ILC solution, see Section 10.3.2. In particular, for vanishing input weighting, the resource-efficient ILC solution converges to the optimal, possibly noncausal, inverse solution, as is shown in this section via a simulation example.

Consider the mechanical system shown in Figure 10.2, with parameters listed in Table 10.1. The continuous-time state-space realization (A_c, B_c, C_c, D_c) of the linearized system dynamics with input F, state $q = \begin{bmatrix} x & \dot{x} & \phi & \dot{\phi} \end{bmatrix}^\top$, and output y is

$$\left[\begin{array}{c|c} A_c & B_c \\ \hline C_c & D_c \end{array}\right] = \left[\begin{array}{cccc|c} 0 & 1 & 0 & 0 & 0 \\ 0 & 0 & 0 & 0 & \frac{1}{m} \\ 0 & 0 & 0 & 1 & 0 \\ 0 & 0 & -\frac{1}{2}\frac{kl^2}{I} & -\frac{1}{2}\frac{dl^2}{I} & \frac{1}{2}\frac{l}{I} \\ \hline 1 & 0 & -\frac{1}{2}l & 0 & 0 \end{array}\right]. \tag{10.33}$$

Assuming zero-order-hold on the input, system G has discrete state-space realization

$$G \overset{z}{=} \left[\begin{array}{c|c} A & B \\ \hline C & D \end{array}\right] = \left[\begin{array}{c|c} e^{A_c\delta} & A_c^{-1}(A - I)B_c \\ \hline C_c & D_c \end{array}\right], \tag{10.34}$$

with sampling interval $\delta = 0.001$ s. The system is in open-loop, i.e., $C = 0$ in Figure 10.1, with reference trajectory r as depicted in Figure 10.3(a), and feedforward signal $f = u$. The resulting system SG has one nonminimum-phase zero and no direct feedthrough ($D = 0$). Since $D = 0$, stable inversion requires

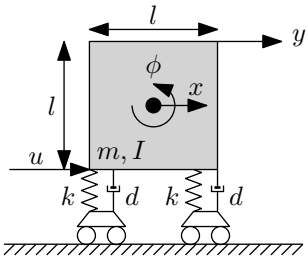

Figure 10.2. The flexible cart system, consisting of a single mass mounted on two spring-damper combinations, is subject to input force u and has translation and rotation freedom x and ϕ, respectively. Position y is the output.

Table 10.1. Parameter values of the flexible cart system.

Parameter	Symbol	Value	Unit
Mass	m	8	kg
Inertia	I	0.0133	kgm^2
Spring constant	k	10^4	N/m
Damping constant	d	10	Ns/m
Length	l	0.1	m

additional preview steps, see also remark (iv) at the end of the previous section. Note that preview information is not required for resource-efficient ILC.

Due to the nonminimum-phase zero, causal inversion yields an unbounded feedforward signal f, see Figure 10.3(b). With stable inversion, i.e., Corollary 10.10, bounded input f and error e shown in Figure 10.3(b) and Figure 10.3(c) are obtained. By selecting $w_{\Delta f}[k] = 0$, for all k, in resource-efficient ILC, see Theorem 10.6 and Algorithm 10.7, one-step convergence of f is obtained. The result for $w_e[k] = 1$, $w_f[k] = 10^{-12}$, $w_{\Delta f}[k] = 0$, for all k, is also shown in Figure 10.3(b) and Figure 10.3(c). The small error indicates the high quality of the inverse.

Due to the finite-length task, the solution for stable inversion is not exact. The inverse system $(SG)^{-1}$ contains one unstable state, which is simulated as a stable system backwards in time with zero terminal condition, see also Corollary 10.10. The evolution of the unstable state is depicted in Figure 10.3(d). For determining the response of system SG, zero initial state is assumed. However, since the unstable state of $(SG)^{-1}$, see Figure 10.3(d), is not exactly zero at $t = 0$ ($x_u(t = 0) = -0.0158$), this assumption is violated resulting in a non-exact output as shown in Figure 10.3(c).

Consider the case where preview information is available, i.e., the reference is zero for $t < 0$, then the unstable state converges to zero for decreasing t since the system is stable in backward time. The result when $N_{pre} = 50$ samples are introduced prior to the reference task of Figure 10.3 is shown in Figure 10.4.

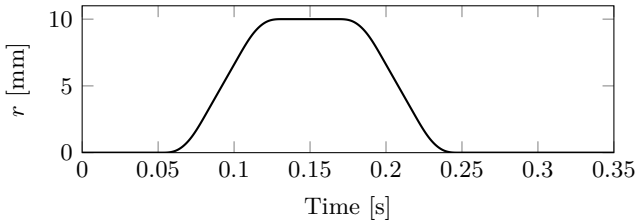

(a) Reference trajectory r is a fourth-order forward-backward movement.

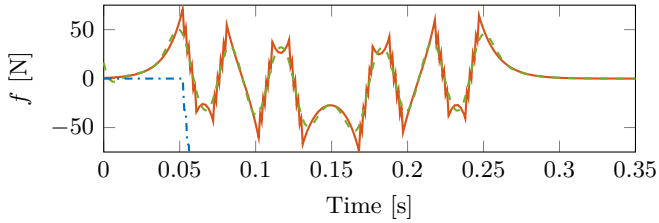

(b) Feedforward f with stable inversion (——) and resource-efficient ILC (- - -) are bounded and almost equal. For regular inversion (-·-·-), f is unbounded.

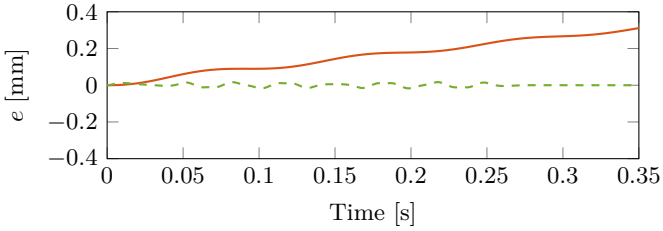

(c) Error e with stable inversion (——) is nonzero, whereas with resource-efficient ILC (- - -) it is almost zero.

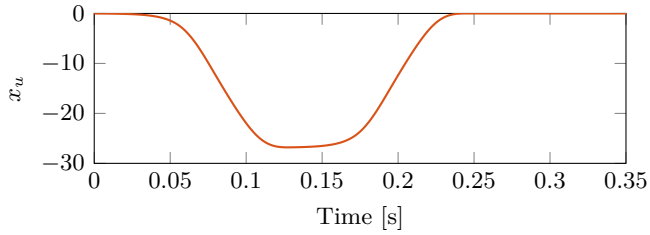

(d) Unstable state for stable inversion converges to zero when $t \to -\infty$.

Figure 10.3. Regular inversion yields an unbounded f. The error with stable inversion is larger than for resource-efficient ILC due to the nonzero unstable state at $t = 0$.

Here, $x_u(t = -0.05) = -1.73 \cdot 10^{-4}$. This confirms that for $N_{pre} \to \infty$ exact results are obtained.

This simulation case study shows that stable inversion yields non-exact results for finite-length tasks, whereas the proposed resource-efficient approach handles finite-time conditions approximately.

10.4 Experimental setup: Industrial flatbed printer

In the next sections, the resource-efficient ILC approach introduced in the previous section is validated on an industrial printer, namely the Océ Arizona 550 GT flatbed printer shown in Figure 10.5.

In contrast to conventional consumer printers, the medium on the flatbed printer is fixed on the printing surface using vacuum and the print heads move in two directions. The print heads are located in the carriage, which can move in one direction over the gantry, which moves in perpendicular direction over the printing surface. The moving mass of the carriage is approximately 32 kg, the maximum medium size is 2.5×1.25 m, and the maximum medium thickness is 50.8 mm. A schematic top view of the system is provided in Figure 10.5(b). The system is controlled via Matlab/Simulink that is running on a host computer connected to a separate xPC target computer. On the target computer the application runs in real-time with a sampling frequency of 1000 Hz. After each trial, the ILC algorithm is executed on the host computer and the resulting feedforward signals are uploaded to a lookup table on the target computer via Ethernet. During the real-time execution of the task, the feedforward signals are read from the lookup table.

The validation of resource-efficient ILC is based on the gantry system of the flatbed printer since (i) printer tasks are typically large, (ii) it is a MIMO system, (iii) it is position-dependent, and (iv) it is a practically relevant system. The gantry position is controlled through two brushed DC motors (u_1 and u_2) and the position is measured through linear encoders with a resolution of 1 µm. Decoupling into a gantry translation and rotation yields a system with inputs u_x, u_φ ($n_i = 2$) and outputs x, φ ($n_o = 2$). Depending on the application, different models G of the gantry system are used and introduced when appropriate.

For both the time-varying system model considered in Section 10.5 as well as the actual experimental system considered in Section 10.6, the same feedback controller C is used, shown in Figure 10.6. The controller achieves a bandwidth (first 0 dB crossing over the open-loop) of approximately 5 Hz for the diagonal terms. A diagonal controller suffices since for low frequencies the system is decoupled and feedback is only effective until the bandwidth. ILC is effective until much higher frequencies where interaction also plays a significant role. Hence, the full MIMO model is used in ILC.

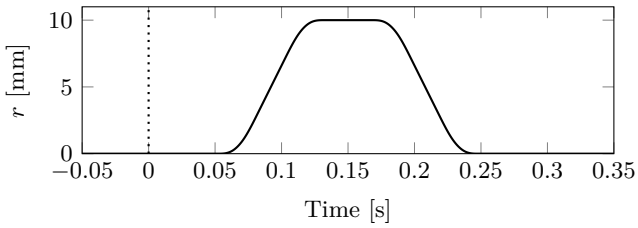

(a) $N_{pre} = 50$ additional zero samples are added prior to the reference in Figure 10.3(a).

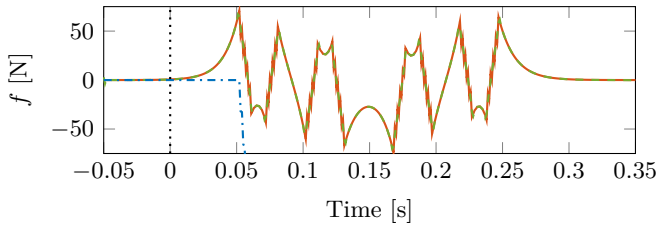

(b) Feedforward f with stable inversion (——) and resource-efficient ILC (- - -) are more alike than in Figure 10.3(b). For regular inversion (-·-·-) f is unbounded.

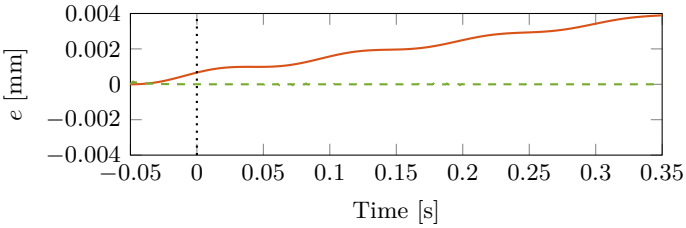

(c) Preview information reduces the error for both stable inversion (——) and resource-efficient ILC (- - -).

Figure 10.4. Regular inversion yields an unbounded f. Preview information significantly reduces the error for stable inversion.

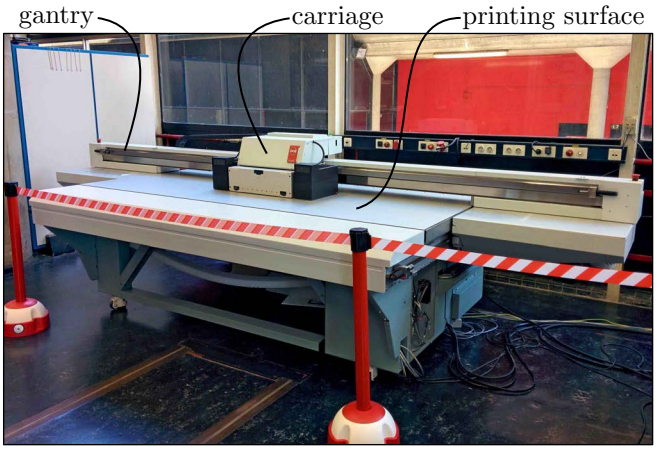

(a) The print heads of the Arizona flatbed printer are located in the carriage, which can move over the gantry. The gantry can move in perpendicular direction and rotate over small angles around the vertical axis.

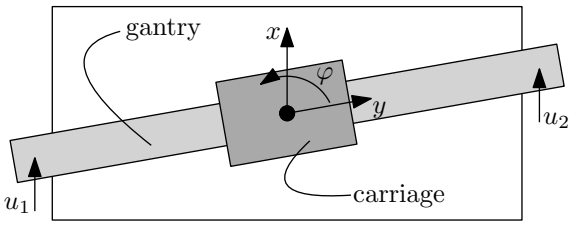

(b) Schematic top view of the flatbed printer. The gantry translation x and rotation φ are controlled via DC motors u_1, u_2.

Figure 10.5. Océ Arizona 550 GT industrial flatbed printer.

10.5 Resource-efficient ILC simulation for the position-dependent printing system

In this section, resource-efficient ILC based on LTI and LTV models is simulated on an LTV model of the flatbed printer, constituting Contribution 10.III. The system is position-dependent, i.e., the dynamics vary during motion. The results reveal the potential of using LTV models based on linearization around trajectories when compared to LTI models for fixed positions.

10.5.1 Position-dependent system

The flatbed printing system introduced in the previous section is considered, see also Figure 10.5. Since the system is inherently position-dependent, a first-

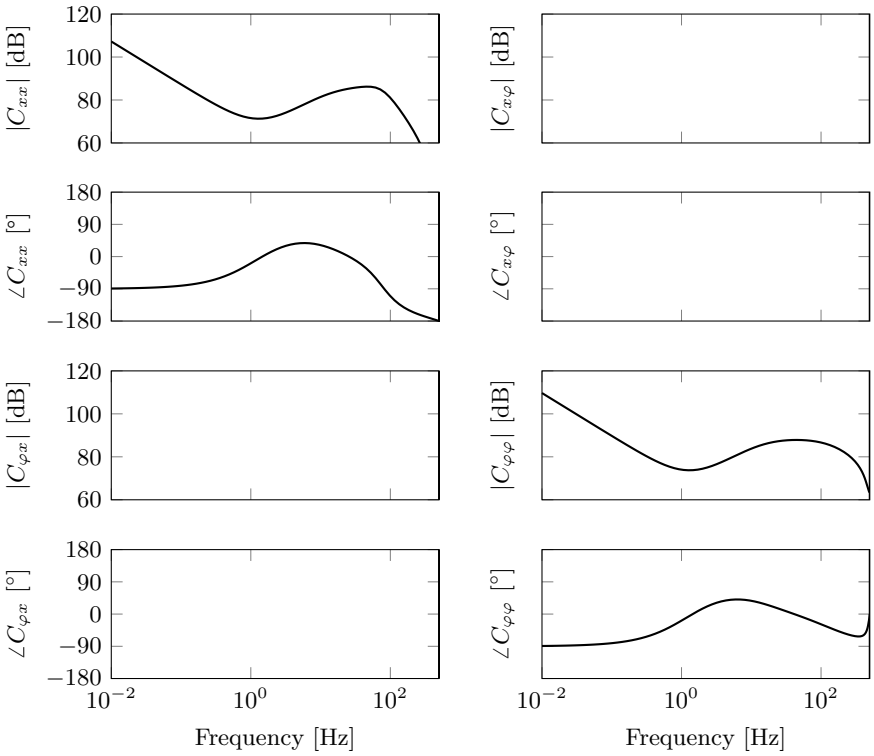

Figure 10.6. Bode diagram of diagonal controller C. Note that the off-diagonals $C_{x\varphi}$ and $C_{\varphi x}$ are empty.

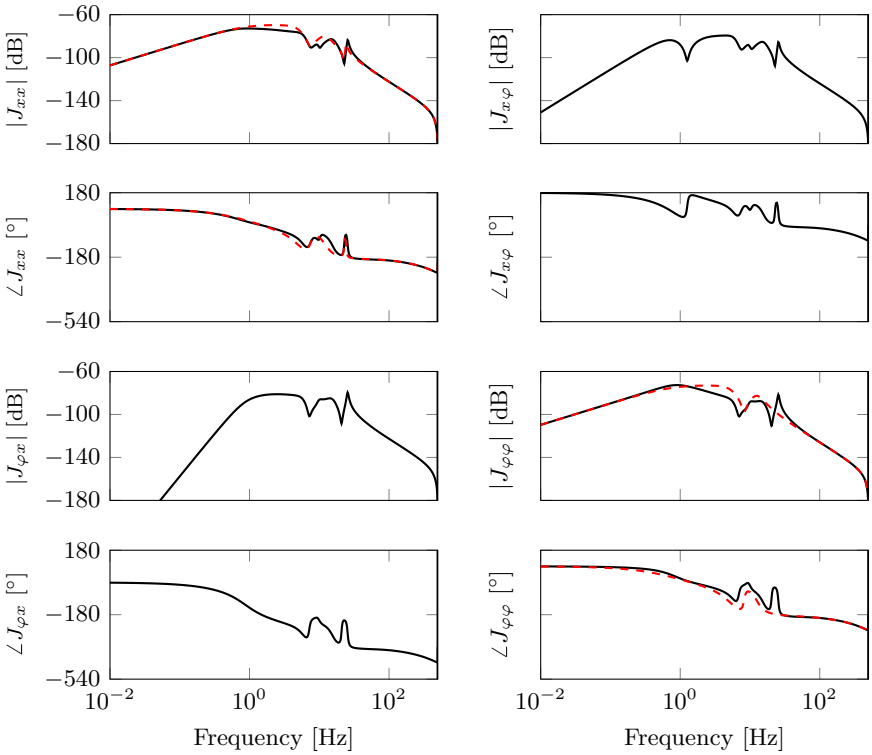

Figure 10.7. Parametric closed-loop gantry model J for carriage position $y = 1.6$ m (- - -) and $y = 6$ m (——). For $y = 1.6$ m, there is no cross-coupling.

principles model is derived to analyze its effect in a simulation study. Due to the moving carriage mass, this model is position dependent. Given a trajectory y, the first principles model can be linearized around this trajectory resulting in an LTV model of the gantry system. Note that linearization around a trajectory is also done in, for example, Felici and Oomen (2015). Figure 10.7 shows Bode diagrams of the closed-loop gantry system J for different carriage positions y, with $y = 0$ at the left side of the table. The feedback controller in Figure 10.6 is used for feedback.

10.5.2 Reference trajectories and performance weights

The carriage trajectory is designed to cover the whole range area of 3.2 m in y direction and 0.8 m in x direction, see Figure 10.8. To keep the results insightful, the rotation φ is controlled using feedback only, with $r_\varphi[k] = 0$, for all k, and ILC is only applied in x direction. The simulated system is thus a multi-input, multi-

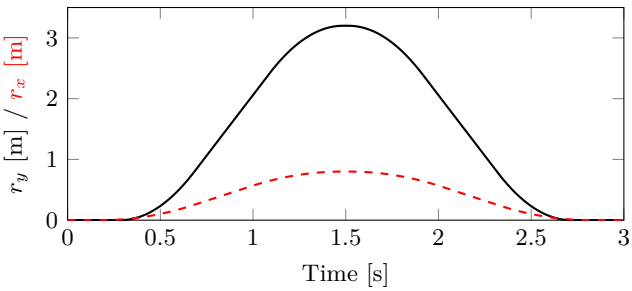

Figure 10.8. Reference trajectory r_y (——) introduces position-dependent dynamics due to the moving carriage mass. Reference r_x (- - -) is a forward-backward movement. Rotation φ is suppressed, i.e., $r_\varphi = 0$.

output system (2×2) and ILC is applied to a multi-input, single-output system (1×2). Note that, although ILC is only applied to x, position y influences the system model through position dependency and rotation φ through the strong cross-coupling (except for $y \approx 1.6$ m), see Figure 10.7.

The weights in (10.12) are selected as $w_e[k] = 10^{10}$, $w_f[k] = 10^{-10}$, $w_{\Delta f}[k] = 0$ in order to achieve high performance in the error norm and fast convergence. After convergence, f_j is in the order of 10^0 and e_j is in the order of 10^{-6}.

10.5.3 Results

Figure 10.9 shows the performance criterion for ILC based on LTI models at several positions y, together with ILC based on the LTV model. When based on the LTV model (·⊖·), one-step convergence is obtained since the model is exact and $w_{\Delta f} = 0$. In this case, an accurate LTV model is available due to the fact that a first-principles model is derived. As will become clear in Section 10.6, such models are not straightforward to obtain in practice. Since in y direction the carriage covers the whole working range (from 0 m to 3.2 m), an obvious choice when using an LTI model would be to use the LTI model with the carriage positioned in the middle of the gantry, i.e., $y = 1.6$ m. With ILC based on this 'averaged' LTI model the convergence is slower (·+·), due to the model mismatch, but eventually the same high performance as with the LTV model is obtained. If a poor LTI model is chosen, for example at $y = 6$ m, there is no convergence (·✱·). Convergence can be guaranteed by introducing robustness through increasing w_f (Van de Wijdeven and Bosgra, 2010). Indeed, for $w_f = 10^2$ there is convergence (·✱·), but at the cost of performance. Note that $y = 6$ m is not feasible for the current system, but might become so for larger printing systems. The result stresses the need for identification of accurate position-dependent models, which is part of future research.

The simulation example shows the benefit of ILC based on an LTV model

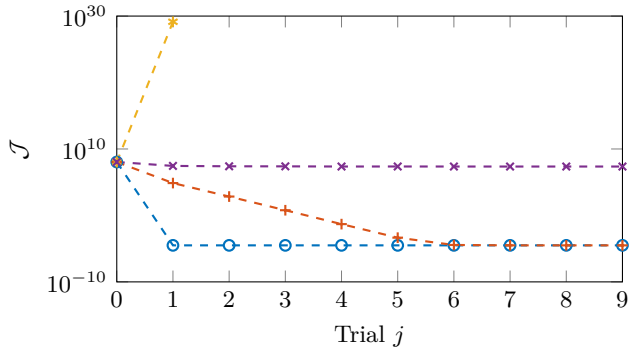

Figure 10.9. Performance criterion for simulations on an LTV system with ILC based on: LTV model, $w_f = 10^{-10}$ (· ⊖ ·); LTI model at $y = 1.6$ m, $w_f = 10^{-10}$ (· + ·); LTI model at $y = 6$ m, $w_f = 10^{-10}$ (· ✱ ·); and LTI model at $y = 6$ m, $w_f = 10^{2}$ (· ✱ ·). The LTI model at $y = 6$ m requires additional robustness (larger w_f) to converge.

when the system to control is LTV. For accurate LTI models, high performance is still achievable but at the cost of slower convergence, whereas for inaccurate LTI models performance needs to be sacrificed to guarantee convergence. Importantly, resource-efficient ILC in Algorithm 10.7 can directly be applied to LTV models, while preserving computational cost $\mathcal{O}(N)$.

10.6 Experimental implementation

In this section, the resource-efficient ILC approach is applied to the industrial flatbed printer in an experiment with task length $N = 100\,000$ which constitutes Contribution 10.IV.

10.6.1 System modeling

The previous section shows the importance of an accurate system model to obtain both fast convergence and high performance in the error norm. However, the accuracy of the derived position-dependent model based on first principles is limited and identification of accurate position-dependent models is part of ongoing research. Still, for the considered range of operation, the simulation study in Section 10.5 reveals that an LTI model is sufficiently accurate to guarantee convergence, albeit at a lower rate compared to the LTV model, see Figure 10.9. This validates the use of LTI models in the present experimental study. For the experiments in this chapter, ILC is based on an LTI model derived from an averaged frequency response function measurement, see Figure 10.10 for the Bode

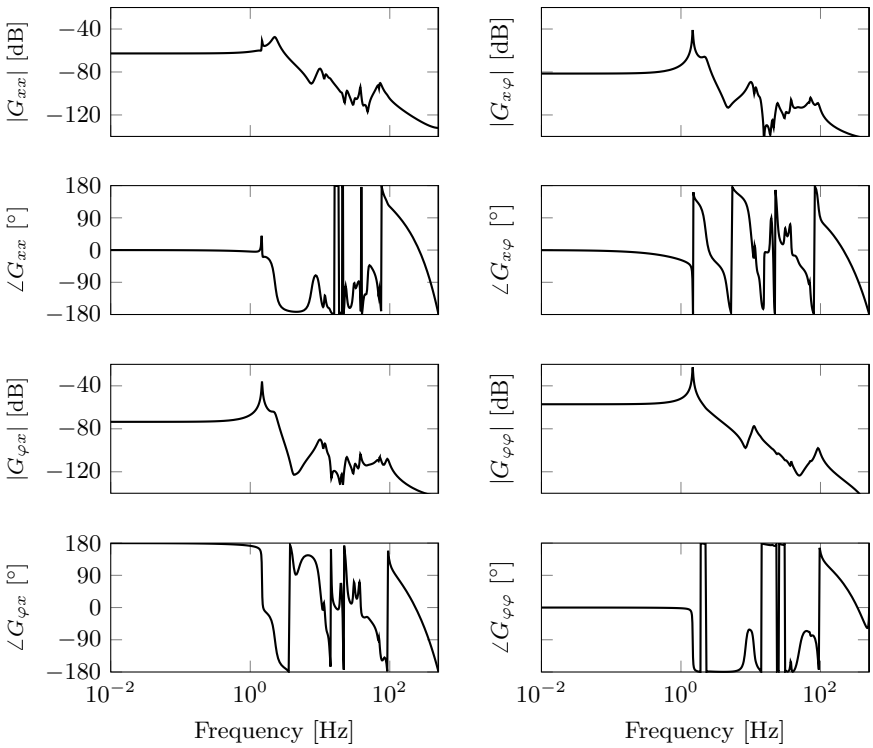

Figure 10.10. Bode diagram of the system G for the 2×2 Arizona gantry based on an averaged frequency response function measurement.

diagram of the model G. For feedback, the feedback controller in Figure 10.6 is used.

10.6.2 Experiment design

Contrary to the simulation case study in Section 10.5, where ILC is applied to a multi-input, single output system, in the experiments ILC is applied to a multi-input, multi-output system. During printing the gantry position is typically fixed while the carriage with the print heads moves over the gantry. In between the printing, the gantry performs a stepping motion in x direction in order to cover the next part of the medium. Without controlling the carriage, this results in the reference trajectories as shown in Figure 10.11, with task length $N = 100\,000$. The small rotation in φ during printing can be used for correcting misalignments.

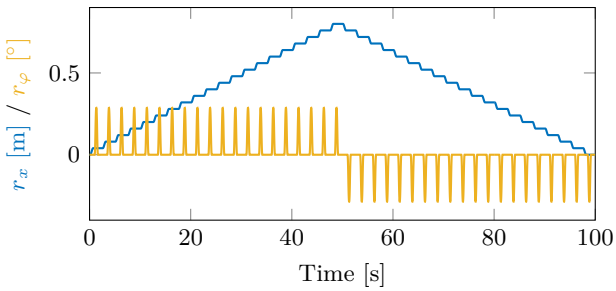

Figure 10.11. The gantry performs a stepping movement in x direction (——), while small rotations in φ (——) can be used for correcting misalignments. The task length is $N = 100\,000$.

The performance weights in Definition 10.5 are selected as

$$w_e = \begin{bmatrix} 10^5 & 0 \\ 0 & 5 \times 10^5 \end{bmatrix}, \qquad w_f = \begin{bmatrix} 10^{-4} & 0 \\ 0 & 5 \times 10^{-5} \end{bmatrix}, \qquad w_{\Delta f} = 0, \tag{10.35}$$

for all k. The choice $w_{\Delta f} = 0$ results in fast convergence of the ILC update, whereas the combination of w_e and w_f ensures minimization of the error, with minimal restriction of the feedforward signal. Note that since an LTI model is used on a position-dependent system, additional robustness ($w_f > 0$) is used to enhance robust convergence properties. As shown in the previous section, this will degrade the performance in terms of the error norm.

10.6.3 Results

The performance criterion when applying resource-efficient ILC is shown in Figure 10.12 for ten trials. Two important aspects are to be noted. First, the decrease in $\mathcal{J}$ indicates convergence of the ILC algorithm, which is enforced by selecting w_f sufficiently high. Second, despite $w_{\Delta f} = 0$, several iteration steps are required to converge to a steady state value due to model mismatches since an LTI model is used.

The time-domain errors are shown in Figure 10.13. In the first trial, $j = 0$, no feedforward is applied, i.e., $f_j[k] = 0$, for all k, yielding $\mathcal{J} = 2272$, $\|e_x\|_\infty = 1122$ µm, and $\|e_\varphi\|_\infty = 506$ µrad. After several trials the performance criterion is decreased by a factor 1000 to $\mathcal{J} = 2.2$ at trial $j = 9$, with $\|e_x\|_\infty = 48$ µm, and $\|e_\varphi\|_\infty = 24$ µrad.

The results show a significant performance enhancement for the position-dependent printing system, even with an LTI model. The performance may be further increased, where the parameter w_f can be used to tune robustness. Either this has to be chosen at a reasonably high value to guarantee robustness for position-dependent dynamics, or an LTV model of the printer has to be made.

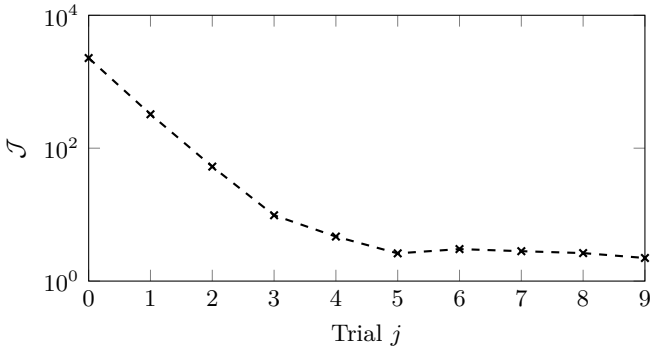

Figure 10.12. The performance criterion $\mathcal{J}$ decreases significantly (more than a factor 1000) over the trials indicating convergence and high performance.

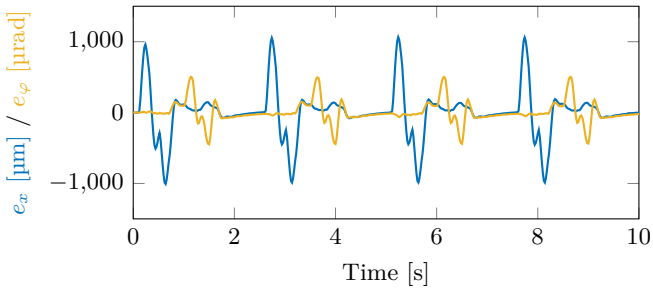

(a) Without ILC; feedback only ($j = 0$).

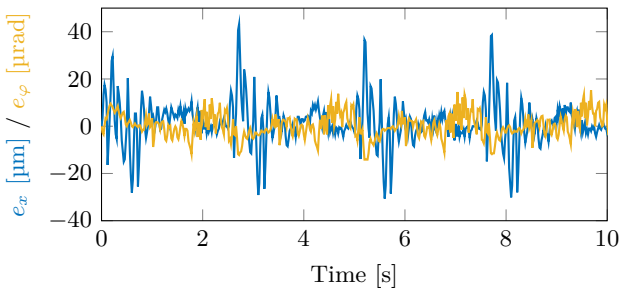

(b) After ten ILC trials ($j = 9$).

Figure 10.13. After several ILC trials both the error signal in x direction (——) and φ direction (——) are significantly reduced (note the scales). Only the first ten seconds is shown.

The latter is presently under investigation. In addition, a $w_{\Delta f}$ weighting may be introduced to reduce trial-varying disturbances. This is not done in the present research as the focus is on the computation load rather than performance, but it is noted that changing this value may improve performance.

Importantly, the results show that resource-efficient ILC is practical for large tasks (here $N = 100\,000$). For such large tasks, lifted ILC is impractical, as is shown in the next section, since it would involve matrices of dimensions $200\,000 \times 200\,000$ ($n_i = n_o = 2$).

10.7 Computational requirements

In this section, the computational load of lifted ILC and resource-efficient ILC are compared, constituting Contribution 10.V. The total computational load Δ_{tot} is split into two parts: $\Delta_{tot} = \Delta_{init} + \Delta_{trial}\, n_{trial}$, where Δ_{init} is the initialization of the algorithm, i.e., all calculations that can be computed a priori off-line, Δ_{trial} the on-line update, i.e., all calculations that need to be executed each trial, and n_{trial} the number of trials.

10.7.1 Analysis of computational complexity

For lifted ILC in Theorem 10.2 the initialization is given by (10.8) since $\underline{Q}$ and $\underline{L}$ are trial-invariant and the trial update is given by (10.7). The initialization (10.8) is dominated by matrix multiplication and inversion, hence $\Delta_{init,lif} \sim \mathcal{O}(N^3)$, when using Schoolbook matrix multiplication and Gauss-Jordan elimination, respectively, see also Strassen (1969). The trial update (10.7) is dominated by matrix-vector multiplication, hence $\Delta_{trial,lif} \sim \mathcal{O}(N^2)$, when using Schoolbook matrix multiplication.

For resource-efficient ILC in Theorem 10.6 the initialization is given by step 1 in Algorithm 10.7 and the trial update by step 2 and step 3 in Algorithm 10.7. Note that the state-space matrices of (10.13) and (10.15a) are trial-invariant and can hence be determined off-line during initialization. The dimensions in all steps are in the order of n_x. Hence, for $n_x \ll N$, $\Delta_{init,low} \sim \mathcal{O}(N)$ and $\Delta_{trial,low} \sim \mathcal{O}(N)$. The analysis is experimentally validated in the next section.

10.7.2 Comparison of computational cost

In this section, the analysis of the previous section is supported by numerical simulations. For the experiment, see Section 10.6, the initialization and trial update time of both approaches were measured on the full signals ($N = 100\,000$) as well as on parts of it, i.e., for smaller N. Results for $\Delta_{tot} = \Delta_{init} + \Delta_{trial}$, i.e., $n_{trial} = 1$, are depicted in Figure 10.14. As the analysis in the previous section indicates, the computation time of lifted ILC for large N is dominated by $\Delta_{init,lif}$ such that $\Delta_{tot,lif} \sim \mathcal{O}(N^3)$, see also the fit $\Delta_{tot,lif} = c_{lif} N^3$ (—).

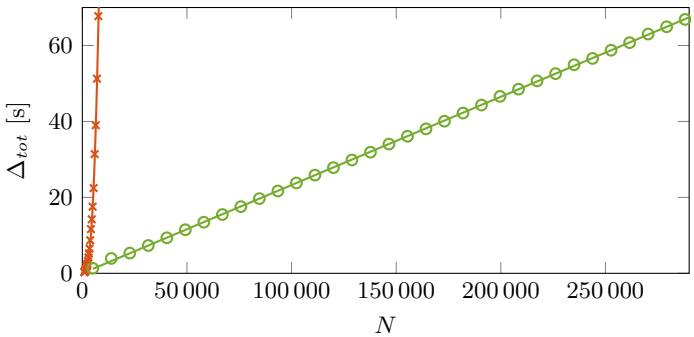

Figure 10.14. The computation time $\Delta_{tot} = \Delta_{init} + \Delta_{trial}$ for lifted ILC (×) grows as $\mathcal{O}(N^3)$, see the fit —, whereas for resource-efficient ILC (○) it grows as $\mathcal{O}(N)$, see the fit —.

Furthermore, the analysis indicates that $\Delta_{tot,low} \sim \mathcal{O}(N)$, as is confirmed by Figure 10.14, see also the fit $\Delta_{tot,low} = c_{low}N$ (—). Hence, especially for large N, the resource-efficient ILC approach is computationally significantly faster than the lifted ILC approach. For comparison, in one hour of calculation time, an experiment with a single trial of length $N \approx 29\,000$ can be calculated with lifted ILC, and of length $N \approx 15 \cdot 10^6$ with resource-efficient ILC, which is over 530 times as large.

The computation time for the initialization and trial update step are displayed separately in Figure 10.15 and Figure 10.16, respectively. The results confirm the analysis of the previous section with respect to the dependence on N, see the fitted lines. Note that $\mathcal{O}(N^n)$ corresponds to a slope n on the double logarithmic scale. For large N, there is insufficient random-access memory (RAM) available for lifted ILC resulting in large computation times $\Delta_{init,lif}$, $\Delta_{trial,lif}$.

For the full experiment task length $N = 100\,000$, $\Delta_{tot,low} = 23.3$ seconds whereas $\Delta_{tot,lif}$ is estimated at 40 hours, under the assumption of sufficient RAM.

10.8 Conclusion and outlook

In this chapter, a unified approach to resource-efficient ILC techniques for LTI/-LTV systems and optimal and general frequency-domain designs is developed. In particular, first it is shown that using the lifted framework, an analytic expression for the optimal feedforward signal for generic norm-based performance criteria can be derived by solving a set of linear equations. However, the actual implementation is troublesome for large tasks since the computation load increases as $\mathcal{O}(N^3)$, with N the task length. In this chapter, an alternative

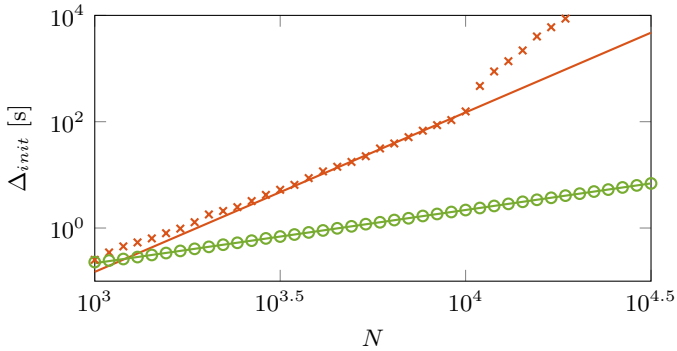

Figure 10.15. The initialization time Δ_{init} for lifted ILC (×) evolves as $\mathcal{O}(N^3)$ as shown by the fit —. For resource-efficient ILC (○) it evolves as $\mathcal{O}(N)$ as shown by the fit —. For large N, there is insufficient RAM available for the initialization of lifted ILC resulting in large computation times.

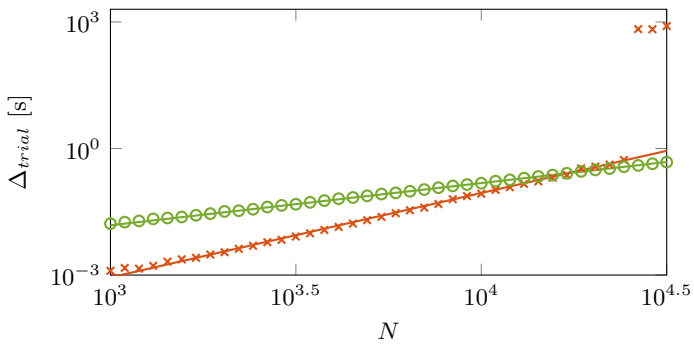

Figure 10.16. The trial update time Δ_{trial} for lifted ILC (×) evolves as $\mathcal{O}(N^2)$ as shown by the fit —. For resource-efficient ILC (○) it evolves as $\mathcal{O}(N)$ as shown by the fit —.

approach based on optimal control theory is presented that yields the same command signal, but at significantly lower computational cost, namely $\mathcal{O}(N)$, for both LTI and LTV systems.

A further analysis of this solution reveals that it is very similar, both in terms of computational techniques as well as the underlying theoretical developments, to common stable inversion techniques. The connections are explicitly established and analyzed, leading to a unified solution for many ILC approaches, both lifted and classical frequency-domain based, for both LTI and LTV systems.

Practical use is demonstrated by successfully applying resource-efficient ILC on an industrial flatbed printer. Simulation results on a position-dependent model reveal that LTV techniques can be very beneficial when applying ILC on position-dependent systems. Since the required first principles model is not sufficiently accurate for ILC design, an LTI model of the experimental system is used. The proposed algorithm, which is $\mathcal{O}(N)$, can be successfully implemented on a large task (here, $N = 100\,000$, with two inputs and two outputs), for which traditional lifted norm-optimal ILC breaks down and is thus impractical to implement.

Ongoing work focuses on further development of feedforward and ILC for position-varying systems, as occurring in, e.g., next-generation motion systems (Oomen et al., 2014). Indeed, LTV models for these type of systems enable high performance, whereas LTI models require additional robustness at the cost of performance as also shown in experiments. These results motivate the ongoing research to development of new identification techniques for position-dependent systems, see, e.g., Groot Wassink et al. (2005) for important steps, and development of ILC techniques compatible with these models.

10.A Proof of Lemma 10.4

In Figure 10.1, J is the transfer function $f \mapsto y$. Let x_G and x_C denote the state of G and C, respectively, then using (10.9)

$$y[k] = C_G x_G[k] + D_G u[k] + D_G f[k], \tag{10.36}$$
$$u[k] = C_C x_C[k] - D_C y[k], \tag{10.37}$$

which can be combined to

$$y[k] = (I_{n_o} + D_G D_C)^{-1} \left(C_G x_G[k] + D_G C_C x_C[k] + D_G f[k]\right), \tag{10.38}$$
$$u[k] = (I_{n_i} + D_C D_G)^{-1} \left(-D_C C_G x_G[k] + C_C x_C[k] - D_C D_G f[k]\right). \tag{10.39}$$

Substitution of these relations into the state equations, rewriting and using the relation $I - (I + X)^{-1}X = (I + X)^{-1}$ yields

$$x_G[k+1] = A_G x_G[k] + B_G u[k] + B_G f[k] \tag{10.40a}$$

$$\begin{aligned} &= (A_G - B_G(I_{n_i} + D_C D_G C_G)^{-1} D_C) x_G[k] \\ &\qquad + B_G(I_{n_i} + D_C D_G)^{-1}(C_C x_C[k] + f[k]), \end{aligned} \tag{10.40b}$$

$$x_C[k+1] = A_C x_C[k] - B_C y[k] \tag{10.41a}$$

$$\begin{aligned} &= (A_C - B_C(I_{n_o} + D_G D_C)^{-1} D_G C_C) x_C[k] \\ &\qquad - B_C(I_{n_o} + D_G D_C)^{-1}(C_G x_G[k] + D_G f[k]). \end{aligned} \tag{10.41b}$$

Combining the above state equations and output equation (10.38), and introducing state $x[k] = \begin{bmatrix} x_G[k] \\ x_C[k] \end{bmatrix}$ yields the state-space realization of J in Lemma 10.4.

10.B Proof of Theorem 10.6

10.B.1 Problem setup

The system dynamics are given by

$$x_{j+1}[k+1] = A x_{j+1}[k] + B f_{j+1}[k], \tag{10.42a}$$

$$y_{j+1}[k] = C x_{j+1}[k] + D f_{j+1}[k], \tag{10.42b}$$

with initial state $x_{j+1}[0] = x_0$ and (A, B, C, D) a state-space representation of the process sensitivity J. Define

$$\Delta x_{j+1}[k] := x_{j+1}[k] - x_j[k], \tag{10.43}$$

$$\Delta f_{j+1}[k] := f_{j+1}[k] - f_j[k], \tag{10.44}$$

then

$$\Delta x_{j+1}[k+1] = A \Delta x_{j+1}[k] + B \Delta f_{j+1}[k], \tag{10.45a}$$

$$\Delta y_{j+1}[k] = C \Delta x_{j+1}[k] + D \Delta f_{j+1}[k], \tag{10.45b}$$

with $\Delta x_{j+1}[0] = 0_{n_x \times 1}$. Since r is trial-invariant,

$$e_{j+1}[k] = S r[k] - y_{j+1}[k] \tag{10.46a}$$

$$= e_j[k] - C \Delta x_{j+1}[k] - D \Delta f_{j+1}[k]. \tag{10.46b}$$

In the remainder of the proof the subscript $j+1$ in general, and index $[k]$ for $w_e[k]$, $w_f[k]$, $w_{\Delta f}[k]$ are omitted for notational convenience. Note that this is not a restriction on the developed results.

The optimal input is given by

$$f_{opt} = \arg\min_{f} \mathcal{J}(f) = f_j + \arg\min_{\Delta f} \mathcal{J}'(\Delta f), \tag{10.47}$$

where

$$\mathcal{J}'(\Delta f) := \tfrac{1}{2}\mathcal{J}(f_{j+1}) = \sum_{k=0}^{N-1} \mathcal{L}(\Delta x[k], \Delta f[k]), \tag{10.48}$$

with

$$\begin{aligned}\mathcal{L}(\Delta x[k], \Delta f[k]) = \tfrac{1}{2}&(e_j[k] - C\Delta x[k] - D\Delta f[k])^\top w_e \\ &\times (e_j[k] - C\Delta x[k] - D\Delta f[k]) \\ &+ \tfrac{1}{2}(\Delta f[k] + f_j[k])^\top w_f (\Delta f[k] + f_j[k]) \\ &+ \tfrac{1}{2}(\Delta f[k])^\top w_{\Delta f}(\Delta f[k]).\end{aligned} \tag{10.49}$$

The steps followed are along the lines of Naidu (2003, Section 5.5).

10.B.2 Hamiltonian, state, costate and open-loop optimal control

Let the Hamiltonian be defined as

$$\begin{aligned}&\mathcal{H}(\Delta x[k], \lambda[k+1], \Delta f[k]) \\ &\quad = \lambda^\top[k+1](A\Delta x[k] + B\Delta f[k]) + \mathcal{L}(\Delta x[k], \Delta f[k]).\end{aligned} \tag{10.50}$$

Let $\mathcal{H}_{opt} = \mathcal{H}(\Delta x_{opt}[k], \lambda_{opt}[k+1], \Delta f_{opt}[k])$, then the optimal state is given by

$$\Delta x_{opt}[k+1] = \frac{\partial \mathcal{H}_{opt}}{\partial \lambda_{opt}[k+1]} \tag{10.51a}$$

$$= A\Delta x_{opt}[k] + B\Delta f_{opt}[k], \tag{10.51b}$$

with

$$\Delta x_{opt}[0] = 0_{n_x \times 1}, \tag{10.52}$$

and the optimal costate by

$$\lambda_{opt}[k] = \frac{\partial \mathcal{H}_{opt}}{\partial \Delta x_{opt}[k]} \tag{10.53a}$$

$$= A^\top \lambda_{opt}[k+1] - C^\top w_e \left(e_j[k] - C\Delta x_{opt}[k] - D\Delta f_{opt}[k]\right), \tag{10.53b}$$

with

$$\lambda_{opt}[N] = 0_{n_x \times 1}. \tag{10.54}$$

The optimal input satisfies

$$\frac{\partial \mathcal{H}_{opt}}{\partial \Delta f_{opt}[k]} = 0, \tag{10.55}$$

from which follows

$$\begin{aligned}\Delta f_{opt}[k] = \gamma\Big(&D^\top w_e e_j[k] - D^\top w_e C \Delta x_{opt}[k] \\ &- w_f f_j[k] - B^\top \lambda_{opt}[k+1]\Big),\end{aligned} \tag{10.56}$$

with

$$\gamma = \left(D^\top w_e D + w_f + w_{\Delta f}\right)^{-1}. \tag{10.57}$$

With substitution of (10.56), relations (10.51b) and (10.53), with boundary conditions (10.52) and (10.54), form the Hamiltonian system

$$\begin{aligned}&\begin{bmatrix}\Delta x_{opt}[k+1] \\ \lambda_{opt}[k]\end{bmatrix} \\ &\quad = \begin{bmatrix} A - B\gamma D^\top w_e C & -B\gamma B^\top \\ C^\top w_e \left(I - D\gamma D^\top w_e\right) C & A^\top - C^\top w_e D\gamma B^\top \end{bmatrix} \begin{bmatrix}\Delta x_{opt}[k] \\ \lambda_{opt}[k+1]\end{bmatrix} \\ &\qquad + \begin{bmatrix} -B\gamma w_f & B\gamma D^\top w_e \\ -C^\top w_e D\gamma w_f & C^\top w_e D\gamma D^\top w_e - C^\top w_e \end{bmatrix} \begin{bmatrix} f_j[k] & e_j[k] \end{bmatrix},\end{aligned} \tag{10.58a}$$

$$\Delta x_{opt}[0] = 0_{n_x \times 1}, \tag{10.58b}$$

$$\lambda_{opt}[N] = 0_{n_x \times 1}. \tag{10.58c}$$

10.B.3 Riccati and vector equations

Next, the co-state is eliminated from (10.58a) using the sweep method (Lewis and Syrmos, 1995) by applying the transformation

$$\lambda_{opt}[k] = P[k]\Delta x_{opt}[k] - g[k], \tag{10.59}$$

which yields

$$\begin{aligned}\Delta x_{opt}[k+1] = \left(I + B\gamma B^\top P[k+1]\right)^{-1} \Big[&\left(A - B\gamma D^\top w_e C\right) \Delta x_{opt}[k] \\ &+ B\gamma D^\top w_e e_j[k] - B\gamma w_f f_j[k] + B\gamma B^\top g[k+1]\Big].\end{aligned} \tag{10.60}$$

Substituting (10.60) and (10.59) in the expression of $\lambda_{opt}[k]$ in (10.58a) and rewriting yields

$$\begin{aligned}\Big[P[k] - \left(A^\top - C^\top w_e D\gamma B^\top\right) P[k+1] \left(I + B\gamma B^\top P[k+1]\right)^{-1} \\ \times \left(A - B\gamma D^\top w_e C\right) - C^\top w_e C + C^\top w_e D\gamma D^\top w_e C\Big] \Delta x_{opt}[k] \\ = g[k] - \left(C^\top w_e - K_g[k] D^\top w_e - C^\top w_e D\gamma D^\top w_e\right) e_j[k] \\ - \left(K_g[k] w_f + C^\top w_e D\gamma w_f\right) f_j[k] \\ - \left(A^\top - C^\top w_e D\gamma B^\top - K_g[k] B^\top\right) g[k+1],\end{aligned} \tag{10.61}$$

where

$$K_g[k] = \left(A^\top - C^\top w_e D\gamma B^\top\right) P[k+1] \left(I + B\gamma B^\top P[k+1]\right)^{-1} B\gamma. \tag{10.62}$$

Relation (10.61) holds for all values $\Delta x_{opt}[k]$, for all k. Hence, the left-hand side of (10.61) should be zero for all k, leading to

$$\begin{aligned}P[k] = \left(A^\top - C^\top w_e D\gamma B^\top\right) P[k+1] \left(I + B\gamma B^\top P[k+1]\right)^{-1} \\ \times \left(A - B\gamma D^\top w_e C\right) + C^\top w_e C - C^\top w_e D\gamma D^\top w_e C,\end{aligned} \tag{10.63}$$

where the matrix identity

$$(\mathcal{A} + \mathcal{B}\mathcal{C}\mathcal{D})^{-1} = \mathcal{A}^{-1} - \mathcal{A}^{-1}\mathcal{B}\left(\mathcal{C}^{-1} + \mathcal{D}\mathcal{A}^{-1}\mathcal{B}\right)^{-1}\mathcal{D}\mathcal{A}^{-1}, \tag{10.64}$$

leads to the matrix difference Riccati equation (10.17a). Also, the right-hand side of (10.61) should vanish for all k, leading to the vector difference equation (10.15a). Evaluating (10.59) at time instance $k = N$ yields

$$\lambda_{opt}[N] = P[N]\Delta x_{opt}[N] - g[N], \tag{10.65}$$

which holds for all $\Delta x_{opt}[N]$ and given the boundary condition from (10.54) yields terminal conditions

$$P[N] = 0_{n_x \times n_x}, \tag{10.66}$$

$$g[N] = 0_{n_x \times 1}. \tag{10.67}$$

10.B.4 Closed-loop optimal control

The closed-loop optimal control follows by substituting (10.59) at $k+1$ and (10.51b) in (10.56), and solving for $\Delta f_{opt}[k]$:

$$\Delta f_{opt}[k] = -L[k]\Delta x_{opt}[k] - L_f[k] f_j[k] + L_e[k] e_j[k] + L_g[k] g[k+1], \tag{10.68}$$

with $L[k]$, $L_f[k]$, $L_e[k]$, and $L_g[k]$ given by (10.14).

Combining (10.51b) with (10.68) yields the state-space system (10.13) with state $\Delta x_{opt}[k]$, inputs $f_j[k], e_j[k], g[k+1]$, and output $f_{opt}[k] = f_j[k] + \Delta f_{opt}[k]$ as given by (10.13).

10.C Proof of Theorem 10.9

The proof is similar to that of Chen (1993) for continuous-time systems. Since $x_s[k]$ and $x_u[k]$ are linearly coupled, the solution is found by applying the sweep method (Lewis and Syrmos, 1995) with

$$x_u[k] = P[k]x_s[k] + g[k], \tag{10.69}$$

which holds for all $x_s[k]$ and since $x_u[N] = 0$,

$$P[N] = 0, \qquad g[N] = 0. \tag{10.70}$$

Evaluating (10.69) at $k+1$ and substituting the dynamics (10.20) yields

$$\begin{aligned}&\Big(A_{us} + A_{uu}P[k] - P[k+1]A_{ss} - P[k+1]A_{su}P[k]\Big)x_s[k]\\ &= -A_{uu}g[k] - B_u u[k] + P[k+1]A_{su}g[k] + P[k+1]B_s u[k] + g[k+1],\end{aligned} \tag{10.71}$$

which holds for all $x_s[k]$ and therefore both sides should vanish. From the left-hand side follows (10.21) and from the right-hande side follows (10.22). State $x_s[k]$ follows from substituting (10.69) into $x_s[k+1]$ in (10.20) and solving forward in time. State $x_u[k]$ directly follows from (10.69).

Chapter 11

The role of feedforward, learning, and feedback in inferential control

The combination of feedback control with inverse model feedforward control or iterative learning control is known to yield high performance. The aim of this chapter is to clarify the role of feedback control in the design of feedforward controllers, with specific attention to the inferential situation. Recent developments in optimal feedforward control are combined with feedback control to jointly optimize a single performance criterion. Analysis and application show that the joint design addresses the specific control objectives. The combined design is essential in control and in particular in inferential control. The results constitute Contribution IV.E.

11.1 Introduction

Many control applications involve both feedback and feedforward controllers. Both are often tuned separately using specific approaches and based on different control goals, e.g., different norms. An example is iterative learning control (ILC) where the feedforward is designed as an add-on to feedback. This chapter addresses the fundamental role of feedback in combination with feedforward and ILC, both for regular and inferential control.

The role of feedback is often assumed fixed in feedforward and ILC design, see e.g., Van der Meulen et al. (2008); Bristow et al. (2006), but also related

The contents of this chapter are published in:
Jurgen van Zundert and Tom Oomen. On Optimal Feedforward and ILC: The Role of Feedback for Optimal Performance and Inferential Control. *IFAC-PapersOnLine* (20th World Congress), 50(1):6093–6098, 2017.

approaches in Boeren et al. (2017). In fact, in Boeren et al. (2017) the performance of the feedforward controller depends on the feedback controller, which is required to satisfy a certain assumption. Notable exceptions are Rogers et al. (2007); Bolder and Oomen (2016), where it is advocated to use a 2D framework, and research on equivalent feedback (Goldsmith, 2002). In this chapter, the aim is to connect feedback and feedforward control design.

Recent interest in inferential control, e.g., for mechatronics (Oomen et al., 2015; Ronde et al., 2012; Voorhoeve et al., 2016), has led to a new interest in controller structures. Inferential control imposes an additional constraint on how to design feedforward and feedback controllers that jointly optimize a single performance criterion, which is not immediate in such situations as pointed out in Bolder and Oomen (2016). However, at present limited guidelines are available on how to actually design the controller. In this chapter, the joint design of feedback with feedforward/ILC in a two degrees-of-freedom inferential control architecture is investigated.

Although there have been important developments in ILC and feedforward design frameworks, the role of feedback control is often not explicitly addressed. The aim of this chapter is to clarify the role of feedback control in the design of feedforward controllers, with specific attention to both the regular and the inferential situation. The method follows from recent developments of norm-optimal ILC and feedforward algorithms, see also Chapter 10. The algorithms are used to show the role of feedback and feedforward control in achieving optimal performance, thereby confirming the claim related to the assumption $SH = 1$ in Boeren et al. (2017). It is also shown that this gives a direct solution to the inferential control problem, providing a solution that falls within the controller structures outlined in the framework of Oomen et al. (2015). As such, this chapter extends Chapter 10 in these two aspects.

The outline of the chapter is as follows. In Section 11.2, the regular and inferential control problems are formulated. The inferential control application of a wafer stage is presented in Section 11.3. In Section 11.4, the control design for the regular case $z = y$ is presented. In Section 11.5, the control design for the inferential case $z \neq y$ is presented. Application to iterative learning control (ILC) is presented in Section 11.6. Section 11.7 contains conclusions and an outlook.

11.2 Problem formulation

In this section, the control objective is formulated. The formulation is split into two parts: the standard control problem with $z = y$ and the inferential control problem with $z \neq y$.

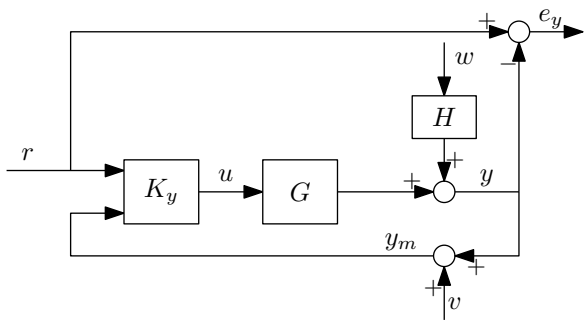

Figure 11.1. Two degrees-of-freedom tracking control architecture for $z = y$ with inputs reference trajectory r and measurement y_m. The control objective is tracking r with y.

11.2.1 Control for $z = y$

Consider the system

$$x[k+1] = Ax[k] + Bu[k] + B_w w[k], \tag{11.1a}$$
$$y[k] = C_y x[k] + H_y w[k], \tag{11.1b}$$
$$y_m[k] = y[k] + v[k], \tag{11.1c}$$

with state $x[k] \in \mathbb{R}^{n_x}$, input $u[k] \in \mathbb{R}^{n_i}$, output $y[k] \in \mathbb{R}^{n_o}$, output measurement $y_m[k] \in \mathbb{R}^{n_o}$, process noise $w[k] \in \mathbb{R}^{n_x}$, and measurement noise $v[k] \in \mathbb{R}^{n_o}$, where

$$w \sim \mathcal{N}(0, \sigma_w^2 I_{n_x}), \qquad v \sim \mathcal{N}(0, \sigma_v^2 I_{n_o}), \tag{11.2}$$

with variances $\sigma_w^2, \sigma_v^2 \in \mathbb{R}_+$.

In order to have y track a pre-specified reference trajectory r, the two degrees-of-freedom control architecture in Figure 11.1 is considered where

$$G \stackrel{z}{=} \left[\begin{array}{c|c} A & B \\ \hline C_y & 0 \end{array}\right], \qquad H \stackrel{z}{=} \left[\begin{array}{c|c} A & B_w \\ \hline C_y & H_y \end{array}\right]. \tag{11.3}$$

The control objective is the design of controller K_y to minimize $e_y = r - y$, with measurement y_m of y available.

Remark 11.1. *For notation convenience, it is assumed that system* (11.1) *is time invariant and without direct feedthrough from* u*. However, all results can readily be extended to the more general case of time-varying systems and systems with direct feedthrough.*

11.2.2 Control for $z \neq y$

In inferential control, there are no means to directly measure the point of interest z. Instead, only measurements y of other locations are available. This control

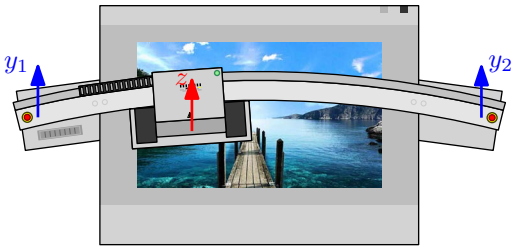

(a) High accelerations of the print heads induce deformations of the gantry causing mismatches between measured positions y_1, y_2 and the actual print head position z.

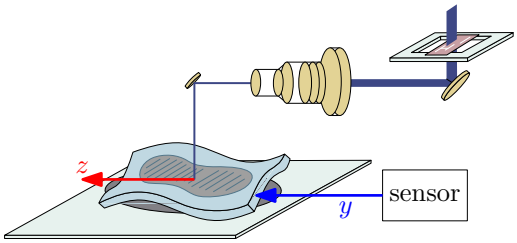

(b) In wafer scanner systems, an optical column directs light to the light sensitive layers of the wafer. The optical column hampers position measurement of the exposed performance location z. Instead, the edge of the wafer stage y is measured.

Figure 11.2. Examples of inferential control problems. Performance location z cannot be measured and only measurements y are available.

challenge may arise from undesired flexibility in the system, as in the printer application of Figure 11.2(a), or from the inability to measure at the desired location, as in the wafer stage application of Figure 11.2(b).

For an inferential setting, $z \neq y$, (11.1) is extended with

$$z[k] = C_z x[k]. \tag{11.4}$$

The extended control architecture is shown in Figure 11.3, where

$$G_z \stackrel{z}{=} \left[\begin{array}{c|c} A & B \\ \hline C_z & 0 \end{array}\right], \qquad H_z \stackrel{z}{=} \left[\begin{array}{c|c} A & B_w \\ \hline C_z & 0 \end{array}\right]. \tag{11.5}$$

The control objective is the design of K_z to minimize $e_z = r - z$, with only measurements y_m of y available.

11.3 Wafer stage application

Wafer stages are key components in wafer scanners used for the production of integrated circuits (Butler, 2011). The stages accurately position the wafer during exposure.

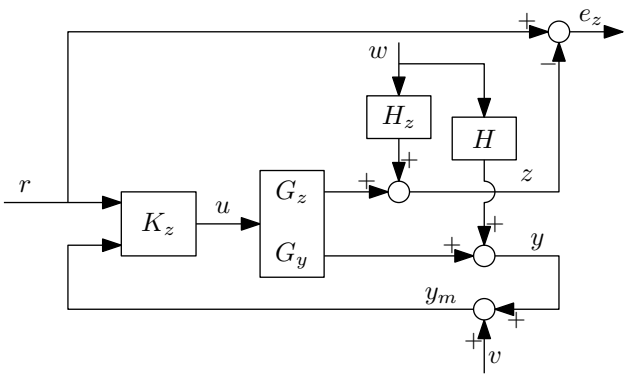

Figure 11.3. Two degrees-of-freedom tracking control architecture for inferential control where the performance variables and measurements are different: $z \neq y$. The control objective is tracking r with z.

The considered system is a simplified version of the wafer stage in Figure 11.2(b) which is assumed to be a rigid body, see Figure 11.4. The wafer stage is actuated by force u and can translate in q_1, q_2 and rotate in ϕ. The point of interest z cannot be measured due to the optical column used for exposure. Instead, the edge of the stage y is measured with a sensor that is located on the fixed world yielding measurement y_m. Note that if there are no rotations, i.e., $\phi = 0$, then $z = y$, otherwise $z \neq y$.

A linearized model of the system in Figure 11.4 is considered. The continuous-time state-space realization of the linearized system dynamics with input u, state $q = \begin{bmatrix} q_1 & \dot{q}_1 & \phi & \dot{\phi} \end{bmatrix}^\top$, and output y is

$$\left[\begin{array}{c|c} A_c & B_c \\ \hline C_{y,c} & 0 \end{array}\right] = \left[\begin{array}{cccc|c} 0 & 1 & 0 & 0 & 0 \\ 0 & 0 & 0 & 0 & \frac{1}{m} \\ 0 & 0 & 0 & 1 & 0 \\ 0 & 0 & -\frac{1}{2}\frac{kl^2}{I} & -\frac{1}{2}\frac{dl^2}{I} & \frac{1}{2}\frac{l}{I} \\ \hline 1 & 0 & 0 & 0 & 0 \end{array}\right]. \tag{11.6}$$

Assuming zero-order-hold on the input, the discretized system has a state-space realization

$$G_y \overset{z}{=} \left[\begin{array}{c|c} A & B \\ \hline C_y & 0 \end{array}\right] = \left[\begin{array}{c|c} e^{A_c\delta} & A_c^{-1}(A - I)B_c \\ \hline C_{y,c} & 0 \end{array}\right], \tag{11.7}$$

with sample time $\delta = 0.001$ s. The parameters are listed in Table 11.1. Furthermore, $B_w = I_4$ and $H_y = 0_{1\times 4}$ in (11.1), with noise variances $\sigma_w^2 = 10^{-6}$, $\sigma_v^2 = 10^{-10}$.

The reference trajectory r consists of a fourth-order forward and backward motion and is provided in Figure 11.5.

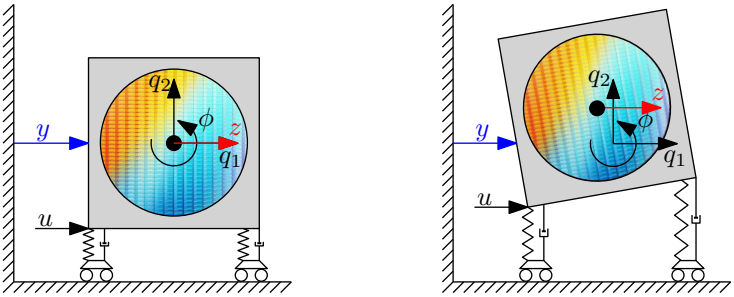

(a) Position y corresponds with point of interest z: $z = y$.

(b) Rotations of the stage introduce a mismatch in position: $z \neq y$.

Figure 11.4. Top view of wafer stage model revealing the inferential control challenge as $z \neq y$ for $\phi \neq 0$.

Table 11.1. Parameter values of the wafer stage model.

Parameter	Symbol	Value	Unit
Mass	m	8	kg
Inertia	I	0.0133	kgm^2
Spring constant	k	10^4	N/m
Damping constant	d	100	Ns/m
Length	l	0.1	m

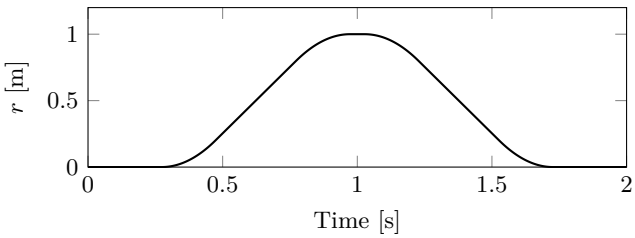

Figure 11.5. Reference trajectory r of length $N = 2001$ samples.

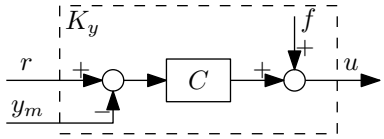

Figure 11.6. Standard feedback/feedforward control.

11.4 Application to $z = y$

In this section, it is assumed that performance variable z can be measured, i.e., $z = y$ ($C_z = C_y$).

11.4.1 Analysis

A common control architecture consisting of feedback controller C and feedforward f is shown in Figure 11.6. Implementation of this controller in the diagram of Figure 11.1 yields

$$e_y = S(r - Gf) - SHw + SGCv, \tag{11.8}$$

with sensitivity $S = (I + GC)^{-1}$.

The first term in (11.8) is completely deterministic and can be influenced by both feedback and feedforward. Note that the term cannot be fully eliminated using feedback C since $S = 0$ is not feasible due to Bode's sensitivity integral (Seron et al., 1997). In contrast, the term can be fully eliminated by feedforward $f = G^{-1}r$.

The second and third term in (11.8) are stochastic and can therefore not be completely eliminated. Both terms can only be influenced by feedback. Assuming that the first term in (11.8) is eliminated by feedforward $f = G^{-1}r$ and that there is no measurement noise, i.e., $v = 0$, then $e_y = -SHw$. This error has minimal variance if it is white. This imposes the condition

$$SH = c \in \mathbb{R}, \tag{11.9}$$

corresponding to Assumption 2.1 in Boeren et al. (2017) where $SH = 1$.

11.4.2 Optimal control

The optimal control law is derived from norm-optimal ILC.

11.4.2.1 ILC

Given data e_j, f_j of current trial j, norm-optimal ILC determines feedforward f_{j+1} for next trial $j+1$ that minimizes

$$\|e_{j+1}\|_{w_e}^2 + \|f_{j+1}\|_{w_f}^2 + \|f_{j+1} - f_j\|_{w_{\Delta f}}^2, \tag{11.10}$$

with $w_e, w_f, w_{\Delta f} \in \mathbb{R}_+$, where $\|(\cdot)\|_w^2 = (\cdot)^\top w(\cdot)$. A common solution method for norm-optimal ILC is lifted ILC which is based on describing input-output relations in lifted/supervector notation (Moore, 1993). In Chapter 10, it is shown that the computation time of the lifted solution method grows as $\mathcal{O}(N^3)$, with N the task length. Moreover, an alternative resource-efficient solution method based on Riccati equations is presented. The method yields exactly the same results, but the computation time grows as $\mathcal{O}(N)$. In the remainder of this section and Section 11.5, the focus is on feedforward control. See Section 11.6 for ILC.

11.4.2.2 Feedforward

Feedforward can be seen as a special case of ILC in which only one trial is performed, i.e., with $w_{\Delta f} = 0$. Consequently, (11.10) reduces to the LQ criterion

$$\sum_{k=0}^{N-1} e_y^\top[k] Q e_y[k] + u^\top[k] R u[k]. \tag{11.11}$$

The weights are selected as $Q = w_e = 10^{10}$, $R = w_f = 10^{-10}$ to minimize e_y with minimal restriction on u. The optimal resource-efficient solution is given by Lemma 11.2.

Lemma 11.2 (Optimal feedforward)**.** *Input u for* (11.1) *with $w, v = 0$ that minimizes* (11.11) *is given by*

$$u_{opt}[k] = -K[k]x[k] + L_g[k]g[k+1], \tag{11.12}$$

with

$$\begin{aligned} P[k] = &-A^\top P[k+1]B(R + B^\top P[k+1]B)^{-1}B^\top P[k+1]A \\ &+ A^\top P[k+1]A + C_y^\top Q C_y, \end{aligned} \tag{11.13}$$

$$P[N] = 0_{n_x \times n_x}, \tag{11.14}$$

$$\begin{aligned} g[k] = &\left(-A^\top P[k+1]\left(I + BR^{-1}B^\top P[k+1]\right)^{-1} BR^{-1}B^\top + A^\top\right) \\ &\times g[k+1] + C_y^\top Q r[k], \end{aligned} \tag{11.15}$$

$$g[N] = 0_{n_x \times 1}, \tag{11.16}$$

$$K[k] = \left(R + B^\top P[k+1]B\right)^{-1} B^\top P[k+1]A, \tag{11.17}$$

$$L_g[k] = \left(R + B^\top P[k+1]B\right)^{-1} B^\top. \tag{11.18}$$

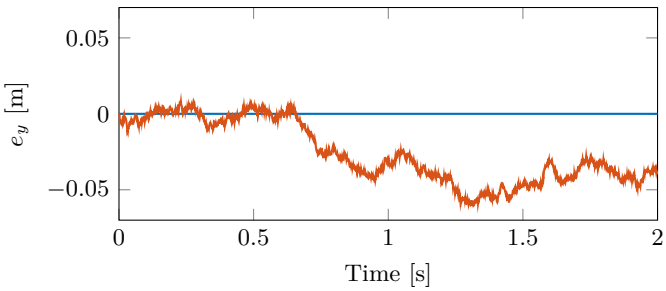

Figure 11.7. Perfect tracking for (11.20) on the system without noise (——) deteriorates under the presence of noise (——).

Proof. Follows from setting $w_{\Delta f} = 0$ and $D = 0$ in Theorem 10.6. □

Next, optimal input (11.12) is used for design of K_y in Figure 11.1.

11.4.3 Feedforward approach

For the case without noise, i.e., $v, w = 0$, (11.8) reduces to

$$e_y = S(r - Gf), \tag{11.19}$$

which is completely deterministic. Perfect tracking can be obtained through feedforward only by selecting, see also Lemma 11.2,

$$u[k] = f_{opt}[k], \tag{11.20}$$

with

$$f_{opt}[k] = -K[k]x_{opt}[k] + L_g[k]g[k+1]. \tag{11.21}$$

Since (11.1) is completely deterministic for $v, w = 0$, optimal state x_{opt} can be calculated a priori as

$$x_{opt}[k+1] = (A - BK[k])x_{opt}[k] + BL_g[k]g[k+1]. \tag{11.22}$$

Note that this approach is also followed in Chapter 10 for feedforward design.

Figure 11.7 shows excellent tracking for (11.20) on the wafer stage system of Section 11.3 without noise ($v, w = 0$). Note that $e_y = 0$ if $\frac{Q}{R} \to \infty$ in (11.11), whereas Lemma 11.2 requires $R > 0$ to avoid singularity. The results confirm the analysis in Section 11.4.1 that the first term in (11.8) can be fully eliminated by feedforward.

Figure 11.7 also shows the results for (11.20) on the true system with noise $(v, w \neq 0)$. Clearly, the high performance is deteriorated by the noise. Note that since (11.20) consists of feedforward only, $C = 0$, $S = 1$ in (11.8) such that

$$e_y = (r - Gf) - Hw = -Hw, \tag{11.23}$$

since (11.20) eliminates the first term as shown by the simulation without noise.

11.4.4 Combined feedforward and feedback

The previous section shows that feedforward control can eliminate all reference induced errors, but cannot compensate for noise induced errors. In contrast, feedback control can compensate for noise induced errors, see also Section 11.4.1. A key observation is that (11.12) includes state feedback on state x, but that this is not exploited in (11.20) by replacing x with x_{opt} in (11.22) assuming a noise free system. In the proposed approach, feedback in (11.12) is exploited to suppress the noise induced errors.

11.4.4.1 Combined feedforward and optimal state feedback

Optimal control law (11.12) can be rewritten as

$$u[k] = -K[k]\Delta x[k] + f_{opt}[k], \tag{11.24}$$

with $f_{opt}[k]$ in (11.21) and

$$\Delta x[k] = x[k] - x_{opt}[k] \tag{11.25}$$

the deviation of the true state from the optimal state (11.22). Control input (11.24) consists of feedforward and state feedback, and assumes that x is available. Since (11.24) uses state x rather than y_m for feedback, v is not fed back in (11.8) such that

$$e_y = S(r - Gf) - SHw. \tag{11.26}$$

Feedforward f_{opt} eliminates all reference induced errors, i.e., the first term, as shown by Section 11.4.3. Since the feedback control is optimal it satisfies (11.9), and yields minimal variance on e_y by creating $SH = c \in \mathbb{R}$.

The spectrum of e_y for application on the wafer stage system of Section 11.3 is shown in Figure 11.8. The figure shows that the feedback control in (11.24) yields a flat spectrum of e_y, confirming whiteness and thus optimality. Figure 11.8 also shows that the spectrum of e_y is not flat for (11.20), indicating non-optimality of the feedforward only approach.

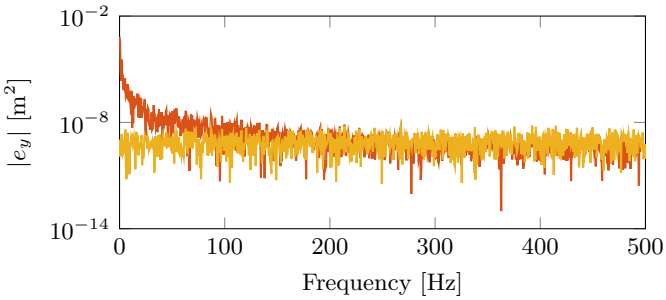

Figure 11.8. The spectrum of e_y for (11.24) (——) is flat confirming optimality, whereas for (11.20) (——) it is colored confirming non-optimality.

11.4.4.2 Combined feedforward and output feedback

Control (11.24) assumes that true state x is available, which is generally not the case. Therefore, x is replaced by an estimate $\hat{x}$ that is obtained through a Kalman filter on the measurable output y_m as given by Lemma 11.3.

Lemma 11.3 (Kalman filter)**.** *State x and output y of system* (11.1) *can be estimated from y_m by*

$$\hat{x}[k+1] = A\hat{x}[k] + Bu[k] + L[k](y_m[k] - \hat{y}[k]), \tag{11.27a}$$

$$\hat{y}[k] = C_y\hat{x}[k], \tag{11.27b}$$

with gain matrix

$$L[k] = (X[k]C_y^\top + \bar{N})(C_yX[k]C_y^\top + \bar{R})^{-1}, \tag{11.28}$$

where X is the solution of the discrete-time dynamic Riccati equation

$$\begin{aligned} X[k+1] = -AX[k]C_y^\top(C_yX[k]C_y^\top + R_n)^{-1}C_yX[k]A^\top \\ + AX[k]A^\top + Q_n, \end{aligned} \tag{11.29a}$$

$$X[0] = 0_{n_x \times n_x}, \tag{11.29b}$$

and

$$\bar{R} = R_n + H_yN_n + N_n^\top H_y^\top + H_yQ_nH_y^\top, \tag{11.30}$$

$$\bar{N} = B_w(Q_nH_y^\top + N_n), \tag{11.31}$$

$$Q_n = \sigma_w^2 I_{n_x}, \tag{11.32}$$

$$R_n = \sigma_v^2 I_{n_o}, \tag{11.33}$$

$$N_n = 0_{n_x \times n_o}. \tag{11.34}$$

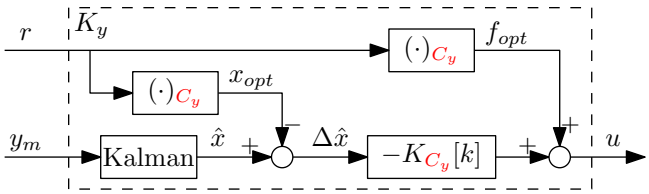

Figure 11.9. Optimal feedforward control and observer based output feedback control implementation. The feedback control is based on state estimate $\Delta\hat{x}$ obtained through a Kalman filter from measurement y_m.

Proof. See, for example, Anderson and Moore (1989). □

Replacing Δx in (11.24) by $\Delta\hat{x}[k] = \hat{x}[k] - x_{opt}[k]$ yields

$$u[k] = -K[k]\Delta\hat{x}[k] + f_{opt}[k]. \tag{11.35}$$

This combination of feedforward control and observer based output feedback control is similar to linear quadratic Gaussian (LQG) control, with the key difference that here an explicit split in feedback and feedforward is made. The complete control structure is shown in Figure 11.9.

Controller (11.35) consists of feedback and feedforward. Feedforward $f_{opt}[k]$ eliminates all reference induced errors, as shown in Section 11.4.3. Feedback control $-K[k]\Delta\hat{x}[k]$ yields minimal variance on e_y if $v = 0$ since then $\hat{x} = x$ and (11.23) is recovered. Similar as for the traditional feedback controller, optimality of Kalman filter (11.27) is achieved when the input, i.e., innovation $y_m - \hat{y}$ is white.

Figure 11.10 and Figure 11.11 show the results for (11.35) on the wafer stage application of Section 11.3. Figure 11.10 shows that the innovation indeed has a flat spectrum, confirming optimality of the Kalman filter. Figure 11.11 shows that the combined feedforward/feedback approach (11.35) outperforms the feedforward only approach (11.20) since it compensates for disturbances through feedback.

In summary: controller K_y with optimal feedforward requires feedback control to whiten trial-varying disturbances and a Kalman filter to whiten measurement noise.

11.5 Application to $z \neq y$

In this section, the inferential control problem is considered where performance variable z differs from output y, i.e., $z \neq y$. Here,

$$C_z = \begin{bmatrix} 1 & 0 & \frac{2}{5}l & 0 \end{bmatrix}. \tag{11.36}$$

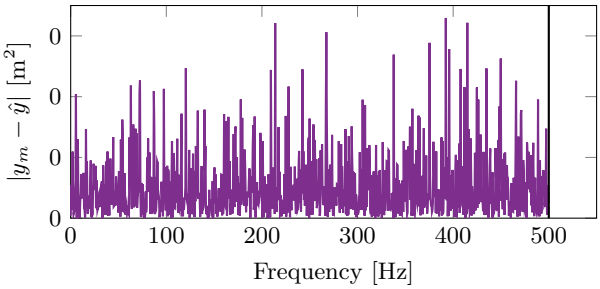

Figure 11.10. Innovation $y_m - \hat{y}$ of the Kalman filter (11.27) under control (11.35) has a flat spectrum confirming optimality.

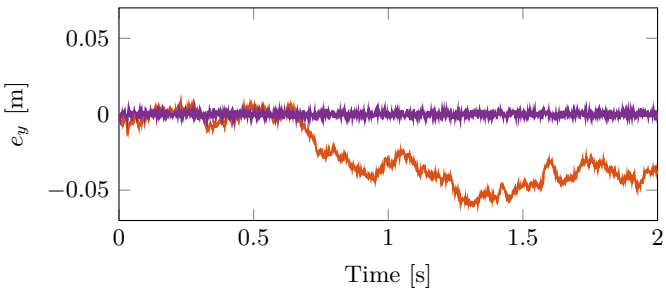

Figure 11.11. The combined feedback and feedforward approach (11.35) (——) achieves high performance, outperforming the feedforward only approach (11.20) (——).

Figure 11.11 shows that (11.35) yields excellent performance in terms of e_y. However, Figure 11.12 shows that the performance in terms of $e_z = r - z$ is poor. The results indicate the importance of proper control architecture design.

The performance is often improved by design of feedforward f_{opt} for z such that it minimizes e_z, see Figure 11.13. However, the design in Figure 11.13 creates a hazardous situation since the feedforward regulates for z, while the feedback regulates for y. Indeed, if the feedforward is optimal and yields $e_z = 0$, then it is counteracted by feedback control since generally $e_y \neq 0$ if $e_z = 0$ and the high performance of feedforward is deteriorated. Instead, feedback and feedforward control should have a common objective.

Both the feedback and feedforward control should be designed for z as shown in Figure 11.14. The combined feedback and feedforward design proposed in Section 11.4 guarantees a common objective for feedback and feedforward. For

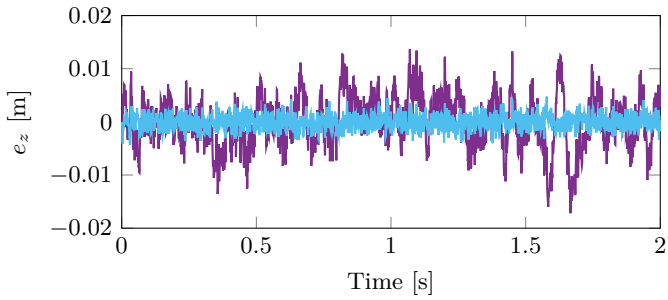

Figure 11.12. The performance in terms of e_z for (11.35) is poor when based on C_y (——), but good when based on C_z (——).

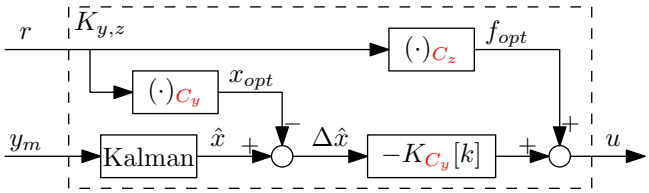

Figure 11.13. Controller implementation in an inferential setting $z \neq y$, where the feedforward is optimized for z and the feedback for y.

$z \neq y$, criterion (11.11) changes to

$$\sum_{k=0}^{N-1} e_z^\top[k]Qe_z[k] + u^\top[k]Ru[k]. \tag{11.37}$$

The optimal solution that minimizes (11.37) directly follows from replacing C_y in Lemma 11.2 with C_z. Note that this indeed affects both feedback and feedforward in (11.35), see also Figure 11.14. Importantly, Lemma 11.3 remains unchanged since it uses measurement y_m and should therefore be based on C_y.

Figure 11.12 shows the results for the combined control approach based on

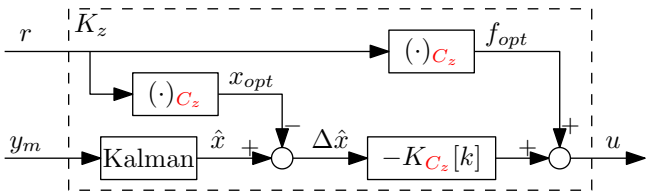

Figure 11.14. Controller implementation in an inferential setting $z \neq y$, where both feedback and feedforward are explicitly designed for z.

criterion (11.37). As a result of the common objective in feedback and feedforward, the explicit design for z outperforms the design for y in terms of e_z.

In summary, a two degrees-of-freedom control architecture is crucial in inferential control, in conjunction with the whitening of the feedback and Kalman filter of Section 11.4.

11.6 Iterative learning control

In this section, the combined design in an ILC setting is analyzed. Whereas inverse model feedforward requires high quality models, ILC can compensate for model mismatches.

The inferential case $z \neq y$ is of particular interest due to the feedback mechanism over trials present in the feedforward update. As pointed out in Bolder and Oomen (2016), the feedback action on y is iteratively compensated by the feedforward update, resulting in counteracting feedback and feedforward action. Similar as for feedforward, both feedback and ILC should be designed on z. The ILC performance objective in terms of $e_{z,j+1}[k]$ reads

$$\begin{aligned}\sum_{k=0}^{N-1} & e_{z,j+1}^{\top}[k] w_e e_{z,j+1}[k] + u_{j+1}^{\top}[k] w_u u_{j+1}[k] \\ & + (u_{j+1}[k] - u_j[k])^{\top} w_{\Delta u} (u_{j+1}[k] - u_j[k]),\end{aligned} \tag{11.38}$$

where j indicates the current trial and $j+1$ the next trial. The solution is a straightforward extension of the results for the feedforward case, see Section 11.4 and Section 11.5.

11.7 Conclusion and outlook

The role of feedforward, learning and feedback is important, especially for inferential control applications. For the regular case $z = y$, the combined feedback and feedforward controller K_y should be designed such that trial-varying disturbances are whitened by feedback. For the inferential case $z \neq y$, a two degrees-of-freedom control architecture is crucial, in conjunction with the whitening of feedback. Norm-optimal ILC automatically provides this solution, but care should be taken, see also Doyle (1978).

In ILC, the rationale is that the system model is approximate, which is compensated through iterations, motivating that alternative frameworks may be essential, see also Doyle (1978). Still, the results are of conceptual interest: (i) $SH = c \in \mathbb{R}$ is a sensible assumption/control goal for disturbance rejection, and (ii) inferential control needs additional attention on controller structures.

Ongoing research focuses on the connection between the various control design approaches for systems that go beyond equidistant sampling, developed in the other chapters, in an inferential control setting.

Chapter 12

Conclusions and recommendations

12.1 Conclusions

The developed resource-aware motion control design framework facilitates to go beyond the performance/cost trade-off present in traditional designs. The framework incorporates feedback control, feedforward control, and learning control design for periodic, non-equidistant sampling schemes. In this section, the main contributions regarding each of these aspects are presented.

12.1.1 Feedback control

Feedback control provides robustness against model uncertainties and unknown disturbances. A loop-shaping control design for linear periodically time-varying (LPTV) systems is presented in Chapter 2, which constitutes Contribution I. The design approach includes stability assessment and performance evaluation based on frequency response function (FRF) measurements and systematic loop-shaping design guidelines similar to well-known guidelines for linear time-invariant (LTI) systems. Experimental validation on a motion system demonstrates the potential of the design approach.

12.1.2 Feedforward control

Feedforward control enables high performance for arbitrary tasks. An important aspect in feedforward control is system inversion. In Chapter 3, an overview and comparison of existing and novel system inversion approaches for nonminimum-phase systems are presented. The approaches are evaluated in view of their

subsequent use, showing inappropriate use that is previously overlooked. This leads to different insights and new approaches for both feedforward and learning control. Extensions to multivariable and time-varying systems are presented as well. The results constitute Contribution II and are extensively used in both feedforward and learning control design approaches.

A variety of feedforward control designs is proposed, which together constitute Contribution III. The system inversion techniques in Chapter 3 enable exact inversion with bounded inputs, even for nonminimum-phase systems, but are mainly restricted to LTI systems. In Chapter 4, exact inversion of nonminimum-phase LPTV systems is presented, which forms Contribution III.A. Despite perfect on-sample tracking, for some systems the approach in Contribution III.A yields poor intersample behavior, especially for non-equidistantly sampled systems. In Chapter 5, a discrete-time inversion approach is proposed that balances the on-sample and intersample performance and constitutes Contribution III.B.

A key observation is that the inversion techniques in Chapter 3 require pre-actuation to enable perfect tracking for nonminimum-phase systems. However, in many applications pre-actuation is absent or undesired. Therefore, the use of pre-actuation is eliminated in Chapter 6, while maintaining perfect tracking. The approach exploits the additional design freedom in overactuated systems and constitutes Contribution III.C.

12.1.3 Learning control

Conventional learning control yields superior performance for exactly repeating tasks. Extending learning control with basis functions enhances the flexibility with respect to task variations. Several learning control approaches, with and without basis functions, are presented, which together constitute Contribution IV.

The performance/cost trade-off can be enhanced by using different sampling frequencies in different control loops to balance the performance and cost over the different control loops. In Chapter 7, optimal learning control design for such multirate systems is presented. The design includes basis functions for enhanced task flexibility and is experimentally validated on an industrial setup of a wafer stage system. The results constitute Contribution IV.A. Multirate systems are a special case of LPTV systems. In Chapter 8, basis functions for general LPTV systems are presented. The approach yields high performance for a variety of tasks and constitutes Contribution IV.B.

Typically, basis functions are selected to be linear in the parameters to enable fast computation of the optimal solution. The performance is, however, limited due to a limited design space. In Chapter 9, rational basis functions are used to increase the design space and thereby enhance the performance. The optimal solution is obtained by solving a sequence of convex optimization problems. This results in high performance and task flexibility at low computational cost and

constitutes Contribution IV.C.

Learning control approaches in which the feedforward signal, rather than the feedforward filter, is learned achieve superior performance for exactly repeating tasks. However, the conventional implementation based on lifted system descriptions is computationally involved, which limits the applicability to large industrial tasks. In Chapter 10, a resource-efficient ILC approach is presented, which significantly reduces the computational load, without affecting performance. The approach enables ILC for large tasks as experimentally demonstrated on an industrial flatbed printing system. The results constitute Contribution IV.D.

Finally, connections between feedforward, learning, and feedback control are presented in Chapter 11. The understanding is essential in inferential control where performance variables cannot be directly measured. A joint design for feedforward, learning, and feedback control is presented, which constitutes Contribution IV.E.

12.2 Recommendations

The presented resource-aware control design framework enhances the performance/cost trade-off in motion systems. The developments have led to new insights and result in the following directions for future research.

12.2.1 Sampling sequence design

Co-design of the controller and the sampling sequence is envisioned to further improve the performance/cost trade-off. In the present framework, the main focus is on the control aspect and often a priori known sampling sequences are considered. However, this is suboptimal in terms of the performance/cost trade-off. For a co-design, a clear understanding of the possibilities and limitations of digital controller implementations is needed, which emphasizes the need to bridge the gap between control design and embedded software.

The main question is how to design the sampling sequence. Relevant aspects include resource availability, performance requirements, uncertainty, and stability. The uncertainty aspect is not only related to uncertain system dynamics, as in the classical robust control theory, but also to uncertainty in sampling times. The latter might require a probabilistic rather than a deterministic approach and also relates to the impact of deadline misses on the performance as considered in, for example, Geelen et al. (2016). The stability aspect is related to closed-loop stability. Note that for feedforward and learning control there is no stability issue and the design may be based on a performance criterion as done in, for example, sparse ILC (Oomen and Rojas, 2017). However, the selection of such a criterion is often nontrivial, especially if fast computations of the solution are required. In feedback control, closed-loop stability is a key aspect and a co-design of the sampling sequence and the controller is challenging, see

also Valencia et al. (2016). In summary, the co-design of the controller and the sampling sequence has potential, but the design is nontrivial and poses many research challenges.

12.2.2 Shared resources

Sharing resources has the potential to enhance the performance/cost trade-off, for example through implementing multiple applications on a single platform. However, it also requires a scheduling policy to allocate resources to the different applications, which necessitates additional control layers. In the present work, often static scheduling policies are considered. From the perspective of resource utilization, other strategies such as dynamic scheduling policies, for example event-triggered or self-triggered policies, may be desired.

12.2.3 Vertical bridges: Connecting different layers of control

Control is present at many abstraction levels. In the present work, the focus is mainly on the low-level motion control design directly connected to the physical actuators and sensors. On top of this low-level control, there is typically a supervisory control layer in which the individual low-level controllers are monitored and where the operation between the controllers is coordinated. This requires a systematic approach to supervisory control design as in, for example, Van der Sanden (2018), in combination with a systematic motion control design approach.

The present work contributes to bridging the gap between the controller design and the embedded software domain. From the perspective of hierarchy, this bridge is in horizontal direction. For an optimal control system design, bridges in vertical direction, e.g., between the low-level control layers and the supervisory layers, are required as well. This allows to raise the abstraction level at which (sub)systems are specified, explored, analyzed, and synthesized. Moreover, it allows for control design and decision making at higher abstraction levels, for example system level, in an early stage of the design process as in Bastos (2018).

Model-based approaches are common across all layers. For the envisioned integrated designs, changes at one of the control layers directly affects other control layers. The evolution of (domain specific) languages or models at one layer requires co-evolution at other layers. Due to the complexity, automated co-evolution of languages and models as in Mengerink (2018) is essential.

12.2.4 Towards Industry 4.0

The amount of data, computational power, and connectivity is constantly increasing in the manufacturing industries. It is often referred to as a new technological revolution called Industry 4.0. It is the fourth major technological disruption after the lean revolution in the 1970s, the outsourcing phenomenon in the 1990s, and the automation in the 2000s. Industry 4.0 includes the developments with respect to cyber-physical systems considered in this research and the internet of things (Pfister, 2011; McEwen and Cassimally, 2013). The internet of things is made up of devices connected to the internet, including temperature sensors, scales, cameras, washing machines, lighting, and smartphones. The result is an abundance of distributed data where resource-aware control design and communication will play a major role. The present framework is envisioned to facilitate optimal control design in conjunction with the sampling communication aspects.

Bibliography

(Ahn et al., 2007) Hyo-Sung Ahn, Kevin L. Moore, and YangQuan Chen. Stability analysis of discrete-time iterative learning control systems with interval uncertainty. *Automatica*, 43(5):892–902, 2007.

(Amann et al., 1996) Notker Amann, David H. Owens, and Eric Rogers. Iterative learning control using optimal feedback and feedforward actions. *International Journal of Control*, 65(2):277–293, 1996.

(Aminifar et al., 2016) Amir Aminifar, Enrico Bini, Petru Eles, and Zebo Peng. Analysis and design of real-time servers for control applications. *Transactions on Computers*, 65(3):834–846, 2016.

(Anderson and Moore, 1989) Brian D. O. Anderson and John B. Moore. *Optimal Control: Linear Quadratic Methods*. Volume 1. Englewood Cliffs, New Jersey: Prentice Hall International, Inc., 1989.

(Anta and Tabuada, 2010) Adolfo Anta and Paulo Tabuada. To Sample or not to Sample: Self-Triggered Control for Nonlinear Systems. *IEEE Transactions on Automatic Control*, 55(9):2030–2042, 2010.

(Antunes and Heemels, 2016) Duarte Antunes and W. P. M. H. Heemels. Frequency-Domain Analysis of Control Loops With Intermittent Data Losses. *IEEE Transactions on Automatic Control*, 61(8):2295–2300, 2016.

(Åström and Hägglund, 1995) Karl J. Åström and Tore Hägglund. *PID Controllers*. 2nd edition. Instrument Society of America, 1995.

(Åström and Wittenmark, 1997) Karl J. Åström and Björn Wittenmark. *Computer Control System Theory and Design*. Third edition. Prentice Hall, 1997.

(Åström et al., 1984) K.J. Åström, P. Hagander, and J. Sternby. Zeros of Sampled Systems. *Automatica*, 20(1):31–38, 1984.

(Athans and Falb, 1966) Michael Athans and Peter L. Falb. *Optimal Control - An Introduction to the Theory and Its Applications*. Mineola, New York: McGraw-Hill Inc., 1966.

(Bamieh et al., 1991) Bassam Bamieh, J. Boyd Pearson, Bruce A. Francis, and Allen Tannenbaum. A lifting technique for linear periodic systems with ap-

plications to sampled-data control. *Systems & Control Letters*, 17(2):79–88, 1991.

(Bamieh and Pearson Jr., 1992) Bassam A. Bamieh and J. Boyd Pearson Jr. A General Framework for Linear Periodic Systems with Applications to H^∞ Sampled-Data Control. *IEEE Transactions on Automatic Control*, 37(4):418–435, 1992.

(Bart et al., 2005) H. Bart, I. Gohberg, M.A. Kaashoek, and A.C.M. Ran. Schur complements and state space realizations. *Linear Algebra and its Applications*, 399:203–224, 2005.

(Bartels and Stewart, 1972) R.H. Bartels and G.W. Stewart. Solution of the Matrix Equation AX + XB = C [F4]. *Communications of the ACM*, 15(9):820–826, 1972.

(Barton et al., 2010) Kira L. Barton, Douglas A. Bristow, and Andrew G. Alleyne. A numerical method for determining monotonicity and convergence rate in iterative learning control. *International Journal of Control*, 83(2):219–226, 2010.

(Bastos, 2018) João Bastos. Modular Specification and Design Exploration for Flexible Manufacturing Systems. Ph.D. thesis, Eindhoven University of Technology, Eindhoven, The Netherlands, 2018.

(Bayard, 1994) David S. Bayard. Extended Horizon Liftings for Stable Inversion of Nonminimum-Phase Systems. *IEEE Transactions on Automatic Control*, 39(6):1333–1338, 1994.

(Benosman et al., 2009) M. Benosman, Fang Fang Liao, Kai-Yew Kai-Yew Lum, and Jian Liang Jian Liang Wang. Nonlinear Control Allocation for Non-Minimum Phase Systems. *IEEE Transactions on Control Systems Technology*, 17(2):394–404, 2009.

(Berger et al., 2015) Thomas Berger, Achim Ilchmann, and Fabian Wirth. Zero Dynamics and Stabilization for Analytic Linear Systems. *Acta Applicandae Mathematicae*, 138(1):17–57, 2015.

(Bittanti and Colaneri, 2009) Sergio Bittanti and Patrizio Colaneri. *Periodic Systems - Filtering and Control*. London, Great Britain: Springer-Verlag, 2009.

(Blanken and Oomen, 2018) Lennart Blanken and Tom Oomen. Multivariable Iterative Learning Control Design Procedures: from Decentralized to Centralized, Illustrated on an Industrial Printer. *Submitted for journal publication* (arXiv: 1806.08550), 2018.

(Blanken et al., 2016a) Lennart Blanken, Sjirk Koekebakker, and Tom Oomen. Design and Modeling Aspects in Multivariable Iterative Learning Control. In *Proceedings of the 55th Conference on Decision and Control*, pages 5502–5507. Las Vegas, Nevada, 2016.

(Blanken et al., 2016b) Lennart Blanken, Jeroen Willems, Sjirk Koekebakker, and Tom Oomen. Design Techniques for Multivariable ILC: Application to an

Industrial Flatbed Printer. *IFAC-PapersOnLine* (7th Symposium on Mechatronic Systems), 49(21):213–221, 2016.

(Blanken et al., 2017a) Lennart Blanken, Frank Boeren, Dennis Bruijnen, and Tom Oomen. Batch-to-Batch Rational Feedforward Control: From Iterative Learning to Identification Approaches, With Application to a Wafer Stage. *IEEE/ASME Transactions on Mechatronics*, 22(2):826–837, 2017.

(Blanken et al., 2017b) Lennart Blanken, Goksan Isil, Sjirk Koekebakker, and Tom Oomen. Flexible ILC: Towards a Convex Approach for Non-Causal Rational Basis Functions. *IFAC-PapersOnLine* (20th World Congress), 50(1):12107–12112, 2017.

(Blanken et al., 2017c) Lennart Blanken, Tim Hazelaar, Sjirk Koekebakker, and Tom Oomen. Multivariable Repetitive Control Design Framework Applied to Flatbed Printing with Continuous Media Flow. In *Proceedings of the 56th Conference on Decision and Control*, pages 4727–4732. Melbourne, Austrialia, 2017.

(Blanken et al., 2018) Lennart Blanken, Goksan Isil, Sjirk Koekebakker, and Tom Oomen. Data-Driven Feedforward Learning using Non-Causal Rational Basis Functions: Application to an Industrial Flatbed Printer. In *Proceedings of the 2018 American Control Conference*, pages 6672–6677. Milwaukee, Wisconsin, 2018.

(Blom and Van den Hof, 2010) Rogier S. Blom and Paul M. J. Van den Hof. Multivariable Frequency Domain Identification Using IV-based Linear Regression. In *Proceedings of the 49th Conference on Decision and Control*, pages 1148–1153. Atlanta, Georgia, 2010.

(Boeren et al., 2014) Frank Boeren, Dennis Bruijnen, Niels van Dijk, and Tom Oomen. Joint input shaping and feedforward for point-to-point motion: Automated tuning for an industrial nanopositioning system. *IFAC Mechatronics*, 24(6):572–581, 2014.

(Boeren et al., 2015) Frank Boeren, Tom Oomen, and Maarten Steinbuch. Iterative motion feedforward tuning: A data-driven approach based on instrumental variable identification. *Control Engineering Practice*, 37:11–19, 2015.

(Boeren et al., 2016) Frank Boeren, Abhishek Bareja, Tom Kok, and Tom Oomen. Frequency-Domain ILC Approach for Repeating and Varying Tasks: With Application to Semiconductor Bonding Equipment. *IEEE/ASME Transactions on Mechatronics*, 21(6):2716–2727, 2016.

(Boeren et al., 2017) Frank Boeren, Dennis Bruijnen, and Tom Oomen. Enhancing feedforward controller tuning via instrumental variables: with application to nanopositioning. *International Journal of Control*, 90(4):746–764, 2017.

(Bohn and Unbehauen, 1998) C. Bohn and H. Unbehauen. Minmax and Least Squares Multivariable Transfer Function Curve Fitting: Error Criteria, Algorithms and Comparisons. In *Proceedings of the 1998 American Control Conference*, pages 3189–3193. Philadelphia, Pennsylvania, 1998.

(Bolder and Oomen, 2015) Joost Bolder and Tom Oomen. Rational Basis Functions in Iterative Learning Control - With Experimental Verification on a Motion System. *IEEE Transactions on Control Systems Technology*, 23(2):722–729, 2015.

(Bolder and Oomen, 2016) Joost Bolder and Tom Oomen. Inferential Iterative Learning Control: A 2D-system approach. *Automatica*, 71:247–253, 2016.

(Bolder et al., 2014) Joost Bolder, Tom Oomen, Sjirk Koekebakker, and Maarten Steinbuch. Using iterative learning control with basis functions to compensate medium deformation in a wide-format inkjet printer. *IFAC Mechatronics*, 24(8):944–953, 2014.

(Bolder et al., 2016) Joost Bolder, Stephan Kleinendorst, and Tom Oomen. Data-driven multivariable ILC: enhanced performance by eliminating L and Q filters. *International Journal of Robust and Nonlinear Control*, 2016. DOI: `10.1002/rnc.3611`.

(Bolder et al., 2017) Joost Bolder, Jurgen van Zundert, Sjirk Koekebakker, and Tom Oomen. Enhancing Flatbed Printer Accuracy and Throughput: Optimal Rational Feedforward Via Iterative Learning Control. *IEEE Transactions on Industrial Electronics*, 64(5):4207–4216, 2017.

(Brinkerhoff and Devasia, 2000) Rob Brinkerhoff and Santosh Devasia. Output Tracking for Actuator Deficient/Redundant Systems: Multiple Piezoactuator Example. *Journal of Guidance, Control, and Dynamics*, 23(2):370–373, 2000.

(Bristow et al., 2006) D.A. Bristow, Marina Tharayil, and A.G. Alleyne. A Survey of Iterative Learning Control. *IEEE Control Systems Magazine*, 26(3):96–114, 2006.

(Bristow and Alleyne, 2008) Douglas A. Bristow and Andrew G. Alleyne. Monotonic Convergence of Iterative Learning Control for Uncertain Systems Using a Time-Varying Filter. *IEEE Transactions on Automatic Control*, 53(2):582–585, 2008.

(Bristow et al., 2010) Douglas A. Bristow, Kira L. Barton, and Andrew G. Alleyne. Iterative Learning Control. In *The Control Systems Handbook: Control System Advanced Methods*. Edited by William S. Levine. Second edition. Chapter 36. CRC Press, 2010.

(Brown and Churchill, 2009) James Ward Brown and Ruel V. Churchill. *Complex Variables and Applications*. Eight edition. New York City, New York: McGraw-Hill, 2009.

(Butler, 2011) Hans Butler. Position Control in Lithographic Equipment: An Enabler for Current-Day Chip Manufacturing. *IEEE Control Systems Magazine*, 31(5):28–47, 2011.

(Butler, 2013) Hans Butler. Adaptive Feedforward for a Wafer Stage in a Lithographic Tool. *IEEE Transactions on Control Systems Technology*, 21(3):875–881, 2013.

(Butterworth et al., 2012) J.A. Butterworth, L.Y. Pao, and D.Y. Abramovitch. Analysis and comparison of three discrete-time feedforward model-inverse

control techniques for nonminimum-phase systems. *IFAC Mechatronics*, 22(5):577–587, 2012.

(Butterworth et al., 2008) Jeffrey A. Butterworth, Lucy Y. Pao, and Daniel Y. Abramovitch. The Effect of Nonminimum-Phase Zero Locations on the Performance of Feedforward Model-Inverse Control Techniques in Discrete-Time Systems. In *Proceedings of the 2008 American Control Conference*, pages 2696–2702. Seattle, Washington, 2008.

(Cantoni and Glover, 1997) M.W. Cantoni and K. Glover. Frequency-Domain Analysis of Linear Periodic Operators with Application to Sampled-Data Control Design. In *Proceedings of the 36th Conference on Decision and Control*, pages 4318–4323. San Diego, California, 1997.

(Chaumette and Hutchinson, 2006) François Chaumette and Seth Hutchinson. Visual Servo Control Part I: Basic Approaches. *Robotics and Automation Magazine*, 13(4):82–90, 2006.

(Chen et al., 2004) Ben M. Chen, Zongli Lin, and Yacov Shamash. *Linear Systems Theory - A Structural Decomposition Approach*. Birkhäuser, 2004, page 415.

(Chen, 1993) Degang Chen. An Iterative Solution to Stable Inversion of Nonminimum Phase Systems. In *Proceedings of the 1993 American Control Conference*, pages 2960–2964. San Francisco, California, 1993.

(Chen, 2016) Mou Chen. Constrained Control Allocation for Overactuated Aircraft Using a Neurodynamic Model. *IEEE Transactions on Systems, Man, and Cybernetics: Systems*, 46(12):1630–1641, 2016.

(Chen and Francis, 1995) Tongwen Chen and Bruce A. Francis. *Optimal Sampled-Data Control Systems*. London, Great Britain: Springer, 1995.

(Chen and Qiu, 1997) Tongwen Chen and Li Qiu. Linear periodically time-varying discrete-time systems: Aliasing and LTI approximations. *Systems & Control Letters*, 30(5):225–235, 1997.

(Chen and Xiao, 2016) Xu Chen and Hui Xiao. Multirate forward-model disturbance observer for feedback regulation beyond Nyquist frequency. *Systems & Control Letters*, 94:181–188, 2016.

(Chu et al., 2016) Bing Chu, David H. Owens, and Christopher T. Freeman. Iterative Learning Control with Predictive Trial Information: Convergence, Robustness, and Experimental Verification. *IEEE Transactions on Control Systems Technology*, 24(3):1101–1108, 2016.

(Clayton et al., 2009) Garrett M. Clayton, Szuchi Tien, Kam K. Leang, Qingze Zou, and Santosh Devasia. A Review of Feedforward Control Approaches in Nanopositioning for High-Speed SPM. *Journal of Dynamic Systems, Measurement, and Control*, 131(6):61101:1–19, 2009.

(Colaneri, 1991) Patrizio Colaneri. Output Stabilization Via Pole Placement of Discrete-Time Linear Periodic Systems. *IEEE Transactions on Automatic Control*, 36(6):739–742, 1991.

(Colaneri and Kučera, 1997) Patrizio Colaneri and Vladimir Kučera. The Model Matching Problem for Periodic Discrete-Time Systems. *IEEE Transactions on Automatic Control*, 42(10):1472–1476, 1997.

(Conway and Horowitz, 2008) Richard Conway and Roberto Horowitz. A Quasi-Newton Algorithm for LQG Controller Design With Variance Constraints. In *Proceedings of the 2008 Dynamic Systems and Control Conference*, pages 1003–1010. Ann Arbor, Michigan, 2008.

(Coppel, 1978) W. A. Coppel. Dichotomies in Stability Theory. In *Lecture Notes in Mathematics*. Volume 629. Springer-Verlag, 1978.

(Desoer and Wang, 1980) Charles A. Desoer and Yung-Terng Wang. On the Generalized Nyquist Stability Criterion. *IEEE Transactions on Automatic Control*, 25(2):187–196, 1980.

(Devasia and Paden, 1994) S. Devasia and B. Paden. Exact Output Tracking for Nonlinear Time-Varying Systems. In *Proceedings of the 33rd Conference on Decision and Control*, pages 2346–2355. Lake Buena Vista, Florida, 1994.

(Devasia and Paden, 1998) S. Devasia and B. Paden. Stable Inversion for Nonlinear Nonminimum-Phase Time-Varying Systems. *IEEE Transactions on Automatic Control*, 43(2):283–288, 1998.

(Devasia, 1997a) Santosh Devasia. Output Tracking with Nonhyperbolic and Near Nonhyperbolic Internal Dynamics: Helicopter Hover Control. In *Proceedings of the 1997 American Control Conference*, pages 1439–1446. Albuquerque, New Mexico, 1997.

(Devasia, 1997b) Santosh Devasia. Output tracking with nonhyperbolic and near nonhyperbolic internal dynamics: Helicopter hover control. *Journal of Guidance, Control, and Dynamics*, 20(3):573–580, 1997.

(Devasia et al., 1996) Santosh Devasia, Degang Chen, and Brad Paden. Nonlinear Inversion-Based Output Tracking. *IEEE Transactions on Automatic Control*, 41(7):930–942, 1996.

(Dijkstra and Bosgra, 2002) B.G. Dijkstra and O.H. Bosgra. Extrapolation of optimal lifted system ILC solution, with application to a waferstage. In *Proceedings of the 2002 American Control Conference*, pages 2595–2600. Anchorage, Alaska, 2002.

(Ding et al., 2006) Jiagen Ding, Federico Marcassa, Shang-Chen Wu, and Masayoshi Tomizuka. Multirate Control for Computation Saving. *IEEE Transactions on Control Systems Technology*, 14(1):165–169, 2006.

(Doyle, 1978) John C. Doyle. Guaranteed Margins for LQG Regulators. *IEEE Transactions on Automatic Control*, 23(4):756–757, 1978.

(Duan and Okwudire, 2018) Molong Duan and Chinedum E. Okwudire. Proxy-Based Optimal Control Allocation for Dual-Input Over-Actuated Systems. *IEEE/ASME Transactions on Mechatronics*, 23(2):895–905, 2018.

(Eckhard et al., 2012) Diego Eckhard, Alexandre S. Bazanella, Cristian R. Rojas, and Håkan Hjalmarsson. On the convergence of the Prediction Error Method

to its global minimum. In *Proceedings of the 16th Symposium on System Identification*, pages 698–703. Brussels, Belgium, 2012.

(Egerton, 2016) R.F. Egerton. *Physical Principles of Electron Microscopy*. Second edition. Springer, 2016.

(Evers et al., 2017) Enzo Evers, Marc van de Wal, and Tom Oomen. Synchronizing Decentralized Control Loops for Overall Performance Enhancement: A Youla Framework Applied to a Wafer Scanner. *IFAC-PapersOnLine* (20th World Congress), 50(1):10845–10850, 2017.

(Evers et al., 2018) Enzo Evers, Bram de Jager, and Tom Oomen. Improved Local Rational Method by Incorporating System Knowledge: With Application to Mechanical and Thermal Dynamical Systems. In *Proceedings of the 18th Symposium on System Identification*. Stockholm, Sweden, 2018.

(Fallows, 2013) James Fallows. The 50 greatest breakthroughs since the wheel. *The Atlantic*, (November), 2013.

(Felici and Oomen, 2015) Federico Felici and Tom Oomen. Enhancing current density profile control in tokamak experiments using iterative learning control. In *Proceedings of the 54th Conference on Decision and Control*, pages 5370–5377. Osaka, Japan, 2015.

(Fossen and Johansen, 2006) Thor I. Fossen and Tor A. Johansen. A Survey of Control Allocation Methods for Ships and Underwater Vehicles. In *Proceedings of the 14th Mediterranean Conference on Control and Automation*, pages 1–6. Ancona, Italy, 2006.

(Franklin et al., 2015) Gene F. Franklin, J. David Powell, and Abbas Emami-Naeini. *Feedback Control of Dynamic Systems*. Seventh edition. Upper Saddle River, New Jersey: Pearson, 2015.

(Fraser et al., 1999) S. Fraser, M.H. Attia, and M.O.M. Osman. Modelling, Identification and Control of Thermal Deformation of Machine Tool Structures, Part 1: Concept of Generalized Modelling. *Journal of Manufacturing Science and Engineering*, 120(3):623–631, 1999.

(Fujimoto and Hori, 2002) Hiroshi Fujimoto and Yoichi Hori. High-performance servo systems based on multirate sampling control. *Control Engineering Practice*, 10(7):773–781, 2002.

(Fujimoto et al., 2001) Hiroshi Fujimoto, Yoichi Hori, and Atsuo Kawamura. Perfect Tracking Control Based on Multirate Feedforward Control with Generalized Sampling Periods. *IEEE Transactions on Industrial Electronics*, 48(3):636–644, 2001.

(Gao and Mishra, 2014) Xuemei Gao and Sandipan Mishra. An Iterative Learning Control Algorithm for Portability Between Trajectories. In *Proceedings of the 2014 American Control Conference*, pages 3808–3813. Portland, Oregon, 2014.

(Geelen et al., 2016) W. Geelen, D. Antunes, J. P. M. Voeten, R. R. H. Schiffelers, and W. P. M. H. Heemels. The Impact of Deadline Misses on the Control

Performance of High-End Motion Control Systems. *IEEE Transactions on Industrial Electronics*, 63(2):1218–1229, 2016.

(Geerardyn and Oomen, 2017) Egon Geerardyn and Tom Oomen. A local rational model approach for $\mathcal{H}_\infty$ norm estimation: With application to an active vibration isolation system. *Control Engineering Practice*, 68:63–70, 2017.

(De Gelder et al., 2006) Edgar de Gelder, Marc van de Wal, Carsten Scherer, Camile Hol, and Okko Bosgra. Nominal and Robust Feedforward Design With Time Domain Constraints Applied to a Wafer Stage. *Journal of Dynamic Systems, Measurement, and Control*, 128(2):204–215, 2006.

(Ghosh and Paden, 2002) Jayati Ghosh and Brad Paden. A Pseudoinverse-Based Iterative Learning Control. *IEEE Transactions on Automatic Control*, 47(5):831–837, 2002.

(Gilson et al., 2011) M. Gilson, H. Garnier, P.C. Young, and P.M.J. Van den Hof. Optimal instrumental variable method for closed-loop identification. *Control Theory & Applications*, 5(10):1147–1154, 2011.

(Glasson, 1983) Douglas P. Glasson. Development and applications of multirate digital control. *IEEE Control Systems Magazine*, 3(4):2–8, 1983.

(Goldsmith, 2002) Peter B. Goldsmith. On the equivalence of causal LTI iterative learning control and feedback control. *Automatica*, 38(4):703–708, 2002.

(Goodwin et al., 2000) Graham C. Goodwin, Stefan F. Graebe, and Mario E. Salgado. *Control System Design*. Upper Saddle River, New Jersey, 2000.

(Goossens et al., 2017) Kees Goossens, Martijn Koedam, Andrew Nelson, Shubhendu Sinha, Sven Goossens, Yonghui Li, Gabriela Breaban, Reinier van Kampenhout, Rasool Tavakoli, Juan Valencia, Hadi Ahmadi Balef, Benny Akesson, Sander Stuijk, Marc Geilen, Dip Goswami, and Majid Nabi. NoC-Based Multiprocessor Architecture for Mixed-Time-Criticality Applications. In *Handbook of Hardware/Software Codesign*. Edited by Soonhoi Ha and Jürgen Teich. Dordrecht: Springer, 2017.

(Gorinevsky, 2002) Dimitry Gorinevsky. Loop Shaping for Iterative Control of Batch Processes. *IEEE Control Systems Magazine*, 22(6):55–65, 2002.

(Grasselli and Longhi, 1991) Osvaldo Maria Grasselli and Sauro Longhi. Robust tracking and regulation of linear periodic discrete-time systems. *International Journal of Control*, 54(3):613–633, 1991.

(Groot Wassink et al., 2005) Matthijs Groot Wassink, Marc van de Wal, Carsten Scherer, and Okko Bosgra. LPV control for a wafer stage: beyond the theoretical solution. *Control Engineering Practice*, 13(2):231–245, 2005.

(Gross et al., 1994) Eric Gross, Masayoshi Tomizuka, and William Messner. Cancellation of Discrete Time Unstable Zeros by Feedforward Control. *Journal of Dynamic Systems, Measurement, and Control*, 116(1):33–38, 1994.

(Gunnarsson and Norrlöf, 2001) Svante Gunnarsson and Mikael Norrlöf. On the design of ILC algorithms using optimization. *Automatica*, 37(12):2011–2016, 2001.

(Haber et al., 2012) Aleksandar Haber, Rufus Fraanje, and Michel Verhaegen. Linear computational complexity robust ILC for lifted systems. *Automatica*, 48(6):1102–1110, 2012.

(Halanay and Ionescu, 1994) Aristide Halanay and Vlad Ionescu. *Time-Varying Discrete Linear Systems: Input-Output Operators. Riccati Equations. Disturbance Attenuation*. Volume 68. Birkhäuser, 1994.

(Hall, 1996) Eldon C. Hall. *Journey to the Moon: The History of the Apollo Guidance Computer*. Reston, Virginia: American Institute of Aeronautics and Astronautics, 1996.

(Hara et al., 2008) Atsushi Hara, Kauaki Saiki, Koichi Sakata, and Hiroshi Fujimoto. Basic Examination on Simultaneous Optimization of Mechanism and Control for High Precision Single Axis Stage and Experimental Verification. In *Proceedings of the 34th Annual Conference of Industrial Electronics*, pages 2509–2514. Orlando, Florida, 2008.

(Hara et al., 1988) Shinji Hara, Yutaka Yamamoto, Tohru Omata, and Michio Nakano. Repetitive control system: A new type servo system for periodic exogenous signals. *IEEE Transactions on Automatic Control*, 33(7):659–668, 1988.

(Hätönen et al., 2006) J. Hätönen, D.H. Owens, and K. Feng. Basis functions and parameter optimisation in high-order iterative learning control. *Automatica*, 42(2):287–294, 2006.

(Hazell and Limebeer, 2008) Andrew Hazell and David J.N. Limebeer. An efficient algorithm for discrete-time H_∞ preview control. *Automatica*, 44(9):2441–2448, 2008.

(Heemels et al., 2008) W. P. M. H. Heemels, J. H. Sandee, and P. P. J. van den Bosch. Analysis of event-driven controllers for linear systems. *International Journal of Control*, 81(4):571–590, 2008.

(Heemels et al., 2012) W.P.M.H. Heemels, K.H. Johansson, and P. Tabuada. An Introduction to Event-triggered and Self-triggered Control. In *Proceedings of the 51st Conference on Decision and Control*, pages 3270–3285. Maui, Hawaii, 2012.

(Heertjes and Van de Molengraft, 2009) Marcel F. Heertjes and René M.J.G. van de Molengraft. Set-point variation in learning schemes with applications to wafer scanners. *Control Engineering Practice*, 17(3):345–356, 2009.

(Heertjes et al., 2016) Marcel F. Heertjes, Bart van der Velden, and Tom Oomen. Constrained Iterative Feedback Tuning for Robust Control of a Wafer Stage System. *IEEE Transactions on Control Systems Technology*, 24(1):56–66, 2016.

(Hernández and Urbano, 1989) Vicente Hernández and Ana M. Urbano. Pole-placement problem for discrete-time linear periodic systems. *International Journal of Control*, 50(1):361–371, 1989.

(Van Herpen et al., 2013) Robbert van Herpen, Tom Oomen, and Maarten Steinbuch. Optimally Conditioned Instrumental Variable Approach for Frequency-Domain System Identification. *Automatica*, 50(9):2281–2293, 2013.

(Van Herpen et al., 2014) Robbert van Herpen, Tom Oomen, Edward Kikken, Marc van de Wal, Wouter Aangenent, and Maarten Steinbuch. Exploiting additional actuators and sensors for nano-positioning robust motion control. *IFAC Mechatronics*, 24(6):619–631, 2014.

(Heuberger et al., 2005) Peter S. C. Heuberger, Paul M. J. Van den Hof, and Bo Wahlberg. *Modelling and Identification with Rational Orthogonal Basis Functions*. Springer, 2005.

(Hill and Ilchmann, 2011) Adrian T. Hill and Achim Ilchmann. Exponential stability of time-varying linear systems. *IMA Journal of Numerical Analysis*, 31(3):865–885, 2011.

(Hirschorn, 1979) Ronald M. Hirschorn. Invertibility of multivariable nonlinear control systems. *IEEE Transactions on Automatic Control*, 24(6):855–865, 1979.

(Hoelzle et al., 2011) David J. Hoelzle, Andrew G. Alleyne, and Amy J. Wagoner Johnson. Basis Task Approach to Iterative Learning Control With Applications to Micro-Robotic Deposition. *IEEE Transactions on Control Systems Technology*, 19(5):1138–1148, 2011.

(Hunt et al., 1996) L.R. Hunt, G. Meyer, and R. Su. Noncausal Inverses for Linear Systems. *IEEE Transactions on Automatic Control*, 41(4):608–611, 1996.

(Jetto et al., 2014) Leopoldo Jetto, Valentina Orsini, and Raffaele Romagnoli. Accurate output tracking for nonminimum phase nonhyperbolic and near nonhyperbolic systems. *European Journal of Control*, 20(6):292–300, 2014.

(Jetto et al., 2015) Leopoldo Jetto, Valentina Orsini, and Raffaele Romagnoli. A mixed numerical-analytical stable pseudo-inversion method aimed at attaining an almost exact tracking. *International Journal of Robust and Nonlinear Control*, 25(6):809–823, 2015.

(Johansen and Fossen, 2013) Tor A. Johansen and Thor I. Fossen. Control allocation - A survey. *Automatica*, 49(5):1087–1103, 2013.

(Kalender and Flashner, 2008) S. Kalender and H. Flashner. Discrete-Time Control of Linear Time-Periodic Systems. *Journal of Dynamic Systems, Measurement, and Control*, 130(4):41009:1–9, 2008.

(Kang, 2016) Chul-Goo Kang. Origin of Stability Analysis: “On Governors” by J.C. Maxwell. *IEEE Control Systems Magazine*, 36(5):77–88, 2016.

(Kasemsinsup et al., 2016) Yanin Kasemsinsup, Marcel Heertjes, Hans Butler, and Siep Weiland. Exact plant inversion of flexible motion systems with a time-varying state-to-output map. In *Proceedings of the 2016 European Control Conference*, pages 2483–2488. Aalborg, Denmark, 2016.

(Khaitan and McCalley, 2015) Siddhartha Kumar Khaitan and James D. McCalley. Design Techniques and Applications of Cyberphysical Systems: A Survey. *Systems Journal*, 9(2):350–365, 2015.

(Kim and Zou, 2008) Kyong-Soo Kim and Qingze Zou. Model-less Inversion-based Iterative Control for Output Tracking: Piezo Actuator Example. In *Proceedings of the 2008 American Control Conference*, pages 2710–2715. Seattle, Washington, 2008.

(Kim and Zou, 2013) Kyong-Soo Kim and Qingze Zou. A Modeling-Free Inversion-Based Iterative Feedforward Control for Precision Output Tracking of Linear Time-Invariant Systems. *IEEE/ASME Transactions on Mechatronics*, 18(6):1767–1777, 2013.

(Knobel et al., 2006) Christian Knobel, Alfred Pruckner, and Tilman Bünte. Optimized Force Allocation: A General Approach to Control and to Investigate the Motion of Over-Actuated Vehicles. *IFAC Proceedings Volumes* (4th Symposium on Mechatronic Systems), 39(16):366–371, 2006.

(Kolman and Hill, 2008) Bernard Kolman and David R. Hill. *Elementary Linear Algebra with Applications*. Ninth edition. Upper Saddle River, New Jersey: Pearson Prentice Hall, 2008.

(Kono, 1980) Michio Kono. Eigenvalue assignment in linear periodic discrete-time systems. *International Journal of Control*, 32(1):149–158, 1980.

(Kurzweil, 2005) Ray Kurzweil. *The Singularity is Near: When Humans Transcend Biology*. New York City, New York: Viking, 2005.

(Lall and Dullerud, 2001) Sanjay Lall and Geir Dullerud. An LMI solution to the robust synthesis problem for multi-rate sampled-data systems. *Automatica*, 37(12):1909–1922, 2001.

(Lambrechts et al., 2005) Paul Lambrechts, Matthijs Boerlage, and Maarten Steinbuch. Trajectory planning and feedforward design for electromechanical motion systems. *Control Engineering Practice*, 13(2):145–157, 2005.

(Lee, 2015) Edward A. Lee. The past, present and future of cyber-physical systems: A focus on models. *Sensors*, 15(3):4837–4869, 2015.

(Lee, 2006) Seung-Hi Lee. Multirate Digital Control System Design and its Application to Computer Disk Drives. *IEEE Transactions on Control Systems Technology*, 14(1):124–133, 2006.

(Lewis and Syrmos, 1995) Frank L. Lewis and Vassilis L. Syrmos. *Optimal Control*. Second edition. New York City, New York: John Wiley & Sons, Inc., 1995.

(Li et al., 2016) Xuefang Li, Deqing Huang, Bing Chu, and Jian-Xin Xu. Modeling Interference Via Symmetric Treatment Decomposition. *International Journal of Robust and Nonlinear Control*, 26(4):697–718, 2016.

(Lindgärde and Lennartson, 1997) Olof Lindgärde and Bengt Lennartson. Performance and Robust Frequency Response for Multirate Sample-Data Systems. In *Proceedings of the 1997 American Control Conference*, pages 3877–3881. Albuquerque, New Mexico, 1997.

(Longman, 2010) Richard W. Longman. On the Theory and Design of Linear Repetitive Control Systems. *European Journal of Control*, 16(5):447–496, 2010.

(Ma et al., 2012) J. Ma, Z. Zheng, and D. Hu. Modular robust reconfigurable flight control system design for an overactuated aircraft. *IET Control Theory & Applications*, 6(11):1620–1632, 2012.

(MacFarlane and Karcanias, 1976) A. G. J. MacFarlane and N. Karcanias. Poles and zeros of linear multivariable systems: A survey of the algebraic, geometric and complex-variable theory. *International Journal of Control*, 24(1):33–74, 1976.

(Mack, 2007) Chris Mack. *Fundamental Principles of Optical Lithography*. West Sussex, United Kingdom: John Wiley & Sons, 2007.

(Marro et al., 2002) Giovanni Marro, Domenico Prattichizzo, and Elena Zattoni. Convolution profiles for right inversion of multivariable non-minimum phase discrete-time systems. *Automatica*, 38(10):1695–1703, 2002.

(McEwen and Cassimally, 2013) Adrian McEwen and Hakim Cassimally. *Designing the Internet of Things*. West Sussex, United Kingdom: John Wiley & Sons, Ltd., 2013.

(McFarlane and Glover, 1990) D.C. McFarlane and K. Glover. Robust Controller Design Using Normalized Coprime Factor Plant Descriptions. In *Lecture Notes in Control and Information Sciences*. Edited by M. Thoma and A. Wyner. Chapter 138. Springer, 1990.

(Mengerink, 2018) Josh Mengerink. The DSL/Model Co-Evolution Problem in Industrial MDSE Ecosystems. Ph.D. thesis, Eindhoven University of Technology, Eindhoven, The Netherlands, 2018.

(Van der Meulen et al., 2008) Stan H. van der Meulen, Rob L. Tousain, and Okko H. Bosgra. Fixed Structure Feedforward Controller Design Exploiting Iterative Trials: Application to a Wafer Stage and a Desktop Printer. *Journal of Dynamic Systems, Measurement, and Control*, 130(5):051006:1–16, 2008.

(Middleton et al., 2004) R.H. Middleton, J.C. Chen, and J.S. Freudenberg. Tracking sensitivity and achievable H_∞ performance in preview control. *Automatica*, 40(8):1297–1306, 2004.

(Mirkin, 2003) Leonid Mirkin. On the H_∞ fixed-lag smoothing: how to exploit the information preview. *Automatica*, 39(8):1495–1504, 2003.

(Mishra et al., 2007) Sandipan Mishra, Joshua Coaplen, and Masayoshi Tomizuka. Precision positioning of wafer scanners: Segmented iterative learning control for nonrepetitive disturbances. *IEEE Control Systems Magazine*, 27(4):20–25, 2007.

(Moore, 1965) Gordon E. Moore. Cramming more components onto integrated circuits. *Electronics*, 38(8):114–117, 1965.

(Moore, 1975) Gordon E. Moore. Progress In Digital Integrated Electronics. *IEDM Technical Digest*:11–13, 1975.

(Moore, 1993) Kevin L. Moore. *Iterative Learning Control for Deterministic Systems*. Springer-Verlag, 1993.

(Moore et al., 1993) Kevin L. Moore, S.P. Bhattacharyya, and Mohammed Dahleh. Capabilities and Limitations of Multirate Control Schemes. *Automatica*, 29(4):941–951, 1993.

(Moylan, 1977) P.J. Moylan. Stable Inversion of Linear Systems. *IEEE Transactions on Automatic Control*, 22(1):74–78, 1977.

(Munnig Schmidt et al., 2011) Robert Munnig Schmidt, George Schitter, and Jan van Eijk. *The Design of High Performance Mechatronics*. Amsterdam, The Netherlands: Delft University Press, 2011.

(Murray et al., 2003) Richard M. Murray, Karl J. Åström, Stephan P. Boyd, Roger W. Brockett, and Gunter Stein. Future directions in control in an information-rich world. *IEEE Control Systems Magazine*, 23(2):20–33, 2003.

(Naidu, 2003) Desineni Subbaram Naidu. *Optimal Control Systems*. Boca Raton, Florida: CRC Press, 2003.

(Nie et al., 2013) Jianbin Nie, Richard Conway, and Roberto Horowitz. Optimal H_∞ Control for Linear Periodically Time-Varying Systems in Hard Disk Drives. *IEEE/ASME Transactions on Mechatronics*, 18(1):212–220, 2013.

(Norrlöf and Gunnarsson, 2002) Mikael Norrlöf and Svante Gunnarsson. Time and frequency domain convergence properties in iterative learning control. *International Journal of Control*, 75(14):1114–1126, 2002.

(Oh et al., 1997) Sang J. Oh, Minh Q. Phan, and Richard W. Longman. Use of Decoupling Basis Functions in Learning Control for Local Learning and Improved Transients. *Advances in the Astronautical Sciences*, 95(2):651–670, 1997.

(Ohnishi and Fujimoto, 2016a) Wataru Ohnishi and Hiroshi Fujimoto. Multirate feedforward control with state trajectory generation based on time axis reversal for plant with continuous time unstable zeros. In *International Conference on Advanced Intelligent Mechatronics*, pages 689–694. Banff, Canada, 2016.

(Ohnishi and Fujimoto, 2016b) Wataru Ohnishi and Hiroshi Fujimoto. Tracking control method for a plant with continuous time unstable zeros: Finite preactuation based on state trajectory regeneration by using redundant order polynomial. In *Proceedings of the 55th Conference on Decision and Control*, pages 4015–4020. Las Vegas, Nevada, 2016.

(Ohnishi and Fujimoto, 2018) Wataru Ohnishi and Hiroshi Fujimoto. Review on multirate feedforward: model-inverse feedforward control for nonminumum phase systems. In *Proceedings of the 4th International Workshop on Sensing, Actuation, Motion Control, and Optimization*, IS1–5. Tokyo, Japan, 2018.

(Ohnishi et al., 2017) Wataru Ohnishi, Thomas Beauduin, and Hiroshi Fujimoto. Preactuated multirate feedforward for a high-precision stage with continuous time unstable zeros. *IFAC-PapersOnLine* (20th World Congress), 50(1):10907–10912, 2017.

(Oomen et al., 2007) T. Oomen, M. van de Wal, and O. Bosgra. Design framework for high-performance optimal sampled-data control with application to a wafer stage. *International Journal of Control*, 80(6):919–934, 2007.

(Oomen, 2018) Tom Oomen. Advanced Motion Control for Precision Mechatronics: Control, Identification, and Learning of Complex Systems. *Journal of Industry Applications*, 137, 2018.

(Oomen and Rojas, 2017) Tom Oomen and Cristian R. Rojas. Sparse iterative learning control with application to a wafer stage: Achieving performance, resource efficiency, and task flexibility. *IFAC Mechatronics*, 47:134–147, 2017.

(Oomen et al., 2005) Tom Oomen, Marc van de Wal, Okko Bosgra, and Maarten Steinbuch. Optimal digital control of analog systems: A survey. In *Proceedings of the 8th Philips Conference on Applications of Control Technology*, pages 139–144. Hilvarenbeek, The Netherlands, 2005.

(Oomen et al., 2009) Tom Oomen, Jeroen van de Wijdeven, and Okko Bosgra. Suppressing intersample behavior in iterative learning control. *Automatica*, 45(4):981–988, 2009.

(Oomen et al., 2011) Tom Oomen, Jeroen van de Wijdeven, and Okko H. Bosgra. System Identification and Low-Order Optimal Control of Intersample Behavior in ILC. *IEEE Transactions on Automatic Control*, 56(11):2734–2739, 2011.

(Oomen et al., 2014) Tom Oomen, Robbert van Herpen, Sander Quist, Marc van de Wal, Okko Bosgra, and Maarten Steinbuch. Connecting System Identification and Robust Control for Next-Generation Motion Control of a Wafer Stage. *IEEE Transactions on Control Systems Technology*, 22(1):102–118, 2014.

(Oomen et al., 2015) Tom Oomen, Erik Grassens, and Ferdinand Hendriks. Inferential Motion Control: Identification and Robust Control Framework for Positioning an Unmeasurable Point of Interest. *IEEE Transactions on Control Systems Technology*, 23(4):1602–1610, 2015.

(Oppenheim et al., 1997) Alan V. Oppenheim, Alan S. Willsky, and S. Hamid Nawab. *Signals and Systems*. Second edition. Prentice-Hall, Inc., 1997.

(O'Reilly, 1983) J. O'Reilly. *Observers for Linear Systems*. London, Great Britain: Academic Press, 1983.

(Owens and Chu, 2009) David H. Owens and Bing Chu. Modelling of nonminimum phase effects in discrete-time norm optimal iterative learning control. *International Journal of Control*, 83(10):2012–2027, 2009.

(Owens et al., 2013) David H. Owens, Chris T. Freeman, and Bing Chu. Multivariable norm optimal iterative learning control with auxiliary optimisation. *International Journal of Control*, 86(6):1026–1045, 2013.

(Owens et al., 2014) David H. Owens, Bing Chu, Eric Rogers, Chris T. Freeman, and Paul L. Lewin. Influence of Nonminimum Phase Zeros on the Performance of Optimal Continuous-Time Iterative Learning Control. *IEEE Transactions on Control Systems Technology*, 22(3):1151–1158, 2014.

(Papaschinopoulos, 1986) Garyfalos Papaschinopoulos. Exponential Separation, Exponential Dichotomy, and Almost Periodicity of Linear Difference Equations. *Journal of Mathematical Analysis and Applications*, 120(1):276–287, 1986.

(Pavlov and Pettersen, 2008) Alexey Pavlov and Kristin Y. Pettersen. A new perspective on stable inversion of non-minimum phase nonlinear systems. *Modeling, Identification and Control*, 29(1):29–35, 2008.

(Pfister, 2011) Cuno Pfister. *Getting Started with the Internet of Things: Connecting Sensors and Microcontrollers to the Cloud*. Sebastopol, California: O'Reilly Media Inc., 2011.

(Phan and Frueh, 1996) Minh Q. Phan and James A. Frueh. Learning Control for Trajectory Tracking using Basis Functions. In *Proceedings of the 35th Conference on Decision and Control*, pages 2490–2492. Kobe, Japan, 1996.

(Pintelon and Schoukens, 2012) Rik Pintelon and Johan Schoukens. *System Identification*. Second edition. Hoboken, New Jersey: John Wiley & Sons, Inc., 2012.

(Pond, 2000) Stephen F. Pond. *Inkjet Technology and Product Development Strategies*. Torrey Pines Research, 2000.

(Ravi et al., 1991) R. Ravi, K. Nagpal, and P. Khargonekar. H^∞ Control of Linear Time-Varying Systems: A State-Space Approach. *Journal on Control and Optimization*, 29(6):1394–1413, 1991.

(Rice and Van Wingerden, 2013) Justin K. Rice and Jan-Willem van Wingerden. Fast calculation of the 'ILC norm' in iterative learning control. *International Journal of Control*, 86(6):1186–1190, 2013.

(Riggs and Bitmead, 2013) Daniel J. Riggs and Robert R. Bitmead. Rejection of Aliased Disturbances in a Production Pulsed Light Source. *IEEE Transactions on Control Systems Technology*, 21(2):480–488, 2013.

(Rios et al., 2018) Shannon A. Rios, Andrew J. Fleming, and Yuen Kuan Yong. Monolithic Piezoelectric Insect With Resonance Walking. *IEEE/ASME Transactions on Mechatronics*, 23(2):524–530, 2018.

(Rogers et al., 2007) Eric Rogers, Krzysztof Galkowski, and David H. Owens. *Control Systems Theory and Applications for Linear Repetitive Processes*. Volume 349. Springer, 2007.

(Ronde et al., 2012) Michael Ronde, René van de Molengraft, and Maarten Steinbuch. Model-based feedforward for inferential motion systems, with application to a prototype lightweight motion system. In *Proceedings of the 2012 American Control Conference*, pages 5324–5329. 2012.

(De Roover and Bosgra, 2000) Dick de Roover and Okko H. Bosgra. Synthesis of robust multivariable iterative learning controllers with application to a wafer stage motion system. *International Journal of Control*, 73(10):968–979, 2000.

(Rosenbrock, 1970) H. H. Rosenbrock. *State-space and Multivariable Theory*. London, Great Britain: Nelson, 1970.

(Routledge, 1881) Robert Routledge. *Discoveries & Inventions of the Nineteenth Century*. Fifth edition. London, Great Britain: George Routledge and Sons, 1881.

(De Rozario and Oomen, 2018a) Robin de Rozario and Tom Oomen. Frequency Response Function Identification of LPV Systems: A Global Approach with Application to Mechanical Systems. In *Proceedings of the 18th Symposium on System Identification*. Stockholm, Sweden, 2018.

(De Rozario and Oomen, 2018b) Robin de Rozario and Tom Oomen. Improving Transient Learning Behavior in Model-Free Inversion-Based Iterative Control with Application to a Desktop Printer. In *Proceedings of the 15th International Workshop on Advanced Motion Control*, pages 455–460. Tokyo, Japan, 2018.

(De Rozario et al., 2017) Robin de Rozario, Tom Oomen, and Maarten Steinbuch. Iterative Learning Control and Feedforward for LPV Systems: Applied to a Position-Dependent Motion System. In *Proceedings of the 2017 American Control Conference*, pages 3518–3523. Seattle, Washington, 2017.

(Saab, 2005) Samer S. Saab. Selection of the Learning Gain Matrix of an Iterative Learning Control Algorithm in Presence of Measurement Noise. *IEEE Transactions on Automatic Control*, 50(11):1761–1774, 2005.

(Saberi and Sannuti, 1990) A. Saberi and P. Sannuti. Squaring down of non-strictly proper systems. *International Journal of Control*, 51(3):621–629, 1990.

(Saberi and Sannuti, 1988) Ali Saberi and Peddapullaiah Sannuti. Squaring Down by Static and Dynamic Compensators. *IEEE Transactions on Automatic Control*, 33(4):358–365, 1988.

(Salt and Albertos, 2005) Julián Salt and Pedro Albertos. Model-Based Multirate Controllers Design. *IEEE Transactions on Control Systems Technology*, 13(6):988–997, 2005.

(Salt and Tomizuka, 2014) Julián Salt and Masayoshi Tomizuka. Hard disk drive control by model based dual-rate controller. Computation saving by interlacing. *IFAC Mechatronics*, 24(6):691–700, 2014.

(Sandberg et al., 2005) Henrik Sandberg, Erik Möllerstedt, and Bo Bernhardsson. Frequency-Domain Analysis of Linear Time-Periodic Systems. *IEEE Transactions on Automatic Control*, 50(12):1971–1983, 2005.

(Van der Sanden, 2018) Bram van der Sanden. Performance Analysis and Optimization for Supervisory Controllers. PhD thesis, Eindhoven University of Technology, Eindhoven, The Netherlands, 2018.

(Sannuti and Saberi, 1987) P. Sannuti and A. Saberi. Special coordinate basis for multivariable linear systems - finite and infinite zero structure, squaring down and decoupling. *International Journal of Control*, 45(5):1655–1704, 1987.

(Santamaria-Navarro et al., 2017) Angel Santamaria-Navarro, Patrick Grosch, Vincenzo Lippiello, Joan Solà, and Juan Andrade-Cetto. Uncalibrated Vi-

sual Servo for Unmanned Aerial Manipulation. *IEEE/ASME Transactions on Mechatronics*, 22(4):1610–1621, 2017.

(Sato, 2008) Masayuki Sato. Inverse system design for LPV systems using parameter-dependent Lyapunov functions. *Automatica*, 44(4):1072–1077, 2008.

(Seron et al., 1997) María M. Seron, Julio H. Braslavsky, and Graham C. Goodwin. *Fundamental Limitations in Filtering and Control*. Springer-Verlag, 1997.

(Shahsavari et al., 2013) Behrooz Shahsavari, Richard Conway, Ehsan Keikha, Fu Zhang, and Roberto Horowitz. H_∞ Control Design for Systems With Periodic Irregular Sampling Using Optimal H_2 Reference Controllers. In *Proceedings of the 2013 Conference on Information Storage and Processing Systems*, V001T03A008. Santa Clara, California, 2013.

(Sharma et al., 2013) Girish Sharma, Abhishek Agarwala, and Baidurya Bhattacharya. A fast parallel Gauss Jordan algorithm for matrix inversion using CUDA. *Computers and Structures*, 128:31–37, 2013.

(Silverman, 1969) Leonard M. Silverman. Inversion of Multivariable Linear Systems. *IEEE Transactions on Automatic Control*, 14(3):270–276, 1969.

(Sinha and Joseph, 1994) S. C. Sinha and P. Joseph. Control of General Dynamic Systems With Periodically Varying Parameters Via Liapunov-Floquet Transformation. *Journal of Dynamic Systems, Measurement, and Control*, 116(4):650–658, 1994.

(Skogestad and Postlethwaite, 2005) Sigurd Skogestad and Ian Postlethwaite. *Multivariable Feedback Control: Analysis and Design*. Second edition. West Sussex, United Kingdom: John Wiley & Sons, Ltd., 2005.

(Sogo, 2010) Takuya Sogo. On the equivalence between stable inversion for nonminimum phase systems and reciprocal transfer functions defined by the two-sided Laplace transform. *Automatica*, 46(1):122–126, 2010.

(Steiglitz and McBride, 1965) K. Steiglitz and L. E. McBride. A Technique for the Identification of Linear Systems. *IEEE Transactions on Automatic Control*, 10(4):461–464, 1965.

(Steinbuch, 2002) Maarten Steinbuch. Repetitive control for systems with uncertain period-time. *Automatica*, 38(12):2103–2109, 2002.

(Steinbuch and Van de Molengraft, 2000) Maarten Steinbuch and René van de Molengraft. Iterative Learning Control of Industrial Motion Systems. *IFAC Proceedings Volumes* (Conference on Mechatronic Systems), 33(26):899–904, 2000.

(Steinbuch et al., 2010) Maarten Steinbuch, Roel J. E. Merry, Matthijs L. G. Boerlage, Michael J. C. Ronde, and Marinus J. G. van de Molengraft. Advanced Motion Control Design. In *The Control Handbook: Control System Applications*. Edited by William S. Levine. Second edition. Chapter 27. CRC Press, 2010.

(Stoev et al., 2017) Julian Stoev, Julien Ertveldt, Tom Oomen, and Johan Schoukens. Tensor methods for MIMO decoupling and control design using frequency response functions. *IFAC Mechatronics*, 45:71–81, 2017.

(Stoica and Söderström, 1981) Petre Stoica and Torsten Söderström. The Steiglitz-McBride identification algorithm revisited - Convergence analysis and accuracy aspects. *IEEE Transactions on Automatic Control*, 26(3):712–717, 1981.

(Strassen, 1969) Volker Strassen. Gaussian Elimination is not Optimal. *Numerische Mathematik*, 13(4):354–356, 1969.

(Suetens, 2009) Paul Suetens. *Fundamentals of Medical Imaging*. Second edition. Cambridge, United Kingdom: Cambridge University Press, 2009.

(Sutanto and Alleyne, 2015) Erick Sutanto and Andrew Alleyne. A semi-continuous Roll-to-Roll (R2R) electrohydrodynamic jet printing system. *IFAC Mechatronics*, 31:243–254, 2015.

(Syrmos et al., 1997) V. L. Syrmos, C. T. Abdallah, P. Dorato, and K. Grigoriadis. Static output feedback - A survey. *Automatica*, 33(2):125–137, 1997.

(Tabuada, 2007) Paulo Tabuada. Event-Triggered Real-Time Scheduling of Stabilizing Control Tasks. *IEEE Transactions on Automatic Control*, 52(9):1680–1685, 2007.

(Teng and Tsao, 2015) Kuo-Tai Teng and Tsu-Chin Tsao. A comparison of Inversion Based Iterative Learning Control Algorithms. In *Proceedings of the 2015 American Control Conference*, pages 3564–3569. Chicago, Illinois, 2015.

(Tien et al., 2005) Szuchi Tien, Santosh Devasia, Qingze Zou, and Santosh Devasia. Iterative Control of Dynamics-Coupling-Caused Errors in Piezoscanners During High-Speed AFM Operation. *IEEE Transactions on Control Systems Technology*, 13(6):921–931, 2005.

(Toivonen, 1992) H.T. Toivonen. Sampled-data Control of Continuous-time Systems with an H_∞ Optimality Criterion. *Automatica*, 28(1):45–54, 1992.

(Tomizuka, 1975) Masayoshi Tomizuka. Optimal Continuous Finite Preview Problem. *IEEE Transactions on Automatic Control*, 20(3):362–365, 1975.

(Tomizuka, 1987) Masayoshi Tomizuka. Zero Phase Error Tracking Algorithm for Digital Control. *Journal of Dynamic Systems, Measurement, and Control*, 109(1):65–68, 1987.

(Torfs et al., 1992) D. Torfs, J. De Schutter, and J. Swevers. Extended Bandwidth Zero Phase Error Tracking Control of Nonminimal Phase Systems. *Journal of Dynamic Systems, Measurement, and Control*, 114(3):347–351, 1992.

(Tousain et al., 2001) Rob Tousain, Eduard van de Meché, and Okko Bosgra. Design strategy for Iterative Learning Control based on Optimal Control. In *Proceedings of the 40th Conference on Decision and Control*, pages 4463–4468. Orlando, Florida, 2001.

(Tsopelakos and Papadopoulos, 2017) Aristomenis Tsopelakos and Evangelos Papadopoulos. Design and Evaluation of Dynamic Positioning Controllers

with Parasitic Thrust Reduction for an Overactuated Floating Platform. *IEEE Transactions on Control Systems Technology*, 25(1):145–160, 2017.

(Vaidyanathan, 1993) P. P. Vaidyanathan. *Multirate Systems and Filter Banks*. Upper Saddle River, New Jersey: Prentice-Hall, Inc., 1993.

(Valencia et al., 2015) Juan Valencia, Dip Goswami, and Kees Goossens. Composable Platform-Aware Embedded Control Systems on a Multi-Core Architecture. In *Proceedings of Euromicro Symposium on Digital System Design*. 2015.

(Valencia et al., 2016) Juan Valencia, E.P. (Eelco) van Horssen, Dip Goswami, W.P.M.H. (Maurice) Heemels, and Kees Goossens. Resource Utilization and Quality-of-Control Trade-off for a Composable Platform. In *Proceedings of the 2016 Design, Automation and Test in Europe Conference & Exhibition*, pages 654–659. Dresden, Germany, 2016.

(Vandebril et al., 2008) Raf Vandebril, Marc van Barel, and Nicola Mastronardi. *Matrix Computations and Semiseparable Matrices Volume 1: Linear Systems*. Baltimore, Maryland: The Johns Hopkins University Press, 2008.

(Verbaan, 2015) C.A.M. Verbaan. Robust Mass Damper Design for Bandwidth Increase of Motion Stages. Ph.D. thesis, Eindhoven University of Technology, Eindhoven, The Netherlands, 2015.

(Vidyasagar, 1986) M. Vidyasagar. On Undershoot and Nonminimum Phase Zeros. *IEEE Transactions on Automatic Control*, 31(5):440, 1986.

(Vinnicombe, 2001) Glenn Vinnicombe. *Uncertainty and Feedback - $\mathcal{H}_\infty$ Loop Shaping and the ν-gap metric*. London, Great Britain: Imperial College Press, 2001.

(Voigtländer, 2015) Bert Voigtländer. *Scanning Probe Microscopy: Atomic Force Microscopy and Scanning Tunneling Microscopy*. Springer, 2015, page 375.

(Voorhoeve et al., 2016) Robbert Voorhoeve, Nic Dirkx, Teun Melief, Wouter Aangenent, and Tom Oomen. Estimating structural deformations for inferential control: a disturbance observer approach. *IFAC-PapersOnLine* (7th Symposium on Mechatronic Systems), 49(21):642–648, 2016.

(Voorhoeve et al., 2018) Robbert Voorhoeve, Robin de Rozario, Wouter Aangenent, and Tom Oomen. Identifying Position-Dependent Mechanical Systems: A Modal Approach with Applications to Wafer Stage Control. *Submitted for journal publication* (arXiv: 1807.06942), 2018.

(Voulgaris et al., 1994) Petros G. Voulgaris, Munther A. Dahleh, and Lena S. Valavani. H^∞ and H^2 optimal controllers for periodic and multirate systems. *Automatica*, 30(2):251–263, 1994.

(Wallén et al., 2013) Johanna Wallén, Svante Gunnarsson, and Mikael Norrlöf. Analysis of boundary effects in iterative learning control. *International Journal of Control*, 86(3):410–415, 2013.

(Van de Wal et al., 2002) Marc van de Wal, Gregor van Baars, Frank Sperling, and Okko Bosgra. Multivariable $\mathcal{H}_\infty/\mu$ feedback control design for high-

precision wafer stage motion. *Control Engineering Practice*, 10(7):739–755, 2002.

(Wang et al., 2016) Cong Wang, Minghui Zheng, Zining Wang, and Masayoshi Tomizuka. Robust Two-Degree-of-Freedom Iterative Learning Control for Flexibility Compensation of Industrial Robot Manipulators. In *International Conference on Robotics and Automation*, pages 2381–2386. Stockholm, Sweden, 2016.

(Wang and Longoria, 2009) Junmin Wang and Raul G. Longoria. Coordinated and Reconfigurable Vehicle Dynamics Control. *IEEE Transactions on Control Systems Technology*, 17(3):723–732, 2009.

(Wang et al., 2014) Rongrong Wang, Zui Zhang, and Junmin Wang. Linear parameter-varying-based fault-tolerant controller design for a class of overactuated non-linear systems with applications to electric vehicles. *IET Control Theory & Applications*, 8(9):705–717, 2014.

(Wang and Lemmon, 2009) Xiaofeng Wang and Michael D. Lemmon. Self-Triggered Feedback Control Systems With Finite-Gain $\mathcal{L}_2$ Stability. *IEEE Transactions on Automatic Control*, 24(3):452–467, 2009.

(Wen and Potsaid, 2004) John T. Wen and Ben Potsaid. An Experimental Study of a High Performance Motion Control System. In *Proceedings of the 2004 American Control Conference*, pages 5158–5163. Boston, Massachusetts, 2004.

(Whitfield, 1987) A. H. Whitfield. Asymptotic behaviour of transfer function synthesis methods. *International Journal of Control*, 45(3):1083–1092, 1987.

(Van de Wijdeven and Bosgra, 2010) J. van de Wijdeven and O.H. Bosgra. Using basis functions in iterative learning control: analysis and design theory. *International Journal of Control*, 83(4):661–675, 2010.

(Van de Wijdeven et al., 2011) J. J. M. van de Wijdeven, M. C. F. Donkers, and O. H. Bosgra. Iterative learning control for uncertain systems: Noncausal finite time interval robust control design. *International Journal of Robust and Nonlinear Control*, 21:1645–1666, 2011.

(Xu et al., 2014) Wenkang Xu, Bing Chu, and Eric Rogers. Iterative learning control for robotic-assisted upper limb stroke rehabilitation in the presence of muscle fatigue. *Control Engineering Practice*, 31:63–72, 2014.

(Yamamoto, 1994) Yutaka Yamamoto. A Function Space Approach to Sampled Data Control Systems and Tracking Problems. *IEEE Transactions on Automatic Control*, 39(4):703–713, 1994.

(Yamamoto and Khargonekar, 1996) Yutaka Yamamoto and Pramod P. Khargonekar. Frequency Response of Sampled-Data Systems. *IEEE Transactions on Automatic Control*, 41(2):166–176, 1996.

(Zadeh, 1962) L. A. Zadeh. From Circuit Theory to System Theory. *Proceedings of the IRE*, 50(5):856–865, 1962.

(Zamani et al., 2016) Mohsen Zamani, Giulio Bottegal, and Brian D. O. Anderson. On the Zero-Freeness of Tall Multirate Linear Systems. *IEEE Transactions on Automatic Control*, 61(11):3611, 2016.

(Zattoni, 2014) Elena Zattoni. Geometric methods for invariant-zero cancellation in linear multivariable systems with application to signal rejection with preview. *Asian Journal of Control*, 16(5):1289–1299, 2014.

(Zheng et al., 2010) Jinchuan Zheng, Weizhou Su, and Minyue Fu. Dual-stage actuator control design using a doubly coprime factorization approach. *IEEE/ASME Transactions on Mechatronics*, 15(3):339–348, 2010.

(Zhou et al., 1996) Kemin Zhou, John C. Doyle, and Keith Glover. *Robust and Optimal Control*. Englewood Cliffs, New Jersey: Prentice Hall, 1996.

(Zou, 2009) Qingze Zou. Optimal preview-based stable-inversion for output tracking of nonminimum-phase linear systems. *Automatica*, 45(1):230–237, 2009.

(Zou and Devasia, 1999) Qingze Zou and Santosh Devasia. Preview-Based Stable-Inversion for Output Tracking of Linear Systems. *Journal of Dynamic Systems, Measurement, and Control*, 121(4):625–630, 1999.

(Zou and Devasia, 2004) Qingze Zou and Santosh Devasia. Preview-based optimal inversion for output tracking: Application to scanning tunneling microscopy. *IEEE Transactions on Control Systems Technology*, 12(3):375–386, 2004.

(Zou and Devasia, 2007) Qingze Zou and Santosh Devasia. Precision preview-based stable-inversion for nonlinear nonminimum-phase systems: The VTOL example. *Automatica*, 43(1):117–127, 2007.

(Zou and Liu, 2016) Qingze Zou and Jiangbo Liu. Multi-objective optimal trajectory design and tracking with non-periodic tracking-transition switching for non-minimum phase linear systems. *International Journal of Control*, 89(11):2371–2383, 2016.

(Van Zundert et al., 2015a) J.C.D. van Zundert, J.L.C. Verhaegh, W.H.T.M. Aangenent, T. Oomen, D. Antunes, and W.P.M.H. Heemels. Feedforward for Multi-Rate Motion Control: Enhanced Performance and Cost-Effectiveness. In *Proceedings of the 2015 American Control Conference*, pages 2831–2836. Chicago, Illinois, 2015.

(Van Zundert and Oomen, 2017a) Jurgen van Zundert and Tom Oomen. An Approach to Stable Inversion of LPTV Systems with Application to a Position-Dependent Motion System. In *Proceedings of the 2017 American Control Conference*, pages 4890–4895. Seattle, Washington, 2017.

(Van Zundert and Oomen, 2017b) Jurgen van Zundert and Tom Oomen. Inverting Nonminimum-Phase Systems from the Perspectives of Feedforward and ILC. *IFAC-PapersOnLine* (20th World Congress), 50(1):12101–12106, 2017.

(Van Zundert and Oomen, 2017c) Jurgen van Zundert and Tom Oomen. On Optimal Feedforward and ILC: The Role of Feedback for Optimal Perfor-

mance and Inferential Control. *IFAC-PapersOnLine* (20th World Congress), 50(1):6093–6098, 2017.

(Van Zundert and Oomen, 2017d) Jurgen van Zundert and Tom Oomen. Stable inversion of LPTV systems with application in position-dependent and non-equidistantly sampled systems. *International Journal of Control*, 2017. DOI: 10.1080/00207179.2017.1380315.

(Van Zundert and Oomen, 2018a) Jurgen van Zundert and Tom Oomen. Beyond Equidistant Sampling for Performance and Cost: A Loop-Shaping Approach Applied to a Motion System. *Accepted for International Journal of Robust and Nonlinear Control*, 2018.

(Van Zundert and Oomen, 2018b) Jurgen van Zundert and Tom Oomen. LPTV Loop-Shaping with Application to Non-Equidistantly Sampled Precision Mechatronics. In *Proceedings of the 15th International Workshop on Advanced Motion Control*, pages 467–472. Tokyo, Japan, 2018.

(Van Zundert and Oomen, 2018c) Jurgen van Zundert and Tom Oomen. On inversion-based approaches for feedforward and ILC. *IFAC Mechatronics*, 50:282–291, 2018.

(Van Zundert and Oomen, 2018d) Jurgen van Zundert and Tom Oomen. System Inversion from the Perspective of Inverse Model Feedforward with Application to a Nonminimum-Phase Benchmark System. In *Proceedings of the 4th International Workshop on Sensing, Actuation, Motion Control, and Optimization*, pages V3–12. Tokyo, Japan, 2018.

(Van Zundert et al., 2015b) Jurgen van Zundert, Joost Bolder, and Tom Oomen. Iterative Learning Control for Varying Tasks: Achieving Optimality for Rational Basis Functions. In *Proceedings of the 2015 American Control Conference*, pages 3570–3575. Chicago, Illinois, 2015.

(Van Zundert et al., 2016a) Jurgen van Zundert, Tom Oomen, Dip Goswami, and W.P.M.H. Heemels. On the Potential of Lifted Domain Feedforward Controllers with a Periodic Sampling Sequence. In *Proceedings of the 2016 American Control Conference*, pages 4227–4232. Boston, Massachusetts, 2016.

(Van Zundert et al., 2016b) Jurgen van Zundert, Joost Bolder, and Tom Oomen. Optimality and flexibility in Iterative Learning Control for varying tasks. *Automatica*, 67:295–302, 2016.

(Van Zundert et al., 2016c) Jurgen van Zundert, Joost Bolder, Sjirk Koekebakker, and Tom Oomen. Resource Efficient ILC: Enabling Large Tasks on an Industrial Position-Dependent Flatbed Printer. *IFAC-PapersOnLine* (7th Symposium on Mechatronic Systems), 49(21):567–574, 2016.

(Van Zundert et al., 2016d) Jurgen van Zundert, Joost Bolder, Sjirk Koekebakker, and Tom Oomen. Resource-efficient ILC for LTI/LTV systems through LQ tracking and stable inversion: Enabling large feedforward tasks on a position-dependent printer. *IFAC Mechatronics*, 38:76–90, 2016.

(Van Zundert et al., 2018a) Jurgen van Zundert, Fons Luijten, and Tom Oomen. Achieving Perfect Causal Feedforward Control in Presence of Nonminimum-

Phase Behavior - Exploiting Additional Actuators and Squaring Down. In *Proceedings of the 2018 American Control Conference*, pages 6031–6036. Milwaukee, Wisconsin, 2018.

(Van Zundert et al., 2018b) Jurgen van Zundert, Tom Oomen, Jan Verhaegh, Wouter Aangenent, Duarte J. Antunes, and W.P.M.H. Heemels. Beyond Performance/Cost Trade-Offs in Motion Control: A Multirate Feedforward Design with Application to a Dual-Stage Wafer System. *Accepted for IEEE Transactions on Control Systems Technology*, 2018.

(Van Zundert et al., 2018c) Jurgen van Zundert, Fons Luijten, and Tom Oomen. Exact and Causal Inversion of Nonminimum-Phase Systems: A Squaring-Down Approach for Overactuated Systems. *Submitted for journal publication*, 2018.

(Van Zundert et al., 2018d) Jurgen van Zundert, Wataru Ohnishi, Hiroshi Fujimoto, and Tom Oomen. Improving Intersample Behavior in Discrete-Time System Inversion: With Application to LTI and LPTV Systems. *Submitted for journal publication*, 2018.

(Van Zundert et al., 2018e) Jurgen van Zundert, Wataru Ohnishi, Hiroshi Fujimoto, and Tom Oomen. System Inversion for Sampled-Data Feedforward Control: Balancing On-Sample and Intersample Behavior. In *Submitted for conference publication*. 2018.

Dankwoord

De tijd vliegt als je het naar je zin hebt. De afgelopen vier jaar zijn voorbijgevlogen omdat het een geweldige ervaring was en ik er altijd veel plezier in had. Daar hebben veel mensen aan bijgedragen die ik hierbij dan ook graag wil bedanken.

Allereerst wil ik mijn promotoren Maurice en Tom bedanken. Maurice, bedankt voor de steun, het vertrouwen en de vrijheid die je mij gegeven hebt. Het is geweldig om te zien hoe snel je schakelt tussen de inhoud en de luchtige kant. Tom, bedankt voor de mogelijkheden die je mij geboden hebt, de prettige en open samenwerking en de vele interessante gesprekken, zowel op inhoudelijk als persoonlijk vlak. Over de jaren heen is 'Groep Oomen' echt een begrip geworden en daar mag je trots op zijn!

I would like to thank the committee members Bing Chu, Hans Butler, Hiroshi Fujimoto, Jeroen Voeten, and Wouter Aangenent for their time and effort taken for providing constructive feedback on this thesis and participating in the defense committee.

Het onderzoek beschreven in dit proefschrift maakt deel uit van een NWO-TTW Perspectief programma waar meerdere industriële partners bij betrokken zijn. Hierbij wil ik hen bedanken voor hun bijdragen en het waarborgen van de praktische relevantie van het onderzoek. De samenwerking met mijn directe projectgenoten Bram, João en Josh heb ik als bijzonder prettig ervaren en is een verrijking voor mijn onderzoek en mijzelf geweest. Daarnaast wil ik mijn projectleider Jeroen Voeten bedanken voor het bijeenbrengen van verschillende disciplines en de daaruitvolgende kruisbestuiving die zo belangrijk is.

Het onderzoek in dit proefschrift is mede tot stand gekomen door de hulp van studenten. Ik wil graag Bart, Enzo, Fons, Joey, Koen, Mark, Niek, Roel, Somanna en Ton bedanken voor hun bijdragen aan dit proefschrift, de interessante discussies en de leerzame momenten.

I would like to thank Hiroshi Fujimoto and his group for the privilege of visiting the University of Tokyo for three months, the hospitality, and the ski

lessons. A special thanks to Wataru Ohnishi for the fruitful collaboration, the interesting discussions, and showing me the beauty of Japan.

De plezierige werkomgeving die ik al die tijd heb gehad heb ik te danken aan de vele leuke collega's van Control Systems Technology en Dynamics & Control. Met jullie was elke pauze, borrel en conferentie genieten, en heb ik ook veel leuke tijden buiten het werk meegemaakt. Ik wil in het bijzonder mijn (oud-)kantoorgenoten Rick, Rolf en Robin bedanken voor het harde lachen en de memorabele momenten!

Ik wil mijn vrienden bedanken voor de vele mooie dingen die we samen hebben meegemaakt. Het is fantastisch om te zien dat, ondanks de spreiding over het (buiten)land, het elke keer weer als vanouds is als we elkaar zien! Ten slotte, wil ik mijn vader, moeder en broer bedanken voor het vertrouwen, de interesse in mijn onderzoek en de rust waar ik al die jaren blind op heb kunnen vertrouwen.

Jurgen van Zundert
Eindhoven, Oktober 2018

List of publications

Peer-reviewed journal articles

- Jurgen van Zundert, Fons Luijten, and Tom Oomen. Exact and Causal Inversion of Nonminimum-Phase Systems: A Squaring-Down Approach for Overactuated Systems. *Submitted for journal publication*, 2018.
- Jurgen van Zundert, Wataru Ohnishi, Hiroshi Fujimoto, and Tom Oomen. Improving Intersample Behavior in Discrete-Time System Inversion: With Application to LTI and LPTV Systems. *Submitted for journal publication*, 2018.
- Jurgen van Zundert, Tom Oomen, Jan Verhaegh, Wouter Aangenent, Duarte J. Antunes, and W.P.M.H. Heemels. Beyond Performance/Cost Trade-Offs in Motion Control: A Multirate Feedforward Design with Application to a Dual-Stage Wafer System. *Accepted for IEEE Transactions on Control Systems Technology*, 2018.
- Jurgen van Zundert and Tom Oomen. Beyond Equidistant Sampling for Performance and Cost: A Loop-Shaping Approach Applied to a Motion System. *Accepted for International Journal of Robust and Nonlinear Control*, 2018.
- Jurgen van Zundert and Tom Oomen. On inversion-based approaches for feedforward and ILC. *IFAC Mechatronics*, 50:282–291, 2018.
- Jurgen van Zundert and Tom Oomen. Stable inversion of LPTV systems with application in position-dependent and non-equidistantly sampled systems. *International Journal of Control*, 2017. DOI: `10.1080/00207179.2017.1380315`.
- Joost Bolder, Jurgen van Zundert, Sjirk Koekebakker, and Tom Oomen. Enhancing Flatbed Printer Accuracy and Throughput: Optimal Rational Feedforward Via Iterative Learning Control. *IEEE Transactions on Industrial Electronics*, 64(5):4207–4216, 2017.
- Jurgen van Zundert, Joost Bolder, Sjirk Koekebakker, and Tom Oomen. Resource-efficient ILC for LTI/LTV systems through LQ tracking and stable inversion: Enabling large feedforward tasks on a position-dependent printer. *IFAC Mechatronics*, 38:76–90, 2016.
- Jurgen van Zundert, Joost Bolder, and Tom Oomen. Optimality and flexibility in Iterative Learning Control for varying tasks. *Automatica*, 67:295–302, 2016.

Peer-reviewed articles in conference proceedings

- Jurgen van Zundert, Wataru Ohnishi, Hiroshi Fujimoto, and Tom Oomen. System Inversion for Sampled-Data Feedforward Control: Balancing On-Sample and Intersample Behavior. In *Submitted for conference publication*. 2018.
- Jurgen van Zundert, Fons Luijten, and Tom Oomen. Achieving Perfect Causal Feedforward Control in Presence of Nonminimum-Phase Behavior - Exploiting Additional Actuators and Squaring Down. In *Proceedings of the 2018 American Control Conference*, pages 6031–6036. Milwaukee, Wisconsin, 2018.
- Jurgen van Zundert and Tom Oomen. LPTV Loop-Shaping with Application to Non-Equidistantly Sampled Precision Mechatronics. In *Proceedings of the 15th International Workshop on Advanced Motion Control*, pages 467–472. Tokyo, Japan, 2018.
- Jurgen van Zundert and Tom Oomen. System Inversion from the Perspective of Inverse Model Feedforward with Application to a Nonminimum-Phase Benchmark System. In *Proceedings of the 4th International Workshop on Sensing, Actuation, Motion Control, and Optimization*, pages V3–12. Tokyo, Japan, 2018.
- Jurgen van Zundert and Tom Oomen. On Optimal Feedforward and ILC: The Role of Feedback for Optimal Performance and Inferential Control. *IFAC-PapersOnLine* (20th World Congress), 50(1):6093–6098, 2017.
- Jurgen van Zundert and Tom Oomen. Inverting Nonminimum-Phase Systems from the Perspectives of Feedforward and ILC. *IFAC-PapersOnLine* (20th World Congress), 50(1):12101–12106, 2017.
- Jurgen van Zundert and Tom Oomen. An Approach to Stable Inversion of LPTV Systems with Application to a Position-Dependent Motion System. In *Proceedings of the 2017 American Control Conference*, pages 4890–4895. Seattle, Washington, 2017.
- Jurgen van Zundert, Joost Bolder, Sjirk Koekebakker, and Tom Oomen. Resource Efficient ILC: Enabling Large Tasks on an Industrial Position-Dependent Flatbed Printer. *IFAC-PapersOnLine* (7th Symposium on Mechatronic Systems), 49(21):567–574, 2016.
- Jurgen van Zundert, Tom Oomen, Dip Goswami, and W.P.M.H. Heemels. On the Potential of Lifted Domain Feedforward Controllers with a Periodic Sampling Sequence. In *Proceedings of the 2016 American Control Conference*, pages 4227–4232. Boston, Massachusetts, 2016.
- J.C.D. van Zundert, J.L.C. Verhaegh, W.H.T.M. Aangenent, T. Oomen, D. Antunes, and W.P.M.H. Heemels. Feedforward for Multi-Rate Motion Control: Enhanced Performance and Cost-Effectiveness. In *Proceedings of the 2015 American Control Conference*, pages 2831–2836. Chicago, Illinois, 2015.
- Jurgen van Zundert, Joost Bolder, and Tom Oomen. Iterative Learning Control for Varying Tasks: Achieving Optimality for Rational Basis Functions. In *Proceedings of the 2015 American Control Conference*, pages 3570–3575. Chicago, Illinois, 2015.

Curriculum vitae

Jurgen van Zundert was born on December 16, 1990, in Zundert, The Netherlands. After finishing his secondary education at the KSE in Etten-Leur, The Netherlands, in 2009, he studied mechanical engineering at the Eindhoven University of Technology in Eindhoven, The Netherlands, where he obtained both his bachelor (2012) and master (2014) degree with great appreciation. During his master he performed an internship at the University of Queensland in Brisbane, Australia, where he worked on sensor evaluation for the purpose of automated driving in the mining industry. In his master thesis, he worked on task flexibility in iterative learning control for industrial printing systems, under the supervision of Joost Bolder, Tom Oomen, Sjirk Koekebakker (Océ Technologies), and Maarten Steinbuch.

In November 2014, Jurgen started his Ph.D. in the Control Systems Technology group at the Eindhoven University of Technology, under the supervision of Tom Oomen and Maurice Heemels. The Ph.D. research focuses on resource-aware control design for high-precision mechatronic systems. The work is part of the research programme Robust Cyber-Physical Systems (RCPS) (No. 12694) which is (partly) financed by the Netherlands Organisation for Scientific Research (NWO). In January-March 2018, Jurgen was a visiting researcher at the University of Tokyo, Tokyo, Japan, as part of a collaboration with Hiroshi Fujimoto and Wataru Ohnishi. His research interests include feedforward control, learning control, non-equidistant sampling, and multirate control.